MECHANICAL AND FUNCTIONAL PROPERTIES OF METALLIC GLASS LATTICES FABRICATED BY LASER POWDER BED FUSION

CONGRUI YANG

PhD

The Hong Kong Polytechnic University

2026

The Hong Kong Polytechnic University

Department of Industrial and Systems Engineering

Mechanical and Functional Properties of Metallic Glass Lattices Fabricated by Laser Powder Bed Fusion

Congrui Yang

A thesis submitted in partial fulfillment of the requirements for the degree of Doctor of Philosophy

August 2025

CERTIFICATE OF ORIGINALITY

I hereby declare that this thesis is my own work and that, to the best of my knowledge and belief, it reproduces no material previously published or written, nor material that has been accepted for the award of any other degree or diploma, except where due acknowledgement has been made in the text.

_____(Signed)

Congrui YANG (Name of student)

.

Abstract

The advancement of materials has long served as a cornerstone of societal progress, with each breakthrough contributing to substantial gains in productivity and technological capability. In the 21st century, the demand for high-strength metallic materials has become increasingly urgent, particularly in aerospace, aviation, and high-speed transportation industries. Among the most promising candidates for next-generation structural materials are metallic glasses (MGs)-that lack crystalline defects such as dislocations and grain boundaries, and exhibit a unique combination of metallic and glass-like properties. These characteristics endow MGs with exceptional mechanical strength, elasticity, and corrosion resistance. However, widespread engineering application of MGs has been limited by manufacturing constraints, especially in fabricating complex architectures.

The emergence of additive manufacturing (AM) has overcome many of these challenges, enabling the production of 3D-printed MG lattice structures with tunable geometries and mechanical properties. Such lattices embody the "material-structure-function" synergy and offer new avenues for tailoring performance in high-performance applications. Despite these advances, the mechanical behavior, failure mechanisms, and functional capabilities of MG lattice structures remain insufficiently understood. In particular, quantitative relationships between microarchitecture, defect distribution, and deformation modes are not well established. Furthermore, the effects of processing-induced heterogeneities such as partial crystallization, porosity, and surface defects on

the long-term structural reliability and functional performance of MG lattice structures remain largely unexplored.

To address these gaps, this thesis investigates the mechanical and functional performance of L-PBF fabricated MG lattices, with the dual aims of establishing robust structure–property relationships and unlocking new application potential. First, the compressive behavior and fracture mechanisms of MG lattices fabricated by conventional L-PBF technology, including strut-based body-centred cubic (BCC) and shell-based triply periodical minimal surfaces (TPMS) architectures, were systematically examined. This investigation aimed to elucidate how structural design influences damage tolerance and energy absorption.

Subsequently, bio-inspired TPMS architectures were fabricated using μL-PBF technology to synergistically enhance both strength and ductility. In situ X-ray computed tomography (XCT) was employed to directly observe their failure processes, leading to the proposal of a hybrid ductilization mechanism that integrates micro- and macro-scale effects in MG lattices.

Lastly, we explored the functional potential of MG lattices in catalysis by developing a comprehensive strategy for high-performance MG electrocatalyst design via multiscale structural engineering. Zr-based MG TPMS lattices were 3D-printed as mechanically robust, ultra-efficient mass transport scaffolds, followed by pulsed electrodeposition (PED) of NiMo amorphous microparticles. The PED process produced hydrangea-like NiMo particles with controlled amorphous heterogeneity, in

which rich compositional interfaces ($Ni_{78}Mo_{22}$/$Ni_{68}Mo_{32}$) were formed, providing abundant interfacial sites that facilitate catalytic reactions. This hierarchical catalyst architecture achieved simultaneous optimization of catalytic activity, mechanical integrity, and mass transport, delivering exceptional overall water-splitting performance and opening new application avenues for 3D-printed MG lattices.

The findings of this work provide essential insights into the structure-mechanical-functional correlations in MG lattices and lay the foundation for the development of advanced, multifunctional cellular materials for future engineering and energy-related applications.

Publications during the PhD period

1. **Yang C.,** Ouyang D., Zhang L., Zhang Y., Tong X., Ke H.*, Chan KC.*, Wang W.*, 2024. The enhancement of damage tolerance of 3D-printed high strength architected metallic glasses by unit cell shape design, Addit. Manuf. 85:104125. (IF：10.3)
2. **Yang C.,** Ding J., Qu S., Ouyang D., Zhang L., Zhang Y., Ke H. *, Song X. *, Chan KC. *, Wang W. *, 2025. High strength bioinspired cellular metallic glasses with excellent energy absorption, Acta Mater. 285:120688 (IF: 8.3)
3. **Yang C.,** Pei C.[#], Sun S., Zhang H., Ke H.*, Ouyang D., Zhang L., Ding H., Zhang Y., Qian Y., Sun B., Chan KC.*, Wang W.*, Multiscale structure engineering in hierarchical metallic glass catalysts for ultra-efficient water splitting, (Submitted to jornal)
4. Zhang Y., **Yang C.,** Tong X., Zhou J., Xiao M., Ke H., Chan KC. *, Wang W. *, 2025. Oxidation sequence modulation induced superior high-temperature tribological performance of Ti-Hf-Nb-V refractory high entropy alloy fabricated through directed energy deposition. Rare metals, 44:2695.
5. Zhang, Y**.**, **Yang, C.**, Ke, H.*, Chan, K.C.*, Wang, W., 2024. A study on the microstructure and mechanical behavior of CoCrFeNi high entropy alloy fabricated via laser powder bed fusion: Experiment and crystal plasticity finite element modelling. Mater. Sci. Eng. A. 893, 14611.
6. Zhang, Y., Yu, K., Qin, B., **Yang, C**., Ye, S., Feng, C., Zhang, F., Ouyang, D., Liu, L., Ke, H.*, Chan, K.C.*, Wang, W., 2024. Origins of strength stabilities at elevated

temperatures in additively manufactured refractory high entropy alloy. Mater. Sci. Eng. A. 915, 147225.

7. Chen C., Pu Z., Qin B., Wang P., **Yang C.**, Chan KC.*, 2024. Elastocaloric effect of NiTi shape memory alloys manufactured by laser powder bed fusion. JMR&T, 33: 3439-3451.

Acknowledgements

I am incredibly grateful to my supervisors, Prof. K.C. Chan and Prof. Weihua Wang, for their unwavering support throughout my four-year PhD journey. I deeply appreciate Prof. Chan's encouragement to pursue my research interests, even when they seemed risky, and his flexibility and willingness to help at any time. His kindness and approach to life have also left a lasting impact on me. I often felt like a kite, exploring freely in the vast academic sky-yet it was Prof. Chan who held the string, keeping me on the right course while granting me the freedom to explore.

I am equally thankful to Prof. Wang for his invaluable guidance, teaching, and mentorship. He encouraged bold innovation and taught us how to break cognitive boundaries. Every time I listened to his lectures, I was reminded of how much more I had to learn and how shallow my understanding of the world still was.

My heartfelt thanks go to Prof. Haibo Ke of the Amorphous Materials Group at SLAB for his generous support throughout this research. From him, I learned the value of optimism and perseverance, as well as what it means to become an independent researcher. The resources provided by SLAB were essential to the success of this work. I also sincerely appreciate the financial support and access to key research facilities that enabled me to carry out this project. I am grateful to PolyU as well, for granting me access to its cutting-edge equipment and research resources, which have been vital to my progress.

Special thanks go to Prof. Xu Song from CUHK and his team members, Dr. Shuo Qu and Dr. Junhao Ding, for their support with L-PBF equipment and experiments. My experience conducting experiments in Prof. Song's lab was immensely rewarding—I gained valuable insight into their deep expertise in AM metallic lattice structures, which continues to inspire me.

I am also deeply thankful to Dr. Di Ouyang from WUT for his early guidance, helping me navigate how to choose a doctoral topic and write academic papers. His advice has had a lasting impact. I also wish to thank Dr. Lei Zhang from NCU for generously teaching me various simulation methods and offering valuable feedback on my manuscripts. Our frequent discussions about doing meaningful research continue to inspire me. If this thesis can provide even a small spark of insight to others in the field, I believe our conversations were truly worthwhile.

My gratitude also goes to my collaborator, Dr. Chaoqun Pei from SZU, for his active involvement in catalytic research discussions and his many insightful ideas. Together, we explored numerous experimental paths. His enthusiasm for science has been infectious and has driven me to pursue the unknown with even greater determination. I also appreciate the valuable suggestions offered by Prof. Lin Liu from HUST, a renowned expert in AM metallic glasses.

My life at PolyU and SLAB has been greatly enriched by my colleagues. I have received generous help and support from Dr. Yongyun Zhang, Dr. Changyong Chen, Dr. Jiaqiang Li, Dr. Ze Pu, Mr. Baliang Qin, Mr. Pengbo Wang, and all other group

members at PolyU. I’m fortunate to have had such wonderful companions in both life and research. My special thanks also go to Mr. Yuyang Qian, Mr. Zida Zhang, Dr. Huaping Ding, Dr. Liliang Shao, Dr. Hang Zhao, Dr. Yuee Zhang, Mr. Rongsheng Bai, Mr. Shilong Sun, Mr. Linchen Liu, Mr. Wentao Cai, Mr. Dingrong Zuo, and everyone in the Amorphous Materials Group at SLAB.

I am also very thankful to my long-time friend Yinghui Shang from CityU. Over the past eight years, from undergraduate to PhD life, we’ve supported and encouraged each other through every high and low. You’ve always been there to catch me when I fell apart emotionally, and this lifelong friendship is something I will treasure forever.

Lastly, I dedicate this to those who know I am not perfect, but still love me. I thank my family, especially my parents, for supporting every decision I’ve made and for giving me a life free of worry. Their unconditional love allowed me to pursue my academic dreams with courage, happiness, and peace of mind.

And to the version of myself who has faced failure and setbacks but continues to move forward with confidence and belief in tomorrow-this is for you. These four years have been filled with growth, and I look forward to the future with hope and determination.

Table of contents

List of figures and tables

Chapter 1 Introduction

1.1 Research background

The importance of material progress to the development of human society is self-evident, as each new material innovation brings about a significant increase in social productivity. In the 21st century, with the development of the advanced manufacturing industry, high-strength metal materials have become increasingly indispensable in the design of components in aerospace, aviation, and high-speed rail transportation. Consequently, the demand for high-strength metal materials is more urgent than ever. In recent decades, a series of high-performance advanced metal materials have been developed. Metallic glasses (MGs), as a typical representative of the new high-strength metal structural materials, show great promise for engineering applications. Lattice metamaterials have recently gained attention as a class of architected materials that combine exceptional physical properties with significant potential for lightweight structural applications. Advances in additive manufacturing (AM) now enable the fabrication of these materials with highly complex microarchitectures, thereby expanding their use across diverse multi-physical environments. Metamaterials are a class of architected materials whose unique properties are determined primarily by their internal microarchitectures rather than their chemical composition. A broad spectrum of unconventional physical properties can be realized in metamaterials through the careful customization of their internal architecture. Lattice metamaterials, as a prominent subclass, consist of periodic arrangements of unit cells and offer substantial

promise for lightweight structural applications. The spatial organization of a lattice's architecture serves as the primary criterion for its classification into homogeneous or inhomogeneous forms. Furthermore, homogeneous lattices are sub-classified based on the constitutive geometry of their unit cells, encompassing categories like shell, plate, truss, hybrid, and hierarchical structures [1, 2].

To date, considerable effort has been dedicated to developing new lattice metamaterials that possess superior mechanical and physical characteristics, as well as to exploring their applications across various industries. To achieve a wide range of unconventional behaviors, considerable effort has been directed toward elucidating the intrinsic relationships between lattice geometries/configurations and their mechanical responses. Moreover, lattice metamaterials have also been engineered to exhibit a variety of unconventional physical properties, such as acoustic [3], electromagnetic/optical [4], thermal [5], and other functional responses [6, 7]. As a result, they hold great promise for multifunctional applications across diverse fields. However, current studies on lattice metamaterials largely focus on materials that can be readily fabricated using established AM techniques. In contrast, some emerging materials with superior intrinsic properties have yet to be widely introduced into the lattice metamaterials domain, mainly due to the challenges associated with their processing and fabrication. Overcoming these barriers and integrating such advanced materials into lattice architectures will not only enrich the design space of

metamaterials but also open up new opportunities for achieving unprecedented combinations of mechanical and multi-physical functionalities.

Metallic glasses (MGs) are typically formed by high-speed cooling, which prevents the internal atoms from crystallizing. As a result, MGs do not have a periodic translational symmetry process, and they are also known as amorphous alloys. Unlike traditional crystalline metal materials, MG exhibits short-range ordered but long-range disordered structural characteristics, without dislocations, grain boundaries, and other microstructural defects. Because they are mainly composed of metal elements and a glassy microstructure, MGs possess both metallic and glass properties. Consequently, MGs exhibit many special mechanical, physical, and chemical properties that are different from those of traditional metallic materials, attracting continuous research interest from physicists and materials scientists worldwide.

The application of MG has largely been limited to fabrication technology. With the rapid development of advanced manufacturing technologies, the challenge of manufacturing cellular MG with complex geometries by conventional manufacturing methods has been addressed. Mature AM technology creates more possible applications for MGs; one aspect of this is 3D-printed MG lattice structures. It has been shown that 3D lattice materials are particularly suitable for the advanced design concept of "material-structure-function" synergy due to their unique advantages, such as high porosity, high specific stiffness, and designability, especially when compared with other porous materials. However, the properties of 3D-printed MG lattice structures remain

largely unexplored, and both their underlying mechanisms and characteristic behaviors are still not well understood.

Thus, this thesis investigates the mechanical and functional properties of 3D-printed MG lattice structures. The compressive behavior and fracture mechanisms were systematically studied to establish structure-property relationships, addressing the current lack of research in this area. The findings lay the groundwork for future efforts to predict mechanical performance based on structural design. Additionally, the mechanical and functional evaluations provide performance data and support the potential application of 3D-printed MG lattices in advanced engineering systems.

1.2 Research objectives

The primary goal of this research study is to fabricate MG lattice structures that exhibit high strength, excellent energy absorption ability, and outstanding catalytic performance through the lattice structure design via Laser Powder Bed Fusion (L-PBF) technology. The aim is to develop novel cellular materials for engineering applications and other functional applications. The project is structured into the following three key areas:

(1) To enhance the damage tolerance of the 3D-printed MG lattices through unit cell shape design, and to avoid the catastrophic failure of the MG lattices.

(2) To utilize bio-inspired structures to further enhance the strength and ductility of 3D-printed MG lattices fabricated via μL-PBF technology. To achieve energy absorption capacities that surpass those of conventional cellular

materials and to elucidate the fracture mechanisms of MG lattices using in-situ X-ray computed tomography (XCT).

(3) To further explore the functional properties of the 3D-printed MG lattices and to achieve outstanding catalytic performance through multi-scale structure modulation.

1.3 Outline of the thesis

This thesis is organized into eight chapters. The current chapter provides an introduction to the MG and lattice structures, as well as the primary research gaps and objectives.

Chapter 2 offers a comprehensive literature review, highlighting various aspects of this project: the development history of MGs, AM technology, metallic lattice structures, and MG lattice structures fabricated by L-PBF process and the lack on research of the 3D-printed MG lattices.

Chapter 3 describes the research methodology, including the materials and geometrical modeling, fabrication, measurements, and microstructure characterization. Theoretical computational approaches, such as the finite element method and finite volume method, are also covered.

Chapter 4 presents the main research results and discussion on enhancing the damage tolerance of the 3D-printed MG lattices through the unit cell shape design.

Chapter 5 presents the main research results and discussion on improving the strength and ductility of the 3D-printed MG lattices through bio-inspired structure design.

Chapter 6 presents the main research results and discussion on the excellent catalytic performance of the 3D-printed MG lattices achieved through multi-scale structural engineering.

Chapter 7 provides a summary and the conclusions drawn from the thesis.

Chapter 8 outlines future research directions for exploring 3D-printed MG lattices.

Chapter 2 Literature review

2.1 Overview

This chapter provides a comprehensive overview of the scholarly research on the topic of this doctoral project. It begins with an introductory overview in Section 2.1, setting the stage for the detailed discussions that follow. Section 2.2 delves into the concept of MGs, covering their definition, microstructure, development, main preparation method, and distinctive properties. Following this, Section 2.3 explores the additive manufactured MGs, such as different manufacturing techonoly and microstructure of MGs, and the defects in 3D-printed MGs. Section 2.4 then shifts the focus to 3D-printed metallic lattice structures, offering an in-depth examination of their design principles, structural classifications, structure-property-mechanism relationships, as well as their unique properties and applications. Section 2.5 extends further to the properties and potential applications of 3D-printed MG lattice structures. The chapter concludes with Section 2.6, which summarizes the key findings and insights gleaned from this systematic review.

2.2 Development and processing of MGs

Glasses are regarded as the fourth class of conventional matter along with gases, liquids and crystals, which exhibit a disordered atomic structure similar to liquids, but behave mechanically like solids. They have been used by humans for more than 3000 years and greatly promoted the development of modern sciences. Among diverse kinds

of glasses, MGs which are primarily composed of metallic elements are rather newcomers to the glass family.

2.2.1 Forming methods of MGs

Since Duwez [8] first produced micrometer-scale amorphous $Au_{75}Si_{25}$ metallic ribbons in 1960 by rapidly quenching molten metal onto a fast-spinning copper wheel , MGs began to draw research attention. With advancements in related theories and processing techniques, a significant breakthrough came in 1975 when Chen [9] fabricated Pd-Cu-Si amorphous alloy rods with diameters between 1 and 3 mm via water quenching, marking the first time MGs reached the millimeter scale and thus initiating the era of BMGs. In 1984, Kui et al. [10] developed centimeter-sized amorphous rods of $Pd_{40}Ni_{40}P_{20}$ by purifying the melt with a fluxing agent (B_2O_3) to reduce heterogeneous nucleation, indicating another major advancement in BMG fabrication.

Although considerable progress has been made in alloy design and fabrication methods—enabling the production of large-sized BMGs-their application was long constrained by the high cost of Pd, relegating BMGs to the realm of fundamental scientific research with limited commercial use. As a result, the development of BMGs entered a period of stagnation. In the 1990s, Inoue and Johnson revitalized the field by adopting a multi-component alloy design strategy. This approach increased the complexity of the alloy systems and the viscosity of the molten metals, leading to the discovery of a wide range of new BMG-forming systems with excellent glass-forming

ability (GFA), such as Pd-based [11], Au-based [12], Cu-based [13], Zr-based [14] , Mg-based [15], Al-based [16], Fe-based [17], Co-based [18], Ni-based [19], and rare-earth-based alloys [20], ushering in a new era for MGs.

With the rapid advancement of BMGs, Inoue [21] proposed three empirical rules for forming BMGs: (1) the alloy must contain at least three elements; (2) the atomic size difference among major elements should exceed 12%; and (3) the mixing enthalpy between the main components should be negative. Despite being empirical, these criteria have guided the development of many high-GFA systems. For example, the $Pd_{42.5}Cu_{30}Ni_{7.5}P_{20}$ alloy developed by Nishiyama et al. [22] currently holds the record for the highest glass-forming ability, with fully amorphous samples reaching diameters up to 80 mm.

At present, casting and thermoplastic forming are the mainstream techniques for shaping BMGs. The casting method involves rapidly injecting the molten alloy into a pre-designed mold, allowing it to solidify into an amorphous state with minimal shrinkage, as the transition is not a first-order phase change [23]. This feature enables high dimensional accuracy in cast components, which are already being used in fields such as mobile phone hinges, frames, card slots, and watch cases [24]. However, due to the critical cooling rate required for amorphization, casting is limited to simple, thin-walled parts. Additionally, the process is highly sensitive to raw material purity and vacuum conditions, which hampers further application.

In contrast, thermoplastic forming involves heating BMGs into their supercooled liquid region, where they exhibit low viscosity and can be shaped more easily. Compared to casting, which requires high vacuum and rapid cooling, thermoplastic forming can be performed in air with simple air-cooling afterward, significantly lowering the environmental constraints. It also allows for high-precision fabrication, including nanoscale features as small as a few tens of nanometers [25]. However, because BMGs remain amorphous in the supercooled liquid region only for a short processing window, this limits the ability to form large, complex 3D components using this method.

Therefore, developing a reliable forming technique capable of producing large, geometrically complex BMG parts remains an urgent challenge in the field of MGs.

2.2.2 Mechanical, functional, and structural characteristics of MGs

Due to the unique disordered atomic structure of MG, compared with the traditional crystalline alloy materials, MG has unique performance characteristics in many aspects.

(1) Excellent mechanical properties. MG is generally characterized by high strength, high hardness and high fracture toughness. So far, the highest reported strength among bulk metallic materials is the compressive strength of Co–Fe–Ta–B bulk glass, reaching 5185 MPa [26]. As shown in **Fig 2. 1**. The highest fracture strength amorphous alloy system is the $Co_{55}Ta_{10}B_{35}$ system, which can reach 6 GPa [27]. The highest fracture toughness is 200 MPa $m^{1/2}$ of Pd-based MG [28]. In addition, MG is

not only characterized by self-sharpening during the fracture process, but also its fracture toughness increases with the increase of strain rate during the dynamic deformation process under the action of high-speed load, which makes it one of the most excellent materials for the core of armor-piercing bullets found so far. These excellent mechanical properties make metal glass show attractive application prospects in structural materials. At present, high-precision products such as micro gears and folding cell phone hinges prepared with metal glass have been gradually popularized and applied in high-end 3C electronic products.

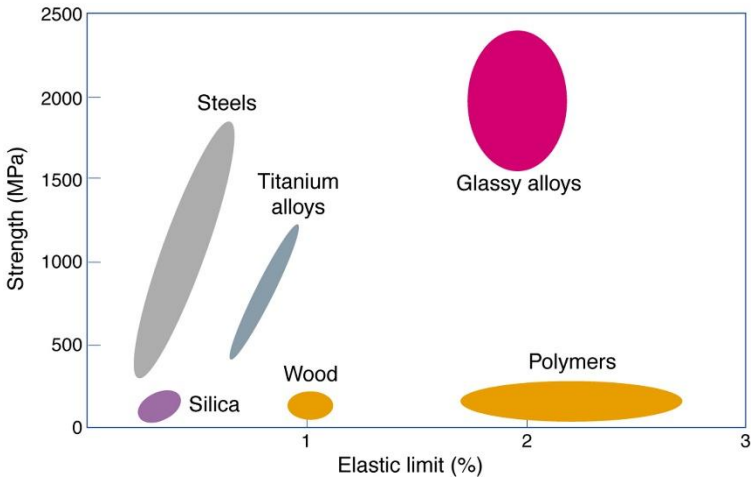

Fig 2. 1 The strength and elastic limit of BMG comparison with other materials.

(2) Large elastic limit. The maximum elastic strain of amorphous alloys can be up to 2.2%, while the elastic limit of conventional crystalline materials is usually less than 0.5%, so amorphous alloys have higher elastic specific function, for example, Zr-based BMG have an elastic specific function of 19 mJ/m^2, which is about nine times higher than that of the most elastic spring steel (2.24 mJ/m^2) [29].

(3) Superplasticity in the supercooled liquid phase region. MG exhibits viscous flow behavior in the supercooled liquid phase region, which is characterized by superplastic deformation, and the elongation of some alloy compositions is even greater than 15,000% [30]. Utilizing superplasticity, MG can be accurately pressed and molded in this temperature interval to achieve near-net-shape, and thus it is also widely used in the production of a variety of fine components.

(4) Excellent soft magnetic properties. Due to magnetic near-neighbor exchange interactions, MG exhibits macroscopic ferromagnetism. In addition, the structural isotropy makes it have small anisotropy, which is also one of the important reasons for its excellent soft magnetic properties [31]. Among the many soft magnetic properties, scholars currently focus on the high saturation magnetic induction B_s, low coercivity H_c, high permeability μ_e, and low loss of iron-based MGs [32].

(5) Excellent corrosion resistance. Corrosion resistance is one of the key evaluation criteria for engineering structural materials. Unlike crystalline materials, MGs lack grain boundaries, phase boundaries, and other crystal defects that are typically prone to corrosion. They also feature a uniform composition that can incorporate a high concentration of elements capable of forming stable passive films. In addition, MGs possess high hardness and strong adhesion between the passive film and the substrate, making the film less likely to peel or delaminate. Since their discovery, the outstanding corrosion resistance of MGs has attracted significant attention [33].

(6) Excellent radiation resistance. With the growing emphasis on carbon peaking and carbon neutrality strategies, nuclear energy has attracted increased attention, thereby driving demand for materials with outstanding radiation resistance. Unlike conventional crystalline materials that suffer from displacement damage under irradiation, MGs possess a unique topologically disordered structure that imparts excellent radiation tolerance. Among them, Fe-based MGs offer a combination of high strength, high hardness, excellent corrosion resistance, high glass transition temperature, thermal stability, and low radioactivity. Furthermore, they are cost-effective and can be fabricated under relatively lenient conditions, making them highly promising candidates for applications in the nuclear energy sector [34].

(7) Excellent electrocatalytic performance. MGs can serve as ideal precursors for the fabrication of electrocatalytic materials via dealloying, offering several key advantages: (i) Their simple atomic structure facilitates the synthesis of nanoporous metals with uniform pore structures; (ii) The multicomponent composition of the precursors provides a broad compositional range and tunable elements, enabling pore structure modulation through alloying strategies; (iii) The precursors possess excellent flexibility, allowing for the fabrication of flexible, self-supporting electrodes when combined with suitable dealloying processes. By tailoring the precursor composition, it is possible to synthesize binary or even multicomponent nanoporous metals that combine high structural stability with superior catalytic activity.

However, MGs also have an obvious disadvantage, namely the intrinsic brittleness of MGs. MGs do not have a dislocation-dominated slip deformation mechanism, and all the plastic deformation during deformation is concentrated in nanometer-wide localized shear bands [35]. The material undergoes adiabatic temperature rise in the shear zone [36], leading to a decrease in viscosity in this region, which quickly transforms the shear zone into a crack and eventually leads to brittle fracture of the amorphous alloy. In order to solve the brittle problem of MGs, researchers have conducted extensive research on this issue, and the main idea at present is to introduce a non-uniform structure in MGs, thus hindering the rapid expansion of a single shear band and further inducing the sprouting of multiple shear bands, as a way to improve the plasticity of amorphous alloys and solve the problem of brittle fracture. One of the two ways in which the non-homogeneous structure can be introduced is by introducing a heterogeneous amorphous phase in the amorphous matrix [37, 38], and the other is by introducing a crystalline phase in the amorphous matrix [39, 40].

2.3 Additive manufacturing of MGs

MGs have a series of advantages over crystalline alloys of the same composition, such as high strength, high elastic limit, excellent soft magnetic properties, excellent wear and corrosion resistance due to their long-range disordered atomic arrangement. However, MGs require rapid cooling from the molten state, which limits the achievable size and shape of MGs and hinders their development and application as emerging structural materials. In recent years, the emergence of 3D printing technology, thanks

to its layer-by-layer processing characteristics, has enabled formed into any complex shape parts, which provides a new idea to solve the two problems of small size and shape limitation of MG forming. This technology is different from the traditional machining method "subtractive manufacturing". Instead, it is an "additive manufacturing" process. First, a 3D digital model of the part is constructed by computer, then according to the process requirements, the model is divided into a series of two-dimensional structures in the height direction according to a certain layer thickness. Finally, the material is stacked layer by layer according to the shape of each layer to produce the final three-dimensional structure. Theoretically, this processing method can produce any complex three-dimensional structure, which meets the modern manufacturing industry's demand for individualized and customized products.

2.3.1 Additive manufacturing approaches for MGs

In recent years, AM technology has rapidly developed into a novel manufacturing technique based on the principle of layer-by-layer material deposition. By transforming complex three-dimensional processing into simplified two-dimensional operations, it significantly reduces the difficulty of fabricating intricate components. This technology is particularly suitable for shaping complex amorphous alloy parts and holds promise for solving the forming challenges that traditional methods cannot overcome, thereby offering a new pathway for the engineering application of amorphous alloys [41].

In 2009, Zheng et al. from the University of California, Davis [42] were the first to report the fabrication of Fe-based MGs using Directed Energy Deposition (DED) 3D

printing with coaxial powder feeding. However, severe crystallization was observed in the lower layers of the 10 mm × 10 mm sample, with only a small amount of amorphous phase retained in the topmost layer. In 2012, Huang Weidong's team from Northwestern Polytechnical University in China [43-45] began investigating the DED 3D printing of Zr-based amorphous alloys. They found that crystallized phases were distributed in the heat-affected zone, while the molten pool region remained fully amorphous. They also revealed the influence of the initial powder particle size on the amorphous content of the final printed part.

In 2013, the Eckert group at the IFW Dresden in Germany [41] became the first to report the use of L-PBF to print Fe-based amorphous alloys, successfully producing three-dimensional scaffold structures. Their study revealed that the scaffolds exhibited a nearly fully amorphous, single-phase structure. Subsequently, other alloy systems such as Zr, Fe, Ti, and Cu based amorphous alloys have also been investigated using L-PBF.

Currently, the main 3D printing technologies for amorphous alloys include the following:

(1) Laser Powder Bed Fusion (L-PBF):

This technique uses powder as the raw material and relies on a high-energy laser beam for layer-by-layer fusion. With a small laser spot size (less than 80 μm) and precise layer thickness control, L-PBF offers high forming accuracy. More importantly, the high scanning speed (up to 15 m/s) leads to rapid cooling of the molten pool (10^4–

10^6 K/s), which promotes the rapid solidification necessary for forming amorphous phases [42, 46].

(2) Directed Energy Deposition (DED):

In DED, powder is continuously blown into a laser focal point on the part's surface, where it melts and solidifies to form the component. Unlike L-PBF, DED does not require a preformed powder bed, making it suitable for large-scale parts due to its faster build speed and larger working envelope [47]. However, the larger laser spot size (0.5–5 mm) and lower scanning speed result in slower cooling rates, making crystallization more likely in amorphous alloys.

(3) Thermal Spray 3D Printing (TS3DP):

Originating from thermal spray coating techniques, TS3DP involves spraying amorphous powders into a hollow mold. After mold removal, the part retains its intended shape. Only the powder surface melts and deposits at ultra-high speeds, enabling both dense microstructure and sufficient cooling to avoid crystallization. This method is suitable for brittle amorphous alloys (e.g., Fe-, Ni-based), but tends to introduce oxides, limiting its use to oxidation-resistant systems [48].

(4) Fused Filament Fabrication (FFF):

Widely used in thermoplastic printing, FFF leverages the thermoplasticity of amorphous alloys, which soften and become deformable above their glass transition temperature. Exploiting their superplasticity in the supercooled liquid region, FFF

enables metallurgical bonding between layers at lower temperatures, avoiding melting-induced crystallization or cracking. However, it is only applicable to alloys with wide supercooled liquid regions and low viscosity [49].

(5) Laser-Induced Forward Transfer (LIFT):

LIFT is a micro/nanoscale 3D printing technique in which amorphous alloy films are first deposited onto a transparent substrate. Pulsed lasers then melt the film into droplets, which are ejected and stacked layer by layer onto a receiving substrate to form 3D structures. With extremely high cooling rates (up to 10^8–10^{11} K/s), LIFT enables forming even alloys with poor glass-forming ability [50].

(6) Laser Foil Printing (LFP):

Using amorphous alloy foils as the feedstock, LFP involves layer-by-layer laser welding and contour cutting to produce large, complex parts. It features low material cost and high density in printed parts. However, the need to repeatedly fix foils and cut boundaries layer-by-layer results in low processing efficiency, limiting its widespread application [51].

(7) Direct Ink Writing (DIW):

DIW mixes amorphous alloy powders with polymer binders to form inks, which are extruded and deposited along a predefined path to build 3D green bodies. After curing, the binder is removed via plasma sintering to obtain fully amorphous structures. Though DIW uses simple equipment and provides high precision, it requires highly

flowable ink precursors and optimized post-treatment to produce high-quality amorphous parts [52].

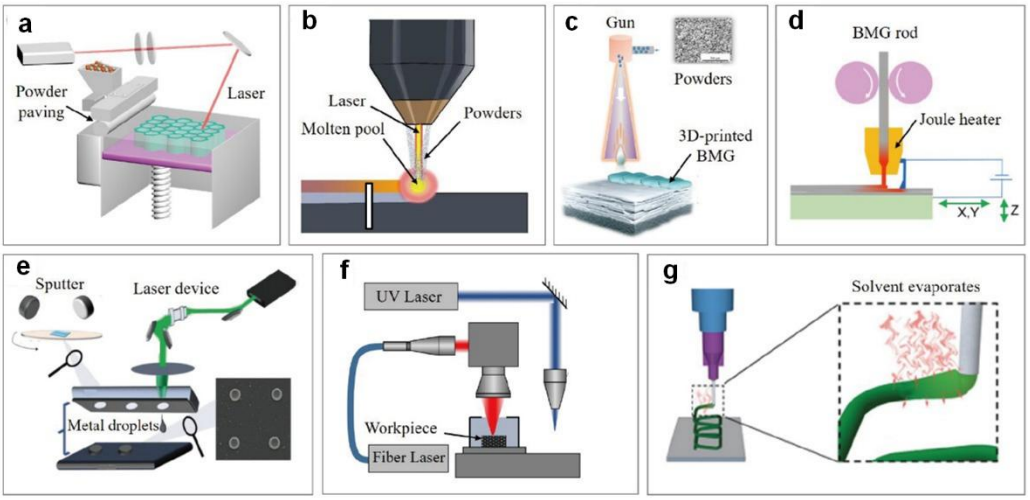

Fig 2. 2 3D printing techniques for BMGs. (a) Laser powder bed fusion [53]; (b) directed energy deposition[54]; (c) thermal spray 3D printing [48]; (d) fused filament fabrication [49]; (e) laser induced forward transfer [50]; (f) laser foil printing [55]; (g) direct ink [52].

As illustrated in **Fig 2. 2**, a wide variety of 3D printing techniques for MGs exist, each with its own advantages and limitations. Among them, L-PBF and LFP, both utilizing high energy laser beams, have attracted the most research attention due to their ability to produce parts with high amorphous content, minimal porosity, and excellent mechanical properties.

Although DED also employs high-energy lasers, its slower scanning speeds lead to reduced cooling rates and consequently lower amorphous content. In contrast, FFF and DIW avoid high-energy beams, offering simpler setups and lower costs. However, their use is restricted to specific alloy systems, and the weak interlayer bonding limits their suitability for load-bearing structural applications.

TS3DP offers high forming speed and density, making it ideal for large-scale production. However, oxide formation on powder surfaces can significantly degrade mechanical performance, restricting it to oxidation-resistant alloys. LIFT, while offering high precision at the micro/nanoscale, suffers from low efficiency and is not suitable for large-scale part fabrication.

In conclusion, the optimal 3D printing technique should be chosen based on the characteristics of the amorphous alloy system and the specific requirements of the target part.

2.3.2 Microstructures and defects in 3D-printed MGs

As mentioned above, the most widely used technologies at present are L-PBF and DED, both of which use laser beams as the energy source. This is mainly because these two laser-based 3D printing methods effectively address the issue of metallurgical bonding between layers, resulting in printed parts with superior mechanical properties.

The parameters of the laser 3D printing process have an important impact on the microstructure of the molded part and thus on its performance. These parameters include: laser power (P), scanning speed (v), scanning pitch (h), powder layer thickness (t), scanning strategy, etc. The energy density E (E = P/vht) of the laser input to the sample can be calculated from some of these parameters [56]. By tuning the relevant parameters, the microstructure of the 3D printed sample can be effectively improved and defects in it, such as holes, microcracks, and crystallization in the heat affected

zone, can be reduced. The Interaction and formation of defects during 3D printing shown in **Fig 2. 3.**

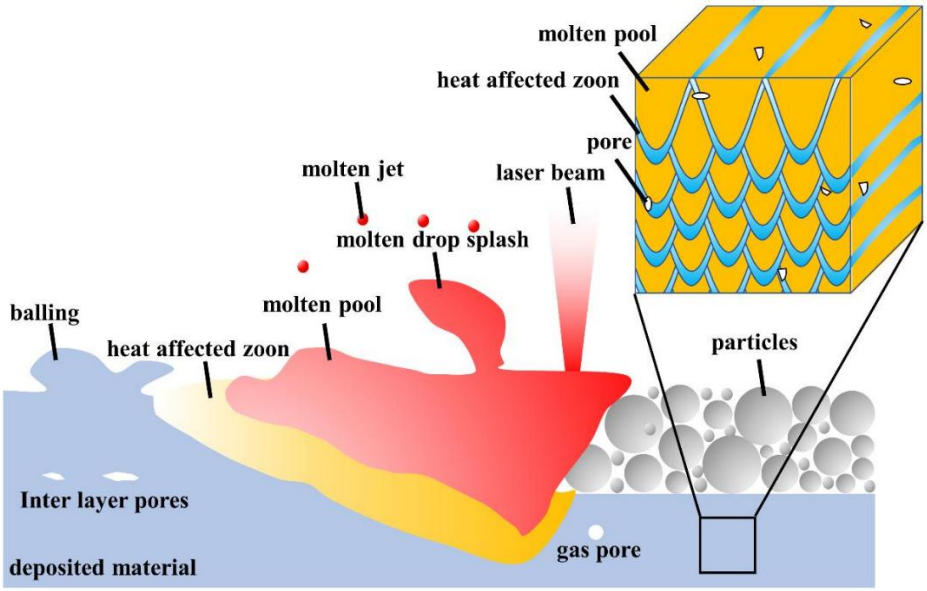

Fig 2. 3 The interaction between laser and powder during 3D printing and the formation of defects [57].

Laser 3D printing of amorphous alloys typically results in two distinct regions: the Molten Pool Zone (MPZ) and the Heat Affected Zone (HAZ), as shown in **Fig 2. 3** When the laser interacts with the amorphous powder, part of the powder and the upper surface of the printed layer melt to form a liquid. After the laser beam moves away, the molten metal rapidly solidifies, creating the molten pool zone. Due to the high scanning speed of the laser, the cooling rate of the micro molten pool can typically reach 10^4-10^6 K/s, far exceeding the critical cooling rate required for most amorphous alloy systems, thus generally enabling the formation of an amorphous structure.

However, the molten material in the upper layer exerts a thermal effect on the already solidified amorphous phase beneath, which can easily induce the precipitation

of crystalline phases. This region, where the temperature is lower than the alloy's melting point but higher than its crystallization temperature, is referred to as the HAZ [58]. Extensive studies have shown that the precipitation of brittle intermetallic compounds in the HAZ is a primary factor contributing to the poor room-temperature ductility and toughness of laser 3D printed MGs.

In addition to the precipitation of crystalline phases, pores and microcracks are also common defects in laser 3D printed amorphous alloys. During the laser scanning process, the amorphous powder undergoes rapid melting and solidification. To form a dense solid, the gases trapped in the powder gaps must be completely expelled during this process. Xing et al. [59] found that different laser energy densities lead to the formation of various types of pores in 3D printed Zr-based MGs, including spherical pores, interlayer pores, open pores, and metallurgical pores. Spherical pores mainly occur under relatively low laser energy density, and are caused by incomplete melting of the powder. Interlayer pores and open pores typically form under moderate laser energy density, resulting from incomplete fusion between layers and insufficient filling within the molten pool. When the laser energy density is high, small metallurgical pores may form on the upper surface of the molten pool due to the escape of tiny gas bubbles during rapid solidification.

Microcracks in laser 3D printed MGs can generally be classified into two types: thermal cracks and cracks induced by residual stress accumulation. Thermal cracks occur due to the mismatch in thermal expansion and contraction around the molten pool

during the laser scanning process. These cracks are typically influenced by laser scanning parameters and the fracture toughness of the alloy system. Specifically, lower cooling rates and alloys with higher fracture toughness are more effective in suppressing the formation of thermal cracks during laser 3D printing [60]. Cracks caused by residual stress accumulation are related to factors such as the geometry of the printed part and the laser scanning strategy. Smaller part sizes and alternating X–Y scanning paths are beneficial in reducing residual stress buildup and thereby help to suppress cracking in the printed components [61]. In addition, the size and distribution of pores in the printed part play a critical role in the formation of microcracks [62]. Microcracks tend to initiate near pores located at the edges of the molten pool, where thermal stresses during laser scanning can cause significant stress concentration, leading to the nucleation and propagation of cracks. Therefore, minimizing pore defects is also an important strategy for mitigating cracking in laser 3D printed MGs.

2.3.3 Mechanical properties of 3D-printed MGs

The mechanical properties of 3D-printed MGs are critical to their application as structural materials. Compared with conventionally cast MGs, the heterogeneous microstructures formed by layer-by-layer and track-by-track deposition in 3D printing significantly affect their mechanical performance. Ouyang et al. [58] found that the compressive strength of 3D-printed Zr-based BMG is 1.5 GPa with no plasticity, which is lower than that of cast BMGs, which exhibit a compressive strength of 1.87 GPa and 0.5% plastic deformation. In addition, the fracture surface of the 3D-printed sample is oriented at 90°, in contrast to the 42° fracture angle observed in cast BMGs, which

corresponds to the direction of maximum shear stress. This difference is mainly attributed to the layer-by-layer stacking process of 3D printing, where the heat-affected zones between layers contain a large number of brittle nanocrystals. These features lead to stress concentrations between layers, causing premature failure, and the resulting cracks tend to propagate along interlayer regions. Subsequent studies have shown that when the amorphous content in 3D-printed BMGs exceeds a certain threshold, the yield strength and fracture mode become comparable to those of cast BMGs with the same composition. However, their plasticity and fracture toughness remain inferior. One important reason is the annealing effect between layers during the printing process, which reduces the concentration of "free volume" in the material. This lower free volume hinders the activation of multiple shear bands during deformation.

Moreover, the presence of pores in 3D-printed BMGs significantly degrades their fatigue performance compared to cast counterparts [63]. The layer-by-layer fabricated laminated structure results in anisotropic fracture toughness [64], while the precipitation of nanocrystals enhances their tribological (friction and wear) performance. These unique properties of 3D-printed BMGs originate from the distinctive microstructures formed by their specialized additive manufacturing process.

Table 2. 1 summarizes the compositions, microstructures, and mechanical properties of 3D-printed BMGs reported in the literature. As shown, the density, amorphous content, and compressive strength of 3D-printed BMGs are comparable to those of cast BMGs. However, their plasticity remains limited. Therefore, improving

the ductility and toughness of 3D-printed BMGs is essential for their further development and practical application.

Table 2. 1 Composition, microstructure, and mechanical properties of 3D-printed BMGs via L-PBF.

Alloy composition (at%)	Microstructure	Sample Sizes (mm)	Yeilding strength (MPa)	Plastic strain (%)	References
$Zr_{52.5}Cu_{17.9}Ni_{14.6}Al_{10}Ti_5$	Crystalization	Φ 3 × 6	600	0	[65]
	Nearly fully amourphous, Porosity:0.2%	Φ 3 × 6	1500	0	[65]
	Nearly fully amourphous, Porosity:1.3%	Φ 3 × 6	1500-1700	<0.5	[66]
$Zr_{55}Cu_{30}Al_{10}Ni_5$	Nearly fully amourphous	Φ 3 × 6	1710	0.5	[67]
	Amorphopous content: 83%, Porosity:0.11%	Φ 3 × 6	1504	0	[59]
$Zr_{48.5}Cu_{47.5}Al_4Co_{0.5}$	Amorphopous content: 76%-95.7%	Φ 7 × 8	1200	0.8	[68]
$Zr_{57.4}Ni_{8.2}Cu_{16.4}Ta_8Al_{10}$	Amorphopous content>90%, Porosity:0.25%	Φ 1.5 × 3	1710	2.15	[69]
$Zr_{50}Cu_{50}$	63% Amorphopous phase+ 36% B2 phase, Porosity:0.76%	Φ 2 × 4	957	3.17	[70]
$Zr_{47.5}Cu_{45.5}Al_5Co_2$	72.6% Amorphopous phase+ 27.4% B2 phase, Porosity:1.6%	Φ 2 × 4	1423	4.65	[71]
$Zr_{60.14}Cu_{22.31}Fe_{4.85}Al_{9.7}Ag_3$	Amorphopous content: 95%, Porosity:0.11%	Φ 3 × 6 Φ 2 × 4 Φ 1 × 2	1770 1758 1734	0.46 0.51 1.43	[72]
$Zr_{59.3}Cu_{28.8}Nb_{1.5}Al_{10.4}$	Nearly fully amourphous, Porosity<1%	2 × 2 × 4	1450-1550	~6	[73]
$Ti_{47}Cu_{38}Zr_{7.5}Fe_{2.5}Sn_2Si_1Ag_2$	Nearly fully amourphous, Porosity=0.5%	Φ 2 × 4	1690	0	[74]
$Cu_{50}Zr_{43}Al_7$	Amorphopous content: 81%, Porosity:1.4%-2%	Φ 4 × 8	1044	0	[75]
$Cu_{46}Zr_{46}Al_8$	Amorphopous content: 88-100%	Φ 3 × 6	1180-1560	0	[76]
$Mg_{60}Zn_{35}Ca_5$	Nearly fully amourphous	-	439.7	0.66	
$Mg_{59}Zn_{35}Ca_5Y_1$	Partial crystallization	-	621.3	1.42	[77]
$Mg_{58}Zn_{35}Ca_5Y_2$	Partial crystallization	-	429.2	2.08	

$Pd_{43}Cu_{27}Ni_{10}P_{20}$	Nearly fully amourphous, Porosity:0.37%	Φ 4 × 6	1138	0	[78]
$Fe_{43.7}Co_{7.3}C_{14.7}B_{4.3}Mo_{12.6}$-$Cr_{15.5}Y_{1.9}$	Nearly fully amourphous with cracks	Φ 3 × 6	100	0	[79]

2.4 3D-printed metallic lattice structures

2.4.1 L-PBF processing and mechanics of metallic lattices

It is critical to use appropriate L-PBF processing parameters to fabricate lattice structures with optimal performance. Factors such as powder morphology, particle size, and chemical composition all play crucial roles [80] in determining the quality of L-PBF-fabricated components. These parameters influence the mechanical properties, such as strength and elastic modulus, of lattice structures in distinct ways. Sing et al. [81] found that among various processing factors, laser power had the most significant impact on the strength, modulus, and dimensional accuracy of printed lattice structures, more so than scanning speed or layer thickness.

The mechanical behavior of lattice structures fabricated via L-PBF is highly sensitive to processing conditions, yet the relationship between these parameters and the resulting properties remains inadequately understood and warrants further investigation. Over the past decade, the rise of additive manufacturing has enabled rapid prototyping, small-batch production, and even large-scale manufacturing. Established alloys like Ti6Al4V and 316L stainless steel [82] have been widely used to produce dense and reliable components. In addition, a growing number of novel alloys [83] have

been developed specifically for AM applications, signaling that both AM technologies and materials are reaching a critical point in their evolution.

Most mechanical tests on SLM-fabricated lattice systems are conducted under compression, as these tests are easier to perform than tensile tests. The typical mechanical properties evaluated include lightweight performance, static tensile and compressive strength, impact resistance, elastoplastic behavior, fatigue resistance, and thermal management. Although terms like “elastic modulus,” “yield strength,” or “tensile strength” are commonly used for both traditional and cellular materials, it's important to recognize that these terms refer to different physical phenomena. On the microscale, mechanical metamaterials behave more like discrete structures, whereas on the macroscale, they approximate homogeneous materials.

Lattice structures are essentially grid frameworks composed of intersecting struts or shells connected at nodes, repeating periodically to form unit cells. Unlike large-scale engineering structures, lattice structures are typically on the millimeter or micrometer scale and are considered a type of cellular material. Maconachie et al. [84] proposed that the unit cells forming lattice structures could be treated as space-filling lattices with distinct mechanical properties, which can be directly compared with those of the bulk materials from which they are made.

Many experiments have been conducted to characterize the mechanical properties of lattice structures under static loading. Maconachie et al. [84] compiled a comprehensive dataset of such properties, while fracture and continuum mechanics of

lattice materials have also become important topics in recent years. Quintana and Fleck [85] reviewed developments in this area and contributed valuable insights to the field. One key limitation of SLM is that unmelted powder must be removed after fabrication, making it unsuitable for forming closed-cell pore structures. This further highlights the design and manufacturing constraints specific to AM-fabricated lattices.

2.4.2 Classification of lattice structures

Lattice materials are a class of cellular materials characterized by periodic arrangements of unit cells in two or three dimensions, resembling the ordered structure found in crystals. Among various material architectures, lattice structures exhibit the highest structural efficiency per unit weight [86] , making them ideal for weight-sensitive applications such as aerospace and automotive engineering [87].

Historically, stochastic foams with millimeter-scale cells were used for thermal insulation and sandwich structures. However, their stiffness and strength degrade rapidly at low relative densities, limiting their use in lightweight structural applications. To overcome this limitation, periodic micro-truss lattices were proposed. These lattices exhibit a linear relationship between relative density and stiffness due to a stretch-dominated deformation mechanism, a behavior commonly observed in truss structures with high connectivity [88].

Subsequent structural optimization led to the development of the most rigid isotropic truss lattice. Yet, its stiffness reaches only about 30% of the theoretical upper

bound proposed by Hashin and Shtrikman, suggesting the need for novel lattice topologies to further approach this limit [89].

(1) Truss lattice structures

Truss lattice structures are a class of cellular materials composed of regularly repeating unit cells in three-dimensional space [90]. Truss lattices are architected metamaterials characterized by a periodic arrangement of struts meeting at nodal junctions [91]. By carefully designing their microscopic structure, these materials can be made to deform primarily through stretching, as defined by Maxwell's criterion [92, 93], meaning that external loads are primarily supported through the axial extension or compression of bars rather than through bending. Compared to earlier bending-dominated stochastic foams, stretching-dominated truss lattices typically demonstrate superior stiffness and strength [94].

Among the most extensively studied truss architectures are three fundamental types [2]within the cubic symmetry group: body-centered cubic (BCC), simple cubic (SC), and face-centered cubic (FCC) (**Fig 2. 4a**). The octet truss, part of the FCC crystal family, resists forces primarily through stretching. In contrast, SC and BCC lattices are bending-dominated, meaning their struts bend unless forces are perfectly aligned with them [94].

To broaden the design space and enable customized mechanical and physical properties, various architectural strategies have been proposed. These include combining fundamental lattice types with tailored volume fractions [86] (**Fig 2. 4a**);

introducing bars with variable cross sections [94] (**Fig 2. 4b**); incorporating curved-beam struts to alter deformation pathways [86, 95, 96] (**Fig 2. 4c**); adopting hollow bar cross sections to reduce weight and control stiffness [97] (**Fig 2. 4d**); and assigning different cross-sectional radii to different constituent bars for targeted mechanical tuning [98] (**Fig 2. 4e**).

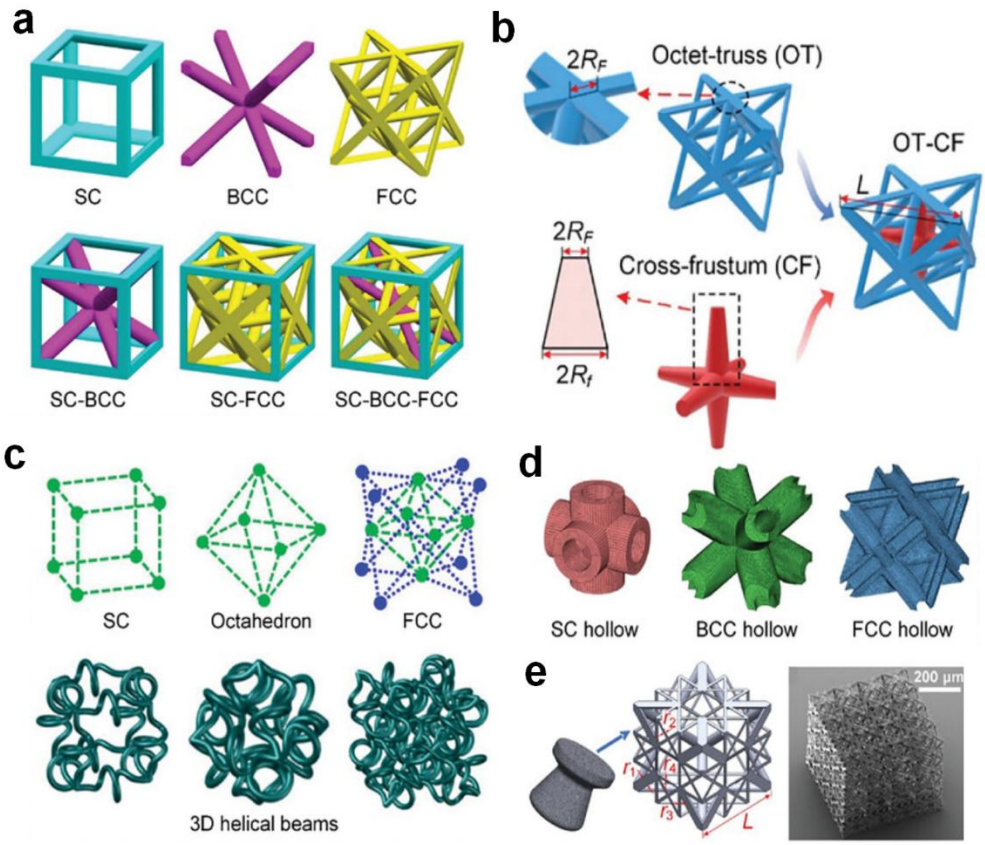

Fig 2. 4 Design principles and AM processes of truss lattices. (a) SC, FCC, and BCC truss lattices within the cubic symmetry group, along with hybrid configurations derived from combinations of these three basic types [99]. (b) Truss lattices featuring variable cross sections assigned to different constituent bars [94]. (c) Truss lattices incorporating curved-beam struts for enhanced deformation control [100]. (d) Truss lattices with hollow strut cross sections to reduce weight and tailor stiffness [97]. (e) Truss lattices with different cross-sectional radii assigned to different bars for mechanical tuning [98].

(2) Plate lattice structures

Although the design of truss lattices has been the subject of considerable research aimed at improving their mechanical and physical properties, their stiffness and strength remain well below theoretical upper bounds due to the fact that external loads are primarily supported through the uniaxial extension or compression of constituent bars [101, 102]. As a result, another class of lattice metamaterials-plate lattices-has attracted increasing attention. These structures consist of periodically arranged plate units connected through shared edges and have demonstrated excellent mechanical and physical properties compared to truss lattices [103, 104].

A recent advancement in metamaterials is the development of single-scale combined plate lattices. These architectures are engineered through the combination of elementary BCC, SC, and FCC plate lattices, with their volume fractions carefully tailored to yield superior isotropic elastic properties (**Fig 2. 5a**) [104, 105]. These lattices undergo stretching-dominated deformation when subjected to arbitrary external loads, characterized by bi-directional expansion or contraction within the plates' tangent planes. Consequently, their design can approach the theoretical limits of stiffness and strength, even at low relative densities [106, 107].

Furthermore, by integrating base lattice structures of different length scales, dual-scale combined plate lattices have been created, exhibiting significantly improved energy absorption performance compared to their single-scale counterparts [108]. To further expand the design space and enable tailored mechanical and physical properties,

a family of parametric plate lattices has been proposed (**Fig 2. 5b**) [109]. This parametric model includes common structures like SC, BCC, and FCC plate lattices, but also extends to novel and less-studied designs such as the Fluorite, flat-plate vintile (FPV) lattices, and flat-plate tesseract (FPT) [109].

In addition, a class of rhombic dodecahedron plate lattices has been developed to achieve isotropic elastic moduli and nearly isotropic yield strength (**Fig 2. 5c**), [110] while cuboidal spherical plate lattices have been topologically optimized to enhance both strength and stiffness (**Fig 2. 5d**) [111]. However, the closed-cell nature of these lattice structures presents challenges for their AM and practical applications. To address this issue, half-open-cell plate lattices have been proposed [104], offering enhanced manufacturability with only a modest compromise in strength and stiffness (**Fig 2. 5e**) [112].

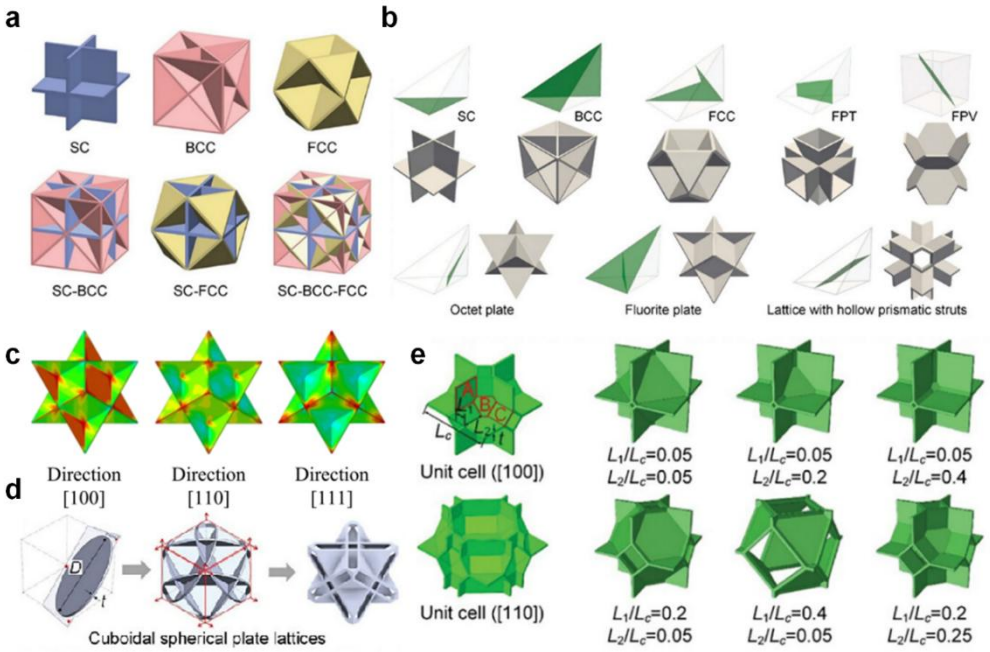

Fig 2. 5 Various plate lattices. (a) Superior isotropic elastic properties are achieved in composite lattices by assembling elementary SC, BCC, and FCC cubic plate lattices with specific, optimized volume ratios [97]. (b) A new parametric plate lattice family enables an expanded design space for tuning target mechanical properties [109]. (c) A new series of rhombic dodecahedron-based plate lattices is presented, demonstrating concurrent isotropic elastic response and near-isotropic yield strength [110]. (d) Topological optimization of cuboidal spherical plate lattices enhances their stiffness and strength [111]. (e) Half-open-cell plate lattices improve additive manufacturability with only a moderate penalty to mechanical performance [112].

(3) Shell lattice structures

Although plate lattices have the potential to approach the theoretical upper bounds of stiffness and strength, their closed-cell topology hinders fabrication with most AM techniques. This limitation also restricts their application in fields requiring efficient mass and heat transfer. In this context, shell lattices emerge as a promising alternative, offering more open architectures that are better suited for manufacturing and multifunctional applications [113], a distinct class of lattice metamaterials composed of periodically arranged, continuous, smooth, and non-intersecting shell surfaces, have attracted growing attention [114, 115]. Owing to their smooth geometries, shell lattices typically exhibit minimal stress concentration, and their open-cell configurations significantly improve manufacturability and suitability for lightweight, multifunctional applications [116, 117].

Among various shell-based designs, triply periodic minimal surfaces (TPMSs) have emerged as the most widely explored. These surfaces are characterized by zero mean curvature, infinite periodicity in three orthogonal directions, and locally

minimized surface area [117]. Six representative TPMS types are illustrated in **Fig 2. 6a** [113]. Owing to their reflectional symmetry about three orthogonal midplanes and rotational symmetry about the three principal axes, these surfaces enable the unit cell to be divided into a minimum of 48 identical subdomains. This extensive symmetry has been leveraged to develop numerical optimization techniques. These methods optimize the mid-surface geometry solely within the fundamental 1/48th tetrahedron to attain target geometric and mechanical/physical properties [113]. These include strategies to eliminate principal curvature peaks [115, 118] and to achieve isotropic elasticity [119] (**Fig 2. 6b**).

The inherent property of TPMS to create two independent, interpenetrating void spaces within a defined volume makes them highly effective for enhancing convective mass and heat transfer in devices like pressure vessels [120] (**Fig 2. 6c**). Moreover, tailored performance characteristics can be achieved by directly combining different TPMS shell lattices in specific volume ratios [121, 122] (**Fig 2. 6d**). Alternatively, wall thickness can be treated as a design variable and optimized to achieve superior isotropic elasticity (**Fig 2. 6e**) [121].

To further expand the design space, a parametric shell lattice model has been proposed, offering far greater tunability than conventional TPMS lattices. Customized mechanical and physical properties are achievable with this model, such as isotropic elasticity, increased stiffness, and tailored Poisson's ratios [123, 124] (**Fig 2. 6f**). In another approach, slightly corrugated shell lattices can be created by introducing mild

undulations into plate lattices. These hybrid structures exhibit enhanced isotropic elasticity, along with remarkable improvements in strength and specific energy absorption [125].

Bone defect repair is inherently complex and remains a costly issue in modern medicine, prompting a growing demand for efficient and easy-to-fabricate bone substitutes. TPMS structures, which mimic the hyperboloidal trabecular architecture of natural bone, have emerged as promising candidates due to their unique geometries that support various cellular processes. In response to the growing interest in TPMS scaffolds, Dong and Zhao [126] reviewed the influence of key design parameters—such as pore size, shape, and porosity—on mechanical performance, permeability, and curvature. Their work guides future scaffold design and optimization.

Kadkhodapour et al. [127] investigated the effects of TPMS core architecture on plastic deformation and failure using both simulations and experiments. They found that stress intensity and mass distribution significantly influence mechanical behavior, especially at lower volume fractions, differentiating TPMS scaffolds from conventional cellular materials. Similarly, Almeida and Bartolo [128] examined Schwarz and Schoen TPMS topologies using finite element analysis, highlighting their superior mechanical performance, high surface area, and high porosity.

TPMS structures have emerged as a powerful tool for designing porous scaffolds due to their open-cell nature and geometrical complexity, which are favorable for cell proliferation and nutrient transport [129]. Their smooth surface transitions result in

reduced stress concentrations compared to traditional lattice designs. Furthermore, TPMS architectures can be designed with spatial gradients in pore size and porosity by defining weight functions or spatially varying porosity profiles, allowing precise control over local mechanical and biological properties.

The increasing research interest in TPMS is also attributed to their natural occurrence in both biological systems and the environment, further reinforcing their relevance in biomedical applications [93,94].

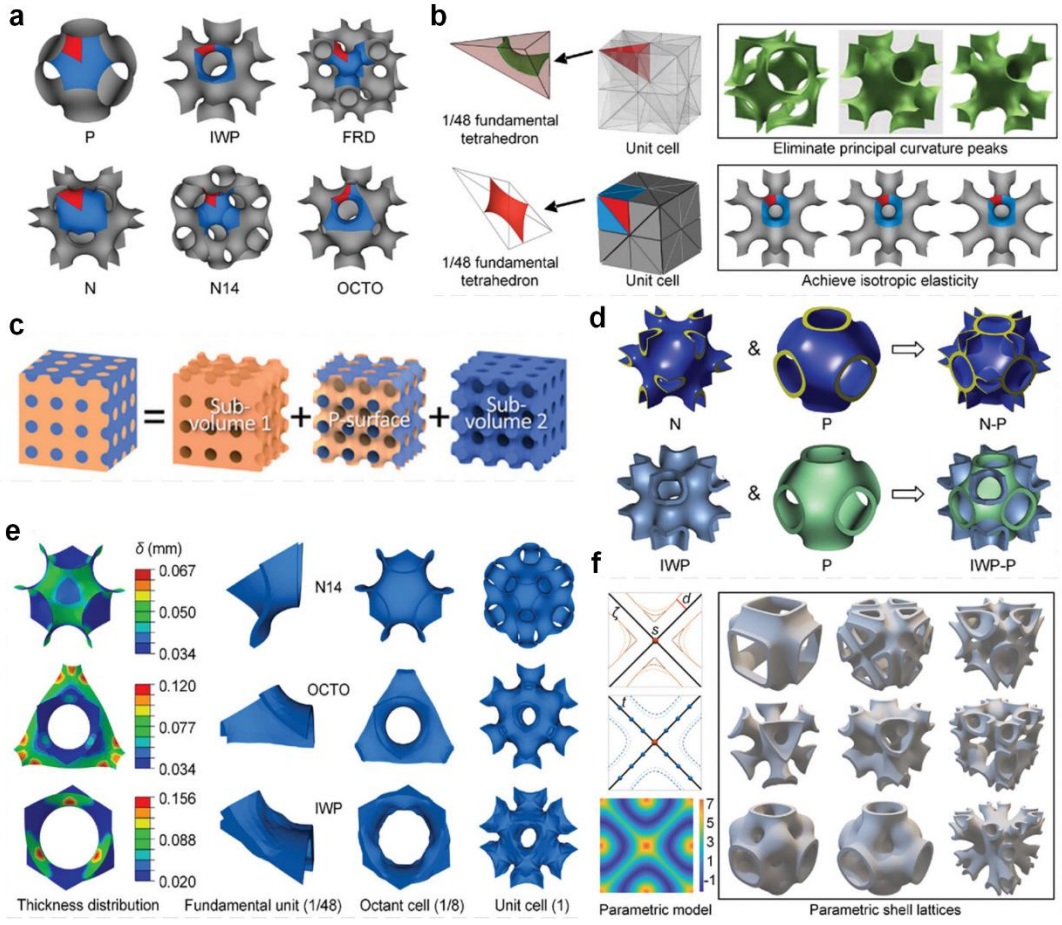

Fig 2. 6 Various shell lattice structures. (a) TPMS surfaces including I-graph-wrapped package (IWP), Primitive (P), FCC rhombic dodecahedron (FRD), N14, Neovius (N) and OCTO [113]. (b) Shell lattice design involves the computational shape optimization of their internal mid-surfaces to

meet predefined mechanical goals [115, 119]. (c) Illustration of the P-surface as a TPMS that partitions a cube-like volume into two non-intersecting sub-volumes, bounded by blue and orange interfaces [120] d) Construction of shell lattices by combining elementary TPMS structures in appropriate volume ratios [130, 131] (e) Design of shell lattices with spatially variable wall thickness to enable performance optimization [113]. (f) A parametric shell lattice model is developed to significantly expand the design space, enabling precise control over target mechanical properties [124].

(4) Functionally graded structures

Functionally graded lattices (FGLs) are a class of inhomogeneous lattice structures characterized by spatially varying geometric parameters within the design domain [132]. They have been widely adopted as highly customizable, tunable, and multifunctional architectures in the field of lattice metamaterials [132]. Progress in additive manufacturing has reached a point where fabricating graded lattices with complex microarchitectures is feasible. This capability facilitates the multifunctional integration within a signle components via strategic graded design [133]. The primary classification of graded lattices into 1D, 2D, and 3D types is determined by the spatial dimensionality of their property gradients [132] (**Fig 2. 7a**).

The key design parameters for FGLs typically include the scale and direction of mesoscale gradient vectors, as well as microarchitectural attributes such as volume fraction, orientation, shape, and feature size [134, 135]. A variety of methods have been found to design and optimize internal architectures with the goal of enhancing the mechanical and physical performance of graded lattices and broadening their practical applications. Among these, connectivity plays a critical role, ensuring smooth

geometric transitions and watertight connections between adjacent unit cells with differing parameters.

For instance, by applying a 1D gradient in strut diameters while maintaining intercellular connectivity, graded truss lattices can be tailored to show progressive and localized failure modes, along with improved pecific energy absorption capacity and splateau stress [135] (**Fig 2. 7b**).

Compared to truss lattices, TPMS-based shell lattices typically offer superior connectivity, which can be controlled via the implicit function parameters that define their surfaces. The relative density of TPMS shell lattices can be finely adjusted by modifying either the unit cell size or the shell wall thickness, thereby enabling effective tuning of both mechanical and thermal properties (**Fig 2. 7c**).

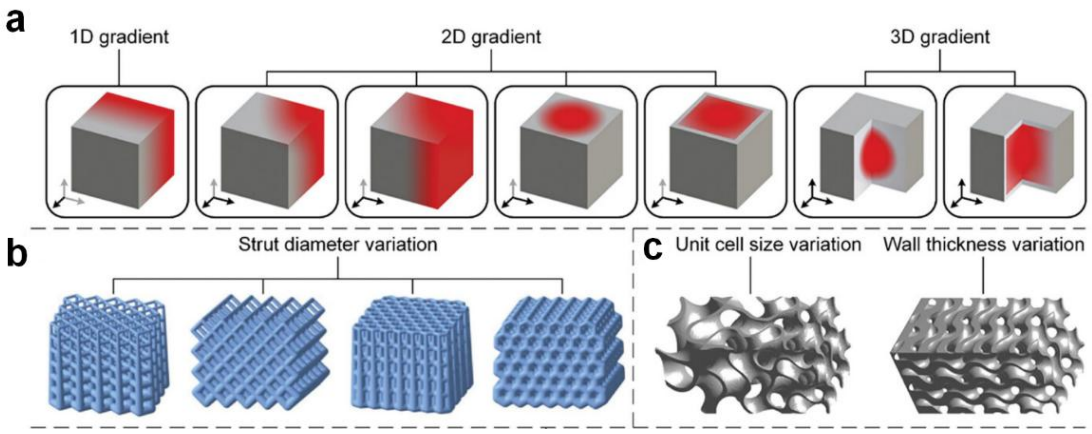

Fig 2. 7 Various graded lattices. Graded lattices with design parameters that change gradually in one, two, or three dimensions. [132]. (b) A one-dimensional gradient in strut diameter is employed in graded truss lattices to tailor their mechanical performance. [135]. (c) By grading key design parameters like unit cell size and wall thickness, shell lattices can be engineered to achieve customizable mechanical and thermal performance [136].

2.4.3 Structure-Mechanism-Property relationship of 3D-printed lattices.

The mechanical properties of lattice metamaterials are governed by two primary factors: the base material's properties and the complex spatial architecture of the solid material and voids. The internal microarchitecture that governs their mechanical behavior also plays a crucial role in determining their physical properties, such as acoustic, electromagnetic, and thermal performance. Through rational microarchitectural design, the property space of lattice metamaterials can be significantly expanded, enabling many unprecedented behaviors. For instance, it is possible to achieve non-positive effective parameters from materials with inherently positive parameters, generate chiral responses from achiral structures, produce anisotropic properties from isotropic configurations, and obtain nonlinear responses from linear materials. As a result, researchers have been continually exploring the intricate relationships between geometric architecture and the mechanical and physical properties of lattice metamaterials.

2.4.4 Unique properties and application of 3D-printed metallic lattices

The aerospace industry is particularly interested in AM due to its potential for lightweighting. For example, internal solid regions in components can be replaced with equal-strength lattice structures to reduce mass. Moreover, AM's ability to produce conformal cooling channels and other complex features makes lattice structures highly attractive for aerospace applications. Zhou et al. developed a lightweight, lattice-based thermal regulator capable of phase-shift thermal control for spacecraft. Compared with

traditional thermal management systems, which often add substantial weight to spacecraft, their L-PBF-fabricated thermal controller achieved a 50% improvement in thermal capacity at comparable mass.

In the biomedical field, AM lattice materials have also found widespread use in medical implants, with the global market projected to reach $116 billion by 2022. SLM is particularly suitable for fabricating implants due to its ability to produce high-quality metallic parts with complex, patient-specific surfaces. Lattice materials are especially advantageous in biomedical applications because they can be engineered with mechanical properties that closely match those of natural bone. These structures not only support osseointegration but also promote healthy bone ingrowth and exhibit excellent implant fixation. Beyond conventional implant production, AM lattice structures also enable innovative functionalities. For instance, Burton et al. proposed implant designs with integrated drug reservoirs to enable antibacterial activity.

In summary, lattice structures have been widely applied in aerospace, biomedical engineering, robotics, and various industrial domains due to their exceptional properties. The use of AM, particularly L-PBF, in designing and manufacturing lattice structures has reached a new stage, leading to significant advancements in performance and functional design.

Inspired by the structural order found in nature, researchers have long sought to mimic natural cellular structures. Hollow configurations such as human bone, honeycomb geometries, and Voronoi patterns formed in foams have been employed in

several engineering applications. These natural forms exhibit optimized structures for strength and weight, making them ideal templates for engineering design. Rational microarchitectural design can greatly expand the property space of lattice metamaterials, enabling unprecedented behaviors such as achieving non-positive effective parameters from inherently positive materials, generating chiral responses from achiral structures, producing anisotropic properties from isotropic configurations, and obtaining nonlinear responses from linear materials.

Excellent Mechanical properties

The homogenized mechanical properties of a lattice metamaterial (e.g., density (ρ), Young's modulus (E), and strength (σ)) are governed by two interdependent factors: the intrinsic properties of its constituent material(s) (including bulk density ρ_s, Young's modulus E_s, and strength σ_s and the topology of its microarchitecture, which defines the spatial distribution of solid and void phases.

Among them, the effective Young's modulus E is a key indicator of the lattice's ability to resist deformation under external loads. Both the relative density ρ/ρ_s and relative Young's modulus E/E_s are dimensionless parameters governed solely by internal geometry, independent of the specific material used. In contrast, relative strength σ/σ_s depends not only on microarchitecture but also on the mechanical characteristics of the base material, such as buckling strength (σ_{bs}), yield strength (σ_{ys}), brittle fracture strength (σ_{fs}) and ultimate strength (σ_{us}),.

Fig 2. 8a and **Fig 2. 8b** show how E_s and σ_s vary with ρ_s for various solid materials [137]. The ratios E_s/ρ_s and σ_s/ρ_s are commonly used to evaluate the specific stiffness and specific strength of solids. Notably, ultralight lattice materials are typically defined as those with $\rho < 10$ kg/m³ or $\rho/\rho_s < 0.1\%$, and are mostly fabricated using micro/nanoscale manufacturing techniques.

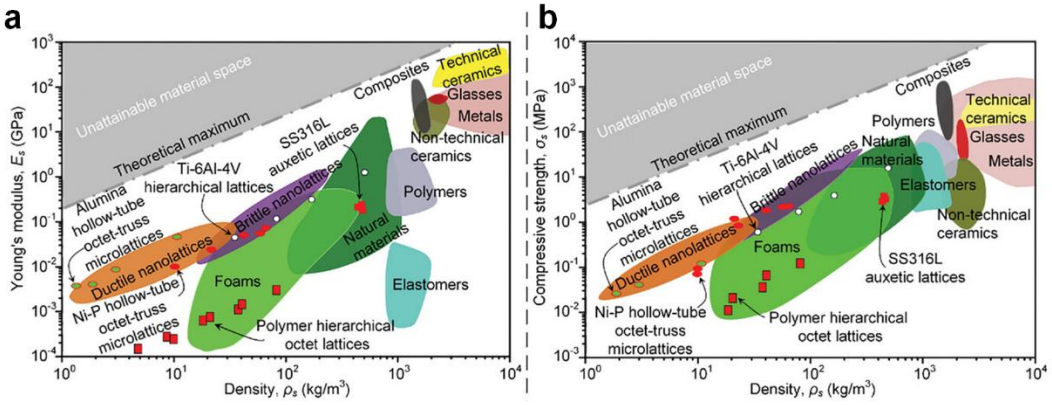

Fig 2. 8 Experimental plots of (a) Young's modulus and (b) compressive strength as functions of density for various solid materials, periodic lattice metamaterials [137].

The relationships between E/E_s, σ/σ_s, and ρ/ρ_s in lattice structures can be described by the Gibson–Ashby model using a power-law expression [92, 138]:

$$\frac{E}{E_s} = C_E \left(\frac{\rho}{\rho_s}\right)^{n_E} \tag{2.1}$$

$$\frac{\sigma}{\sigma_s} = C_\sigma \left(\frac{\rho}{\rho_s}\right)^{n_\sigma} \tag{2.2}$$

Here, C_E and C_σ are scaling coefficients, and n_σ and n_E are exponents determined by the deformation mode of the lattice. For bending-dominated lattices, $n_E \geq 2$ or $n_\sigma \geq 3/2$; for stretching-dominated lattices, $n_E \approx 1$ or $n_\sigma \approx 1$.

To determine the deformation mode, the Maxwell connectivity number m is often used [139, 140]:

$$m = b - 3j + 6 \tag{2.3}$$

where b is the number of struts and j is the number of nodes. If $m \geq 0$ the lattice is stretching-dominated; if $m \leq 0$, it is bending-dominated.

The variation trends of E/E_s and σ/σ_s with respect to ρ/ρ_s for several representative lattice types will be further illustrated in the following sections

Tuning Mechanical Properties

One of the simplest yet most effective applications of cellular structures lies in tailoring their mechanical properties, particularly the effective stiffness. This tuning can be achieved not only at the bulk scale through homogeneous lattice designs but also locally, by adjusting density or modifying architectural features, such as thickening struts or altering cell geometry. It is well established that porosity and stiffness in lattice structures are strongly interrelated. This relationship is accurately captured by the Ashby–Gibson models [141], originally developed for foams. Based on these models, the stiffness of a lattice can typically be predicted from its porosity. Moreover, beyond porosity levels, the design of the unit cell itself plays a critical role in determining stiffness. This effect has been extensively explored in the literature across a wide range of unit cell configurations and porosity levels [142, 143]. AM lattice structures are increasingly used in medical implants, with the global market projected to reach USD

147 billion by 2027 [144]. Their patient-specific designs and bone-matching stiffness make them ideal for reducing stress shielding and promoting long-term implant performance [145]. Optimal bone replacement lattices require adequate strength, elastic modulus compatibility, and architectural features—such as high surface area for effective cell seeding and sufficient permeability to support nutrient transport and bone in-growth.

Impact and energy absorption

Energy absorption is the ability of a material to sustain applied loads without catastrophic failure, while impact absorption describes this behavior under high strain-rate conditions. The absorbed energy is quantified by the area under the stress–strain curve up to failure or, in compression, to full densification.

Cellular materials are well known for their excellent energy and impact absorption. For decades, aluminum foam sandwich panels have been used in industry, for instance, as crash protection in vehicles by placing foam cores between solid face sheets. Similar foam-based sandwich structures have also been widely adopted for impact protection in packaging, thermal insulation, and structural protection in construction, where lightweight design is particularly advantageous. Additionally, these structures provide excellent vibration damping due to their inherent energy absorption capabilities, which helps suppress vibration transmission.

For high-velocity impacts or blast protection, metal lattice structures are generally more suitable than polymer-based ones. This is because metals can undergo irreversible

deformation mechanisms, such as buckling, plastic deformation, and fracture, during energy absorption, resulting in higher impact resistance. In impact protection scenarios, the event typically delivers an impulse rather than a steady energy load, so thick faceplates are commonly employed to absorb the force, following the same principles used in ideal energy absorbers [146]. However, for weight-sensitive applications, the demand for lightweight designs has grown significantly, and cellular lattice materials offer promising solutions in such contexts.

Research on energy-absorbing structures often begins with quasi-static testing, predominantly under compression, and is then extended to dynamic testing at impact velocities more relevant to specific applications [147]. Overall, the energy absorption performance of cellular structures can be effectively optimized by tuning their architectural design and relative density.

Fig 2. 9 illustrates a typical force–displacement response of a metallic lattice material under low strain rate compression. The curve features a broad plateau region with nearly constant load, flanked by two sharp increases in force. The initial rise corresponds to the elastic response of the structure, while the final rise marks the onset of densification.

An ideal energy-absorbing material should exhibit a long, flat plateau at a stress level slightly below the peak stress tolerable by the protected object. It must absorb the required amount of energy before entering the densification phase.

Figure 2.9 illustrates a typical compressive stress–strain response, from which several mechanical parameters—such as compressive strength and plateau stress—can be derived. Among these, the most critical parameter for comparison is the specific energy absorption (SEA), which quantifies the amount of energy absorbed per unit mass (J/g), and is defined as:

$$SEA = \frac{\int \sigma_0^{\varepsilon_D} d\varepsilon}{\rho} \tag{2.4}$$

where ε_D represents the densification strain and ρ represents the density of the lattice structure. Another important metric is the energy absorption efficiency (η), which evaluates how closely a lattice material's energy absorption performance approaches that of an ideal absorber, based on a specified maximum allowable transmitted stress σ_{peak}.

$$\eta = \frac{\int \sigma_0^{\varepsilon_D} d\varepsilon}{\sigma_{peak} * 100\%} \tag{2.5}$$

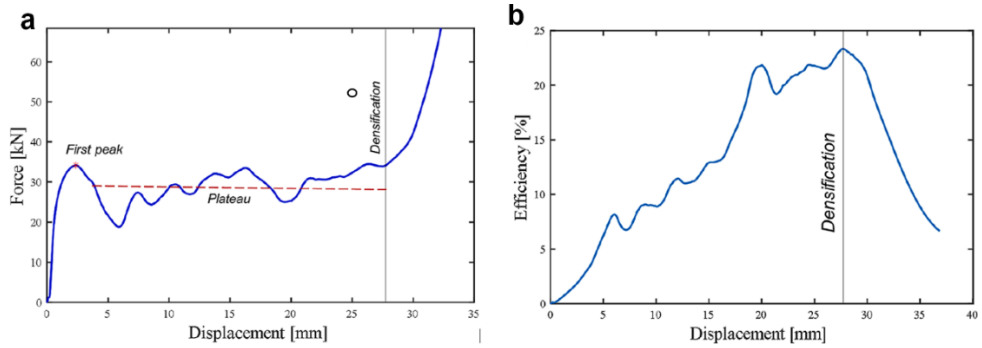

Fig 2. 9 Energy absorption performance of metallic lattices. (a) Typical compression load–displacement curve of a metallic lattic. (b) Energy absorption efficiency versus displacement.

At high strain rates approaching impact velocities, the Kolsky bar, is the most commonly used method for testing. This technique has been extensively employed to investigate the mechanical behavior of cellular materials fabricated by metal AM processes under strain rates approaching $10^3 s^{-1}$ [148].

However, applying the SHPB method to cellular structures presents several challenges. These include the limited diameter of the pressure bars relative to the size-dependent behavior of cellular materials, the difficulty in achieving sufficient crushing throughout the plateau region, and the inherently low wave impedance of cellular materials, which makes it difficult to obtain strong signals when using metallic bars [149].

For testing at even higher strain rates, light gas guns offer a viable alternative [149]. When studying the blast response of cellular materials, a ballistic pendulum combined with explosive loading is typically used to sandwich and test the specimen [150].

High surface area

Lattice structures inherently possess a highly interconnected pore network, which results in an exceptionally high surface-area-to-volume ratio. This attribute is one of several morphological characteristics that can be leveraged to evaluate and differentiate lattice architectures across various applications. For example, the study in [143] compared strut-based and sheet-based lattice designs, revealing notable differences in surface area despite identical densities. The findings also showed that while overall porosity may be similar, pore sizes can vary significantly, with some configurations

featuring dual or even multiple pore size distributions. Such comparisons are especially useful in applications requiring specific surface-related properties, such as maximized surface area.

In addition to high surface area, metallic lattices produced by additive manufacturing tend to exhibit substantial surface roughness. This roughness enhances the effective surface area beyond what is predicted by idealized models, offering potential advantages for certain applications. For instance, in biomedical implants, rough surfaces have been found to promote bone cell attachment and early-stage bone tissue growth, thereby supporting better osseointegration [151]. Other fields that may benefit from increased surface area include heat exchangers, catalytic systems, battery electrodes [152], and materials used in chemical processing or corrosion-prone environments. However, it's important to consider that structural degradation or morphological changes over time could affect performance. For example, although gyroid-based thin-sheet lattices may offer excellent catalytic efficiency, they could degrade faster than thicker, strut-based alternatives.

Moreover, surface morphology is closely related to other functional properties like permeability and thermal conductivity. Surface roughness not only adds to the total surface area but also influences fluid dynamics and heat transfer efficiency. Specifically, rougher surfaces can trigger localized turbulence near material boundaries, reducing the overall flow rate. While pore size and inter-strut spacing largely dictate fluid flow, surface characteristics become increasingly important as these spaces shrink. As pore

dimensions decrease and surface roughness grows, these effects are expected to become more pronounced, impacting the structure's overall performance.

High permeability

Architected cellular materials have shown significant promise in biomedical applications, particularly as orthopedic implants and scaffolds for bone tissue engineering [153, 154]. In this context, a central design challenge is achieving an optimal balance between mechanical strength and biological performance to closely replicate natural bone tissue.

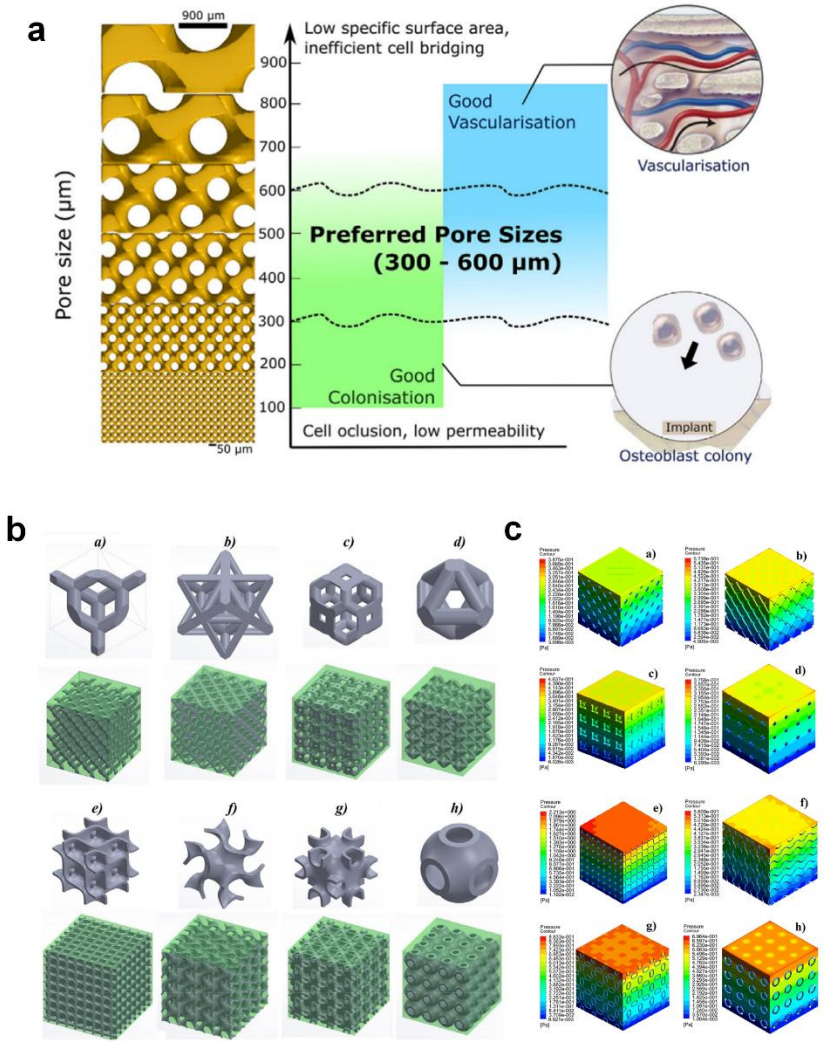

Fig 2. 10 High permeability of architected cellular materials shows significant promise in biomedical applications. Pore size and scaffold porosity significantly influence the permeability of prosthetic devices, thereby affecting cell colonization, bone formation, and vascularization [155]. (b) Unit cells and their corresponding scaffold domains (grey) and fluid domains (green) [156]. (c) Simulation results showing pressure profiles in counter using an inlet velocity of 0.1.

Among the various biological parameters that require optimization, fluid permeability plays a pivotal role in designing a biologically functional scaffold. A highly permeable scaffold facilitates the efficient transport of cells, nutrients, and growth factors, thereby supporting proper bone regeneration post-implantation (as illustrated in **Fig 2. 10a**). For instance, Kemppainen et al. [157] noted that low-permeability structures are more likely to promote the formation of cartilaginous tissue rather than healthy bone. In light of this, extensive studies have focused on the permeability of lattice scaffolds fabricated via AM. Literature sources [158-160] consistently report that, beyond porosity (%), factors such as lattice unit architecture, pore size and morphology, and geometric features play crucial roles in tuning permeability.

For example, Bobbert et al. [142] experimentally investigated the permeability of four different TPMS structures fabricated from Ti6Al4V using the L-PBF process. A total of 64 samples were tested (four structures across four density levels ranging from approximately 30% to 60%). The study revealed that permeability (quantified as water flow under pressure) decreased with increasing apparent density and also varied significantly across different lattice geometries at the same density. Additionally, an inverse correlation between permeability and surface area was observed, attributed to

increased frictional resistance. However, since higher surface areas are often associated with higher porosity and increased permeability, this suggests that porosity has a more dominant effect than frictional losses caused by surface area.

Ali et al. [156] further compared different lattice architectures suitable for bone scaffolds using computational fluid dynamics (CFD). Specifically, they examined strut-based and sheet-based TPMS structures (**Fig 2. 10b**), focusing on two key geometric parameters. The first is the ratio of the largest to smallest pore size (D/d), which characterizes channel constriction; narrower channels increase flow tortuosity and reduce permeability. The second is the ratio of unobstructed flow area to total inlet area (A/A_0), indicating the presence of straight flow paths between inlet and outlet. These findings indicate that, at equivalent porosities, TPMS structures generally exhibit lower permeability than strut-based lattices, a result consistent with previous studies [143]. Furthermore, while all the tested designs displayed permeability values within the range of human trabecular bone, the diamond-type TPMS lattice emerged as the most promising due to its higher permeability, elevated wall shear stress, and favorable convex surface morphology. Across all scaffold geometries, simulations indicated that pressure was highest at the inlet and progressively declined toward the outlet, approaching zero. This trend aligns with the boundary conditions defined in the models. The corresponding pressure distributions within the 3D geometries are presented in **Fig 3.10b** as contour plots.

Du Plessis et al. [143] also emphasized the importance of high tortuosity in bone implant design. A more complex flow path ensures that nutrients reach a greater volume of the lattice structure, thereby enhancing cell seeding and promoting bone tissue growth.

2.5 Research progress and potential applications of 3D-printed MG lattices

Despite their excellent mechanical properties, MGs are typically limited to simple geometries such as foils, thin plates, or small-diameter rods due to the extremely high cooling rates required during their formation. Shen et al.[51] fabricated 3D, large dimensions of amorphous structures with complex geometry via LFP technology, which expands MG products to 3D arbitrary geometries with large dimensions due to the inherited advantages of the LFP technology which would open many potential applications. Unlike crystalline metals that typically deform through dislocation slip or grain boundary activity, BMGs primarily deform via shear band mechanisms , which are highly sensitive to structural length scales [161]. L-PBF enables the high-precision fabrication of personalized or customized metal components while avoiding the additional cost, time consumption, and material waste commonly associated with traditional plastic processing methods. Moreover, not all materials are suitable for L-PBF, which partly explains the limited research on fabricating MG lattice structures using this technique. In addition to their outstanding mechanical properties, MGs also exhibit a range of unique functional characteristics, including but not limited to catalytic

activity, biocompatibility, corrosion and wear resistance, optical properties, energy absorption capability, soft magnetic behavior, and magnetocaloric effects. These functional properties can be further enhanced by structuring MGs into three-dimensional lattice architectures.

2.5.1 Enhanced catalytic performance of 3D-printed MG lattices

Yang et al. [162] successfully fabricated Zr-based MG structures with varied geometries, including cubes, hollow forms, and lattice architectures, via L-PBF process coupled with dealloying. As shown in **Fig 2. 11a**, the study compared the degradation efficiency of methyl orange under identical conditions for three samples: an amorphous alloy lattice, a cubic sample subjected to the same dealloying process, and a polycrystalline copper plate. The lattice sample showed superior degradation, removing MO completely within 15 min, about four times faster than the cubic sample and nine times faster than polycrystalline copper.

Moreover, the lattice structure with the highest degradation rate demonstrated excellent stability during cyclic degradation tests. As depicted in **Fig 2. 11b**, the degradation efficiency showed no significant decrease after four cycles, indicating outstanding catalytic durability. The degradation mechanism aligns with the classical advanced Fenton process [163]: the 3D bulk catalyst features a hierarchical porous structure where Cu reacts with H_2O_2 to generate hydroxyl radicals, which act as strong oxidants to decolorize the dye.

The lattice sample's superior catalytic performance is primarily attributed to its larger specific surface area and hierarchical porous architecture. In degradation experiments with equal mass loading (27.2 g/L) across three 3D-printed samples, the lattice exhibited the largest total surface area (~25 m^2), nearly three times that of hollow samples and 19 times that of cubic samples, as illustrated in **Fig 2. 11c**. This extensive reactive surface area, combined with the micron/nanoscale fractured porous structure, not only provides abundant catalytic active sites (e.g., pore edges and surfaces) [164], but also facilitates effective adsorption of dye molecules, promotes thorough water transport, and ensures timely removal of degradation by-products, thereby sustaining and enhancing the degradation reactions.

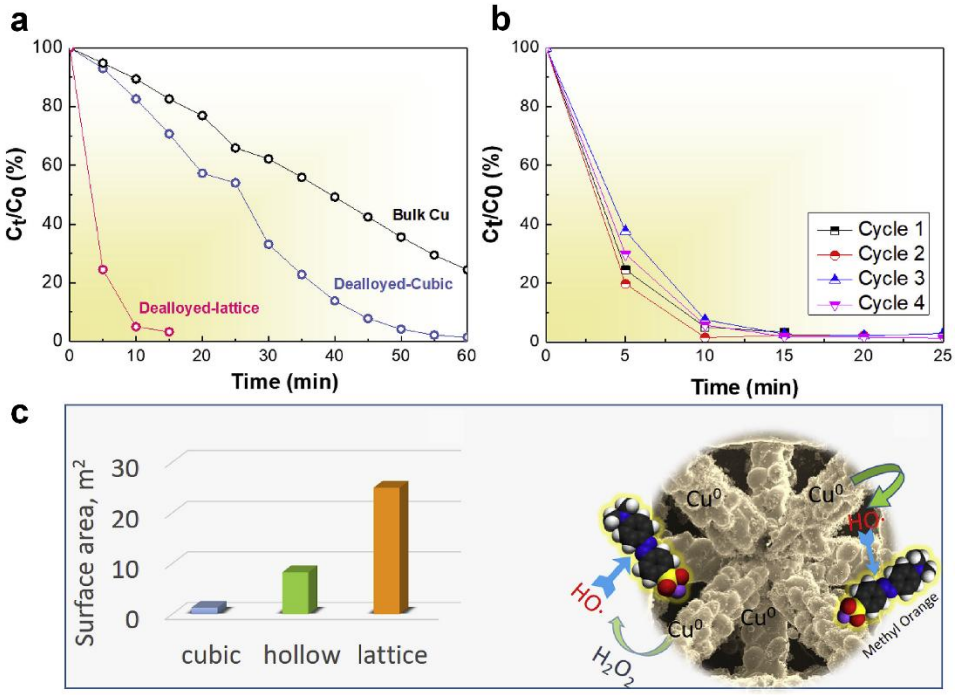

Fig 2. 11 3D printing of Zr-based BMGs with enhanced catalytic properties. (a) Comparison of methyl orange degradation kinetics among 3D-printed MG samples with nanoporous surfaces—specifically lattice and cubic geometries—alongside a polycrystalline copper reference. (b) Evaluation

of the catalytic durability of the dealloyed lattice structure over multiple degradation cycles. (c) Quantitative analysis of surface area across differently shaped 3D-printed MG architectures (left), and conceptual diagram (right) illustrating how hierarchical porous design enhances catalytic degradation efficiency[162].

2.5.2 Biocompatibility advantages of 3D-printed MG lattices

For many years, BMGs have been explored as promising candidates for biomedical applications-ranging from orthopedic and cardiovascular implants to dental devices and fillers-thanks to their exceptional strength, low elastic modulus, superior wear resistance, and excellent biocompatibility [163]. However, a major limitation in their clinical deployment lies in the restricted geometric flexibility of cast BMGs, which complicates the fabrication of intricate structures. AM offers a viable solution to overcome this challenge.

Zhang et al. [85] investigated the mechanical behavior and biocompatibility of additively manufactured glassy $Zr_{60.14}Cu_{22.31}Fe_{4.85}Al_{9.7}Ag_3$ components. The 3D-printed BMG exhibited a high yield strength of 1600 MPa, excellent fracture toughness (36 $MPa \cdot m^{1/2}$), and a relatively low Young's modulus (~80 GPa). Notably, complex porous structures could be readily fabricated via L-PBF, as demonstrated in **Fig 2. 12a-b**. The printed porous BMG samples exhibited compressive strengths nearly three times higher than those of porous titanium with equivalent geometry and 70% porosity, while maintaining a substantially lower Young's modulus of just 13 GPa (**Fig 2. 12c–d**)-a value closely matching that of human cortical bone.

Fig 2. 12e presents an L-PBF-fabricated BMG acetabular cup with an average pore diameter of 500 μm and 70% porosity, showing the technique's ability to directly produce biomedical components with tailored architectures. The biocompatibility of the printed BMG was assessed through MG63 cell culture assays and benchmarked against both polymeric materials and Ti6Al4V alloy. As shown in **Fig 2. 13a**, the Zr-based BMG exhibited low cytotoxicity and a favorable cell proliferation profile, with MG63 cells displaying significantly higher growth rates on the BMG surface than on Ti6Al4V over a five-day period. This indicates not only good biocompatibility but also biosafety of the printed glass.

Interestingly, the porous BMG samples demonstrated enhanced cell compatibility compared to their dense counterparts, suggesting that the open porous network fosters improved cell adhesion and proliferation. Further insights are provided in **Fig 2. 13**, which display the morphology of A375 cells after 24 hours of incubation on different substrates. On the BMG surface (**Fig. 2.13b**), cells adhered robustly and adopted a rounded, spread-out morphology, which is typical of mesenchymal or stem-like phenotypes favorable for tissue regeneration. Additionally, the number of cells attached to the BMG surface surpassed those on Ti6Al4V (**Fig 2. 13c**), and was statistically comparable to that of the control group (**Fig 2. 13d**), further confirming the outstanding biocompatibility of 3D-printed BMGs.

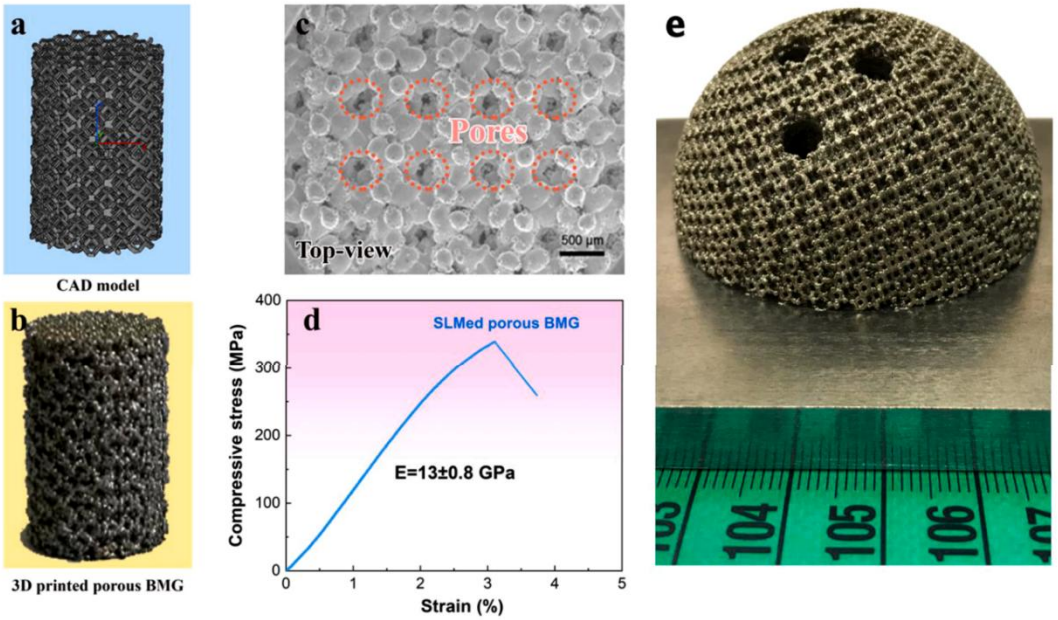

Fig 2. 12 Zr-based porous BMG samples.(a) CAD models of porous scaffold architecture and (b) the resulting Zr-based MG structure fabricated via L-PBF. (c) SEM image showing the detailed surface topology of the 3D-printed porous MG. (d) Compressive stress–strain response of the L-PBF-produced porous BMG, indicating its mechanical performance. (e) An example of a 3D-printed MG acetabular cup featuring interconnected pores for potential biomedical implantation[72].

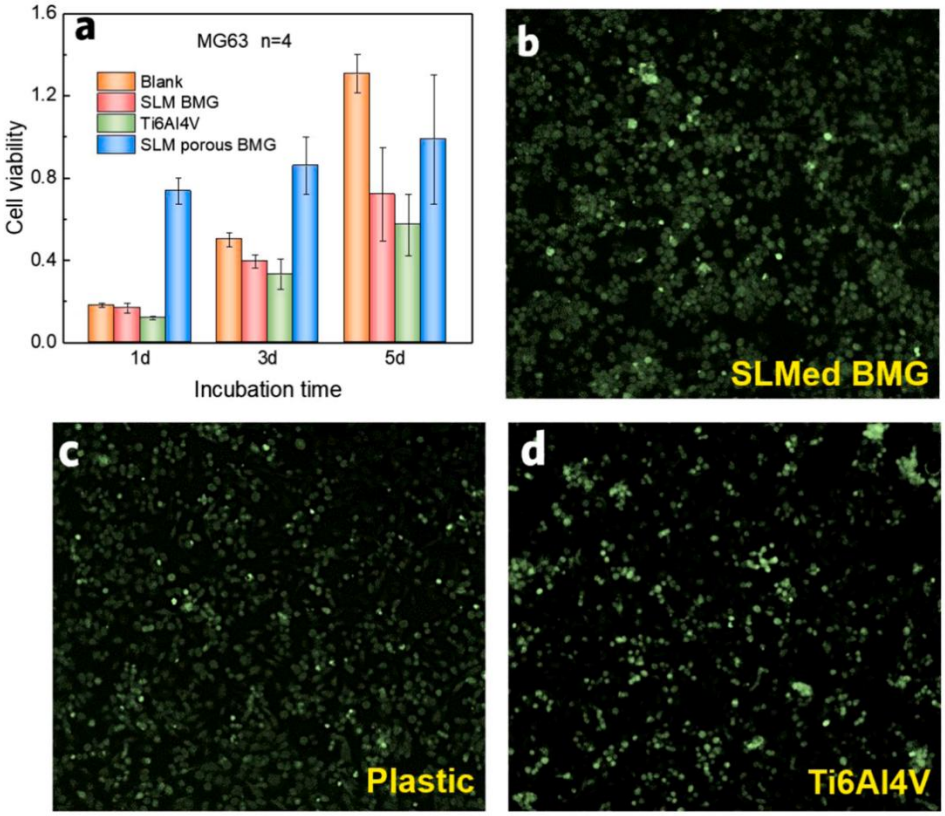

Fig 2. 13 Outstanding biocompatibility of 3D-printed BMGs. (a) Absorbance measurements of MG63 cells cultured on different substrates (3D-printed MG, Ti6Al4V alloy, and blank control) over 1 to 5 days, used to evaluate cell proliferation behavior. Morphological comparison of A375 cells after 24 hours of culture on three different surfaces: (b) 3D-printed MG, showing tight cell adhesion and spherical spreading; (c) plastic surface and (d)Ti6Al4V alloy.

2.5.3 Energy-Absorption potential of 3D-printed MG lattices

Over the last decade, BMGs have emerged as promising candidates for developing energy-absorbing cellular materials due to their near-ideal strength, which surpasses that of their crystalline counterparts [165, 166]. While monolithic BMGs are intrinsically brittle, their transformation into cellular forms, such as foams [167, 168] and honeycomb architectures [169] , has produced structures capable of significant plastic deformation at room temperature, thereby unlocking considerable energy-absorption potential [169, 170]. These BMG-based architectures retain the high

strength of their parent alloys and consistently outperform traditional metal foams in terms of energy absorption [170, 171]. As a result, BMGs have become a promising base material for engineering advanced cellular structures tailored for energy-dissipation applications.

2.6 Summary

3D-printed metallic lattice structures hold unique properties due to the designable and controllable geometries, which demonstrate wide-ranging applicability across diverse disciplines. Employing MGs as the parent materials can further enhance its mechanical and functional properties, since they have extraordinary mechanical properties and other unique properties. However, there is a lack of reports on the 3D-printed MG lattices, which directly hinders their application in the aforementioned scenarios. Thus, in this thesis, we utilized different L-PBF systems to fabricate MG lattice structures with various geometries, thereby establishing an initial understanding of the structure – property relationships for this class of materials. We further investigated their mechanical properties and deformation mechanisms to enhance performance through structural design. In addition, we explored the catalytic behavior of these MG lattices, broadening the scope of their functional applications. This work provides valuable data support for the diverse potential applications of MG lattice structures.

Chapter 3 Research methodology

3.1 Overview

This chapter delineates the research methodologies employed in this study. Section 3.1 provides a thorough overview of the approaches taken. Section 3.2 details the techniques utilized for geometric modeling of the lattice structure and the parent materials for the fabrication. Section 3.3 outlines the methodologies adopted for microstructure characterization, and Section 3.4 illustrates the techniques utilized for property measurements. Section 3.5 elaborates on the computational modeling techniques used, highlighting the theoretical framework and simulations that support the experimental findings.

3.2 Materials and microstructure characterization

The gas atomized equimolar ZrCuFeAlAg MG powder (ShanDong LianHong New Material Technology Co.,Ltd China), with a nominal particle size between 0 μm to 53 μm, was used in the L-PBF process for the specimen fabrication. The powder morphology was observed in scanning electron microscopy (SEM, Sigma 300, Zeiss, Germany), showing the spherical MG powders with a little satellite powder are fabricated by gas atomization process, as displayed in **Fig 3. 1**. The microstructure of HEA powder was investigated in SEM equipped with an energy disperse spectroscopy (EDS, X-Xax, Oxford Instruments, UK) detectors, illustrating with the even alloying element distribution after gas atomization process. The MG specimens including bulk and lattices were fabricated in a selective laser melting system (SLM 125 HL, SLM

Solutions Group AG, Germany) equipped with a single 400W IPG fiber laser under continuous Aron atmosphere, as the oxygen content during the full process below 300ppm. And a zig-zag scanning strategy with a 67 ° rotation is used in the subsequent building layer during the process. The scanning speed was set as 1400 mm/s, while the layer thickness was 60 μm. To study the effect of heat input on the microstructure and the mechanical properties, the laser powers were the variables in this study, ranging from 120 W to 220 W with a power increment of 10 W. A pre-heated 60702 Zr substrate to 100 ℃ was used in this study to reduce the residual stress in fabricated samples. The printed samples fabricated by different laser power of were cut from the substrates by the electrical wire cutting machine for the subsequent tests.

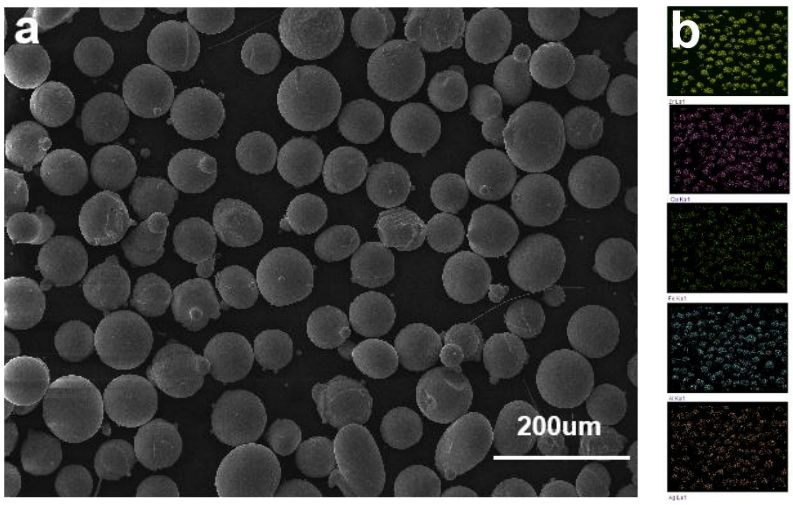

Fig 3. 1 The $Zr_{60.14}Cu_{22.31}Fe_{4.85}Al_{9.7}Ag_3$ powder used in the L-PBF approach of (a) the morphology in SEM, (b) corresponding EDS element maps.

The XRD results show that the powder has a completely amorphous structure with no crystalline phase precipitation. The DSC results show that the powder has a significant glass transition temperature (T_g) of 414°C and a crystallization temperature

(T_x) of 475°C shown in Fig 3.2. The SEM results show that the powder has good sphericity, uniform particle size and high surface quality, meeting the requirements of L-PBF forming experiments. The composition is similar to the nominal one, as shown in **Table 3.1**.

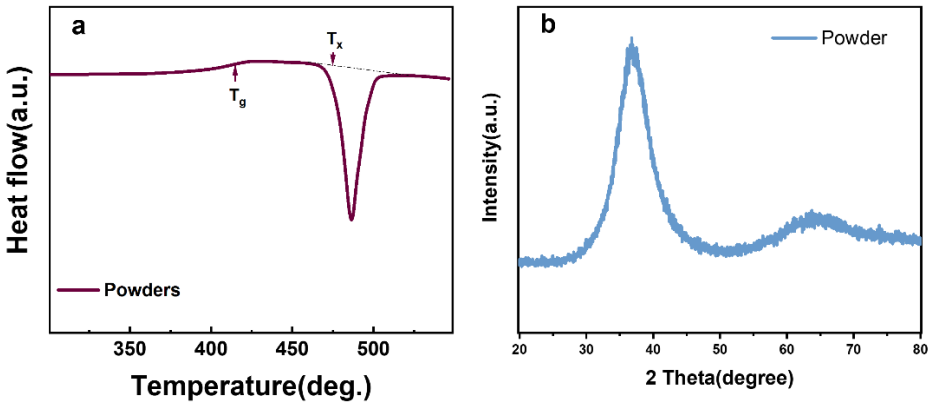

Fig 3. 2 $Zr_{60.14}Cu_{22.31}Fe_{4.85}Al_{9.7}Ag_3$ powders: (a)DSC; (b) XRD.

Table 3. 1 The comparison between nominal and actual composition of powders.

Composition	Zr	Cu	Fe	Al	Ag
Nominal (at%)	60.14	22.31	4.85	9.7	3
Actual (at%)	57.23	27.1	4.95	8.46	2.26

3.2.1 Paramters orthogonal test

In order to investigate the effects of process parameters on the microstructure as well as mechanical properties of 3D printed samples, the final laser energy density was adjusted by changing the laser power and scanning speed, and a series of samples were prepared and obtained. The detailed orthogonal test process parameters are shown in **Table 3. 2.**

Table 3. 2 Process parameters of the L-PBFed $Zr_{60.14}Cu_{22.31}Fe_{4.85}Al_{9.7}Ag_3$ BMG samples.

Laser Power	Energy density (J/mm³)				
	Scan Speed				
	1300 mm/s	1400 mm/s	1500 mm/s	1600 mm/s	1700 mm/s
120 W	15.38	14.28	13.33	12.5	11.76
130 W	16.67	15.48	14.44	13.54	12.75
140 W	17.95	16.67	15.56	14.58	13.73
150 W	19.23	17.86	16.67	15.62	14.71
160 W	20.51	19.05	17.78	16.67	15.69

After the parameters optimization in chapter 3.1.2, a good combination of parameters is chosen based on the XRD and DSC results and OP images of printed samples as the best parameter to fabricate all the lattice materials shown in **Table 3.3**.

Table 3. 3 Process parameters of the L-PBFed $Zr_{60.14}Cu_{22.31}Fe_{4.85}Al_{9.7}Ag_3$ lattices in this study.

Parameter	Value
Laser power	160 W
Layer thickness	60 μm
Scan speed	1400 mm/s
Spot size	80 μm
Hatch type	Stripe
Hatch distance	100 μm

The samples prepared in the orthogonal test are shown in **Fig 3. 3**, and the size of a single square is 6 × 6 × 6 mm^3. Some of the samples prepared at high energy densities had spheroidization on the surface (samples in the red box), which led to serious scraping between the squeegee and the samples during the powder spreading process, and therefore the printing of the corresponding samples was stopped in advance. Except

for the above samples with poor forming quality due to spherification, the rest of the samples printed at energy densities had good forming quality and high surface quality.

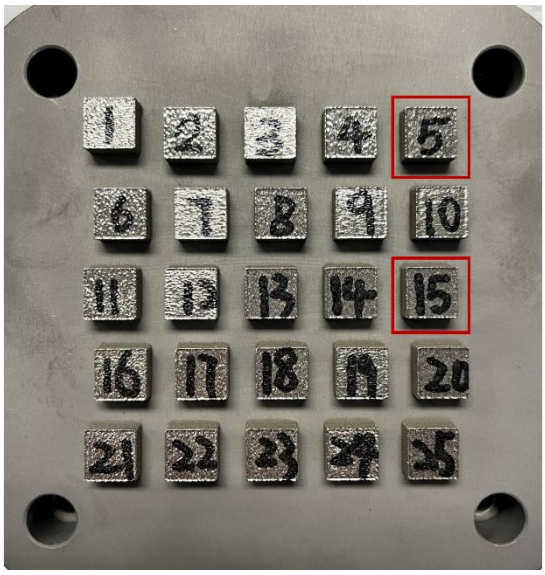

Fig 3. 3 The photographs of L-PBFed samples under different processing parameters.

Table 3. 4 Process parameter, porosity, crystalline and mechanical properties of L-PBFed $Zr_{60.14}Cu_{22.31}Fe_{4.85}Al_{9.7}Ag_3$ BMG samples (σ_c is the compressive strenghth).

laser Power (W)	Scanning speed (mm/s)	Energy density(J/mm^3)	Relative Porosity (%)	Crystalline(%)	σ_F (MPa)
130	1300	16.67	0.75	20.57	-
140	1300	17.95	0.43	18.93	1509 ± 50
150	1300	19.23	1.06	18.49	1472 ± 99
140	1400	16.67	0.19	23.39	-
150	1400	17.86	1.37	21.84	-
160	1400	19.05	0.12	27.80	-
120	1500	13.33	0.62	19.00	1071± 26
130	1500	14.44	0.30	18.41	1082±19
140	1500	15.56	1.54	21.87	-
150	1500	16.67	2.86	25.00	-
140	1600	16.67	0.79	22.08	-
150	1600	15.62	0.47	26.73	-
160	1600	16.67	0.90	27.48	-
120	1700	11.76	3.39	12.27	-
130	1700	12.75	1.78	21.65	-
140	1700	13.73	0.7	19.81	-
150	1700	14.71	0.93	23.79	-
160	1700	15.69	2.58	27.79	-

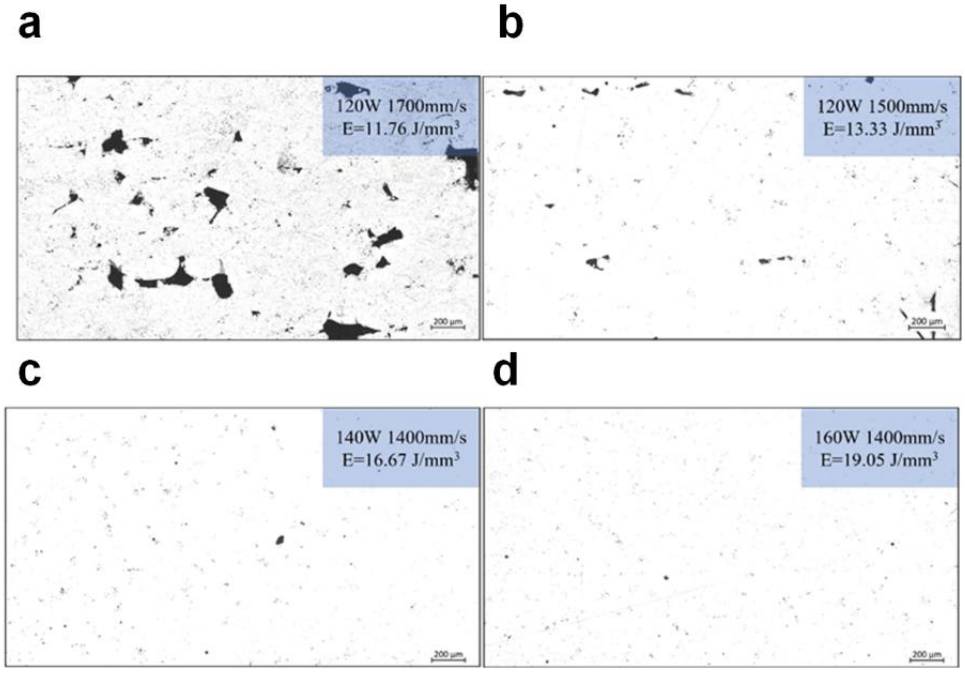

Fig 3. 4 Optical images showing the samples with various porosities. (a) Porosity 3.39%, energy density 11.76J/mm^3; (b) Porosity 0.62%, energy density 13.33J/mm^3; (c) Porosity 0.19%, energy density 16.67J/mm^3; (d) Porosity 0.12%, energy density 19.05J/mm^3.

Fig 3. 4 shows the cross-sectional optical microscopy images of four sets of samples prepared at different energy densities. The number of holes in the cross-section gradually decreases as the energy density increases, which is consistent with the results measured by Archimedes' method. In addition to the change in the number of holes, the morphology is also gradually changing. When the energy density is relatively low, the sample cross section has a large number of holes caused by unmelted powder, in addition to a large number of interlayer holes caused by insufficient remelting of the upper melt pool to the lower pool (**Fig 3. 4 a**). As the energy density gradually increases, the holes caused by the unmelted powder and the interlayer holes gradually disappear and are replaced by open holes (**Fig 3. 4c-d**). As the energy density continues to increase,

the sample becomes very dense. So the higher the laser power, the lower the porosity of the final sample obtained, which is consistent with the reports in the literature.

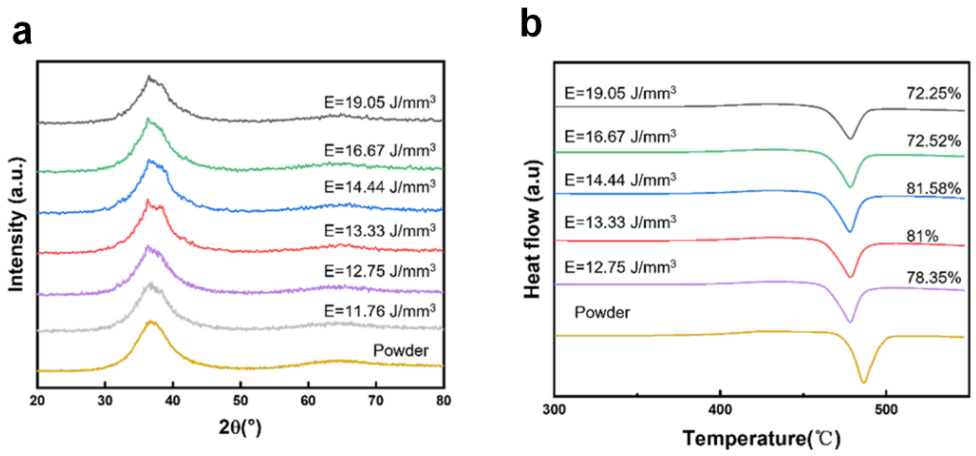

Fig 3. 5 XRD and DSC curves of the L-PBFed samples fabricated under different energy densities, compared with the original powders.

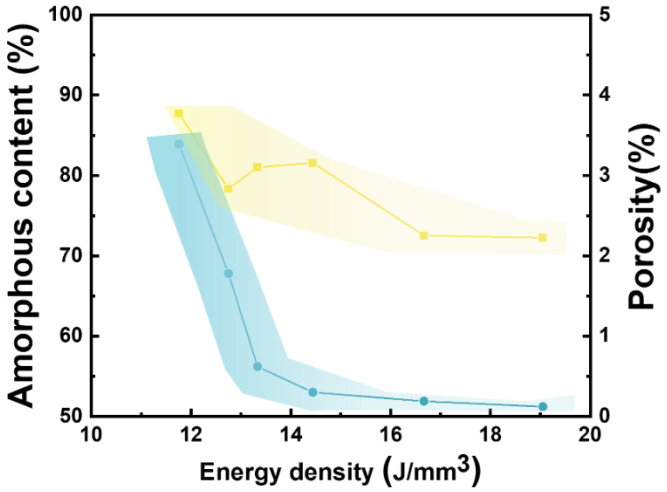

Fig 3. 6 Correlation between the amorphous content/porosity fractions and the energy density of L-PBFed samples for mechanical properties test.

To investigate the connection between process, structure and performance, a series of amorphous alloy samples with specific process parameters were prepared, and the process parameters are shown in **Table 3. 2**. Six groups of samples were selected from

them for XRD and DSC tests, and the results are shown in **Fig 3. 5**. **Fig 3. 5a** shows the XRD results of the powder and different samples, and it can be found that the structure of L-PBF formed $Zr_{60.14}Cu_{22.31}Fe_{4.85}Al_{9.7}Ag_3$ amorphous alloy is closely related to the energy density. When the energy density is less than 11.76 J/mm^3, the XRD results show complete diffuse scattering peaks, indicating that the sample is completely amorphous; when the energy density is 13.33 J/mm^3, some low-intensity crystallization phase diffraction peaks start to appear on the diffuse scattering peaks of amorphous formation Subsequently, the amorphous content of each group of samples was tested using DSC. **Fig 3. 5b** shows the DSC results of the corresponding samples, and it can be found that the amorphous content decreases from 87.73% to 72.25% when the energy density increases from 11.76 J/mm3 to 19.05 J/mm3. **Fig 3. 6** shows the trend of crystallization fraction and densification with energy density for all process parameters. The crystallization fraction exhibits an overall increasing trend with the increasing energy density. And the porosity is below 0.62% with the energy density range from 14.44 J/mm^3 to 19.05 J/mm^3. And when the energy density is below 14.44 J/mm^3, the porosity rapidly increases to 3.39% while the energy density equals 19.05 J/mm^3.

3.3 Morphology characterization

The structural features of the different lattices were characterized by FF35 X-ray computed tomography (CT) (YXLON, Germany) in **Fig 3. 7**. VEGA 3 scanning electron microscope (SEM) (TESCAN, Brno) was used to investigate the surface morphology of the printed lattices.

Fig 3. 7 X-ray computed tomography system.

To deeply analyze the manufacturing deviations from the L-PBF process, the actual relative densities of the printed lattices were measured by the dry weighing method. A wire-cut electrical discharge machining process was used to remove all specimens from the platform, and the wire-cut surfaces were then polished mechanically with sandpaper. The samples were then weighed after being dried, polished, and cleaned. To determine the total volume occupied by a lattice, all specimens were measured three times using a vernier caliper.

3.4 Measurement of properties

3.4.1 Compression tests

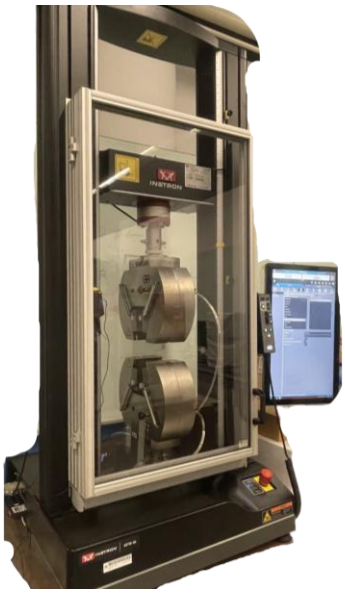

Fig 3. 8 Compression test machine.

We used a 68TM-50 universal testing machine (Instron, USA), as shown in Fig 3. 8, to obtain the room temperature compressive properties of fabricated MG lattices. Every test was performed under displacement control with a strain rate of 1.0 × 10-3 s-1 at room temperature and stopped until totally collapse. Pre-load force were set as 50N. We used a DSLR camera positioned nearby to record the compression deformation behavior of the MG lattices, capturing one image every 2 seconds.

3.4.2 Electrochemical measurements

All electrochemical measurements were conducted at 323 K using an electrochemical workstation (CHI 660E, Shanghai, China). The electrocatalytic performance for both the HER and OER was evaluated in 1.0 M KOH using a standard three-electrode setup, with the synthesized catalyst directly serving as the working

electrode. Contact angle measurements were performed using a Data Physics OCA15 instrument, with both water droplets and gas bubbles set to a volume of 4 μL. For OER testing, high-purity oxygen was continuously bubbled through the electrolyte to saturate the solution and maintain the O_2/H_2O equilibrium potential at 1.23 V vs. RHE. For HER testing, high-purity nitrogen was purged through the electrolyte for 30 minutes before and during the measurements to remove dissolved oxygen. The polarization curves were obtained by linear sweep voltammetry at a low scan rate of 0.5 mV s^{-1} to eliminate the influence of double capacitance. All polarization curves presented in this work were undertaken iR-corrected with a level of 90%. The Tafel slope was calculated according to the Tafel equation, as follows: $\eta = b \log j + a$, where η, j, b, and a are the potential (V), current density (mA cm^{-2}), Tafel slope (mV dec^{-1}), and intercept, respectively. The chronopotentiometry tests were recorded by applying a current density of 10 mA cm^{-2}. Electrochemical impedance spectroscopy (EIS) was conducted at the open-circuit potential of each sample over a frequency range of 100 kHz to 0.01 Hz, using an AC voltage amplitude of 5.0 mV. Cyclic voltammetry (CV) measurements were performed within a narrow non-Faradaic potential window at varying scan rates (20, 40, 60, 80, and 100 mV s^{-1}) to determine the double-layer capacitance (C_{dl}), which was then used to estimate the electrochemically active surface area (ECSA).

3.5 Computational modeling

3.5.1 Finite element method

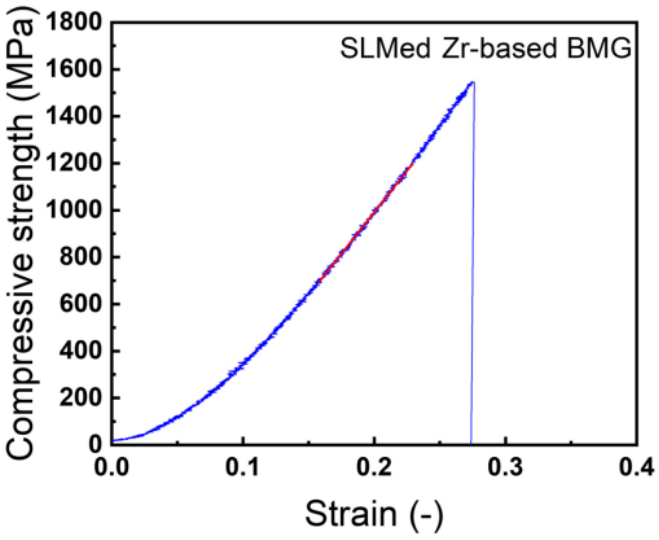

Fig 3. 9 Representative uniaxial compressive stress versus strain response of L-PBF-built Zr-based BMG.

To elucidate the strengthening mechanism of the MG lattices, the linear finite-element (FE) quasi-static compression simulation was conducted to investigate the stress distribution by the commercial software COMSOL multiphysics. Mechanical properties of 3D-printed $Zr_{60.14}Cu_{22.31}Fe_{4.85}Al_{9.7}Ag_3$ for the FE method are illustrated in **Fig 3. 9.** We simulated experimental compression conditions by placing the BCC meshes between two rigid flat plates. The top plates were allowed to move only along the Z-axis, while the bottom plates were fixed in all directions (**Fig 3. 10**). The model was meshed using free tetrahedral elements. To account for static friction between the plates and the samples, the frictional coefficient was set to 0.15.

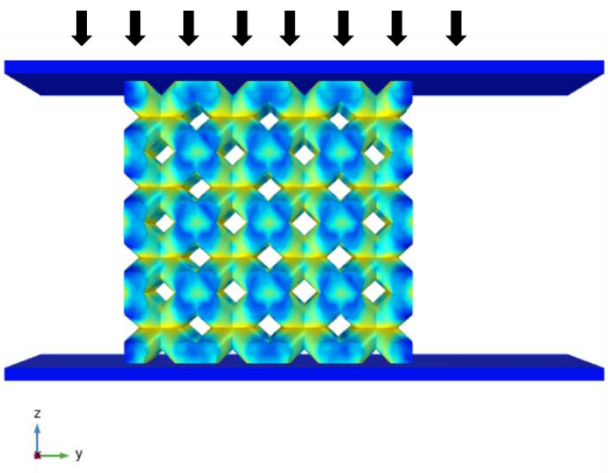

Fig 3. 10 Shematic diagram of compression process simulation of MG lattices.

The representative uniaxial compression stress versus strain response was presented in **Fig 3. 9**. The solid parent 3D-printed Zr-based BMG under 19.23 J/mm3 energy density has a compressive strength of 1509 MPa and Young's modulus of 72.0GPa. This data was used for normalizing the compressive strength and elastic modulus for MG lattices in this study. 3D printed Zr-based BMG only has the elastic stage; thus, the linear explicit finite element method was applied to study the stress distribution of MG lattices. And the discussion based on the simulation results only focuses on the elastic stage, to ensure the reliability of the simulation results. To analyze the elastic stress distribution in Zr-based MG structures under large deformation, we adopt a finite-deformation continuum framework, governed by the equilibrium equation:

$$\nabla \cdot (FS)^T + Fv = 0, F = I + \nabla u \tag{3.1}$$

where the first Piola–Kirchhoff stress tensor **S** accounts for both additional stress contributions and elastic responses through:

$$S = S_{ad} + J\,\mathrm{F}_{inel}^{-1}(C{:}\,\varepsilon_{el})\,F_{inel}^{-T} \tag{3.2}$$

Here, the elastic Green–Lagrange strain tensor is defined as

$$\varepsilon_{el} = \frac{1}{2}(F_{el}^{T}F_{el} - I), F_{el} = FF_{inel}^{-1} \tag{3.3}$$

For purely elastic analysis of MGs, the inelastic deformation gradient F_{inel} can be assumed to be the identity tensor.

3.5.2 Finite volume method

Geometric deviations introduced during the L-PBF process were quantitatively assessed using micro-focus computed tomography (micro-CT, ZEISS Xradia Versa610). The 3D reconstructed models of the printed lattice structures were imported into VGSTUDIO software for fluid permeability and mass transport analysis. Fluid flow simulations were conducted using the Navier–Stokes equations for incompressible fluids with constant density and viscosity. A pressure gradient of 1 Pa was applied across all models, with the outlet pressure fixed at zero to evaluate steady-state flow behavior.

Geometric deviations introduced during the L-PBF process were quantitatively assessed using micro-focus computed tomography (micro-CT, ZEISS Xradia Versa610). The 3D reconstructed models of the printed TPMS structures were imported into VGSTUDIO software for fluid permeability and mass transport analysis. Fluid flow simulations were conducted using the Navier–Stokes equations (Eq. 3.4) for incompressible fluids with constant density and viscosity. A pressure gradient of 1 Pa

was applied across all models, with the outlet pressure fixed at zero to evaluate steady-state flow behavior.

$$\rho \frac{\partial \upsilon}{\partial t} - (\upsilon \cdot \nabla)\upsilon + \frac{\nabla P}{\rho} - \mu \nabla^2 \upsilon - F = 0 \quad (3.4)$$

Where ρ is the density of the transport fluid (kg/m^3), υ is the fluid velocity (mm/s), and μ is the dynamic viscosity coefficient of the fluid (Pa s); ∇ and P are the del operator and pressure (Pa), respectively; and F denotes other forces (gravity or centrifugal force; in this case, F = 0). $\upsilon \cdot \nabla = 0$.

Chapter 4 The enhancement of damage tolerance of 3D-printed high strength MG lattices by unit cell shape design

4.1 Introduction

In future deep space exploration, spacecraft will encounter increasingly complex and variable environments. Their internal precision instruments will impose higher demands on load-bearing and protective structures. It has already been observed that the small size of debris can potentially cause damage to operational space systems. Spacecraft architects incorporate implicit protection into the vehicle architecture to mitigate the risk of function loss or mission failure resulting from collisions with small -sized debris, especially particles ranging from 1 to 5 mm in diameter [172]. Hence, Structural materials must meet specific criteria for the mechanical properties of advanced aerospace materials, including high strength, impact resistance, and excellent energy absorption capabilities.

Though the above crystallized metallic structural materials boast impressive mechanical properties, they fall short of meeting the rigorous requirements of future aerospace materials. BMGs hold a prominent position in the realm of spacecraft materials due to their advantages such as high hardness, high strength, large elastic limits etc. [173], and have become a highly coveted material in both spacecraft shielding and advanced structural applications [29, 174-178]. In addition to its excellent mechanical properties, BMGs exhibit distinctive functional characteristics [22, 179-182], including biocompatibility [72], catalytic properties [162], corrosion resistance

[72], wear resistance [183], optical properties, soft magnetic properties and energy absorption capacity.

However, research on BMGs structural materials has remained stagnant due to the challenges posed by the large-scale production and their inherent brittleness at room temperature. Particularly, research regarding 3D-printed structural BMGs as energy-absorbing materials is rarely reported. In this case, the relationship between the lattice structure and damage tolerance, as well as other mechanical properties, remains unclear. The exploration of energy absorption in BMG structures is still largely confined to the 2D or microscopic level [161, 184].

Conventional fabrication methods are incapable of producing BMGs with complex shapes due to the requirement of having a sufficiently high cooling rate. In recent years, the emergence of AM technology, with its layer-by-layer processing capabilities, has enabled the production of fully glassy components with intricate shapes [185, 186]. This development offers a new approach to address the two challenges associated with amorphous alloy forming: size limitations and shape constraints [162, 187]. The compressive strength of 3D-printed BMGs (1000-2500 MPa) is comparable to that of as-cast BMGs [185]. By utilizing AM technology, structural BMGs can be designed and fabricated with tailored mechanical properties to meet the specific demands of the aerospace applications. Compared to random foams, lattice structures composed of periodic repeating unit cells offer a higher degree of

designability and controllability [188], making them more suitable for comprehensively summarizing deformation behavior and pursuing higher performance.

The body centered cubic (BCC) structure is the most common and well studied strut-based structure [189]. With its simple configuration, it is suitable for establishing the structure-property relationship for new materials. Besides, triply periodic minimal surface (TPMS) structures, a novel lattice structure, are intriguing for their uninterrupted and sleek surfaces, facilitating extensive surface areas and unbroken internal passages. The diamond lattice (D-TPMS) is a type of TPMS structure that exhibits superior energy absorption capabilities compared to other TPMS structures [190]. TPMS lattice structures offer potential advantages over strut-based lattices in terms of manufacturability and mechanical properties, as they exhibit zero mean curvature at every point, thereby avoiding stress concentration at the nodes.

In this chapter, utilizing the AM technology, we fabricated the 3D lattices BMG with a strut-based BCC lattice and a sheet-based TPMS lattice. Subsequently, an investigation of the compressive deformation behavior of the 3D-printed architectural BMG was conducted to establish a structure-property relationship for guiding future BMG structural designs. It was found that the issue of extreme brittleness remains a significant challenge in the context of BMG lattice structures. The D-TPMS lattices failed to demonstrate their superior energy absorption capabilities due to catastrophic failure. In contrast, BCC lattices exhibited better adaptability to the brittle BMG due to continuous crushing. Drawing inspiration from unit cell designs with the potential to

alter deformation behavior, we formulated a novel structural design strategy that optimizes unit cell configurations within BCC lattices [191]. The body-centered tetragonal (BCT) unit cell can be envisioned as a variation of the body-centered cubic (BCC) unit cell, with a slight decrease in height along one direction, where $a = b \neq c$. As the BCC unit cell transforms into the BCT unit cell, alterations in stress distribution within the lattices result in the initiation of microfractures in struts. This leads to the progressive formation and propagation of crack bands, thereby avoiding catastrophic failure. Subsequently, the proposed design strategy was evaluated in the framework of the BCC structure with different strut lengths, and finally achieved the simultaneous enhancement of compressive strength and energy absorption capacity. More importantly, our strategy effectively changed the failure mode of the structural BMGs, marking a significant step toward addressing the challenge of brittleness in BMG lattice structures.

4.2 Methodology

4.2.1 Manufacture and modeling of lattice structures

Gas-atomized equimolar $Zr_{60.14}Cu_{22.31}Fe_{4.85}Al_{9.7}Ag_3$ MG powders (ShanDong LianHong New Material Technology Co., Ltd China), with a nominal particle size ranging from 0 μm to 53 μm, were used in the L-PBF process for the specimen fabrication. The powder morphology was observed in scanning electron microscopy equipped with an energy disperse spectroscopy (SEM, Sigma 300, Zeiss, Germany) detector. **Fig 4. 1a** shows the spherical MG powders fabricated by the gas atomization

process. The SEM results indicate that the powders exhibit good sphericity, uniform particle size, and high surface quality, meeting the requirements for L-PBF forming experiments. **Table 4. 1** presents the comparison between the nominal composition and actual composition of MG powders. The MG specimens, including bulk and lattices, were manufactured using a selective laser melting system (SLM 125 HL, SLM Solutions Group AG, Germany).

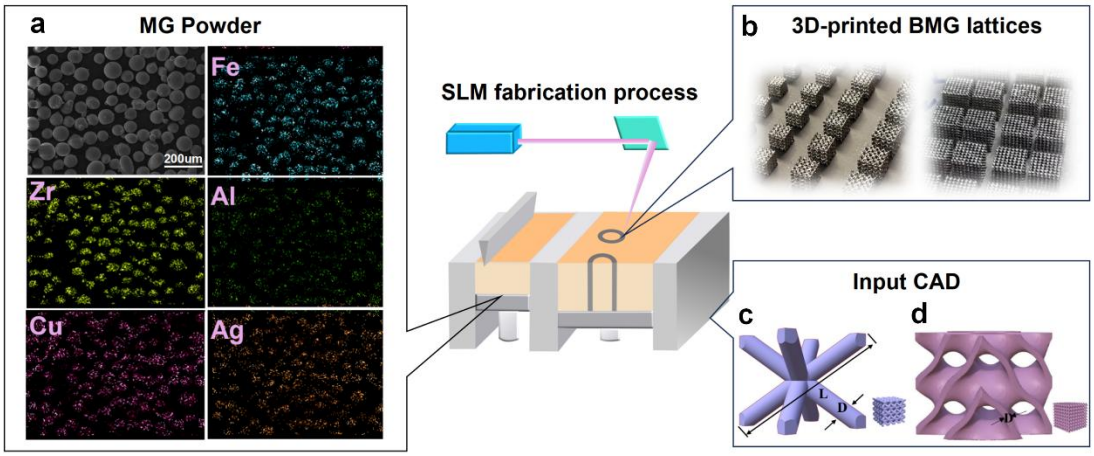

Fig 4. 1The design, fabrication of the 3D-printed BMG lattices. (a) The morphology in SEM of $Zr_{60.14}Cu_{22.31}Fe_{4.85}Al_{9.7}Ag_3$ MG powder used in the L-PBF approach corresponding EDS element maps. (b) 3D-printed BMG specimens. CAD models of the unit cell of (c) BCC and (d) D-TPMS.

Table 4. 1 The comparison between the nominal and actual composition of powders.

Composition	Zr	Cu	Fe	Al	Ag
Nominal (%)	60.14	22.31	4.85	9.7	3
Actual (%)	57.23	27.1	4.95	8.46	2.26

In this paper, we have selected a classical strut-based BCC lattice structure and a novel sheet-based D-TPMS structure for our initial attempt to integrate MG into cellular structures. Printed MG lattices shown in the **Fig 4. 1b**. COMSOL and Magics software were used to create 3D models and slice the 3D stereo-lithography (STL) files for 3D printing, as shown in **Fig 4. 1c-d**. The geometric properties of BCC are shown in **Table 4. 2**. These four BCC structures (D0.8L2.8- D0.8L4.0) have cubic unit cells with decreasing side lengths so as to obtain diverse porosities (D and L refer to the diameter and the length of the structure of the unit cell). The TPMS structure's geometric model can be mathematically estimated through implicit methods [192]. This approach generates 3D surfaces as the solution of level set function Φ = c, referred to as the c-level set. The Diamond surfaces of the structure are described by the following approximations：

$$\Phi_D(x,y,z) = \sin(\omega x)\sin(\omega y)\sin(\omega z) + \cos(\omega x)\sin(\omega y)\sin(\omega z) + \sin(\omega x)\cos(\omega y)\sin(\omega z) + \sin(\omega x)\sin(\omega y)\cos(\omega z) = c \quad (4.1)$$

where x, y and z are spatial coordinates, $\omega = 2\pi/l$ and l is the length of a unit cell.

A 3D model of the TPMS sheet geometry (**Fig 4. 1d**) is created by extracting the zero-level surface from Eq. 1 in a MATLAB script, i.e., the surface defined by Φ = 0, and then offsetting the surface uniformly in both directions. The geometric properties of D-TPMS are shown in **Table 4. 2**. These four TPMS structures have the same cubic unit cells with increasing shell thickness to obtain diverse decreasing porosities (T

refers to the shell thickness). The porosity of the TPMS was set consistent with the BCC lattices to have a better comparison.

Table 4. 2 Geometrical specifications of the BCC and TPMS lattices.

Lattice sample code	Nominal shell thickness (mm)	Strut Diameter (mm)	Strut length of Unit Cell (mm)	Unit cell size (mm)	Number of cells (x,y,z)
D0.8L4.0	/	0.8	4.0	2.31× 2.31×2.31	(4,4,4)
D0.8L3.6	/	0.8	3.6	2.10 × 2.10 × 2.10	(4,4,4)
D0.8L3.2	/	0.8	3.2	1.85 × 1.85 × 1.85	(4,4,4)
D0.8L2.8	/	0.8	2.8	1.62 × 1.62 × 1.62	(4,4,4)
T293	293	/	/	2.5 × 2.5× 2.5	(4,4,4)
T345	345	/	/	2.5 × 2.5× 2.5	(4,4,4)
T403	403	/	/	2.5 × 2.5× 2.5	(4,4,4)
T468	468	/	/	2.5 × 2.5× 2.5	(4,4,4)

4.2.2 Morphological and microstructure characterization of the 3D-printed BMG lattices

The structural features of the BMG lattices were characterized using FF35 X-ray computed tomography (CT, YXLON, Germany). The CT tests were conducted at a voltage of 150 kV and a current of 30 μA. To evaluate the densification level of the 3D-printed lattices, a representative BCC lattice structure with dimensions of 2.31×2.31×2.31 unit cells was scanned. Commercially available image analysis software, VG Studio Max 3.5 (Volume Graphics GmbH, Heidelberg, Germany), was employed for further data analysis and visualization. The porosity *P* of the lattices was calculated as

$$P = \left(1 - \frac{\rho}{\rho_0}\right) \times 100\% \tag{4.2}$$

where ρ is the density of the structural alloys, ρ_0 is the densitiy of the bulk alloys.

The phases in the original MG powders and 3D-printed BMG lattices were investigated by X-ray diffractometer (XRD, Rigaku SmartLab 9KW, Japan) with a 2θ range from 20° to 80° and a differential scanning calorimeter (DSC 250, TA, USA) with a heating rate of 20K/min. Mechanical properties of 3D-printed BMG were tested in accordance with ASTM E9-09, where the compressive strength represents the maximum stress at or before fracture for brittle materials. The sample sizes of the BCC and TPMS lattices are provided in **Table 4. 2**.

4.2.3 Unit cell shape design on BCC structure to enhance the damage tolerance.

Since strut-based BMG lattices demonstrate a superior capacity to inhibit the expansion of impact-induced crack penetration through local fracture, we initially selected the BCC lattice as our baseline model. In the context of macro lattice structure design studies, the compressive deformation behavior of the meshes is influenced by the coupled mechanisms of bending and buckling. Drastic buckling behavior can be mitigated by increasing the bending component through unit cell shape design. Thus, to address the inherent brittleness of BMG during compressive deformation, unit cells are designed to increase the bending component of the load applied to the struts. These specially designed BCT structures (D0.8L3.2-90%- D0.8L3.2-70%) are derived from the cubic unit cell: D0.8L3.2, by scaling the unit cell in the z-axis direction using the corresponding multiplier α (ranging from 90% to 70%), as depicted in **Fig 4. 2b**. This method of altering the unit cell shape maintains consistent porosity across the entire mesh, facilitating meaningful comparisons of different unit cell shapes under the same volume fraction. **Table 4. 4** indicates the geometrical specifications of the BCT lattices.

Table 4. 3 Geometrical specifications of the BCT lattices.

Lattice sample code	Unit cell size (mm)	Number of cells (x,y,z)	Angles between the applied load and the beam (°)	Measured porosity (%)
D0.8L3.2-90%	1.85 × 1.85 × 1.66	(4,4,4)	32.47	40.8

D0.8L3.2-85%	1.85 × 1.85 × 1.57	(4,4,4)	31.01	39.2
D0.8L3.2-80%	1.85 × 1.85 × 1.48	(4,4,4)	29.50	39.6
D0.8L3.2-70%	1.85 × 1.85 × 1.29	(4,4,4)	26.33	39.4

4.3 Results

4.3.1 Morphological characteristics and microstructure of the 3D-printed BMG lattices.

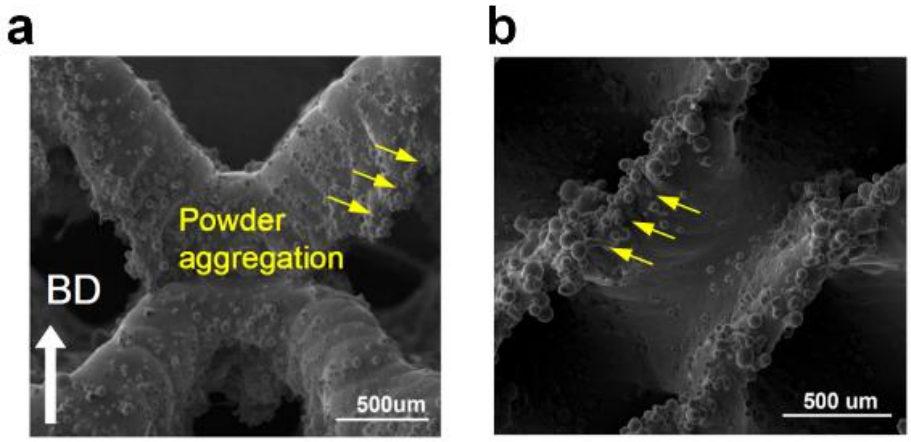

Fig 4. 2 SEM images of the outside surface of 3D-printed BMG lattices:(a) BCC and (b) D-TPMS.

Fig 4. 2 a-b illustrates the SEM images of 3D-printed BMG lattices characterized by low roughness and a defect-free structure. However, it is noteworthy that some residual, unmelted powder adhered to the outer surface, resulting in deviations between the measured and designed porosity levels of the lattices.

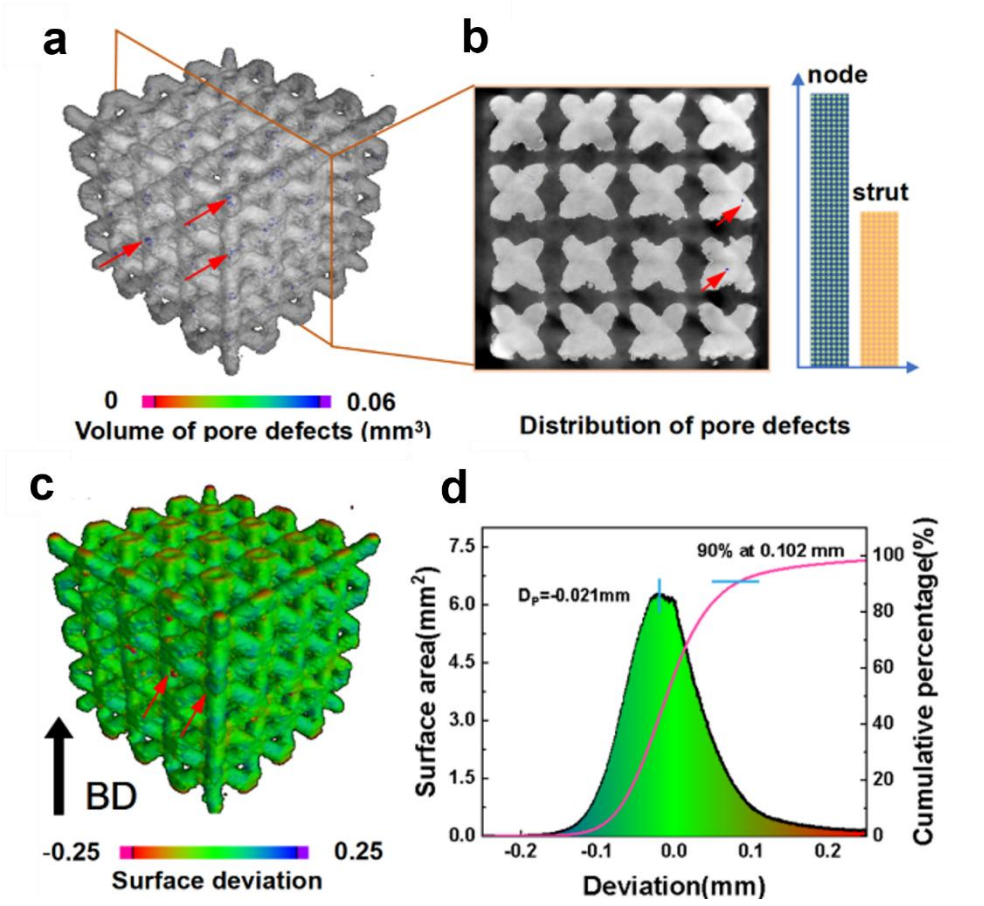

Fig 4. 3 Morphological characteristics of 3D-printed BMG lattices. (**a**) Three-dimensional pores distribution of BCC BMG lattices and (**b**) data statistics of the number of pores distributed at nodes and struts. (**c**) Three-dimensional surface deviation maps and (**d**) statistical surface deviation distributions of BCC BMG lattices (D_p was the peak surface deviation, 0.102 indicated the intercepts for 90% of the cumulative percentage.)

3D-printed BCC specimens were quantitatively evaluated by the X-ray CT method (**Fig 4.3 a-d**). From the defect volume distribution data presented in **Fig 4. 3a**, it is evident that the internal pores within the fabricated lattice predominantly measure below 0.001 mm^2, resulting in a mere 0.06% defect volume ratio. This signifies that the sample's density exceeds 99.9%. We counted the number of the pores distributed at the nodes and struts in **Fig 4. 3b**, which were 523 and 828, respectively. The distribution

histogram indicates that the pores are more likely to appear at the nodes. The predominant green coloration within the contours in **Fig 4. 3c-d** denotes surface deviations, which exhibit a commendable acceptability level, with 90% of deviations measuring below 0.13 mm.

Table 4. 3 shows the dry weight of 3D-printed BMG lattices. Due to the different structures, the measured average mass ranges from 2.32 g to 4.92 g, and porosities range from 59.5%-16.1%. For the four BCC structures, the mass deviations: $\eta_m = \frac{|m_d - m|}{m} \times 100\%$, are below 4%. These deviations came from the error caused by the wire cutter and the powder aggregation on the struts and nodes as shown in the SEM figures in **Fig 4. 3a**, which are acceptable results for small dimensions lattices within 10 mm.

Mass deviations η_m in TPMS structures exceed 14%, which is influenced by various factors due to their unique shell-based design. To efficiently design the geometries, TPMS structures offer inherent advantages but require discretization into mesh models for additive manufacturing. Enhanced calculation accuracy is essential. Despite the influence from the input mesh model, the large melt pool size and over-melting during the fabrication process made the residual particles more likely adhere to the surfaces; thus, the measured average weights *m* of TPMS lattices are all bigger than the designed m_d. As the nominal thickness increases, the volume fraction increases, while the deviation decreases. One of the primary reasons is that the nominal thickness setting is too small compared to the laser spot size (80 μm). The overmelting

phenomenon significantly impacts the relative densities. As the nominal setting increases, the effect of overmelting decreases, bringing m closer to the designed m_d. The nominal thickness designed in this study is constrained by overall dimensions to maintain porosity consistent with the BCC structures.

Table 4. 4 Geometrical characteristics of the as-designed lattices and mass comparison of the as-built lattices and as-designed lattices.

Lattice sample code	Designed m_d (g)	Measured average m (g)	Deviation η_m (%)	Measured porosity (%)
D0.8L4.0	2.41	2.32 ± 0.03	3.88	59.5
D0.8L3.6	2.05	2.02 ± 0.01	1.49	52.1
D0.8L3.2	1.71	1.73 ± 0.08	1.16	42.6
D0.8L2.8	1.36	1.39 ± 0.04	2.16	30.6
T293	3.04	4.07 ± 0.01	25.3	41.3
T345	3.59	4.42 ± 0.02	18.78	35.8
T403	4.22	4.97 ± 0.01	15.09	28.0
T468	4.92	5.78 ± 0.01	14.88	16.1

Fig 4. a-b shows the XRD and DSC results of the Zr-based MG powders and the 3D-printed BMG. The XRD pattern of the powders exhibits a broad halo diffraction peak without any detectable crystalline peaks, demonstrating a fully glassy structure. The 3D-printed BMG exhibits a similar broad diffraction peak with small crystalline peaks on it, with the nanocrystalline maybe induced during the 3D-printng process in the heat-affected zone (HAZ) [193]. DSC results also indicate that there exists partial

crystallization in the printed BMG. The amorphous content of the 3D-printed samples was determined using the equation Am.% = ΔH/ΔHp [43], where Am.% represents the fraction of the amorphous phase, and ΔH and ΔHp denote the crystallization enthalpies of the printed samples and the original amorphous powders, respectively. From the DSC results, it can be inferred that the amorphous content in 3D-printed BMG is 72.25%. Generally, the BMG has a smaller amorphous fraction than the porous MG because the 3D-printed lattice exhibits significantly larger molten pools due to less constraint in S regions.

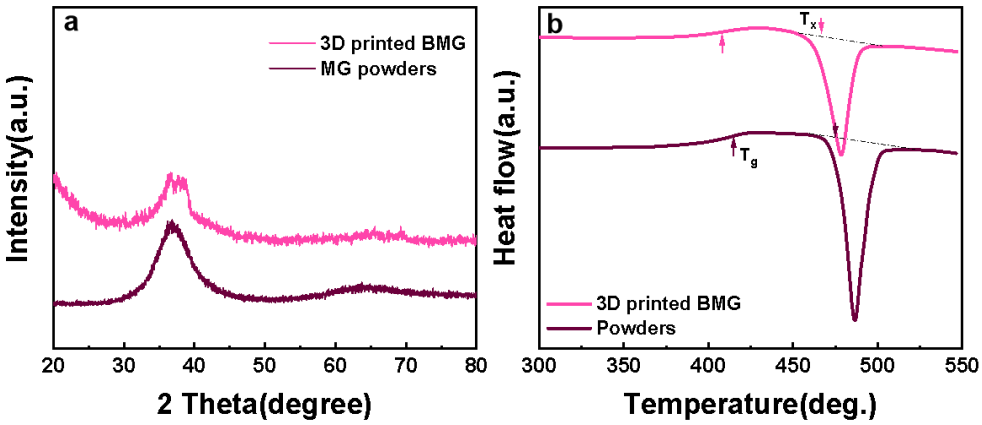

Fig 4. 4 (a) XRD patterns and (h) DSC plots of the 3D-printed BMG and MG powders, respectively.

4.3.2 Mechanical properties of 3D-printed BMG lattices.

Fig 4. 5 displays the compressive stress-strain curves for BCC lattices and TPMS lattices with various porosities. For crystalline ductile metallic lattices, the stress-strain curves can be divided into three regions: an elastic deformation region before the first peak value is reached, a plateau region combining buckling and bending deformation, and a final densification region corresponding to rapid stress increase [194]. When it

comes to MG lattices, their compression behavior is similar to that of brittle metallic lattices. The stress-strain curves of MG also exhibit three stages, as shown in **Fig 4. 5a-b**: an elastic deformation region before collapse strength σ_c (0- I), an extensive failure stage characterized by a dramatic drop in stress (I-II), a continuous local failure with decreasing low stress (II-III). **Fig 4. 5c-j** shows the deformations behavior and failure mechanisms of diverse porosities BCC lattices and TPMS lattices. For MG BCC lattices with high porosities (>50%), the compressive deformation behavior ends at stage II, with a single long fracture band throughout the whole structure due to catastrophic failure, leading to the stress suddenly dropping to 0 in the stress-strain curves (refer to I-II and I'-II' in **Fig 4. 5c-d**). The fracture angle measured from SEM figures is approximately 45°, consistent with the classical BCC lattice fracture mode. Furthermore, as the porosities decrease to less than 50%, the significant stress drop observed in stage II is reduced to a lesser extent. This behavior is clearer when the porosity decreases to 30.6% (specimen D0.8L2.8), at stage II (I"'-II"'), and this dramatic drop is manifested as a single significant reduction rather than multiple discontinuous drops. This corresponds to the propagation of multiple crack bands inside the structure (as shown in **Fig 4. 5f**), leading to the beam fracture at various locations until the entire structure collapses. The lower porosity introduced here corresponds to smaller pore sizes, which hinder the connection of crack bands under loading, thus preventing catastrophic failures. However, it remains challenging to completely avoid the dramatic stress drops in stage II by controlling pore size and porosity.

Unlike BCC structures that consist of struts and nodes, TPMS structures lack nodes, which reduces stress concentrations. From previous FE results of the Diamond TPMS structure [190], sheet-based structures exhibit a homogeneous failing manner, where all layers demonstrate relatively uniform deformations under applied loads. However, due to the brittle materials characteristics, TPMS MG lattices did not behave better than BCC structures as expected. They exhibit high strength but with catastrophic failure under compression. At porosities higher than 30%, multiple cracks rapidly propagate the structures in the loading direction. In **Fig 4. 5g-h**, we can clearly see that the crack bands separate the lattices into several parts. However, since the crack propagation direction is parallel to the loading direction, the lattices can maintain structural integrity for a while to bear the load in the Z direction. However, due to severe damage, the load-bearing capacity is maintained at low-stress levels with a continued detachment of the broken parts from the structure. When the porosity decreases below 30%, the crack band becomes singular, and the fracture angle is 45% (**Fig 4. 5i-j**). As the porosity decreases, the fracture mode of the TPMS MG lattices is contrary to that of the BCC MG lattices. Compared with the sheet-based structure TPMS, more stress fluctuations occur on strut-based BCC structure, and localized fracture of the struts absorbs the compression energy, thus avoiding primary crack generation and rapid penetration throughout the sample.

In summary, when the loading stress exceeds the elastic limit of the brittle material, these artificially introduced porous structures dissipate the input energy by proliferating

microcracks as the applied strain increases. As the energy in the material is dissipated and the stress is relaxed, there is no main crack penetration. This is the result of quasi-static loading of the porous structure to enhance the deformability and damage resistance of brittle materials.

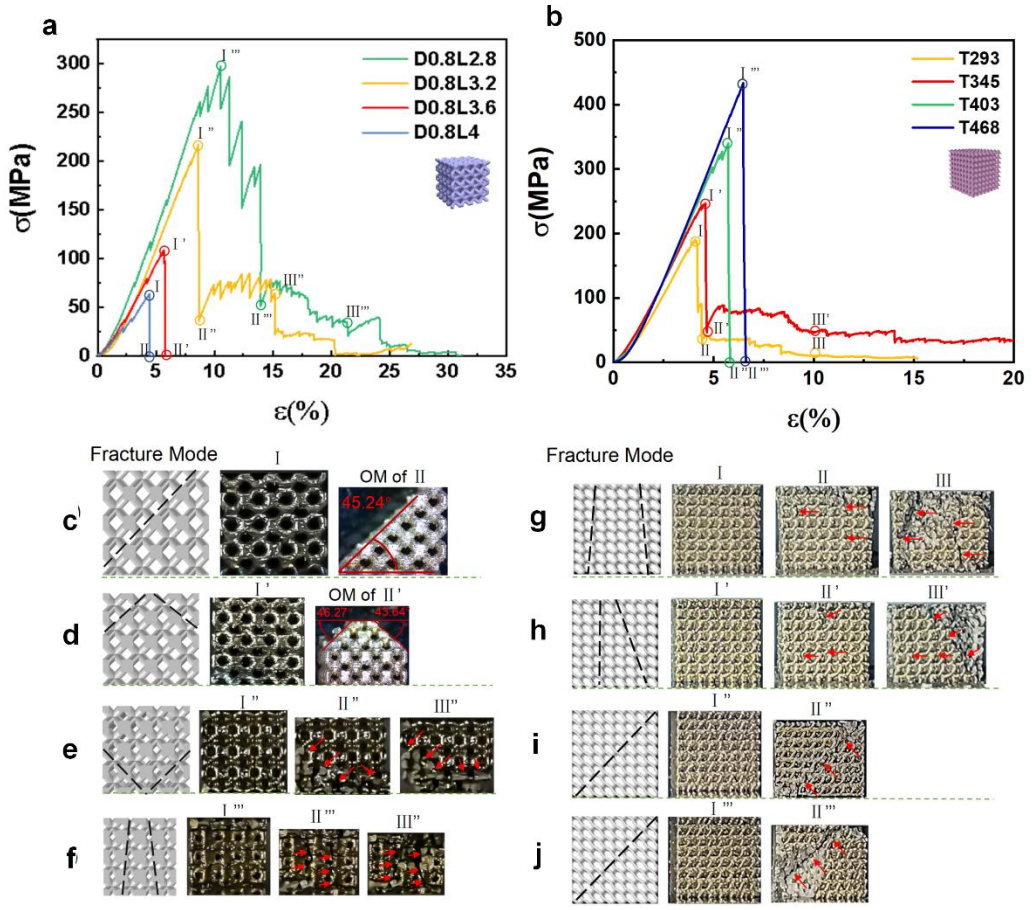

Fig 4. 5 Compressive stress-strain curves of 3D-printed BMGs with diverse porosities: (a) BCC lattices (b) TPMS lattices. Deformation behavior and fracture mode of diverse porosities of BCC BMG lattices: (c) D0.8L4 (d) D0.8L3.6 (e) D0.8L3.2 and (f) D0.8L2.8 and TPMS BMG lattices (g) T293 (h) T345 (i) T403 (j) T468. The red arrow indicates the crack bands.

4.3.3 Ashby predicted model.

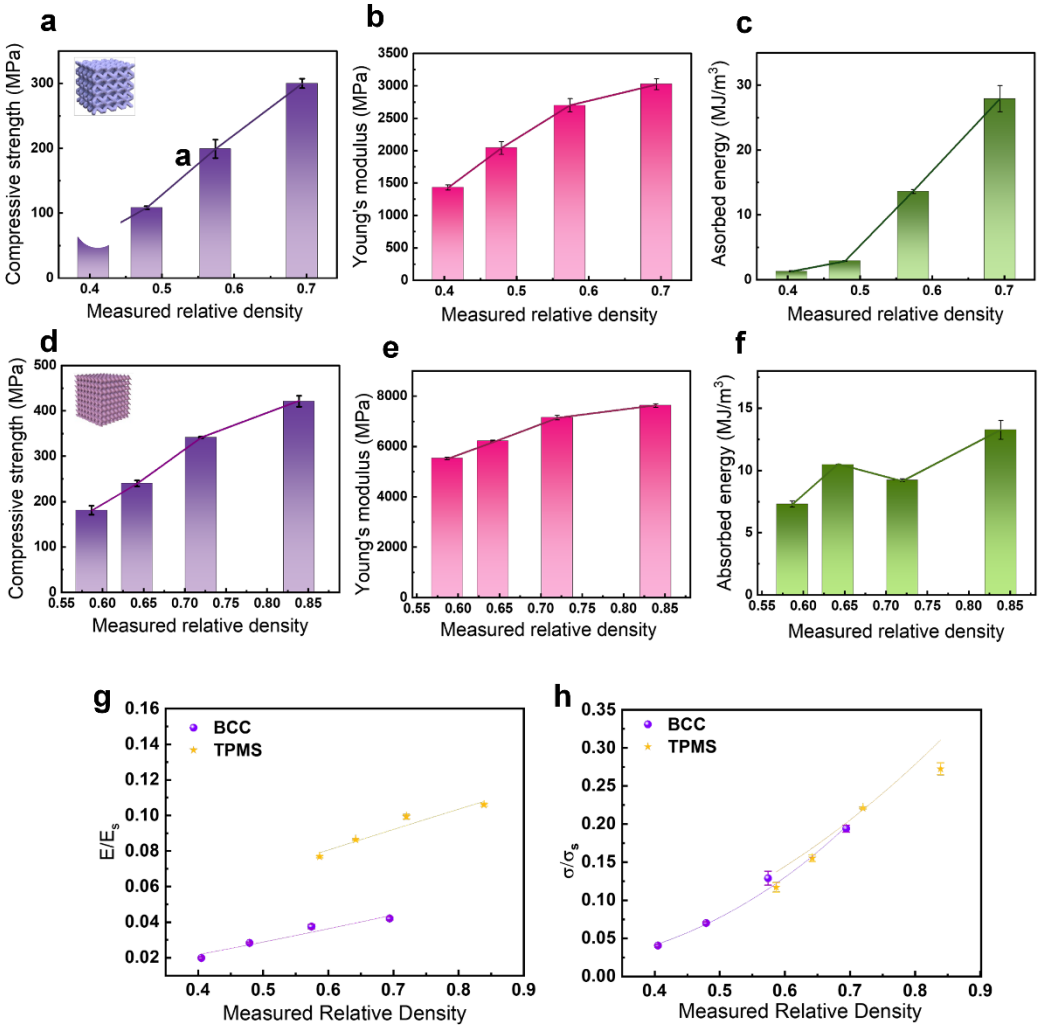

Fig 4. 6 Mechanical properties of BCC BMG lattices (a-c) and TPMS BMG lattices (d-f)**:** Compressive strength, Young's modulus, Energy absorption versus the measured relative density. Comparison on (g) normalized elastic modulus (h) normalized compressive strength.

Variations in compressive strength σ, Young's modulus E, and energy absorption W with measured porosities of two types of lattices are shown in **Fig 4. 6a-c** for BCC lattices and **Fig 4. 6d-f** for TPMS lattices. The strength ranges from 50 MPa to 300 MPa for BCC lattices and 150 MPa to 450 MPa for TPMS lattices. Young's modulus E ranges from 1.0 to 3.0 GPa for BCC lattices, and from 5.0 to 8.0 GPa for TPMS lattices. Energy

absorption capacity, namely the amount of energy absorbed per unit volume of cellular solids, is determined by the area under the stress-strain curve up to the densification strain:

$$W = \int_0^{\varepsilon_c} \sigma(\varepsilon) d\varepsilon \tag{4.3}$$

Since the BMG in this study is extremely brittle, the collapse strain ε_c (point III in **Fig 4. 5**) is used instead of the densification strain. If BMG lattices cause catastrophic failure and do not have stage III, only the former two stages are considered to calculate the energy absorption. Energy absorption requires an optimum combination of large collapse strain and high plateau stress. Thus, for the brittle foams, avoiding the abrupt stress drop at stage II and extending the plateau region at stage III is vital for enhancing the energy absorption ability.

Based on the classic theory of cellular solids, the structure-property relationship of different unit cell MG lattices can be established. The normalized compressive strength σ and the normalized elastic modulus E of the porous structure can be represented as a function of relative density by power laws [195, 196]:

$$\frac{E}{E_S} = C_1 \bar{\rho}^{n_1} \tag{4.4}$$

$$\frac{\sigma}{\sigma_s} = C_2 \bar{\rho}^{n_2} \tag{4.5}$$

Where σ and E_s are the compressive strength and Young's modulus of the raw material, Zr-based BMG. The exponents n_1, n_2, along with the coefficients C_1, C_2, serve to characterize the mechanical properties of the distinct geometries of unit cells, and

the exponents are more representative since they follow power laws. It is important to note that the relative densities of the lattices in this work are measured densities, not nominal relative densities. Many previous investigations have used the nominal relative density to establish the structure-property relationship, but greater precision is necessary, especially when manufacturing errors are significant and must be taken into account. It also lacks persuasiveness when compared with other cellular materials in terms of nominal relative density, particularly for specimens with significant fabrication deviations [197].

Fig 4. 6g-h shows the normalized elastic modulus and normalized compressive strength. In this study, the mechanical properties along the <100> direction are calculated because of the anisotropy of lattice structures. For the normalized elastic modulus, the fitting exponent of the TPMS structure is 0.872, which is smaller than that of the bending-dominated BCC lattices (1.26). The fitting exponents are obtained from the nonlinear curve fitting results based on Eq 4.4 and Eq 4.5. The small exponent of the TPMS structure means that the compressive modulus decreases were slowly with decreased density compared to the BCC lattice, amplifying the advantage in the low-density range. As an example, based on the fitting equations in **Fig 4. 6g**, Young's modulus of the TPMS structure is 2.05 times that of the BCC lattice at a relative density of about 0.58. Similar experimental results in previous literature indicated that the TPMS structure outperforms BCC lattices in regard to the modulus [190]. However, unlike most BCC lattices with exponents greater than 2, the BCC MG lattice in this

study has a much lower exponent than in previous works. This suggests that BCC structures perform better on BMG than expected. For compressive strength (**Fig 4. 6h**), the fitting exponent of the TPMS structure is 2.28, which is also slighter smaller than for BCC lattices (2.84). At approximately the same relative density of 0.58, BCC BMG lattices even exhibit slightly higher compressive strength than TPMS BMG lattices. This result contrasts with findings in other works on ductile materials, such as 316L stainless steel and maraging steel [190, 198, 199]. Modest stress fluctuations occur during the elastic stage (Stage I) of BCC MG lattices in **Fig 4. 5**, indicating that some small parts of the struts fracture inside the lattices to release the stress. This allows the entire lattice to bear more loading until it fails. In contrast, TPMS structures with smoother surfaces are less prone to break at stress concentration points for releasing internal energy. As a result, their stress curves form straight lines without fluctuations during the elastic stage.

The above experimental phenomena indicate that for brittle materials, the optimum and suitable structure is different due to the different failure mechanism and materials characteristics; hence, the structure design strategy cannot follow that of ductile cellular materials. A novel design method should be developed based on the compression experimental results of BMG lattices, considering the failure characteristics of brittle materials.

4.3.4 Enhanced damage tolerance of designed unit cell shape BMG lattices.

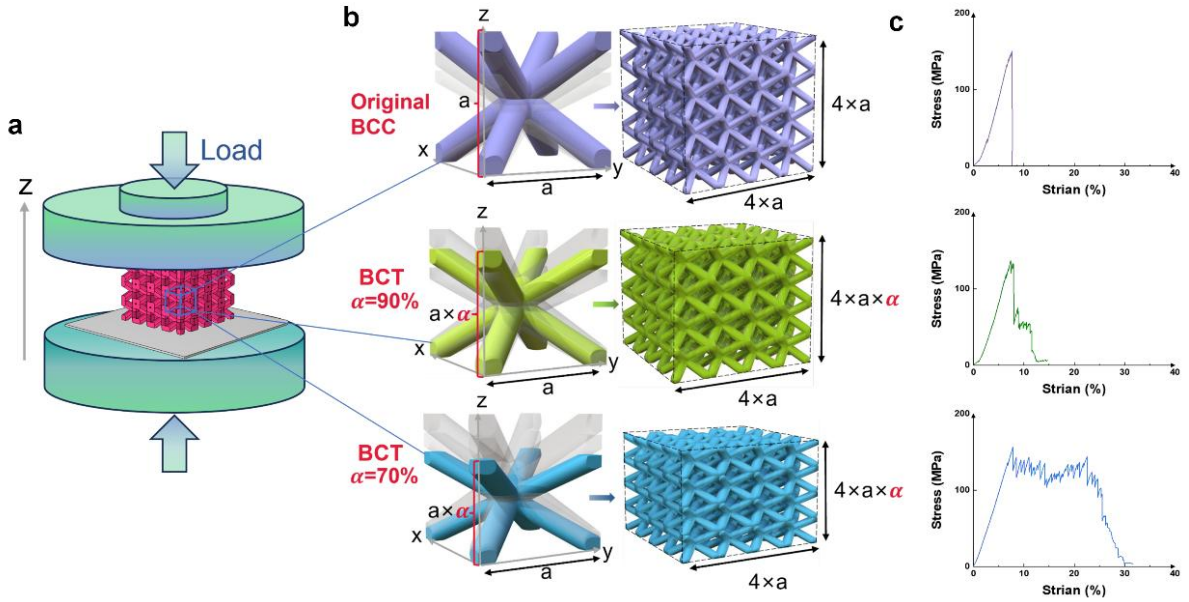

Fig 4. 7 Schematics of unit cell shape design strategy. (a) compression test and load direction (b) BCC unit cell shape design: the original BCC lattice and BCT-90%, BCT-70%. (c) The enhancement of damage tolerance of designed lattices.

It was found that the deformation characteristics mainly depend on the geometries of the unit cell rather than the relative density. In this study, the unit cell design is based on the original BCC structure (D0.8L3.2). The BCC unit cell was transformed into a BCT unit cell, being compressed in the z-direction to different degrees. α represents the scaling degree in the z-direction. Detailed geometrical information for the BCT lattices is provided in **Table 4. 4**. Visible enhancements in the damage tolerance were investigated through the stress-stain curves with increasing multiplier α in **Fig 4. 7 c**.

From the compression results and deformation phenomenon in **Fig 4. 8a-b and Fig 4. 8c-d**, a clear transition from catastrophic fracture to sequential localized fracture was observed with the scaling degree. For the BCT structure with a slight scaling degree

($\alpha = 90\%$), the stress drops to 50 MPa immediately after the compressive strength σ reached 136 MPa (**Fig 4. 8b**). Two main cracks could be seen in the deformation process (**Fig 4. 8a**) at ε =10%. Two cracks propagated rapidly and divided the lattices into several big parts that no longer bear any stress at ε =15%.

Table 4. 5 Geometrical specifications of the BCT lattices.

Lattice sample code	Unit cell size (mm)	Number of cells (x,y,z)	Angles between the applied load and the beam (°)	Measured porosity (%)
D0.8L3.2-90%	1.85 × 1.85 × 1.66	(4,4,4)	32.47	40.8
D0.8L3.2-85%	1.85 × 1.85 × 1.57	(4,4,4)	31.01	39.2
D0.8L3.2-80%	1.85 × 1.85 × 1.48	(4,4,4)	29.50	39.6
D0.8L3.2-70%	1.85 × 1.85 × 1.29	(4,4,4)	26.33	39.4

In **Fig 4. 8d**, the designed BCT structure with a large scaling degree ($\alpha = 70\%$) displays an enhanced stress level after the elastic deformation region, which is close to the plateau region of the ductile metallic lattices. Multiple small crack bands occur but no main crack bands through the entire lattices; thus, no rapid stress drop at stage II after lattices reach the compressive strength σ of 156 MPa. At stage II-III, the stress fluctuates from 100 to 140 MPa for a strain rate of approximately 17.7%, corresponding to the continuous crushing of the struts. The direction of the crack bands is along the

loading direction, thereby maintaining a high-stress level in a long region. The rapid stress drop was postponed significantly, and the whole lattices still maintained 102 MPa at ε =25%.

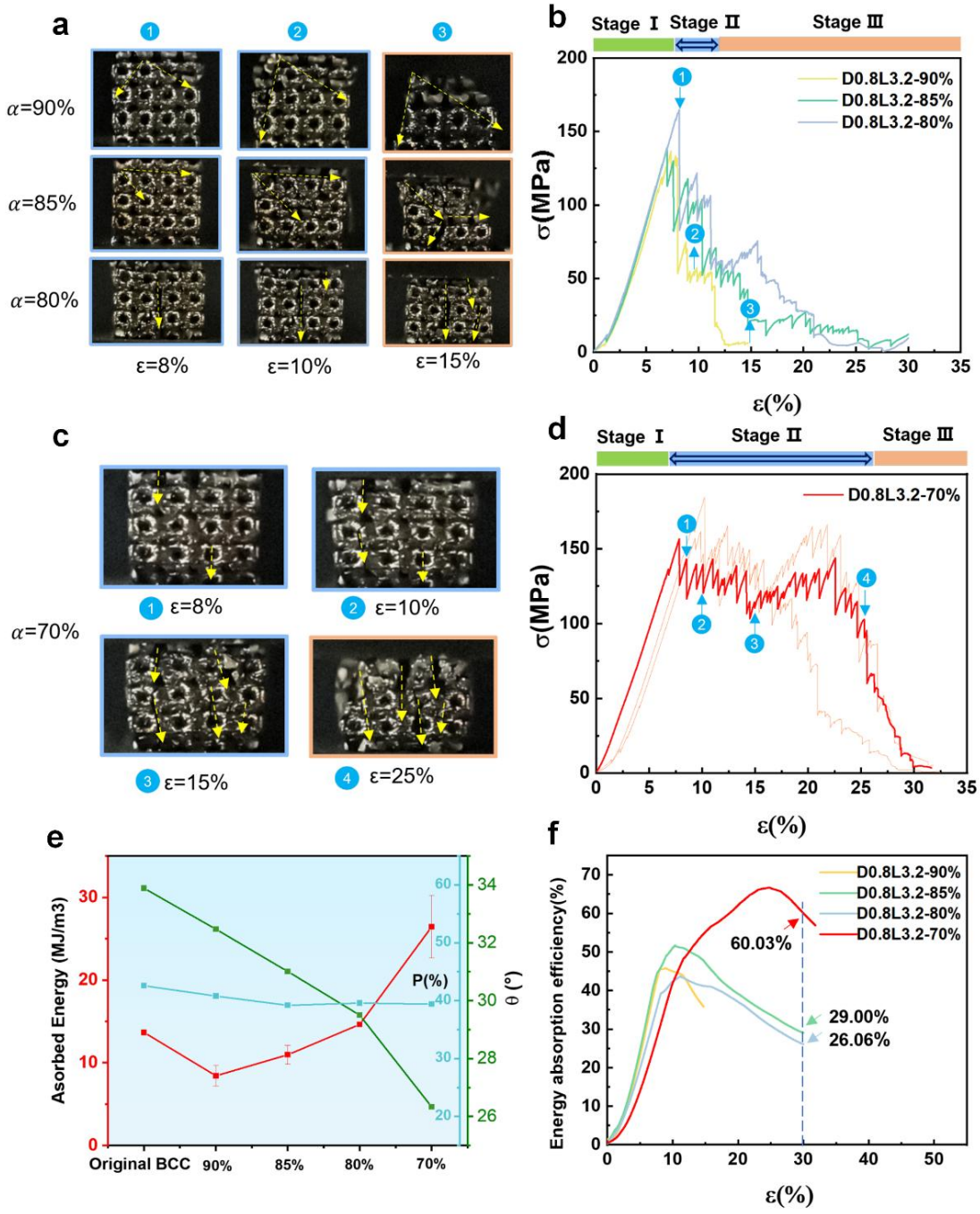

Fig 4. 8 Mechanical performance of designed BCT lattices. (a) Deformation process and (b) stress-strain curves of the designed BCT lattices with slight scaling degree: D0.8L3.2-90%, D0.8L3.2-85%

and D0.8L3.2-80%. (c) Deformation process and (d) stress-strain curves of the BCT lattices with a large scaling degree: D0.8L3.2-70%. Increasing energy absorption performance with the increased scaling degree of the lattices(e) Absorbed Energy (f) Energy absorption efficiency.

To absorb more energy when compressed, ideal absorption materials had a long plateau. The absorbing ability of porous structures is demonstrated solely by W. The energy absorption efficiency, denoted as η, serves as an indicator of the energy absorption capacity of engineered lattice structures, relative to the product of the maximum stress σ and strain. The value of η can be calculated by[200]:

$$\eta = \frac{W}{\sigma\varepsilon} \tag{4.6}$$

The BCT lattice possesses a greater energy absorption capability, resulting from its unique mechanical deformation behavior, compared to the original BCC structure. The absorbed energies of the fabricated BCT MG lattices gradually increased with decreasing angles θ between the applied load and the beam. From **Fig 4. 8e**, the absorbed energy of the original BCC (θ = 33.89 °) is 13.67 MJ/ mm^3. As the angle θ of the unit cell decreases to 26.33°, the absorbed energy of the BCT lattice is 29.25 MJ/ mm^3 (almost 2.2 times that of the original BCC). The energy absorption efficiencies of the fabricated different BCT MG lattices (**Fig 4. 8f**) with 30% strain are 26.06%, 29.00, and 60.03%, respectively. The results also indicate that the unit cell shape design has a significant positive influence on the absorption efficiencies of 3D-printed BMG lattices, attributable to the high-stress level in the plateau region. Especially for D0.8L3.2-70%, the energy absorption efficiency at 30% is close to the highest energy absorption

efficiencies of the amorphous metal nano-honeycomb (70%-90%) [201] and is higher than that of the open-cell lattice structure (50%) [200].

4.4 Discussion

4.4.1 Principles to improve the damage tolerance of BMG lattices through unit cell shape design.

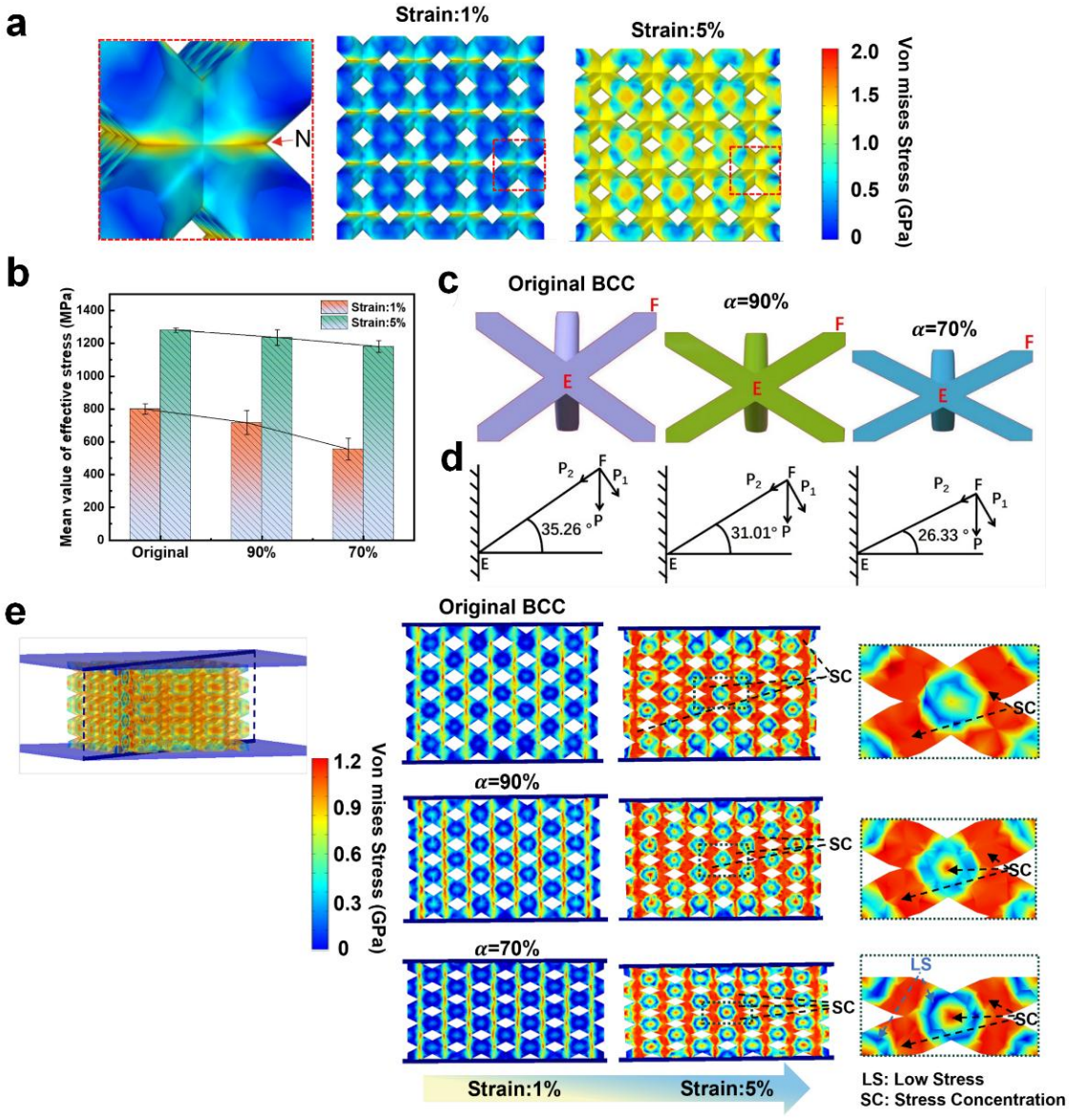

Fig 4. 9 Stress analyses of the designed BCC lattices. (a) FE predicted stress distributions at different strains for BCC lattices. (b) Mean value of equivalent stress of N point of the BCC lattice and BCT lattices at 1% and 5% overall deformation. (c) Orthogonal cross-section and (d) Force analysis diagram

of the BCC unit cell and the BCT unit cell with different scaling degrees: D0.8L3.2, D0.8L3.2-90% and D0.8L3.2-70%. (e) FE predicted stress distributions (orthogonal cross-section) at different strains for the BCC lattice and BCT lattices: D0.8L3.2, D0.8L3.2-90% and D0.8L3.2-70%.

Clear enhancement in the damage tolerance of the BCT lattices (**Fig 4. 8**) was observed from the compression results and deformation phenomena in the deformed unit cell. In this section, theoretical analysis is used to elucidate the factors behind this transformation. To precisely evaluate the mechanical properties like collapse strength and elastic modulus through geometry information of unit cells and the intrinsic properties of raw material, a basic model was formed based on those deformation modes [202, 203]. To better understand the influence of the designed structure on mechanical behavior, the load P applied on a z-axis strut is separated by two components P1 and P2, where P1 represents the load along the bending direction (**Fig 4. 9c-d**), and P2 represents the load along the buckling direction. Obviously, P2 decreases with decreasing θ of the unit cell, whilst on the contrary, the bending component P1 increases. This tendency is consistent with the other material lattices deformation behaviors under compression [191].

However, a different mechanism is at play when dealing with brittle BMG. The increased force P1 induces vertical fracture at various positions inside the lattices, while the decreased force P2 reduces the stress concentration in the direction of the diagonal, avoiding the fast propagation of the main crack bands. This point is substantiated by the numerical results obtained from finite element analysis. From the linear-elastic simulation models in Fig 6a, the stress is concentrated on the nodes (N point) of the

BCC lattices. The lower mean value of the equivalent stress at point N in the BCT lattices at 1% and 5% overall deformation (elastic stage). **Fig 4. 9b** indicates that the D0.8L3.2-70% lattices have lower stress concentration at the N point, consistent with the decrease in the component P2. The reasons for the transition of this fracture mode can be intuitively determined from the orthogonal cross-section of the stress distribution results in **Fig 4. 9e**. It was found that the maximum von Mises stresses observed in the original BCC unit cell were distributed nearby the nodes but formed localized high-stress bands along the diagonal line. With the decrease of the component P2, higher amounts of high-stress distribution were concentrated in the struts rather than the nodes. Low-stress areas were presented between the nodes and struts in the D0.8L3.2-70% lattices, acting like a wall that blocks the rapid propagation of cracks along the diagonal direction. Hence, multiple crack bands along the vertical direction appeared instead of a single crack band along the diagonal.

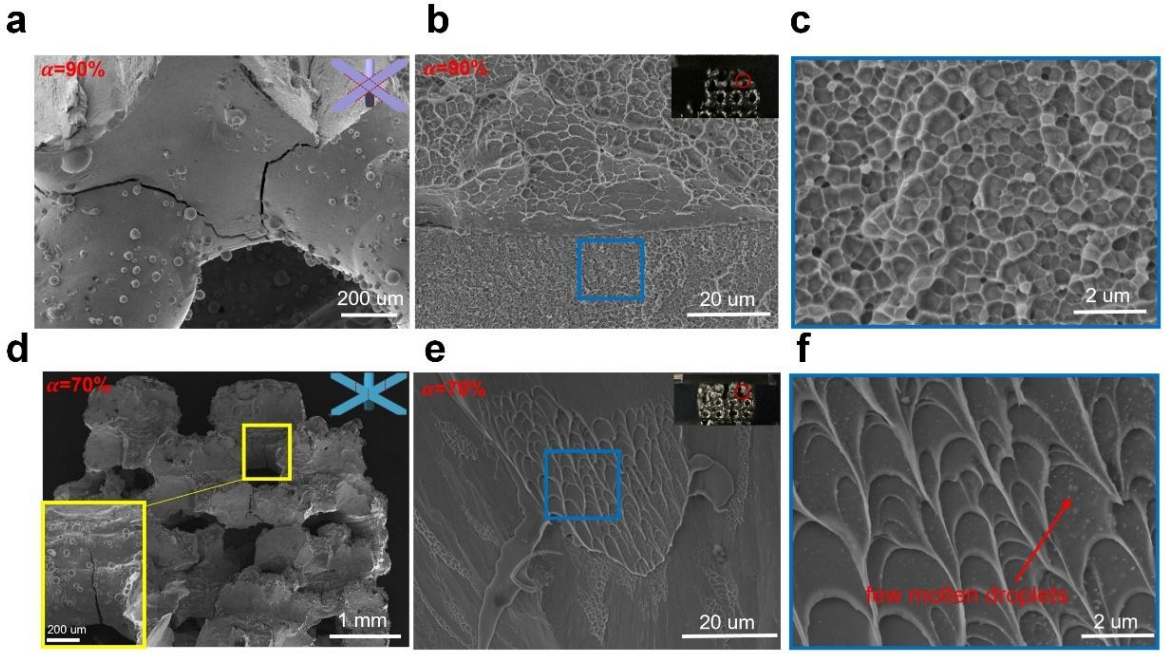

Fig 4. 10 Crack surface and fractography of designed BCC BMG lattices. SEM images of exemplary compression test sample after crack initiation: (a)D0.8L3.2-90%: crack propagate along the diagonal line (b-c) fracture morphologies: dimple-like pattern. (d) D0.8L3.2-70%: crack propagate along the vertical direction (e-f) fracture morphologies: vein-like pattern.

The transformative crack extending behavior of the BCT lattice can be investigated from the fracture surface of the lattices. As shown in **Fig 4. 10a**, the trajectories of the cracks follow the junctions between the nodes and struts, which are areas of high von Mises stress, and propagate rapidly along the diagonal direction throughout the entire lattice. In D0.8L3.2-90% lattices with larger θ, the fracture surface displays a dimple-like pattern (**Fig 4. 10b-c**), a typical feature of quasi-cleavage brittle fracture in MGs. For D0.8L3.2-70% lattices with the smallest θ (**Fig 4. 10d**), since there is a low-stress area between the nodes and struts, cracks no longer extend along the diagonal direction. Instead, they deflect along the vertical direction and are

restricted by the porosities, preventing them from propagating throughout the entire structure. In addition, a typical fracture (**Fig 4.10 e-f**) of the molten pool region of MG was observed. Many molten droplets were observed in the vein-like structure, demonstrating that concentration of elastic energy causes temperature increase over the Tg of the MG, while the energy is released in instantaneous fracture, and localized remelting occurs. This indicates that the deformation behavior of original BCC lattices is just fast crack propagation along the crack band compared to the BCT lattices with smaller θ. When the θ decreases, multiple small crack bands cause incompleteness of the structures with the complex stress distribution, and the struts make it easier to achieve the elastic limit that causes localized remelting of MP, which bears more loading. This result verifies the increased stress level at the plateau region.

4.4.2 Applying the present enhancement strategy in the future.

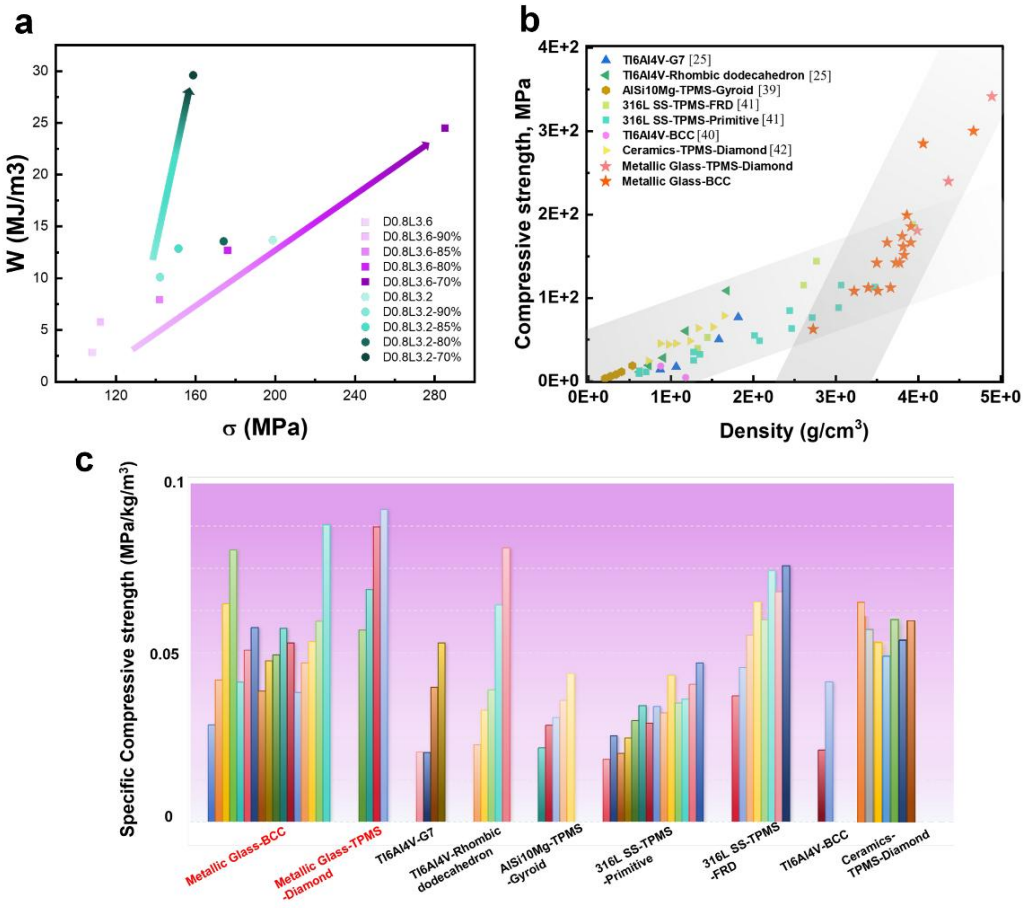

Fig 4. 11 Primary results on applying the present strategy to BCC BMG meshes. (a) the energy absorption capacity against compressive strength: the arrow points in the direction of $\boldsymbol{\theta}$ reduction. (b-c) compressive strength and specific compressive strength comparing the mechanical properties of MG meshes with other cellular structures [191, 204-207].

This work is the first attempt to combine the lattice structures with BMGs to achieve high damage tolerance of brittle structural materials with high strength. By the introduction of the designed unit cell with almost constant porosity, appreciable enhancement of the mechanical properties can be well obtained.

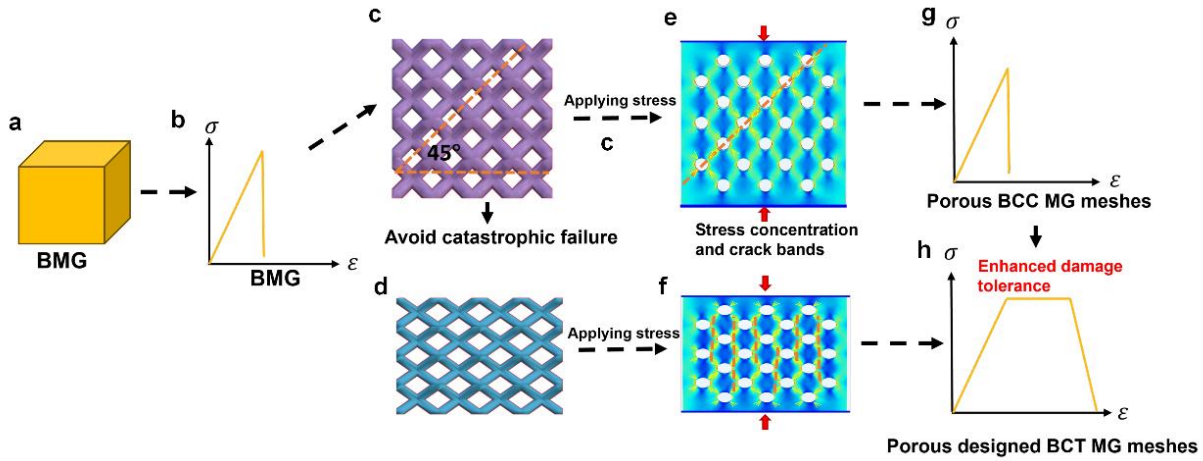

Fig 4. 12 An instance of implementing the present strategy for future lattice design to achieve improved mechanical performance. The introduced porosity based on original BCC lattices (c) is hard to effectively inhibit the intrinsic single crack band of BMG meshes (e, g). Designed BCT BMG meshes (d) with multiple crack bands (f) to achieve a better performance (h).

To verify the viability of the present strategy, we also designed the same shape for BCC lattices with different strut lengths and then measured the mechanical properties of 3D-printed BMG lattices under compression. **Fig 4. 11a** exhibits the active influence on both absorption energy capacity and compressive strength on BCC lattices with different strut lengths. The scatter with the darker color represents the BCT lattices with smaller θ. The compressive strength of the original BCC lattice (D0.8L3.6) is 108MPa, and when the deform multiplier α =70%, the compressive strength increase to 285 MPa. The absorbed energy also increased by 8.5 times, which is a significant improvement. For the D0.8L3.2 BCC structure, we can see that there is a positive effect on the energy absorption capacity with the increasing deform multiplier α. Thus, establishing an accurate structure-property relationship for the present structure strategy based on different unit cells is essential to synergistically enhance the

compressive strength and damage tolerance for meeting the high-performance requirements for energy absorber applications. In comparison with other cellular structures (**Fig 4. 11b-c**), BMG lattices exhibit outstanding strength-to-weight ratios, which shows the potential comparable ability of the MG lattices for the high strength need in the automobile and aerospace industries.

The schematic approach, which applies the current strategy for designing strut-based lattices, is depicted in **Fig 4. 12**. At room temperature, brittle BMGs have zero compressive plasticity (**Fig 4. 12a-b**). The complex BCC lattices can be simplified as 2D BMGs with artificial holes (**Fig 4. 12e-f**). Through unit cell design, the distribution of the high-stress bands can prevent the 45° main crack band under compressive loading, which leads to catastrophic failure (**Fig 4. 12e**). After unit cell design, micro cracks do not easily penetrate the neighboring pores and the linkage between the main crack and the microcracks can be avoided, and multiple small vertical crack bands occur which postpone the catastrophic failure (**Fig 4. 12f**). Small region fracture releases the energy concentration, the stress concentration is relaxed, and the stress state becomes complex with the variation of the lattices, thus improving the failure resistance of brittle BMG meshes. This design method can simultaneously improve compressive strength and damage tolerance. However, the structural anisotropy induced by this strategy leads to its limitations, as it can only improve the damage tolerance of unidirectional lattice structures.

4.5 Conclusions

To sum up, BMG meshes with BCC and TPMS cells were printed using the L-PBF method. It was found that the deformation behavior of these lattices can be summarized into three stages: an elastic deformation region before collapse strength, an extensive failure stage characterized by a dramatic drop in stress, and continuous localized fracture with a decreasing low stress. Unexpectedly, the BCC structures outperform TPMS structures in terms of absorption energy because the multiple fractures of the struts release partial energy, thereby postponing the collapse of the structures. This result suggests that BCC lattice may be more suitable for highly brittle materials than TPMS structure to prevent the fast propagation of the main crack band, causing catastrophic failure.

Based on the influencing effects of the deformed BCC unit cell shape on the compressive deformation behavior, BCT lattices with increased multiple cracks were designed to enhance the damage tolerance of the lattices effectively. The catastrophic failure of the MG lattices was avoided by inducing localized fracture through reducing the angle θ of the unit cell. Compression test results showed that BCT BMG lattices have a positive impact on both absorption energy capacity and compressive strength. By employing this design strategy on the BCC MG meshes with different strut lengths, the energy absorption of the designed BCT lattices increased by nearly 8.5 times compared to the original BCC lattices. Simultaneously, the compressive strength increased synergistically by about 2.5 times. These results confirm that our method is

effective in mitigating the catastrophic failure of brittle BMGs and enhancing the fracture behavior of BMG lattice structures, demonstrating their high potential for high-strength absorber applications.

Chapter 5 High strength bioinspired MG lattices with excellent energy absorption

5.1 Introduction

Chapter 4 examined the effect of unit size and shape on the damage tolerance of MG lattices, demonstrating that structural configuration can markedly enhance their energy absorption. However, the absorbed energy did not reach the desired performance level. Accordingly, **Chapter 5** investigates the use of specialized structures to further improve the energy absorption of MG lattices, with the goal of achieving properties comparable to those of other metallic materials.

BMGs often undergo catastrophic failure (**Fig 5. 1a-b**) instead of elastic buckling or plastic yielding, mainly due to strain softening caused by uncontrolled localized shear band deformation. Therefore, BMGs have only a limited energy absorption capacity in the elastic deformation region, seeking architectural design to alter the localized deformation mode is the way to solve this longstanding dilemma (**Fig 5. 1c-d**). Bio-inspired structures[208, 209], like the honeycomb pattern [210] found in beehives or the hierarchical architecture of nacre (mother of pearl) [211-213], offer exceptional energy absorption properties. These natural designs have evolved to efficiently manage and dissipate energy, and their principles can be mimicked in engineered materials to create robust, lightweight structures [214]. The skeletons of sea urchins, one of the most renowned natural biomineralized porous structures, exhibit strength-to-weight ratio surpasses that of brick and concrete, attributed to the crack-

confined effect of their highly porous structure [215], thereby protecting them from impacts, fractures, wear, and particularly predator attacks. Butterfly wings are natural porous hybrid materials, composed of various components arranged in precise geometries and scales to create a unified structure [216]. The topology of its inner porous layer maximizes structural stiffness while minimizing weight, thereby exhibiting optimized mechanical behavior under bending loads [217]. TPMS-like structures are open cell structures that been investigated in the sea urchin spines [218] (Fig 5.1e) and butterfly wings[219] (**Fig 5. 1f**), lightweight materials based on the TPMS structure exhibit outstanding performance both in the specific strength and energy absorption [190, 220, 221]. This also provides a feasible way for improving the energy absorption capability of MGs from the perspective of structural design.

In this work, by adjusting the unit cell shape and relative densities, we designed and prepared four typical TPMS structures: Diamond (D), Gyroid (G), Primitive (P) and I-graph-wrapped (IWP) using $Zr_{60.14}Cu_{22.31}Fe_{4.85}Al_{9.7}Ag_3$ MG powders via the micro laser powder bed fusion (μL-PBF) technique. We systematically studied the deformation process and the failure mode of different TMPS structures during loading and compared their specific strength and energy absorption performance. To visualize the appearance and propagation of internal fractures during loading, the Digital Volume Correlation (DVC) method during in situ XCT compression testing was employed to study the failure modes in detail. A long-stress plateau characteristic was observed in TPMS MG structures during failure, which contributed to a hybrid ductilization

mechanism at both the macro and micro levels. Two bio-inspired TPMS MGs simultaneously achieved high strength and excellent energy absorption, representing the highest level compared to other similar structural materials.

5.2 Methodology

5.2.1 Manufacture and modeling of lattice structures

Same gas-atomized $Zr_{60.14}Cu_{22.31}Fe_{4.85}Al_{9.7}Ag_3$ MG powders, were utilized in the μL-PBF process for fabricating specimens. The MG specimens in chapter 5 were produced using a micro-selective laser melting (μL-PBF) system (Han's Laser M100μ). Unlike conventional L-PBF machines, the μL-PBF system features a laser spot size of 25 μm, which ensures high precision in the printed samples[222]. The system utilizes a 500W IPG fiber laser and operates under a constant flow of Argon gas. During the entire process, the oxygen levels were maintained below 100 ppm. The laser scanning speed, power, and layer thickness were set to 1500 mm/s, 150W, and 10 μm, respectively.

TPMS structures possess a unique characteristic of mean curvature of zero at all points, which helps prevent stress concentration—an essential factor for brittle materials like metallic glasses to avoid catastrophic failure. The geometric characteristics of these TPMS structures are detailed in **Table 5. 1**. All types of TPMS structures are designed with cubic unit cells, featuring progressively smaller side lengths to achieve different porosity levels. The shell thickness was kept uniform across all structures to ensure that variations in shell thickness did not influence the results. The geometric model of the TPMS structure can be mathematically approximated using

implicit equations[192]. The Diamond (D), Gyroid (G), Primitive (P), and I-graph-wrapped (IWP) surfaces are defined by the following approximations:

$$\Phi_D(x,y,z) = \sin(\omega x)\sin(\omega y)\sin(\omega z) + \cos(\omega x)\sin(\omega y)\sin(\omega z) + \sin(\omega x)\cos(\omega y)\sin(\omega z) + \sin(\omega x)\sin(\omega y)\cos(\omega z) = c$$

$$\Phi_G(x,y,z) = \cos(\omega x)\sin(\omega y) + \sin(\omega z)\cos(\omega y) + \sin(\omega x)\cos(\omega z) = c$$

$$\Phi_{IWP}(x,y,z) = 2[\cos(\omega x)\cos(\omega y) + \cos(\omega y)\cos(\omega z) + \cos(\omega z)\cos(\omega x)] - [\cos(2\omega x) + \cos(2\omega y) + + \cos(2\omega z)] = c$$

$$\Phi_P(x,y,z) = \cos(\omega x) + \cos(\omega y) + \cos(\omega z) = c \quad (5.1)$$

x, y, and z represent the spatial coordinates, while ω = 2π/l, where l denotes the length of a unit cell. Using a MATLAB script, four 3D models of various TPMS sheet geometries were generated. The process involved extracting the zero-level surface defined by Eq 5.1, where Φ = 0, and then uniformly offsetting this surface in both directions.

Table 5. 1 presents the dry weight of the 3D-printed TPMS lattices. The relative densities (RDs) range from 10% to 36% due to changes in the form and size of the unit cells. The D type and IWP type have larger surface areas compared to the G type and P type, resulting in higher relative densities despite having similar sheet thickness levels. In this study, the measured RDs were used for analysis, as they are more reliable than the designed RDs.

Table 5. 1 Geometrical characteristics of the TPMS structures in this study.

Lattice sample code	Unit cell size(mm)	Number of cells(x,y,z)	Measured average *m*(g)	Measured relative densitiy (%)
2.5P	2.5	(4,4,4)	0.70±0.006	10.22
2P	2	(4,4,4)	0.850±0.002	12.39
1.5P	1.5	(4,4,4)	1.13±0.001	16.60
1P	1	(4,4,4)	1.55±0.001	22.62
2.5G	2.5	(4,4,4)	0.93±0.005	13.54
2G	2	(4,4,4)	1.07±0.005	15.70
1.5G	1.5	(4,4,4)	1.42±0.004	20.74
1G	1	(4,4,4)	1.99±0.008	29.19
2.5D	2.5	(4,4,4)	1.08±0.007	15.80
2D	2	(4,4,4)	1.39±0.000	20.37
1.5D	1.5	(4,4,4)	1.66±0.001	24.32
1D	1	(4,4,4)	2.47±0.013	36.15
2.5IWP	2.5	(4,4,4)	1.20±0.001	17.60
2IWP	2	(4,4,4)	1.33±0.003	19.44
1.5IWP	1.5	(4,4,4)	1.79±0.008	26.21
1IWP	1	(4,4,4)	2.47±0.013	36.16

5.2.2 *In situ* compression test and fracture behavior analysis

In this study, we employed the Digital Volume Correlation (DVC) technique to examine the deformation and damage processes of TPMS MG structures. Unlike ductile materials, where plastic deformation is the primary mode of deformation, cellular BMG structures experience deformation primarily through brittle fracture. As a result, conventional testing methods struggle to capture the complex fracture behaviors, as techniques like digital image correlation (DIC) can only assess surface strain. DVC, an extension of 2D DIC, tracks 3D displacements of naturally occurring microstructural

features under load and maps strains using correlation algorithms. Therefore, DVC is the most suitable technique for investigating and analyzing complex fracture deformations within and throughout the porous structures.

The DVC procedure relies on 3D models reconstructed from X-ray computed tomography (CT, XPloreVista 2000). CT scans were performed at a voltage of 150 kV and a current of 110 μA under various compression strains. With a voxel size of 3.213 μm, the scans were able to capture detailed microstructural features. Scanning was performed at each failure stage by pausing the load and allowing it to remain static for 1 hour for CT imaging. A total of 5-6 stages were analyzed for each TPMS structure.

To analyze the failure mechanisms of TPMS structures, we conducted linear quasi-static compression simulations using the Structural Mechanics simulation module in the commercial software VGSTUDIO MAX. The solid parent material, a 3D-printed Zr-based BMG with the same printing parameter as the TPMS structures, has a compressive strength of 1509 MPa and a Young's modulus of 72.0 GPa. These parameters were used as the material properties in the simulation. By using the actual 3D reconstruction model rather than the design CAD model, we eliminated the effects of fabrication deviations. The minimum element size was set to 4 voxels, and the applied load was maintained at 1 kN.

5.3 Results

5.3.1 Microstructure and morphological characteristics of the 3D-printed TPMS lattices

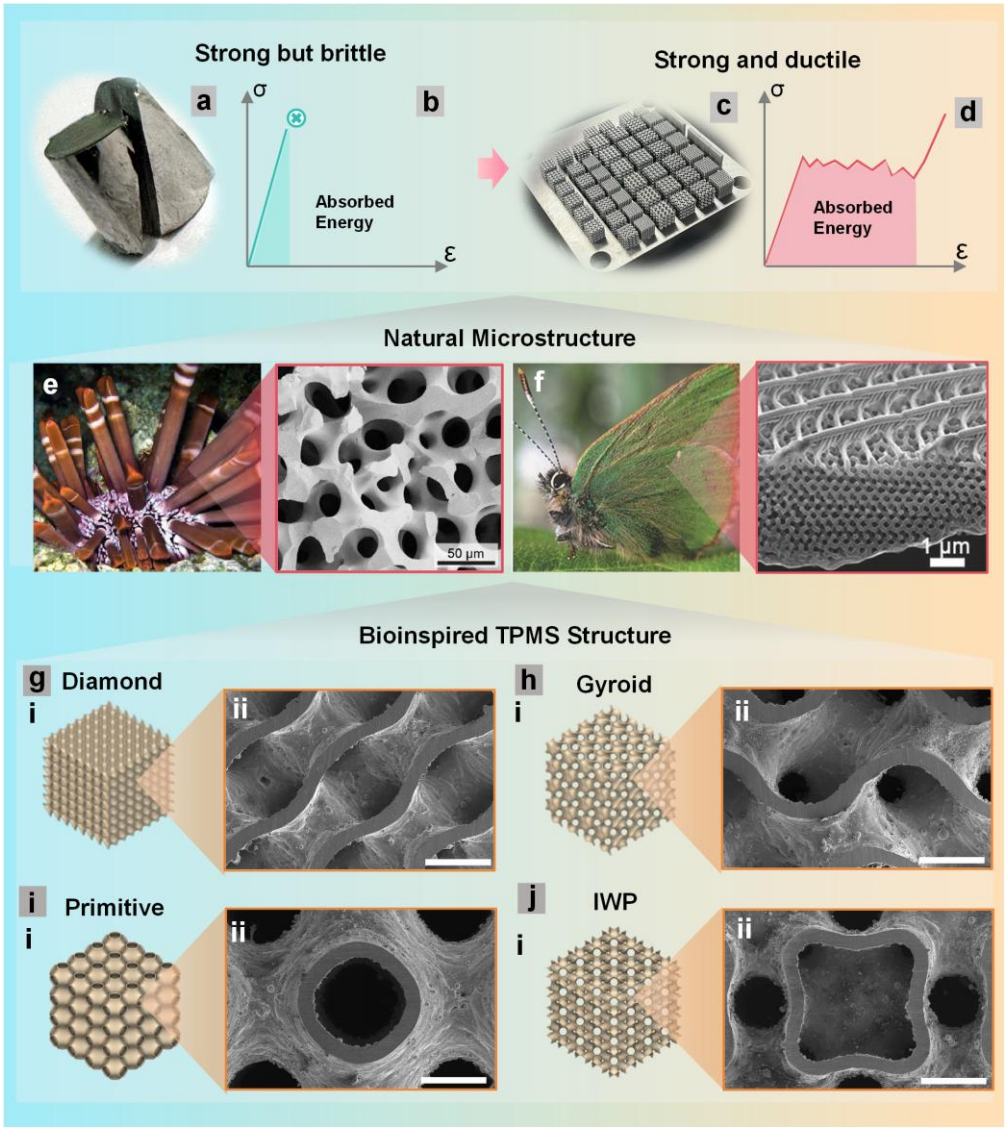

Fig 5. 1 Design and preparation of bioinspired TPMS structures for enhancing the absorbed energy of brittle BMG. (a-b) BMG exhibit room temperature brittleness. (c-d) 3D-printed TPMS MG structures exhibit ductile-like deformation with enhanced energy absorption. SEM images of TPMS-like structures found in nature: (e) sea urchin skeleton (reproduced with permission from [218] 2020, Elsevier); and (f) butterfly wings (reproduced with permission from [219] 2017, Wiley). Four bioinspired (g) D-, (h) G-, (i) P-, (j) IWP-type TPMS structures: (i) CAD models of structure with (ii)

corresponding SEM images of the 3D-printed structures with the outside surfaces. The scale bar is 500 μm.

As shown in **Fig 5. 1g-j ii**, the TPMS structures demonstrate excellent surface quality, which is attributed to the finer laser beam size and smaller layer thickness. The sheet thickness of the TPMS structures, as measured in the SEM images, ranges from 100 to 120 μm across different unit cell types (**Fig 5. 2**), with only slight variations within the error range. **Fig 5. 3** also displays the corresponding EDX mapping diagrams for each structure type, revealing a uniform distribution of the five elements without noticeable segregation areas or significant differences among the various TPMS structures. Overall, the high printing quality ensures that the mechanical performances are not compromised by defects or atomic-scale variations.

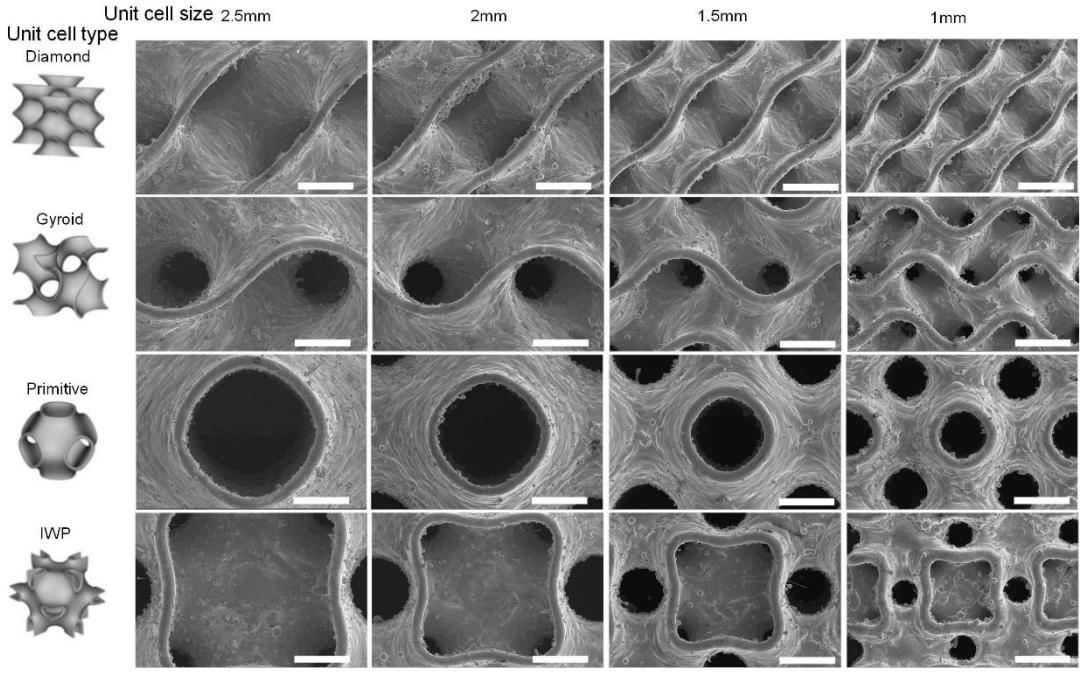

Fig 5. 2 SEM images of the outside surface of 3D-printed TPMS lattices, demonstrating high printing precision and good surface quality, with minimal unmelted powder adherence. Scale bar is 500um.

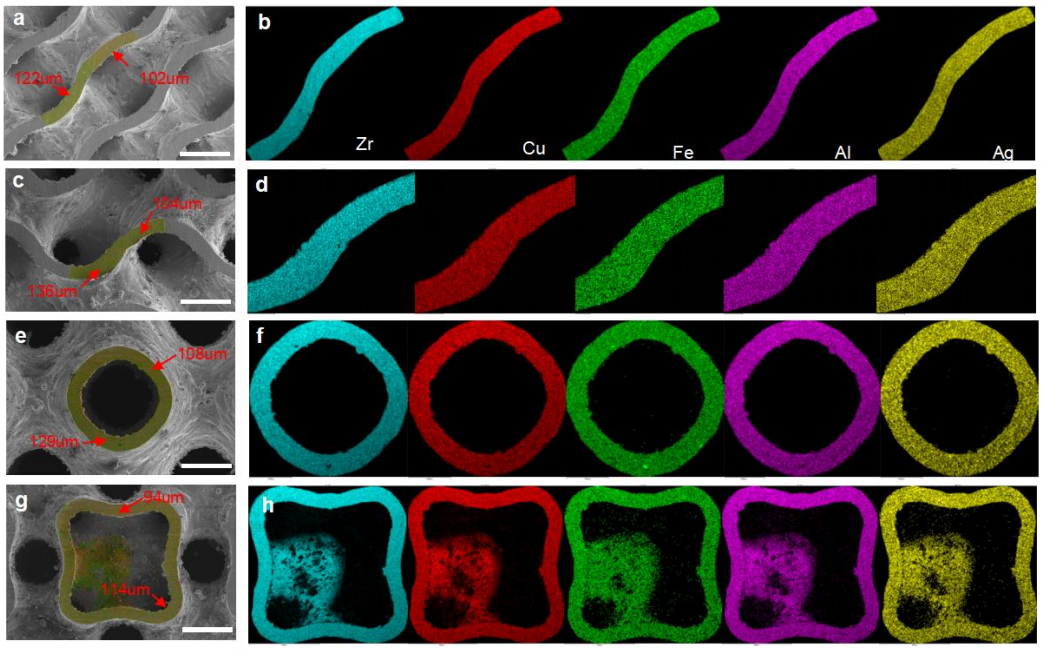

Fig 5. 3 SEM images of (a) D-, (b) G-, (c) P-, (d) IWP-type structure and corresponding (b-h) EDX mapping images. Scale bar is 500um.

The base material of MG powders is highly sensitive to the energy density input and heat accumulation during the 3D printing process. Excessive beam power can lead to severe crystallization of the printed specimen, while improper layer thickness or scanning strategies can cause heat buildup in the heat-affected zone. To assess the impact of various unit cell shapes and volumes on the amorphous content, the amorphous content (A_m.%) of the 3D-printed TPMS structures can be assessed by DSC curves (**Fig. 5. 4**). As shown in **Fig. 5. 5**, the structures generally exhibit a high amorphous level of approximately 80%, with the P-type structure featuring a unit cell size of 2.5 achieving an especially high amorphous content of 88%. **Fig. 5. 6** displays a

representative crystalline region (i.e., heat-affected zone, HAZ) and a fully amorphous region (molten pool, MP) within a printed MG lattice. In the HAZ region, spherical nanocrystals with diameters ranging from 50 to 200 nm are randomly distributed. The majority of nanocrystals in the HAZ are under 50 nm in diameter, while a few larger nanocrystals, between 150 and 200 nm, are found near the boundaries. Compared to BMG with amorphous content over 92%[187], the smaller size of these nanocrystals and the narrower width of the HAZ region are notable. This is likely due to the porous structure, which helps to reduce thermal accumulation to a certain extent.

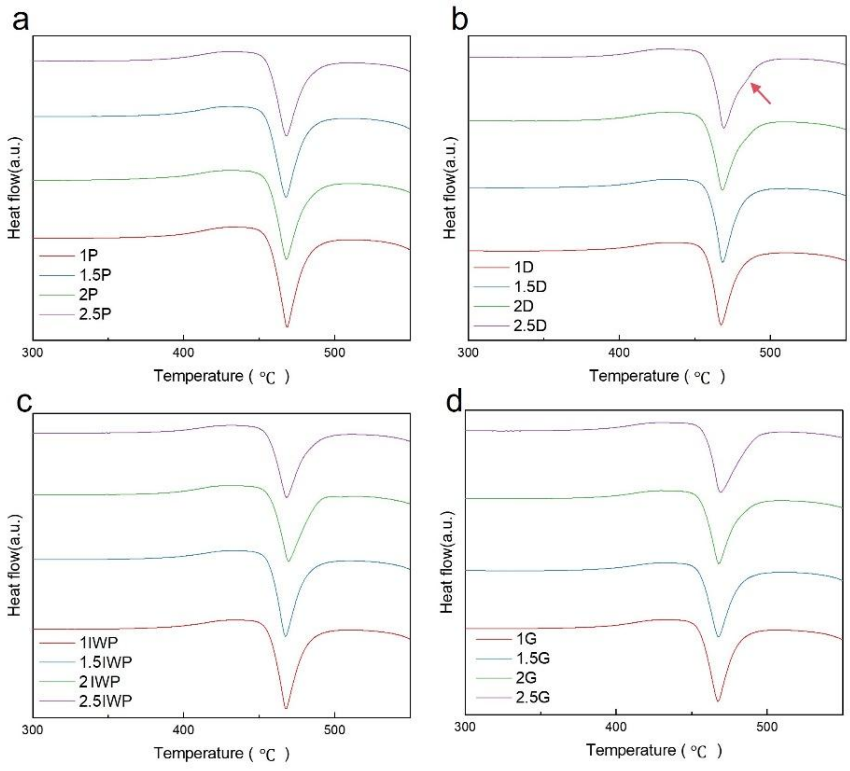

Fig 5. 4 DSC curves of the TPMS MG lattices: (a) P-type, (b) D-type, (c) IWP-type, (d) G-type.

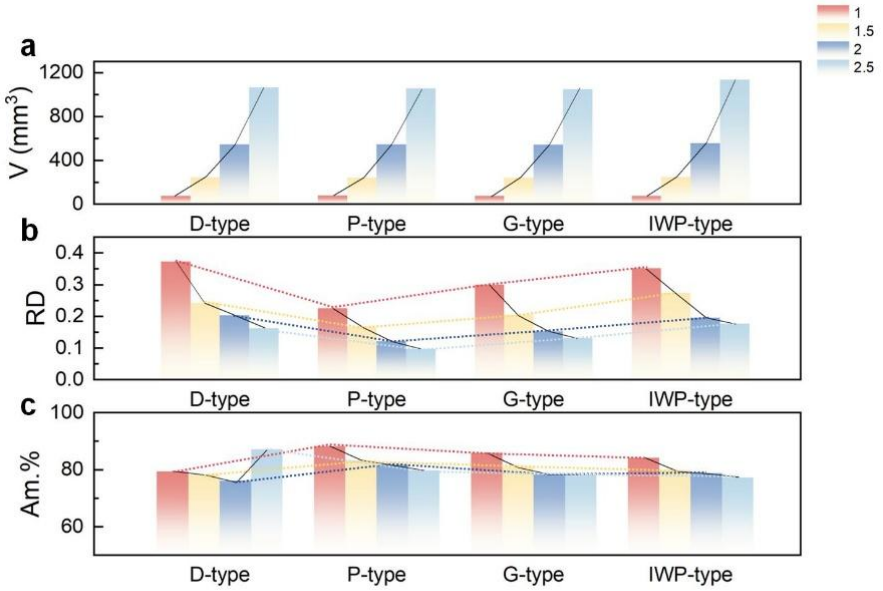

Fig 5. 5 Variations of Amorphous content of the 3D printed MG TPMS structures with different type and RD. (a) Volume of the cubic, (b) Measured relative densities and (c) Amorphous content of the printed different type TPMS MG structures.

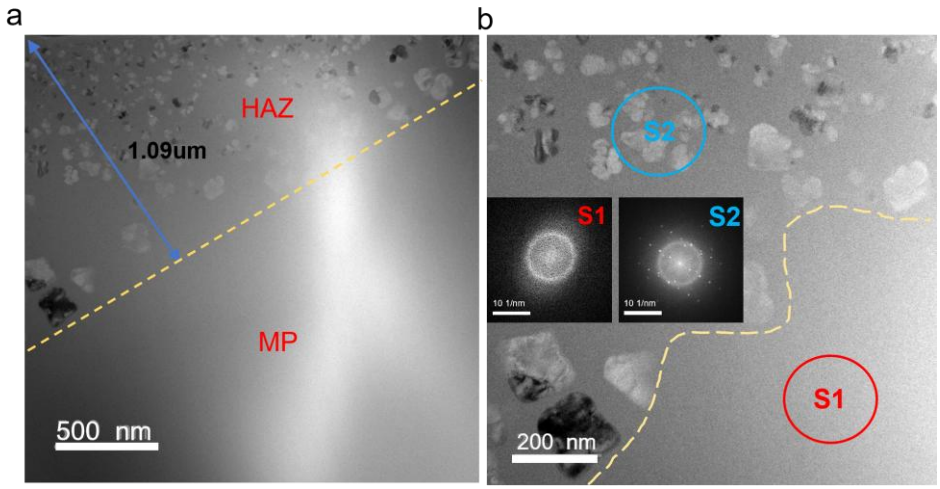

Fig 5. 6 Microstructure Characterization of L-PBFed MG lattices. (a) TEM bright-field images show the molten pool (MP) and heat affected zone (HAZ). (b) The selected area electron diffraction (SAED) pattern of MP and HAZ, respectively.

5.3.2 Mechanical performance of 3D-printed TPMS lattices.

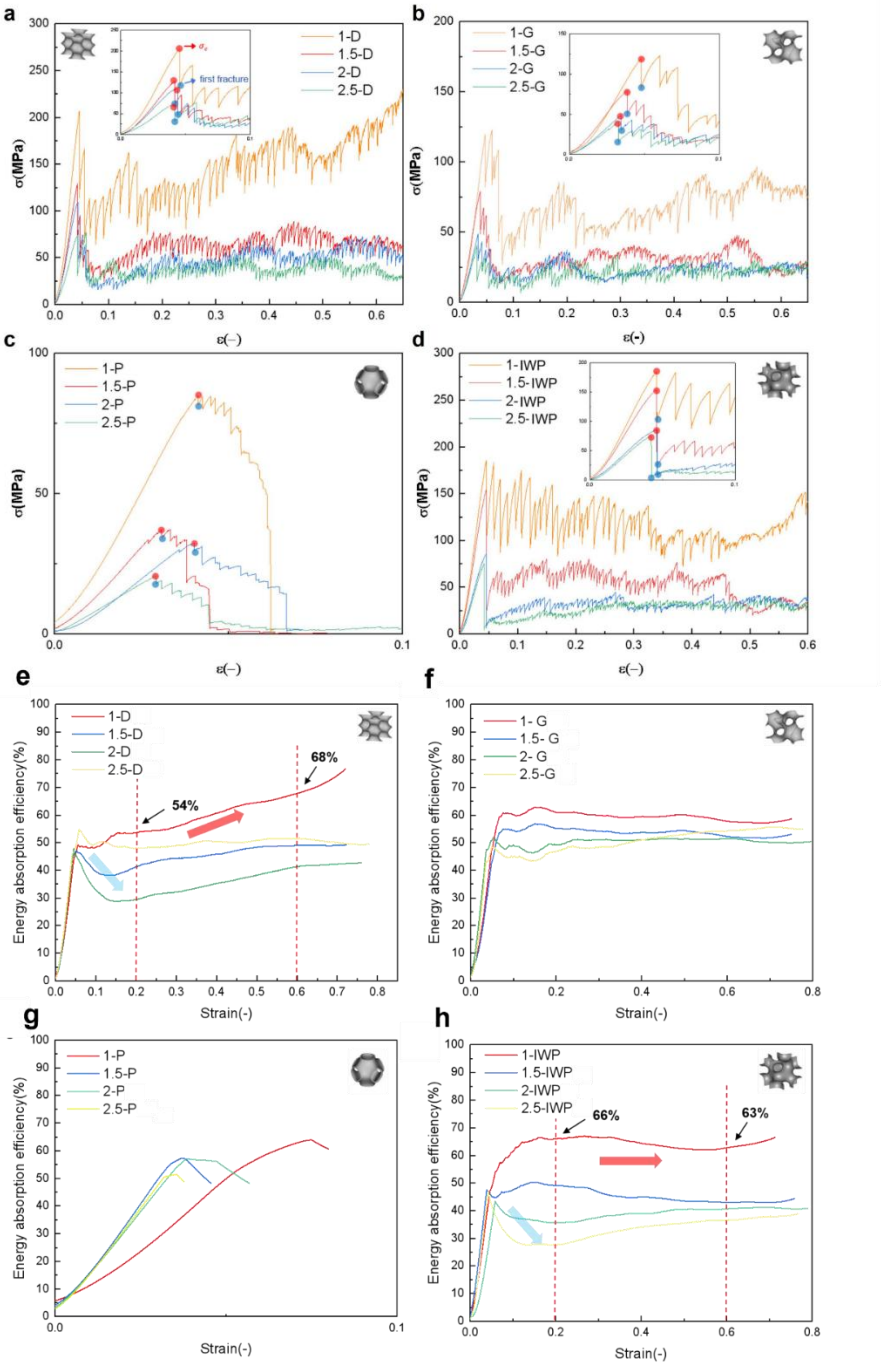

Fig 5. 7 Mechanical behavior of the TPMS MG structures. Stress-strain curves of the different type TPMS MG structures with diverse relative densities: (a) P-, (b) G-, (c) D- and (d) IWP. Energy absorption efficiency of the different type TPMS MG structures with diverse relative densities: (e) P-, (f) G-, (g) D- and (h) IWP.

The compressive stress-strain curves of TPMS lattices with different porosities are shown in **Fig 5. 7a–d**. Unlike ductile materials, which exhibit a plateau region characterized by a combination of bending and buckling deformation after the elastic stage, MG meshes release energy through brittle fracture while maintaining high stress levels. As shown in **Fig 5. 7**, different TPMS structures exhibit distinct compressive behaviors. For instance, P-type structures experience catastrophic failure, while other types display a certain degree of damage resistance. Upon reaching compressive strength, the MG structure undergoes its first fracture, which significantly determines its energy absorption capacity and damage tolerance. Here, the extent of the first stress drop is used to compare the effect of the initial fracture on the failure mode of different types of structures. It is calculated as the ratio of the stress drop at the first fracture to the compressive strength. Another important factor is the propagation path of the crack. The P-types show a slight stress drop at the first fracture, but the stress quickly decreases to zero, indicating a poor damage tolerance.

Failure mode dominates the energy absorption efficiency. **Fig 5. 7e-h** illustrates varying trends in η across different TPMS types and RDs. Overall, the stress-strain curve is largely governed by the fracture mode, which significantly impacts on the energy absorption efficiency, resulting in distinct behaviors across different structures. In the next section, we examine the fracture modes shown in **Fig 5. 9** to further explain the varying behavior of η.

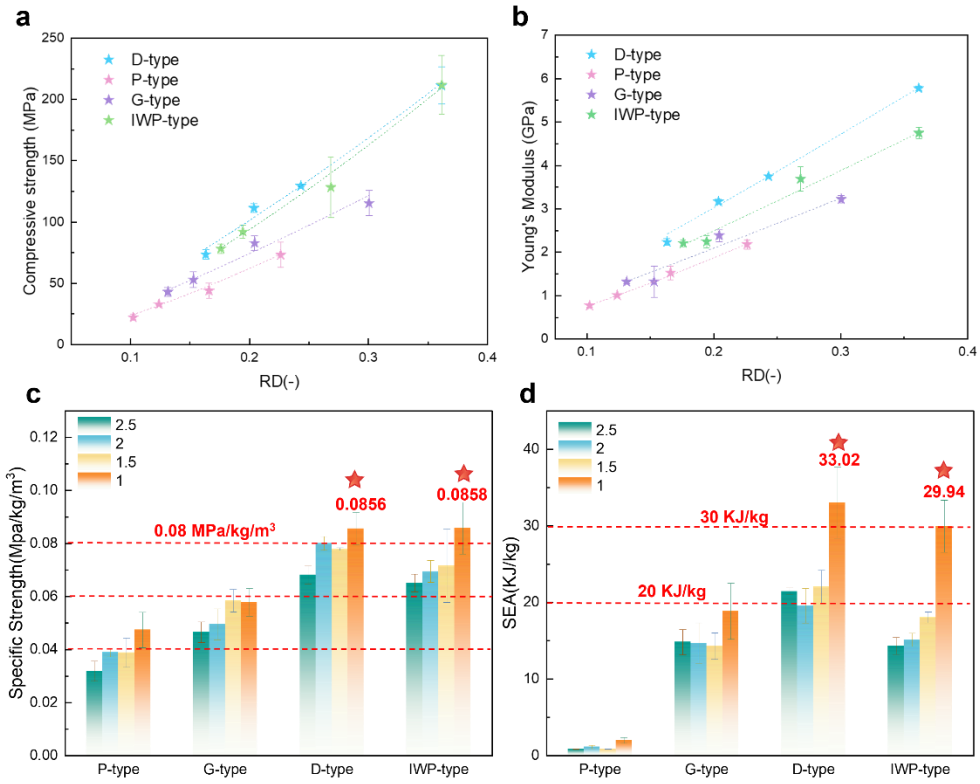

Fig 5. 8 Mechanical performance comparison. (a) Ashby map of the compressive strength based on the varying RDs of TPMS structures. (b) Ashby map of the elastic modulus based on the varying relative densities of TPMS structures. Mechanical performance comparison among the different types of TPMS MG structures: (c) Specific strength, (d)SEA.**Fig 5. 8a** illustrates the variations in compressive strength with the measured relative density (RD) for the four types of TPMS structures. The D-type and IWP-type MG structures clearly outperform the G-type and P-type in terms of strength. For compressive strength, the fitting curve exponents for the G-type and P-type MG structures are slightly lower, highlighting their advantage in the low-density range. However, in the high-density range, the D-type and IWP-type structures exhibit exceptionally high strengths exceeding 200 MPa. Young's modulus ranges from 0.8 to 5.7 GPa (**Fig 5. 8b**), which is relatively

low compared to metallic cellular materials, contributing to the large elastic limit of the BMG.

5.3.3 Failure mode of different 3D-printed TPMS lattices.

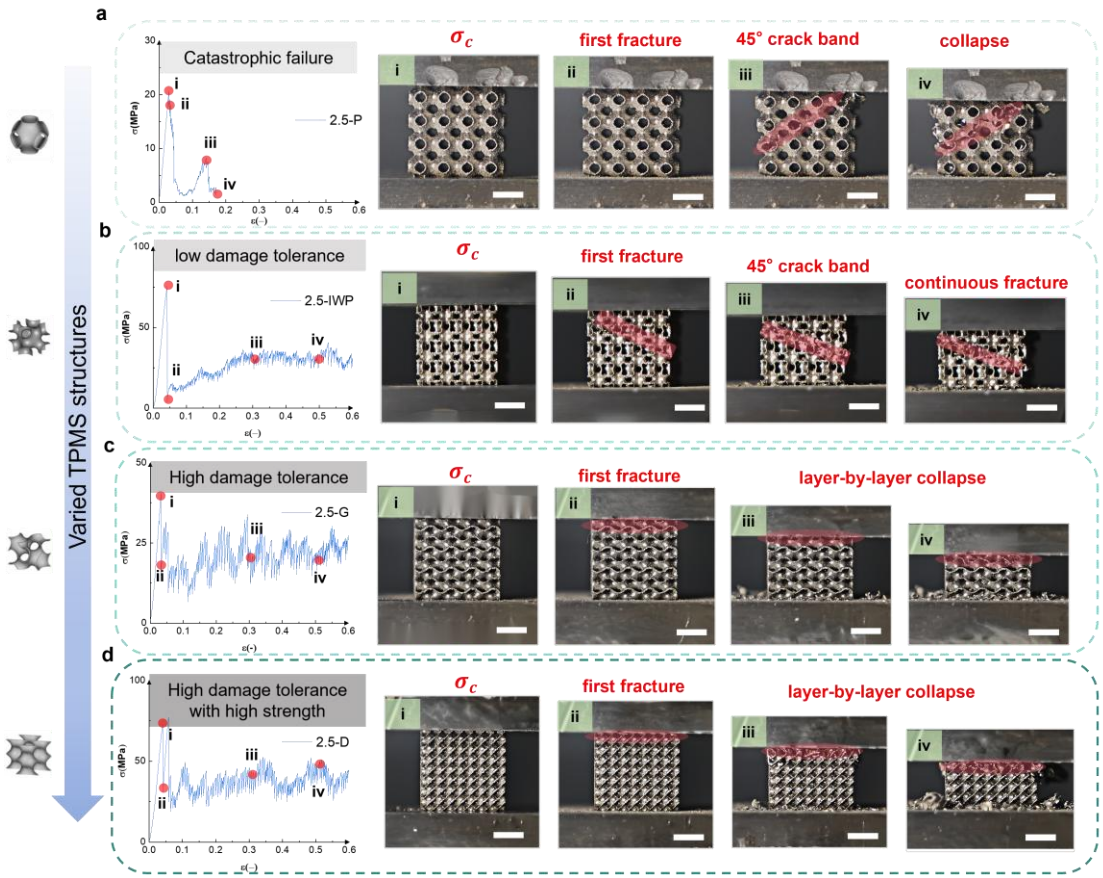

Fig 5. 9 Deformation behaviors and fracture modes of BMG lattices with different TPMS structure. Stress-strain curves of different unit cell type with the same unit cell size: (a)2.5-P (b) 2.5-IWP (c) 2.5-G (d) 2.5-D, corresponding images of fracture process captured from the four stages: (i) compressive stress (ii) first fracture (iii) strain at 0.3 (iv) strain at 0.5 (for (a)2.5-P specimen, (iii) strain at 0.15 (iv) strain at collapse). The scale bar is 4 mm.

From **Fig 5. 9a-d**, it is evident that different types of TPMS structures exhibit distinct stress-strain curves, indicating that the unit cell shape significantly affects their mechanical performances. The differences are primarily due to the various failure

modes. Here, we compare different types of TPMS structures with the same unit cell size of 2.5mm. As shown in **Fig 5. 9a**, the P-type MG structure exhibits catastrophic failure, with cracks quickly propagating through the entire structure after the elastic stage, characterized by typical 45° shear fractures (**Fig 5. 9a iii**). In **Fig 5. 9b**, the IWP-type MG structure exhibits a hybrid failure mode. Initially, shear fractures cause a dramatic stress drop (**Fig 5. 9b ii**), followed by continued fractures around the shear crack band (**Fig 5. 9b iii**), leading to a continuous collapse with a slight increase in stress (**Fig 5. 9b iv**). Due to the severe damage at the first fracture, the stress during the collapse stage remains very low. Thus, preventing severe first fracture is a critical challenge. The G-type and D-type MG structures exhibit a layer-by-layer collapse mode (**Fig 5. 9c-d**). Fractures typically initiate at the upper load surface (**Fig 5. 9c ii, Fig 5. 9d ii**), causing a smaller stress drop at the first fracture. This initial fracture leads to a continuous stress drop as new fractures develop within the first layer (**Fig 5. 9c iii, Fig 5. 9d iii**). As loading progresses to subsequent layers (**Fig 5. 9c iv, Fig 5. 9d iv**), the stress increases again, maintaining structural integrity. Consequently, the entire structure shows a generally stable stress level during compression, with periodic fluctuations.

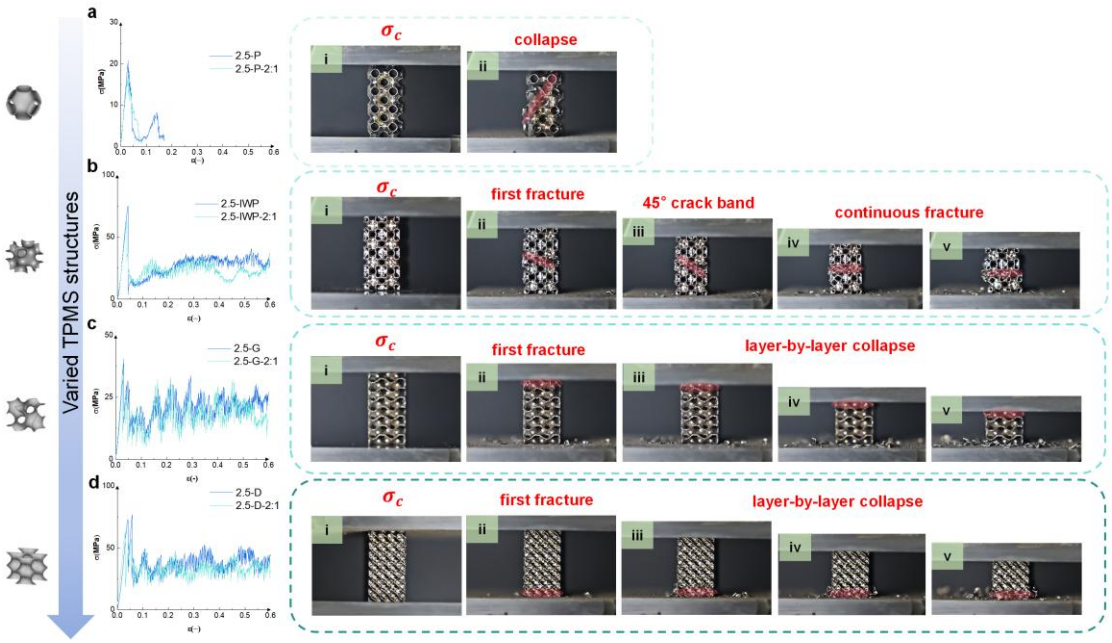

Fig 5. 10 Deformation behaviors and fracture modes of 2:1 aspect ratio MG lattices with different TPMS structure. Stress-strain curves of different types of TPMS lattices: (a)2.5-P (b) 2.5-IWP (c) 2.5-G (d) 2.5-D, corresponding images of fracture process captured from deformation stages.

Fig 5. 10 further elaborates the mechanical behavior on the 2:1 aspect ratio MG lattices with varying unit cell shape. The results indicate no significant differences; the fracture modes remain consistent with those observed in the 1:1 aspect ratio samples

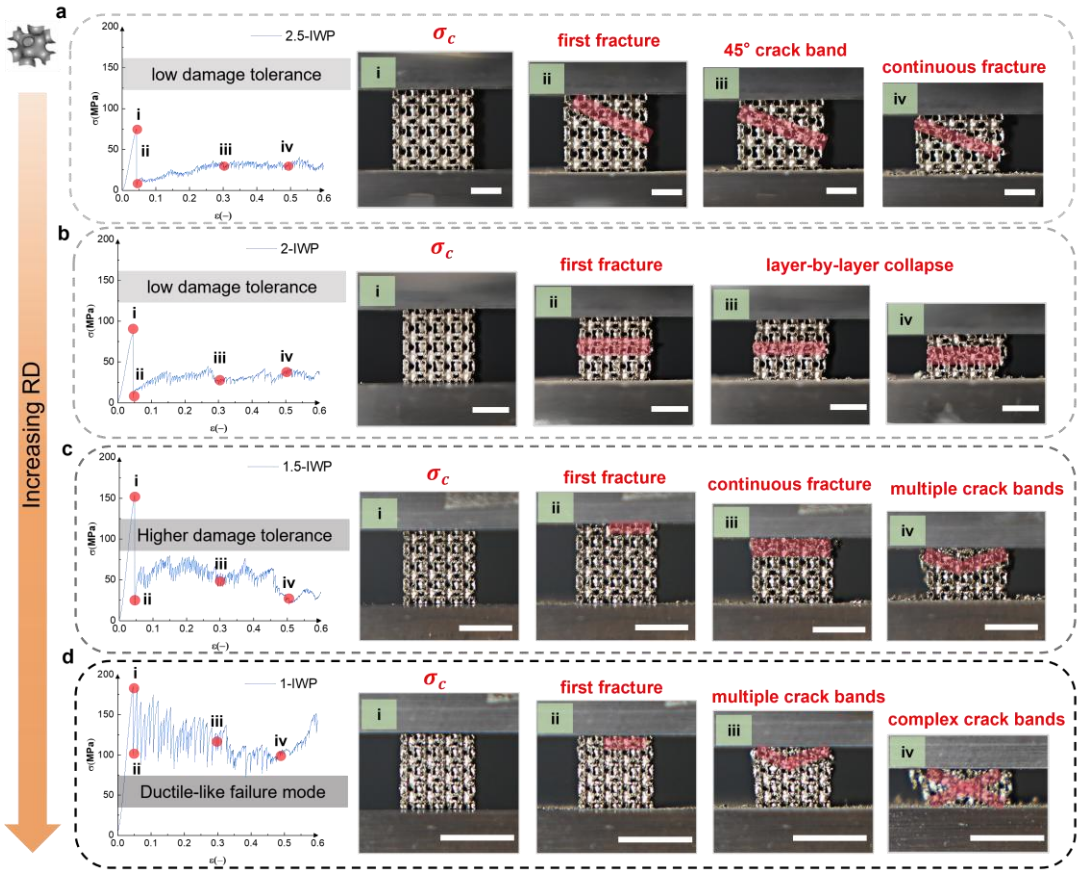

Fig 5. 11 Deformation behaviors and fracture modes of BMG lattices with different unit cell size. Stress-strain curves of same unit cell type with increasing RD (e) 2.5-IWP (f) 2-IWP (g) 1.5-IWP (h)1-IWP, corresponding images of fracture process captured from the four stages: (i) compressive stress (ii) first fracture (iii) strain at 0.3 (iv) strain at 0.5. The scale bar is 4 mm.

Increasing the RD of the MG structure is an efficient way to lower the first stress drop degree in **Fig 5. 12**, so there is a clear trend of a greater stress drop with decreasing RD. A significant transformation in the failure mode is observed in the IWP structure (**Fig 5. 11 a-d**) as the RD increases. As the RD increases from 0.175 to 0.361, the degree of the first stress drop decreases, leading to a higher plateau stress. This improvement is due to a change in the failure pattern: the main crack band initially forms diagonally (**Fig 5. 11a ii-iv**) but shifts to a horizontal direction (**Fig 5. 11b ii-iv**) with higher RD.

A diagonal crack band signifies extensive damage to the structure, impairing load bearing ability during deformation. In contrast, a horizontal crack band indicates that the fracture occurs within a single layer, allowing the remaining parts of the structure to maintain their integrity. Consequently, the structure can support the load throughout the deformation process until collapse. Notably, **Fig 5. 11d** shows that the 1-IWP MG structure with the highest RD exhibits a significantly high stress level after the elastic deformation region, demonstrating a pseudo-ductile fracture. During the collapse of each layer (**Fig 5. 11d ii**), multiple high-frequency stress fluctuations are observed, corresponding to the propagation of local cracks along the TPMS walls. This behavior resembles the formation of multiple micro shear bands (**Fig 5. 11d iii**), resulting in a jagged stress curve similar to the plastic deformation of solid BMGs. Additionally, a second reinforcement stage (**Fig 5. 11d iv**) is observed after the stress fluctuation phase in the 1-IWP MG structure, further enhancing its load-bearing and energy absorption capacities. This phenomenon is discussed in the next section with reference to the DVC analysis.

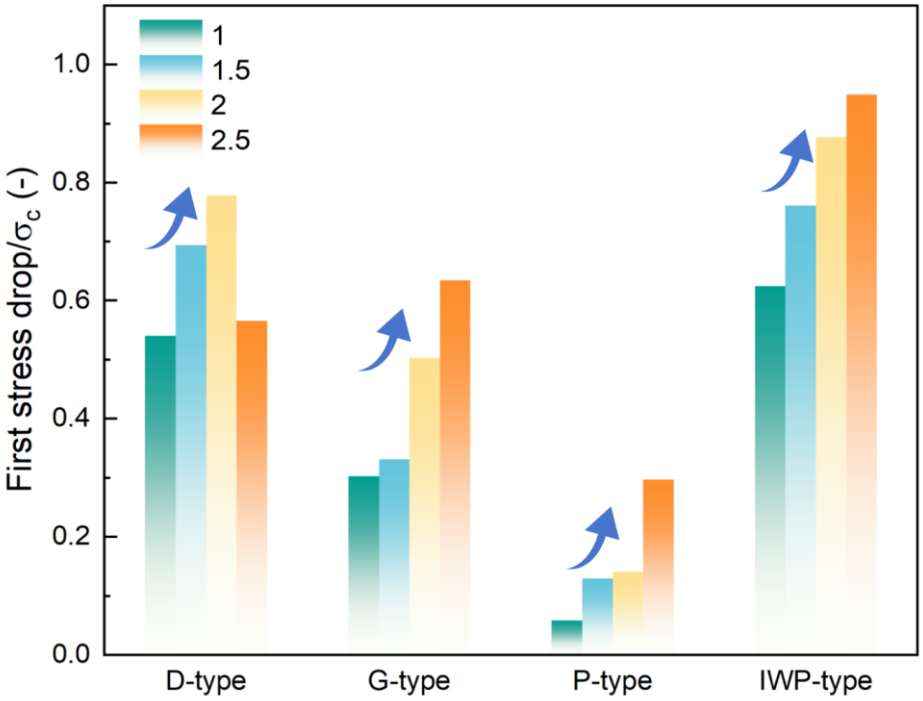

Fig 5. 12 First Fracture degree of different of the printed different type TPMS MG structures.

For the P-type MG structure, which experiences catastrophic failure, the value of the η peaks (**Fig 5. 7e**) at the compressive strength limit (elastic limit) and drops to zero as the structure collapses, indicating that there is no energy absorption during the failure process. Ideal energy-absorbing materials feature a long plateau at a high stress level throughout the deformation process, thus the energy absorption behavior after the elastic stage is more crucial. The G-type MG structures with a layer-by-layer fracture mode exhibit stable energy absorption performance (**Fig 5. 7f**). The 1-G specimen maintains approximately 60% of its energy absorption capacity throughout the fracture process until a strain of 0.8 is reached, which is comparable to ideal open-cell absorbers. The energy absorption performance of D-type (**Fig 5. 7g**) and IWP-type (**Fig 5. 7h**) structures shows a dependence on RD, with improved efficiency observed in MG

structures with higher RD. MG structures with lower RD (unit cell sizes of 2 and 2.5) show a decreasing trend in energy absorption after reaching compressive strength, due to severe initial fractures. The η of 2.5-IWP MG structures at strain levels of 0.2 and 0.6 are 30% and 40%, respectively. MG structures with the highest RDs show high η values, with the η of 1-D MG structures at strain levels of 0.2 and 0.6 reaching 54% and 68%, respectively, increasing with the failure process. For the 1-IWP MG structures, η values at strain levels of 0.2 and 0.6 are 66% and 63%, respectively, demonstrating stable high efficiency during the whole deformation process. Both types of structures exhibit excellent average energy absorption efficiency, exceeding 60% throughout the entire deformation stage, which surpasses most open-cell lattice structures.

The high specific strength of the MG significantly enhances its energy absorption capacity. While most lightweight metallic materials achieve ideal specific energy absorption (SEA) by being soft and easily deformable, resulting in generally lower strength. This result demonstrates that high strength and excellent energy absorption can be achieved simultaneously with BMG. As shown in **Fig 5. 8 c-d**, both 1-IWP and 1-D MG specimens achieve a high specific strength exceeding 0.08 MPa/kg/m^3, along with an outstanding SEA of approximately 30 kJ/kg. The results indicated that the influence of unit cell shape and unit cell size on the absorption efficiencies of TPMS MG structures is substantial.

5.4 Discussion

5.4.1 DVC and FE analysis based on *in situ* X-ray computed tomography

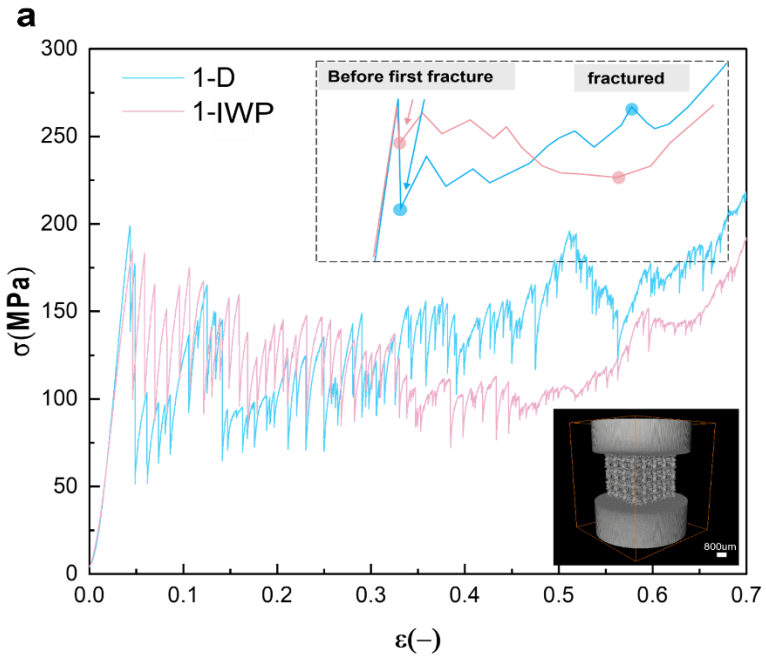

Fig 5. 13 Stress-strain curves of 1-IWP and 1-D MG structures.

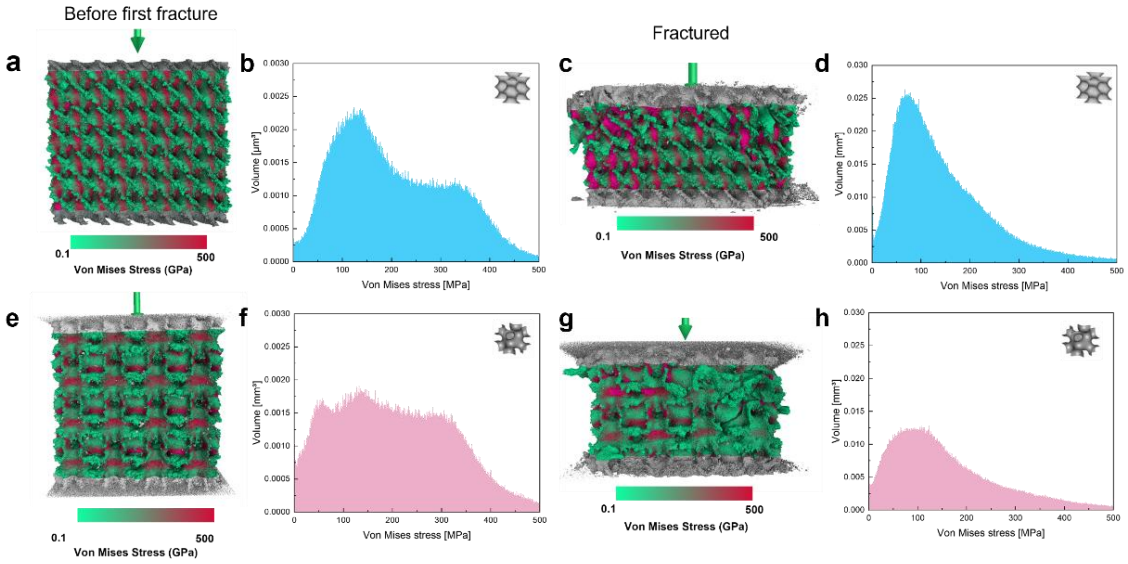

Fig 5. 14 Stress distribution FE simulation based on the CT- reconstruction TPMS structures under the different deformation stage. Stress distribution at the original states of 1-D MG structure: (a-b) and 1-IWP MG structure: (e-f). Stress distribution at the fractured states of 1-D MG structure: (c-d) and 1-IWP MG structure: (g-h).

The D-type and 1-IWP-type MG structures exhibit exceptional SEA and specific strength due to their high damage tolerance. **Fig 5. 13a** shows the stress-strain curves for these two MG structures, highlighting their differences. The 1-D MG structure exhibits a significant stress drop at the first fracture, followed by a continuous upward trend in stress. In contrast, the 1-IWP MG structure shows a relatively flat decreasing trend with slight fluctuations in stress. The two distinct behavior stages marked in **Fig 5. 13a** were analyzed using stress distribution FE simulations. **Fig 5. 14a** and **5. 14e** display the stress distribution of the 1-D and 1-IWP MG structures at their initial states. Compared with the 1-IWP MG structure, the 1-D MG structure shows a more concentrated stress distribution (**Fig 5. 14b**), which explains its greater susceptibility to severe initial fractures as it releases significant stress concentrations. In contrast, the 1-IWP structure exhibits a more homogeneous stress distribution (**Fig 5. 14f**), which helps avoid severe initial fractures. After fracturing, the stress concentrations are somewhat relaxed in both MG structures. Notably, in the 1-D MG structure (**Fig 5. 14d**), the peak of the high stress concentrations has dissipated, yet higher von Mises stress (**Fig 5. 14c**) remains in the non-fractured regions compared to the 1-IWP structure (**Fig 5. 14g**). This is due to the extensive small localized fractures in the 1-IWP structure, which result in a more fragmented overall structure that bears relatively lower stresses (**Fig 5. 14h**).

The fracture mode analysis based on images captured during compression tests, is limited to 2D observations and cannot effectively capture the complex crack propagation within 3D cellular structures that extends beyond a single plane[223].

Therefore, this study employs *in situ* Digital Volume Correlation (DVC) analysis to observe the deformation process of structural materials in 3D space, offering a more comprehensive understanding of the fracture mechanisms in these TPMS structures.

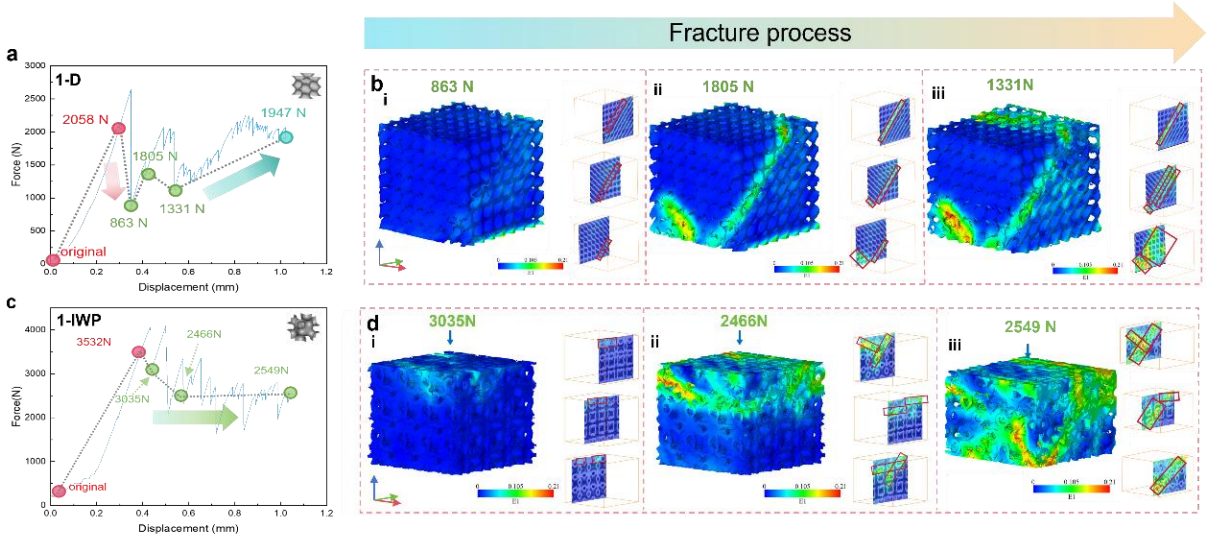

Fig 5. 15 DVC analysis based on the *in situ* X-ray CT of TPMS MG structures. The force–displacement curves of (a)1-D and (c)1-IWP specimens from *in situ* compression tests. (b) Strain distribution diagrams of deformations stages of 1-D specimen (from first fracture stage) obtained from DVC calculations. (i) force at 863N, (ii)1805N, (iii) 1331N. (d) Strain distribution diagrams of deformations stages of 1-IWP specimen (from first fracture stage) obtained from DVC calculations. (i) force at 3035N, (ii)2466N, (iii) 2549N. Deformation stages corresponding to the curve with highlighted data points in (a) and (c).

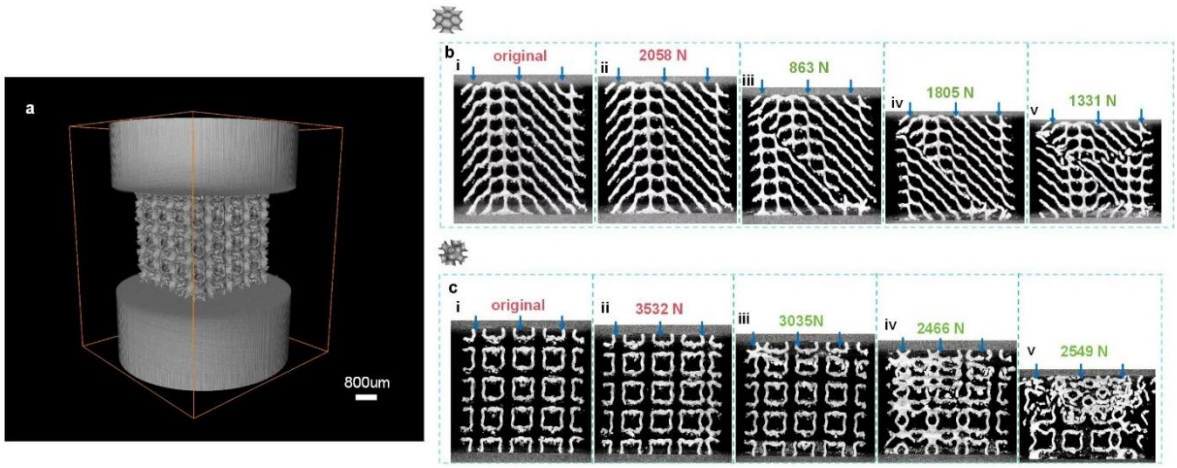

Fig 5. 16 In-situ compression X-ray CT test. (a)Schematic diagram. (b) X-ray projection images of deformation stages of 1-IWP specimen corresponding to the curve with highlighted data points in Fig 5.15 (a). (c) X-ray projection images of deformation stages of 1-D specimen corresponding to the curve with highlighted data points in Fig 5.15(c).

A similar stress variation trend was exhibited in the in-situ compression tests compared to the ex-situ measurements of 1-D structures **(Fig 5. 15a**) and 1-IWP structures (**Fig 5. 15c**). For the 1-D MG structure, the first fracture causes a significant force drop to 863 N. Corresponding projection images (**Fig 5. 16b iii**) reveal a single crack band oriented diagonally. However, the 3D strain diagram (**Fig 5. 15b i**) shows that, while the diagonal crack damages most of the structure, it does not extend throughout the entire volume, stopping near the bottom. During the compressive process (**Fig 5. 15b ii**), the crack does not continue along the original diagonal path. Instead, a new crack band forms along a different diagonal direction, interfering with the progression of the primary crack. This critical turning point prevents catastrophic failure and significantly affects the level of subsequent stresses. To better understand

this crack propagation mechanism, we simulated the stress distribution in the 1-D structure following the first fracture.

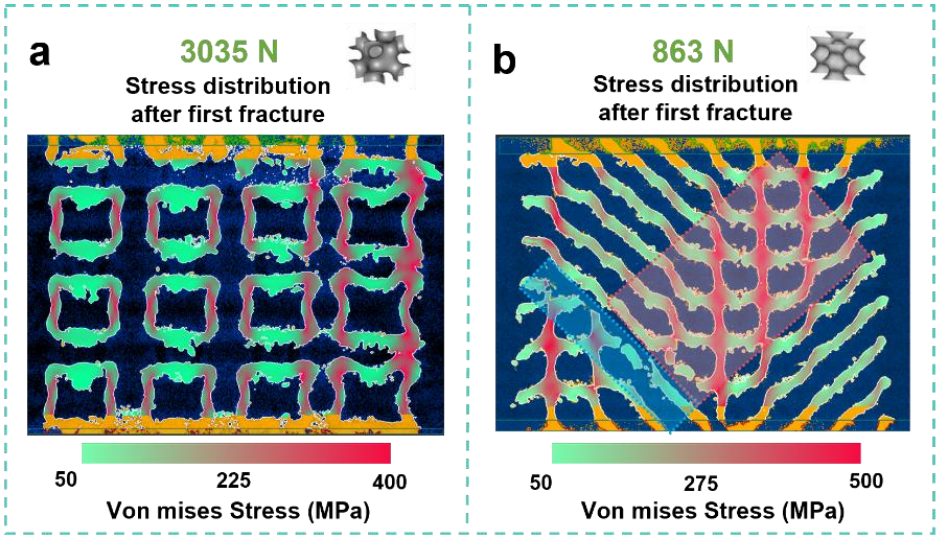

Fig 5. 17 Stress distribution at the first fracture stage obtained from FEM results:(a) 1-IWP, (b) 1-D.

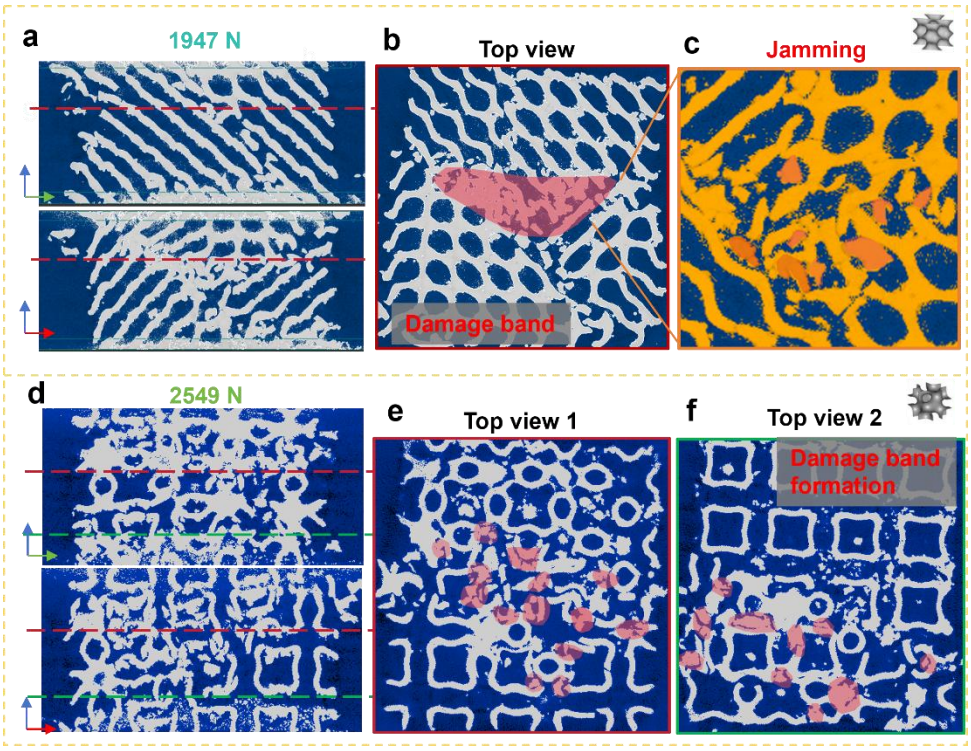

Fig 5. 18 X-ray reconstruction slice of the damage bands appeared in the last deformation stages: (a) side view (b-c) top view of 1-D specimen, (d) side view (e-f) top view of 1-IWP specimen.

As shown in **Fig 5. 17b**, the stress is concentrated on a plane roughly perpendicular to the original crack plane, with lower stress levels around the original crack tip. These finite element method (FEM) results align with observations of secondary crack formation during the in-situ compression test. This fracture behavior coincides with the crack propagation mechanism in all-brittle systems[224], if a plane of weakness or potential cleavage exists and is approximately perpendicular to the plane of the original crack, this interface may fracture and create a secondary crack, thereby hindering the progression of the primary crack. The crack continues to propagate along these two directions, as shown in **Fig 5. 15b iii**, resulting in ongoing local fractures that reduce the stress level in a limited area. Another turning point occurs at the final deformation stage (**Fig 5. 15a**), where the stress begins to increase without a stress drop, and a vertical damage band becomes visible as seen in **Fig 5. 18a**. Damaged bands found in architected ceramics have proved essential in enhancing the energy absorption capacity [225, 226]. In **Fig 5. 18b-c**, the development of these damage bands, driven by microfractures and local jamming, leads to fragments becoming lodged within the porous structure, causing further densification under load. The displacement vector diagram in **Fig 5. 19** reveals a clear interface: the displacement vectors of the upper and lower portions of the fracture surface move in opposite directions, both converging towards the fracture surface. This movement continuously compresses the central vertical damage bands, leading to gradual crushing and effective energy dissipation.

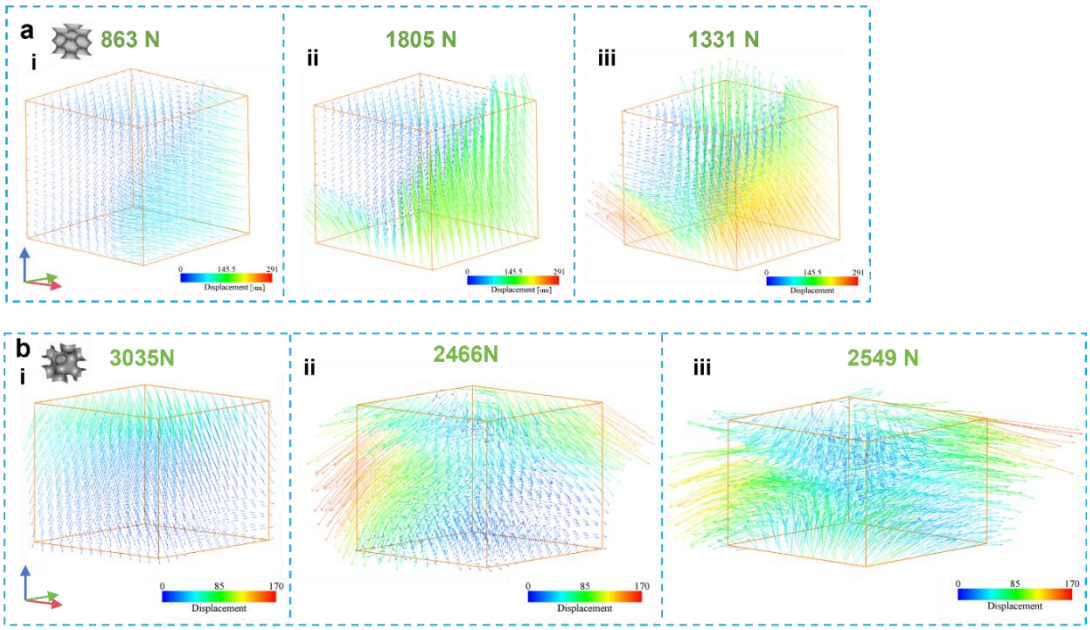

Fig 5. 19 Displacement vector diagrams of (a) 1-D specimen and (b) 1-IWP specimen corresponding to the strain distribution diagrams from Fig 5.15 b and d.

1-IWP TPMS MG lattices also exhibit excellent energy absorption capacity due to their ductile-like plateau stress level during the deformation process. Unlike 1-D lattices, 1-IWP MG lattices demonstrate a layer-by-layer collapse without a large main crack band extending through the entire structure. Hence, there are no dramatic stress drops during deformation; instead, the fractures appear to be localized in the upper layer (**Fig 5. 15d i**) and then slowly propagate to the next layer (**Fig 5. 15 ii**). In **Fig 5. 15d i**, the first fracture is localized within the upper layer, and there is no clear stress concentration after the initial fracture (**Fig 5. 17e**) during the loading process. As a result, multiple localized fractures continuously occur (**Fig 5. 15 iii**) while maintaining a high stress level. In **Fig 5. 18d**, localized crack bands are evenly distributed throughout the structure with no obvious locations of aggregation. From the top view, some traces of the initial formation of the damage bands can be seen in **Fig 5.**

18e-f. Due to the decentralized location of the crack bands, it is more difficult for 1-IWP structures to form extensive damage bands, tut it has the advantage of more uniform structural deformation.

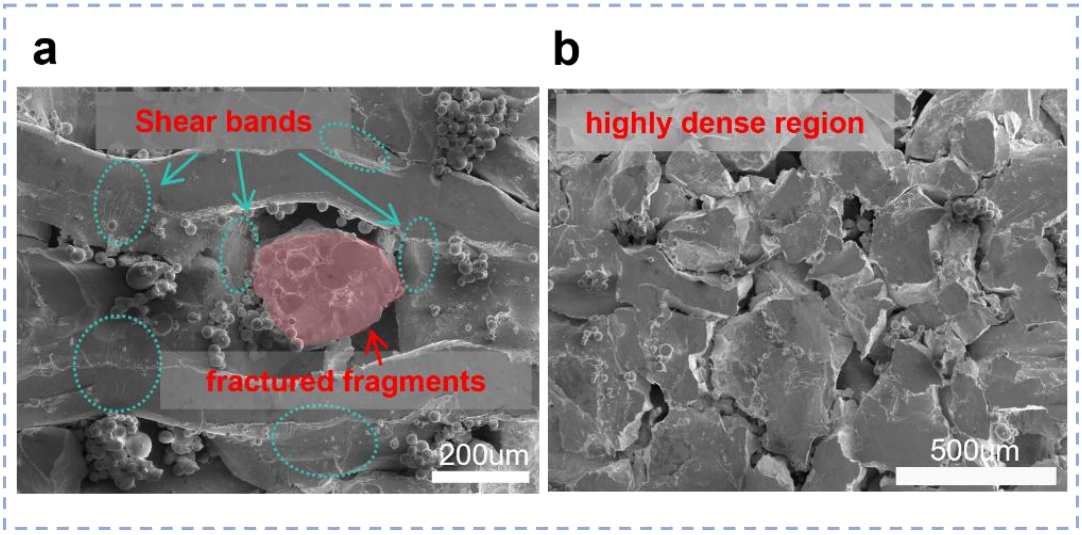

Fig 5. 20 SEM images of the fractured specimen with (a) shear bands and (b) jamming of the fractured fragments.

By examining the SEM images of the MG structures after the compression test, we can clearly observe that a large fragment (red-shaded region in **Fig 5. 20**) is jammed by the surrounding structure. Additionally, we find a surprising number of shear bands (**Fig 5. 20**) appearing in the undamaged regions around the fractured fragments. MG exhibits macroscopic brittleness but has been shown to exhibit plastic deformation at the micro-level, primarily through highly localized shear. Its plastic deformation capacity is closely related to the formation, expansion, and proliferation of shear bands.[227]. One significant external factor influencing plastic deformation in MG is the stress state[228]. Due to the fragments being jammed in the pores, the stress state

surrounding the damage bands becomes complex and non-homogeneous, which more readily facilitates the nucleation of shear bands.

Overall, these two MG structures exhibit different fracture modes, yet both achieve excellent energy absorption efficiency. It is crucial to avoid severe initial fractures that can cause extensive structural damage; instead, localized fractures should be managed to allow uniform deformation, stress release, and maintenance of stress levels. Even if the primary crack band causes significant damage, damage bands can form at the fracture interfaces under continued loading. Fractured fragments may become lodged in the pores, leading to ongoing defragmentation. Energy dissipation occurs through the reorientation, friction, and deformation of these fragments within the damage bands, while the remaining intact structure maintains high strength. At the microscopic level, the complex stress state triggers the formation of multiple shear bands in MGs, reducing the occurrence of brittle fractures and allowing the structure to undergo complete compression to the densification stage (**Fig 5. 20**).

5.4.2 Ductilization mechanism of Bio-inspired TPMS MG

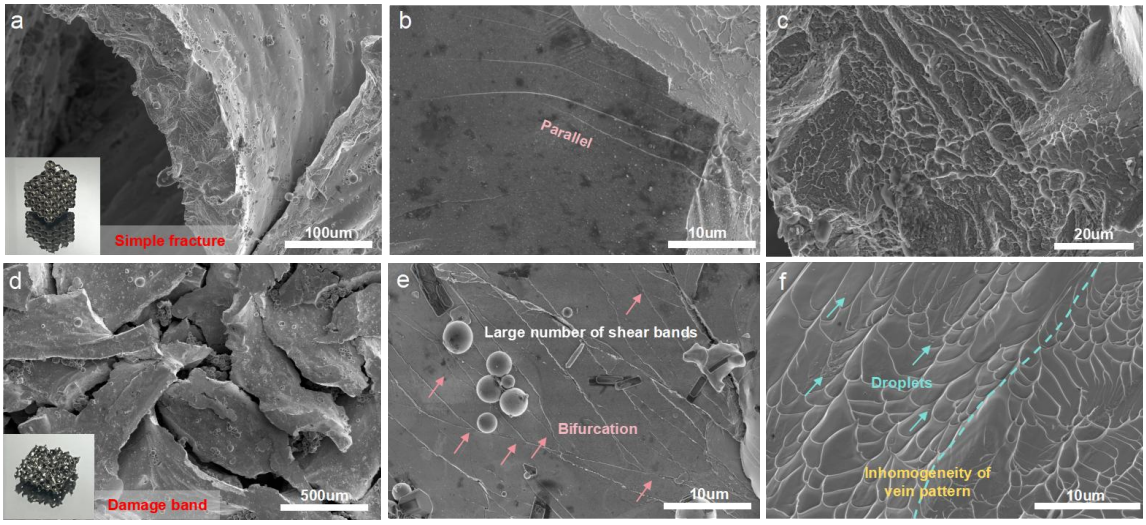

Fig 5. 21 Crack features and fracture morphologies of P- and D-type MG lattices. (a) P-type MG lattices with simple fracture. (b-c) A few shear bands on the shell near the fracture surface and the corresponding fracture morphology. (d) D- type MG lattices with damage bands formed during compression. (e-f) Numerous shear bands on the shell within the damage band zone and the corresponding fracture morphology.

To better understand the ductilization mechanism during the collapse process, two typical MG lattices were selected to observe fracture morphologies at the microstructural level. **Fig 5. 21a** shows the simple fracture of the P-type MG lattice without further interaction of fractured fragments. Only a few parallel shear bands were observed on the shell (**Fig 5. 21b**), indicating the limited plasticity of the MG. A dimple structure, commonly observed in brittle Zr-based BMGs[229], was noted in the corresponding fracture morphology (**Fig 5. 21c**). **Fig 5. 21d** shows the macro damage bands formed during the fracture of the D-type lattice. Numerous shear bands, displaying bifurcation, were observed on the shell, indicating strong interactions between shear bands (**Fig 5. 21e**). The fracture morphologies exhibit typical vein patterns and multiple droplet traces (**Fig 5. 21f**), suggesting localized remelting and more complex deformation behavior, which dissipates additional energy.

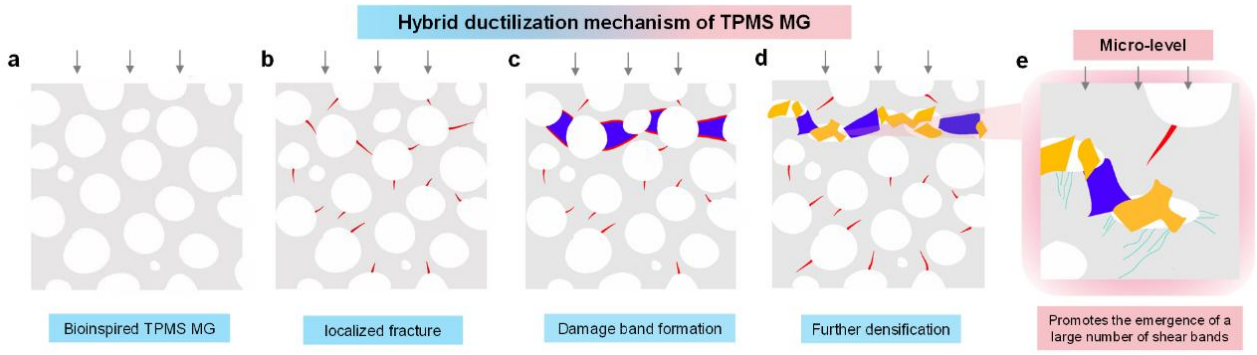

Fig 5. 22 Schematic diagram of a hybrid ductilization mechanism of Bio-inspired TPMS structure at macro and micro level. (a) elastic deformation. (b) localized fracture and microcracking. (c) damage band formation. (d) damage band propagation and further densification. (e) emergence of multiple shear bands induced by the complex stress fields.

From the analysis combining the fracture mode and fracture morphology, we recognized this is a hybrid ductilization mechanism during the 1-IWP and 1-P MG structures deformation process. At the macro level, damage bands formed by localized fractures result in fractured fragments jamming inside the pores, creating a jamming zone (**Fig 5. 22c**). Further densification (**Fig 5. 22d**) of these jammed fragments—through processes such as fracture reorientation, friction, and deformation—continues to dissipate energy while maintaining a high stress level. At the micro level, localized fractures and the formation of damage bands lead to structural heterogeneity. This results in complex stress distributions and stress fields. Under a multi-axial stress state, MG exhibits ductile-brittle transition behavior, which promotes the emergence of numerous shear bands (**Fig 5. 22e**). This hybrid mechanism, operating at multiple scales, results in amorphous toughening and mutually reinforces itself. Macroscale fracture modes initiate damage bands, which in turn stimulate the formation of nanoscale shear bands. The interaction of these multiple shear bands further prevents large-scale fractures from occurring at the macroscale.

5.4.3 Advantages on utilizing MG as the absorber materials.

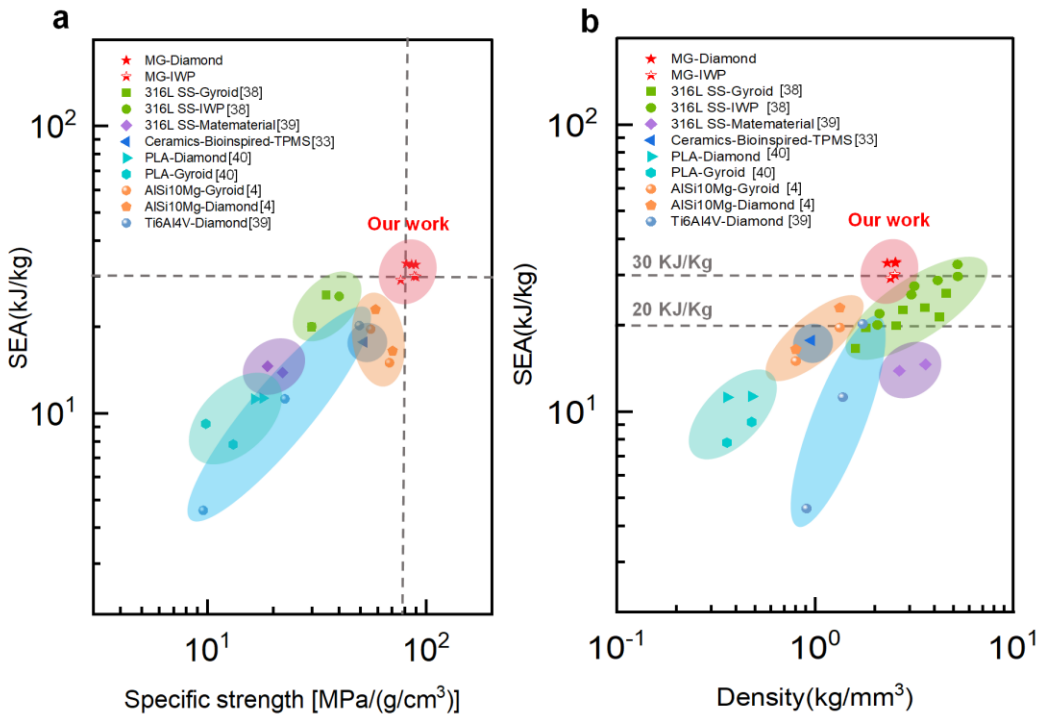

Fig 5. 23 Mechanical properties comparison for various cellular materials.(a) The comparison diagram of specific energy absorption versus specific compressive strength for various cellular materials. (b) Comparison of SEA of various cellular materials[206, 225, 230-232].

The hybrid ductilization mechanism enables the TPMS MG lattices to achieve ductile-like failure modes, expanding their potential structural applications. Once the catastrophic failure of BMGs is ameliorated, they can be utilized as energy-absorbing structural materials in many engineering applications. SEA is a common factor that is used to evaluate its energy absorbed capacity. The SEA data for TPMS MG lattices and other cellular materials are compared in **Fig 5. 23a**. The SEA of TPMS MG lattices exceeds 30 kJ/kg, which is notably high among cellular metallic materials and surpasses that of ceramics and polymers with similar structures. Additionally, when considering

specific strength, as shown in **Fig 5. 23b**, TPMS MG lattices are positioned in the top right corner of the graph. These results suggest that TPMS MG lattices are strong candidates for the next generation of energy-absorbing materials, combining both high strength and excellent energy absorption capabilities.

5.5 Conclusions

In this chapter, BMG lattices with four bioinspired TPMS structures were fabricated using the μL-PBF method. The 3D-printed MG lattices demonstrated high precision and excellent fabrication quality, exhibiting remarkable energy absorption capacities and high compressive strength. The exceptional energy absorption of the MG TPMS lattices is attributed to controlling the fracture mode, thereby avoiding catastrophic failure and achieving macro-plasticity comparable to that of ductile metallic materials.

Through DVC analysis using in-situ X-ray CT technology, the failure process, including the first fracture and fracture propagation path, has been clearly investigated. The first fracture was found to be crucial for the damage tolerance of MG lattices, with the structures experiencing severe fractures throughout all layers exhibiting low stress resistance. The IWP-type TPMS MG meshes displayed a more uniform stress distribution and a layer-by-layer collapse during the deformation process. Although D-type TPMS meshes demonstrate considerable SEA, their high energy absorption is more attributable to their extensive damage bands.

Combining with the investigation of fracture morphology, we found that the ductilization mechanism of MG TPMS is a hybrid mode involving both macro and micro levels. Localized fractures cause the formation of damage bands, which induce complex stress fields around the fractured fragments. MG exhibits microscopic plasticity by promoting the emergence of multiple shear bands within these complex stress fields, constituting a synergistic multiscale ductilization mechanism (from nm to μm to mm) during the failure process of TPMS MG meshes. This work presents a novel approach to enhancing the toughness and plasticity of MG through bio-inspired structural design, achieving excellent SEA with high strength in cellular MG materials. These findings indicate that structural MG is a strong candidate for the next generation of energy-absorbing materials in engineering applications.

Chapter 6 Multiscale structure engineering in hierarchical metallic glass lattice catalysts for ultra-efficient water splitting

6.1 Introduction

The advancement of additive manufacturing technology offers a feasible approach for fabricating catalysts with tunable mass transfer and mechanical properties through various architectural designs [93, 208, 233, 234]. In **chapter 5**, TPMS lattices, characterized by periodic implicit surfaces with zero mean curvature [235], offer particularly promising structural advantages. Their highly interconnected, non-tortuous pore networks provide exceptional volume-specific surface area and mechanical properties [215], with permeability and mechanical properties being readily adjustable through structure type and relative density modifications [208, 236]. MG TPMS lattices combine excellent mechanical and mass transport properties, making them strong candidates for catalyst scaffolds. Therefore, **chapter 6** explores the functional potential of MG TPMS lattices in catalysis, further broadening their prospective applications.

Hydrogen energy has emerged as a promising decarbonization vector capable of reshaping the global energy paradigms through a carbon-neutral alternative to fossil fuels [237, 238]. Within hydrogen production technologies, electrolytic water splitting stands unrivaled in sustainability metrics, though its industrial implementation remains constrained by fundamental electrocatalyst limitations [239]. Consequently, extensive research efforts have been dedicated to developing highly efficient electrocatalysts to

enhance the performance of water electrolysis [240-243]. Maximizing water-splitting efficiency requires concurrent engineering across four critical axes in catalytic electrode design [244]. First, the intrinsic activity of catalytic sites should be boosted, particularly to overcome the kinetically demanding four-electron pathway in the oxygen evolution reaction (OER) [245]. Second, enhancing charge transport efficiency, requiring a metallic conductor to minimize polarization losses [246]. Thirdly, optimizing mass transport, balancing electrolyte permeation with gas bubble expulsion dynamics [247, 248]. Lastly, ensuring structural resilience, addressing mechanical degradation from cyclic hydrodynamic stresses [249]. Catalysts frequently face challenges such as airflow impact and material compression during operation. The tendency of powder catalysts to detach and the brittleness of porous solid catalysts further limit their long-term stability [250]. Therefore, the development of highly efficient metal-based water electrolysis catalysts, optimized across multiple scales, remains a significant challenge.

MGs further elevate this paradigm through their inherent atomic disorder and nanoscale compositional fluctuations. Their high-density, low-coordination environments facilitate the formation of high-spin states [173], thereby enhancing intermediate adsorption/activation and reducing the catalytic reaction barriers [251, 252]. Consequently, MGs have emerged as highly promising and competitive catalysts. Recent studies demonstrate that MGs with disordered, homogeneous structures exhibit nano-scale structural inhomogeneities that significantly influence various properties,

including catalytic performance [253, 254]. For instance, Feng et al. reported that Ni-P nano-structured MGs exhibit remarkable nanoscale structural inhomogeneities at the interfaces. This unique interface structure plays a significant role in improving performance during electrocatalytic reactions [255]. Similarly, Lin et al. discovered that the abundant structural inhomogeneities, particularly in the interface regions, in Fe-based MGs significantly reduce the overpotential for the hydrogen evolution reaction (HER) [256]. Therefore, designing amorphous structures with highly inhomogeneous characteristics provides a novel pathway for the development of high-performance catalytic materials.

While 3D printing enables macro-architecture modulation, catalytic performance primarily depends on the microstructure of the active material [208, 257]. This scale dichotomy finds resolution in pulsed electrodeposition (PED) – a temporal-field modulated synthesis enabling nanoscale metallic structure design [258]. When synergistically combined, these technologies permit hierarchical integration of macro-architected TPMS scaffolds with microstructurally optimized catalytic surfaces, presenting a highly promising approach for developing efficient catalysts across multiple dimensional scales. Thus, in **chapter 6**, we constructed NiMo@Zr-based metallic glass hierarchical catalysts (denoted by NiMo@Zr MGHCs) through 3D-printed Zr-MG TPMS lattice substrate integrated with PED-synthesized NiMo-MG heterointerfaces. NiMo@Zr MGHCs exhibit remarkable superhydrophilic and superaerophobic properties, along with outstanding bifunctional activity for both HER

and OER. Remarkably, it achieves an ultra-low cell voltage of 1.438 V @ j = 100 mA cm^{-2} (in alkaline media) with the outstanding durability over 200 hours for overall water-splitting. Our work demonstrates the powerful synergy between 3D printing and PED in creating multifunctional catalysts with co-optimized mechanical strength, mass transport, and catalytic activity across multiple scales, opening new avenues for advanced water electrolysis technologies.

6.2 Methodology

6.2.1 Geometric modeling and fabrication of Zr-based MG substrates

Same Zr-based MG powders introduced in early chapter were employed as feedstock for substrate fabrication via μL-PBF process. MG substrates were fabricated using a BLT-S200GX μL-PBF system, which differs from standard L-PBF equipment by offering a refined laser spot size of just 30 μm, enabling the production of high-resolution components. The system is equipped with a 500 W IPG fiber laser and operates in a controlled Argon atmosphere, maintaining oxygen levels below 100 ppm throughout the build process. Key processing parameters included a laser power of 150 W, a scanning speed of 1500 mm/s, and a layer thickness of 20 μm.

The geometric characteristics of the three TPMS structures are summarized in **Table 6.1**. These TPMS geometries can be mathematically described using implicit equations that approximate their surfaces [192]. The Diamond (D), Gyroid (G) structures were introduced in the early chapter. Fischer-Koch S (S) surfaces are defined by the following approximations:

$$\Phi_S(x,y,z) = \cos(2\omega x)\sin(\omega y)\cos(\omega z) + \cos(2\omega y)\sin(\omega z)\cos(\omega x) + \cos(2\omega z)\sin(\omega x)\cos(\omega y) = c \quad (6.1)$$

x, y, and z represent the spatial coordinates, while ω = 2π/l, where l denotes the length of a unit cell. The process involved extracting the zero-level surface defined by Eq. 6.1, where Φ = 0, and then uniformly offsetting this surface in both directions.

Table 6. 1 Geometrical characteristics of the 3D printed Zr-based MG lattice substrates.

Lattice sample code	Unit cell size(mm)	Number of cells(x,y,z)	Measured average *m*(g)	Measured porosity (%) from CT
S	1	10*10*0.5	0.244±0.02	52.0%
G	1	10*10*0.5	0.135±0.02	72.3%
D	1	10*10*0.5	0.127±0.03	71.7%

6.2.2 Synthesis of NiMo@Zr MGHCs

Several chemical reagents were purchased from Macklin (Shanghai, China), including nickel sulfate hexahydrate ($NiSO_4 \cdot 6H_2O$, 98.5%), sodium molybdate dihydrate ($Na_2MoO_4 \cdot 2H_2O$, 99.5%), trisodium citrate dihydrate ($C_6H_5Na_3O_7 \cdot 2H_2O$, 99.5%), sodium chloride (NaCl, 99.5%), and ammonium hydroxide solution (NH_4OH, 25–28%). All reagents and solvents were used as received from commercial suppliers without further purification.

The 3D printed Zr-based MG substates were carefully detached from the baseplate via wire cutting, then subjected to ultrasonic cleaning to ensure surface integrity before the PED process. Subsequently, NiMo coating was in situ electrochemically deposited on the Zr-based MG structure using an electrolyte solution composed of 0.375 M $NiSO_4 \cdot 6H_2O$, 0.25M Na2MoO4·$2H_2O$, 0.17M NaCl and 0.55M H_5NO.

Electrodeposition was performed in a three-electrode system employing a saturated Hg/HgO reference electrode, the High-Purity Platinum Sheet counter electrode, and the Zr-based MG substrate as the working electrode. Next, the deposition parameters were carefully controlled with pulse on (0.25A, 16 ms) and off (0 mA, 4 ms) for 1 hour at 323 K. After the detailed characterization, both anodic reaction (OER) and cathodic reaction (HER) were conducted in an alkaline solution (1 M KOH) to test the catalytic performance.

6.3 Results

6.3.1 Multi-scale structure engineering in NiMo@Zr MGHCs

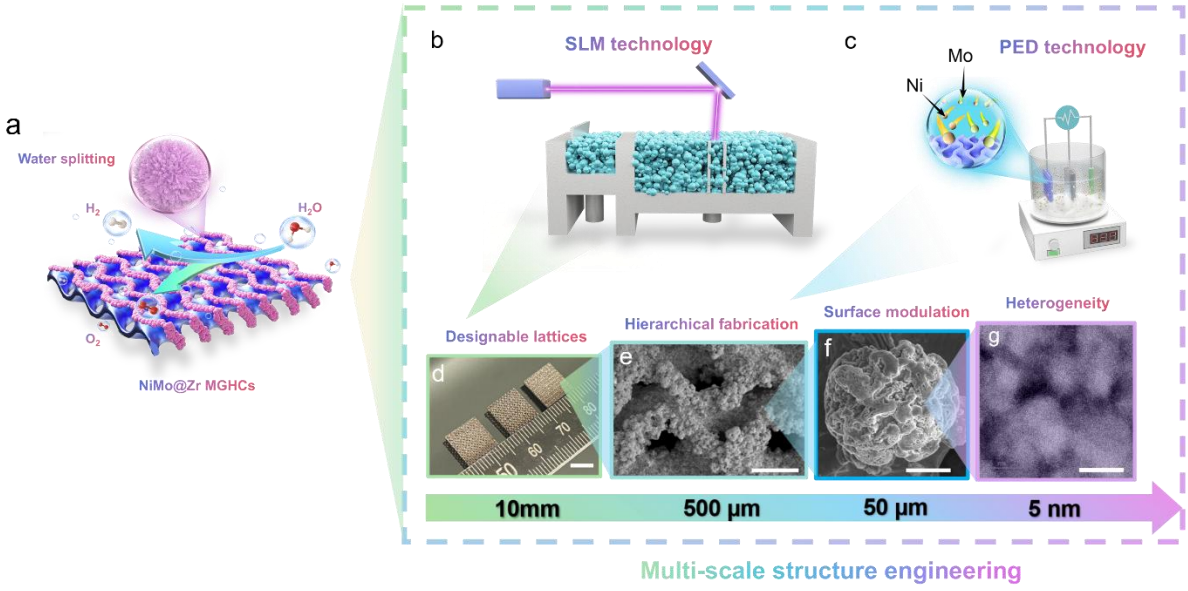

Fig 6. 1 Synthesis and multi-scale modulation strategy of NiMo@Zr MGHCs. (a) Schematic of NiMo@Zr MGHCs. (b) Schematic of the L-PBF technology used to fabricate the Zr-based MG lattice substrates. (c) Schematic of the PED technology used to deposit NiMo on the substrates. (d) 3D printed Zr-based MG substrates with different lattice structures. (e) SEM images of NiMo@Zr MGHCs fabricated via PED process. (f) SEM images illustrating the hydrangea-like architecture of NiMo at the micro level. (g) HAADF-STEM images of the NiMo atomic structure.

A multiscale modulation strategy was demonstrated from the macro-architecture of the MG substrates to the atomic structure of the NiMo MG, achieving highly efficient performance in bi-functional water splitting of the NiMo@Zr MGHCs (**Fig 6. 1a**). The realization of the multiscale modulation relies on the combination of these two technologies: L-PBF (**Fig 6. 1b**) and PED (**Fig 6. 1c**). SLM was first employed to fabricate the Zr-based MG lattice substrates, with its high accuracy and moderate cost. Considering the requirement of the catalysts for high surface area, excellent electrical conductivity and superior mechanical properties, Zr-based porous MGs were identified as promising substrate candidates by advanced 3D printing. Our previous research on the influence of architectural design on the mechanical properties and morphology of Zr-based MG TPMS lattices[235] provides compelling evidence that structural architecture exerts a substantial influence on catalytic performance. This correlation arises from the ability to precisely modulate both surface morphology and mass transport properties through the strategic selection of distinct TPMS geometries (**Fig 6. 1d**). After 3D printing, Ni and Mo atoms were deposited onto the surface of 3D-printed Zr-based substrates through PED, forming a NiMo@Zr MGHCs (**Fig 6. 1e**). By tuning the electroplating parameters, we can further modulate the surface morphology of the NiMo@Zr MGHCs with resulting NiMo structures that adopt a hydrangea-like morphology with complex, grooved surfaces (**Fig 6. 1f**) to regulate their wettability and bubble adhesion characteristics. Meanwhile, the microstructure of the NiMo (**Fig 6. 1g**) was controlled as atomic disorder and nanoscale heterostructure to further elevate the catalytic activity of the NiMo@Zr MGHCs.

6.3.2 Mechanical performance and transport responses of 3D-printed TPMS lattice substrates

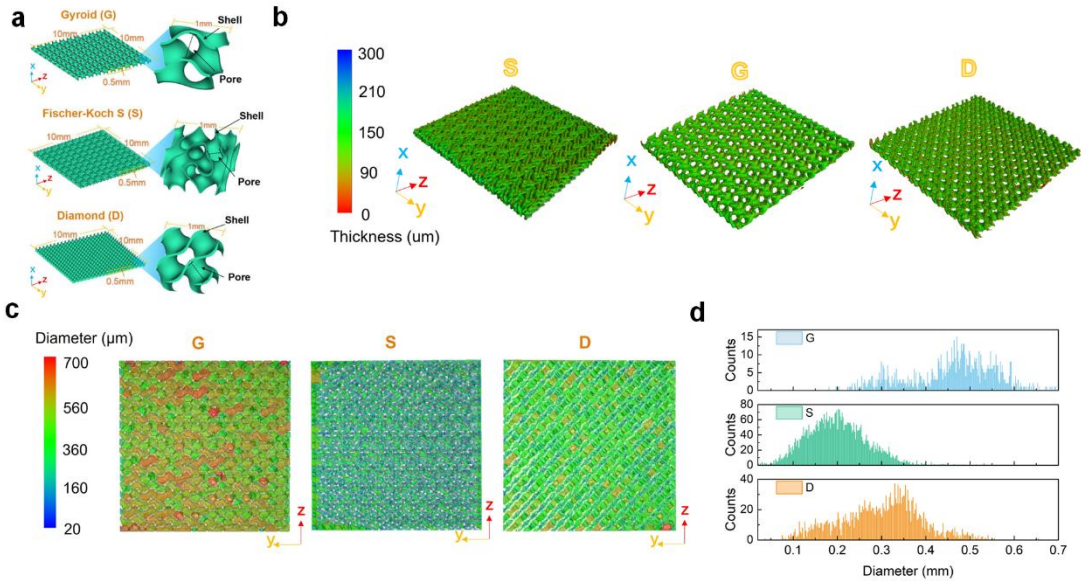

Fig 6. 2 Morphological structure of Zr-based MG TPMS lattice substrates. (a) CAD model of three types of TPMS structures of hierarchical catalyst substrates: G, S and D. (b) Shell thickness distribution and (c) pore diameter distribution derived from micro-CT-reconstructed 3D models of three types of TPMS lattices. Comparison of (d) Pore size distribution profiles.

Three types of TPMS structures with high surface area and favorable permeability—Gyroid (G), Fischer-Koch S (S), and Diamond (D)—were selected as architectural models for fabricating Zr-based MG lattice substrates (**Fig 6. 2a**). Micro-computed tomography (micro-CT) reconstruction (**Fig 6. 2b**) verified the high geometric fidelity and printing quality of the structures. A single-channel scanning strategy was employed to control the shell thickness, which ranged from 90 to 150 μm—near the resolution limit of current L-PBF systems. Porosity measurements derived from micro-CT revealed significant variations among the TPMS architectures: the S-Zr MG exhibited the highest relative density (RD) and the lowest porosity (~52%),

while the D- and G-Zr MG showed higher porosities (~72%). Pore sizes of different types of substrates can be directly investigated based on the 3D reconstructed model (**Fig 6. 2c**). Although the D- and G- Zr MG exhibit similar overall porosity, the G-Zr MG clearly shows a larger average pore diameter and a broader pore size distribution, with a bimodal peak between 200–600 μm (**Fig 6. 2d**), indicative of a hierarchical pore network. In contrast, the D structure shows a narrower pore size range of 100–500 μm, while the S structure features predominantly sub–300 μm pores, with minimum diameter as small as 20 μm.

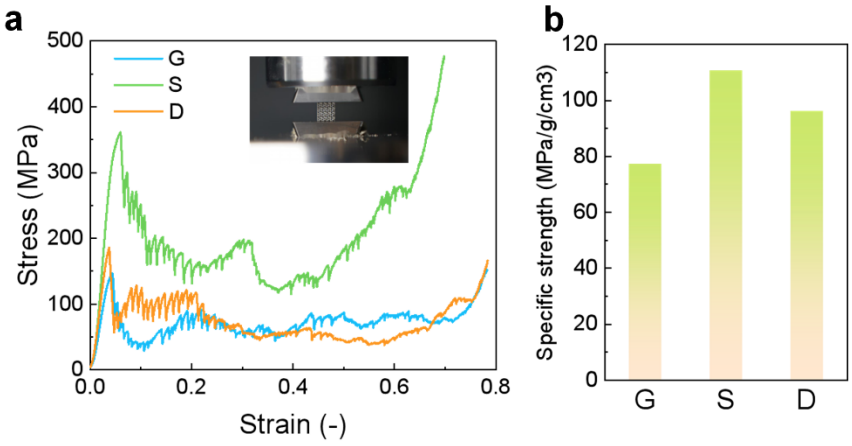

Fig 6. 3 Mechanical performance of Zr-based MG TPMS lattice substrates. (a) Stress-strain curves, and (b) Specific strength across the three TPMS lattices.

Damage-resistant, high-strength catalysts are essential for the long-term durability and operational stability of electrocatalytic systems. To assess the mechanical properties of the 3D-printed Zr-based MG substrates, uniaxial compression tests were conducted on 4 mm cubic samples. The resulting stress–strain curves (**Fig 6. 3a**) show high compressive strength and an extended stress plateau following the elastic region,

indicating excellent damage tolerance of the printed structures. Among them, the S-Zr MG demonstrated the highest compressive strength, exceeding 300 MPa, which correlates with its maximum relative density (RD). When specific strength is considered (**Fig 6. 3b**), the S-Zr MG achieved the highest value—over 110 $MPa \cdot kg^{-1} \cdot cm^{-3}$—surpassing many conventional metallic cellular materials. In contrast, the G-Zr MG exhibited a lower specific strength of 78 $MPa \cdot kg^{-1} \cdot cm^{-3}$ due to its geometric characteristics. Notably, even the lowest-performing G-Zr MG surpassed typical catalyst support requirements, such as nickel foam[259], by ten times while retaining the porosity critical for mass transport.

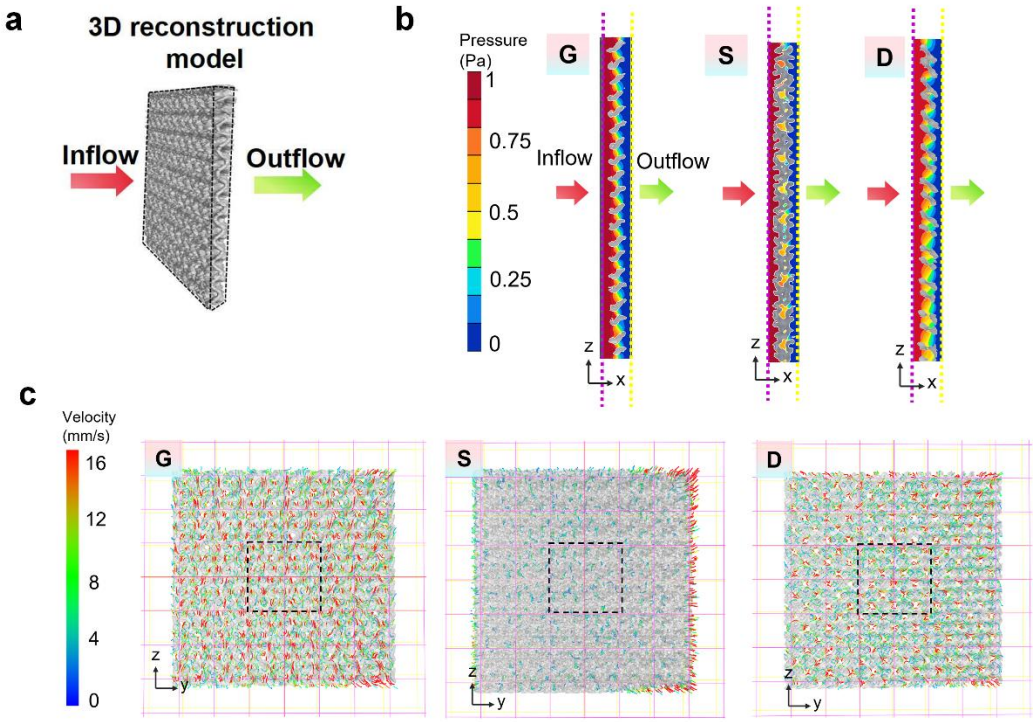

Fig 6. 4 Transport performance of Zr-based MG TPMS lattice substrates. (a) Schematic illustration of the fluid flow simulation, showing flow direction (left to right) through the 3D-reconstructed lattice model. (b) Pressure contours (Pa) for different types of TPMS lattices. (c) Velocity streamlines reveal distinct flow patterns across the three TPMS lattices.

Based on the 3D reconstruction model of the Zr-based MG substrates, the transport performance was analyzed to evaluate how different lattice architectures influence fluid flow behavior (**Fig 6. 4a**). Efficient mass transport minimizes concentration polarization and ensures stable electrochemical performance. The fluid flow behavior was simulated using a voxel-based finite volume method (FVM) that directly incorporates the actual microstructural features obtained from CT scans, including pore shape and connectivity, thereby avoiding geometric simplification inherent to conventional mesh generation techniques. This method offers superior fidelity by inherently accounting for manufacturing-induced variations and imperfections in the additively fabricated substrates. Under standardized simulation conditions with a 1Pa pressure difference between the inflow surface and outflow surface (**Fig 6. 4b**), the G-Zr MG and D-Zr MG structures exhibited continuous and extended velocity streamlines (**Fig 6. 4c**), indicative of higher permeability compared to the S-Zr MG structure, which exhibited shorter, more tortuous streamlines due to its lower porosity.

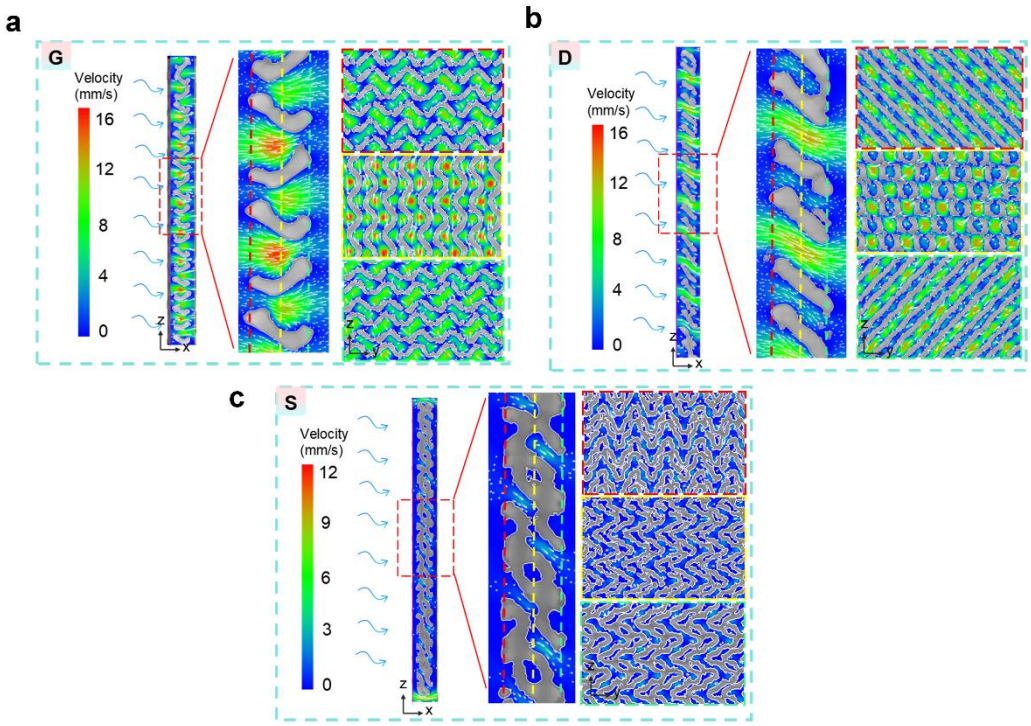

Fig 6. 5 Two-dimensional velocity contour maps of a representative cross-section, showing localized flow acceleration zones (red) and stagnation regions (blue): (a) G-Zr MG, (b) D-Zr MG and (c) S-Zr MG.

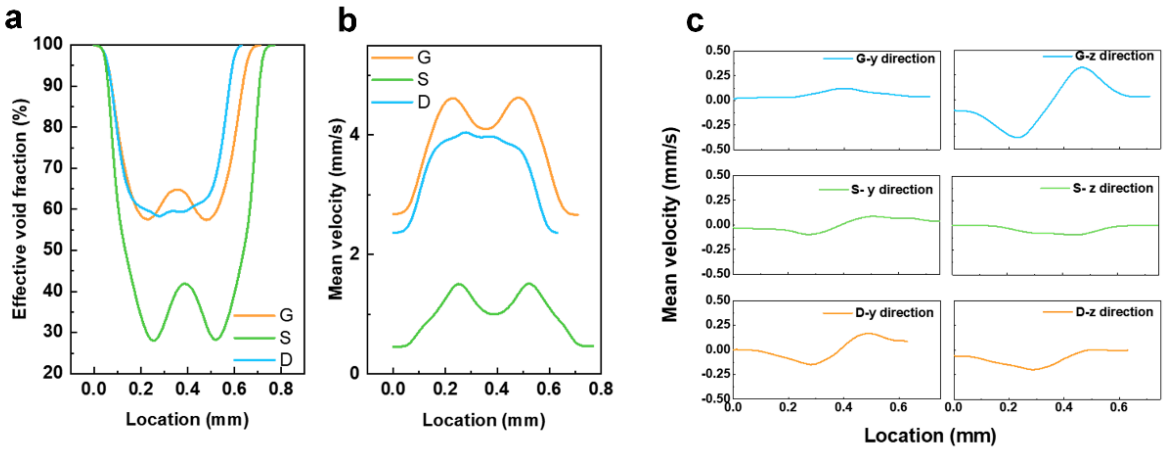

Fig 6. 6 Effective voids and mean velocity of the different types structure.(a) Axial variation of effective void fraction and (b) normalized average velocity along the primary flow direction (x-axis). (c) Transverse flow components (y- and z-directions) quantified by mean flow velocity magnitude, highlighting anisotropic transport behavior.

Velocity contour maps of the cross-sections reveal localized increases in flow velocity within G-Zr MG (**Fig 6. 5a**), suggesting the presence of flow instabilities that promote enhanced mixing. In contrast, the D-Zr MG shows less velocity fluctuation across the structure (**Fig 6. 5b**). Interestingly, despite D-Zr MG and G-Zr MG having nearly identical overall porosities (~28%), they display markedly different flow behaviors. G-Zr MG shows fluctuations in effective void fraction along the flow direction (**Fig 6. 6a**) with the highest mean flow velocity (**Fig 6. 6b**), whereas D-Zr MG maintains a relatively uniform distribution with a lower velocity. Although the overall porosity of S-Zr MG is approximately 50%, the effective void fraction within the internal region drops to only ~30% (**Fig 6. 6a**), resulting in a significantly lower mean velocity compared to the other two structures (**Fig 6. 6b**). Furthermore, G-Zr MG demonstrated significantly enhanced vertical transport (z-direction velocity component; **Fig 6. 6c**), enabling multidimensional reactant flow beyond the primary x–y plane, in contrast to the more uniform but less efficient flow patterns observed in D-Zr MG. This comprehensive analysis identifies G-Zr MG as the optimal catalyst substrate, offering a well-balanced combination of high local flow velocity, high permeability, and sufficient mechanical strength.

6.3.3 Superhydrophilicity/Superaerophobicity and multi-scale structure of NiMo@Zr MGHCs

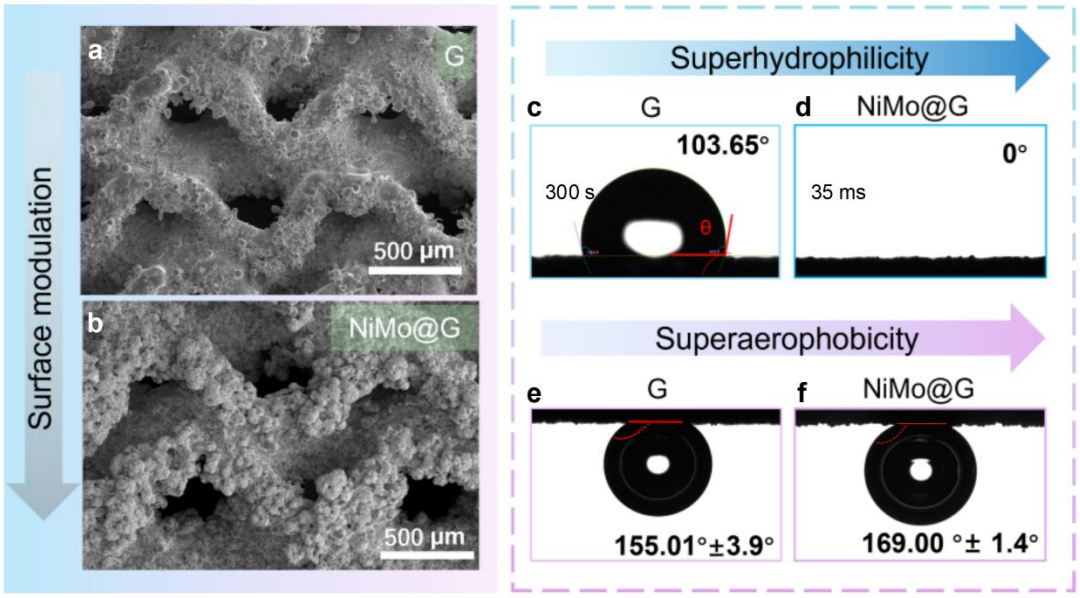

Fig 6. 7 Wettability and bubble adhesion characteristics and of NiMo@ G. (a) SEM images comparing the surface morphology of as-printed Zr-based MG substrate G with (b) corresponding NiMo@G after PED. (c) Images of water contact angles of 103.65° when water droplets are dropped on the surfaces of the G substrate. (d) The wetting behavior demonstrating superhydrophilic properties of NiMo@G. (e) Under electrolyte conditions, quantitative bubble adhesion measurements show that the G substrate without PED treatment exhibits a contact angle of 155.0° ± 3.9°, while (f) NiMo@G demonstrates a significantly enhanced superaerophobic surface with a contact angle of 169.0° ± 1.4°.

The surface morphology of catalysts serves as a crucial design parameter for regulating their wettability properties, where an optimal balance between superhydrophilicity (enhancing electrolyte wetting) and superaerophobicity (prompt bubble detachment) significantly improves the efficiency and durability of water-splitting systems[260, 261]. The optimal catalyst substrate G (**Fig 6. 7a**) and all other substrates were observed using SEM, showing no internal defects such as pores or cracks apart from minor surface-adhered unmolten powder particles. These residual particles caused slight surface roughness, which beneficially increased the surface area

and enhanced the adhesion of Ni and Mo atoms during the subsequent PED process. A large number of uniform hydrangea-shaped NiMo particles ranging in size from approximately 60 to 100 μm , were observed on NiMo@G (**Fig 6. 7b**)and across all substrate variants after PED[262]. NiMo flowers grown on the substrate surface create a hierarchically complex morphology that enables precise tuning of the surface wettability in the NiMo@Zr MGHCs.

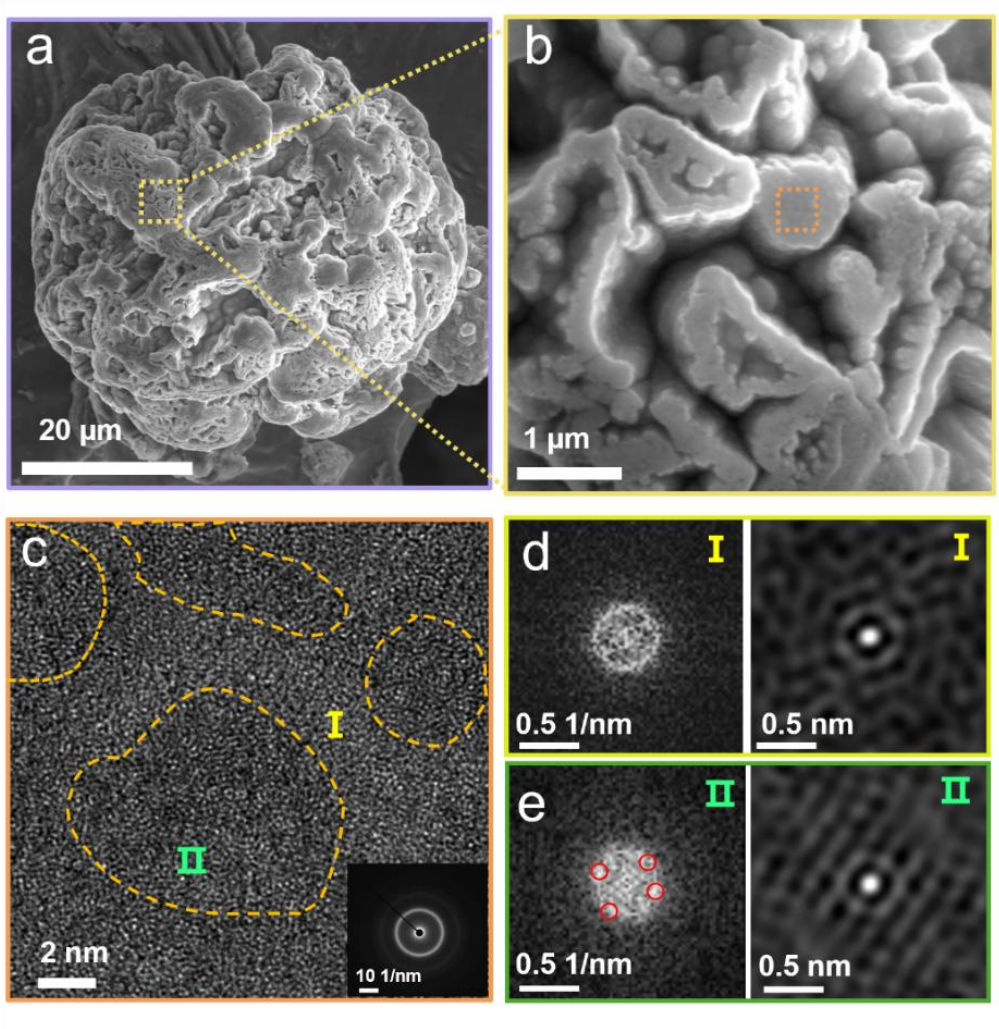

Fig 6. 8 Microstructure of NiMo particles.(a-b), SEM images illustrating the hydrangea-like architecture of NiMo grown on the Zr-based MG substrate via PED. (c), HRTEM image with an insert SAED pattern, revealing two distinct regions: (I) interfacial area and (II) clustered structure. (d-e) FFT

patterns and autocorrelation images of region I and region II from panel i, respectively, confirming the coexistence of structural inhomogeneity.

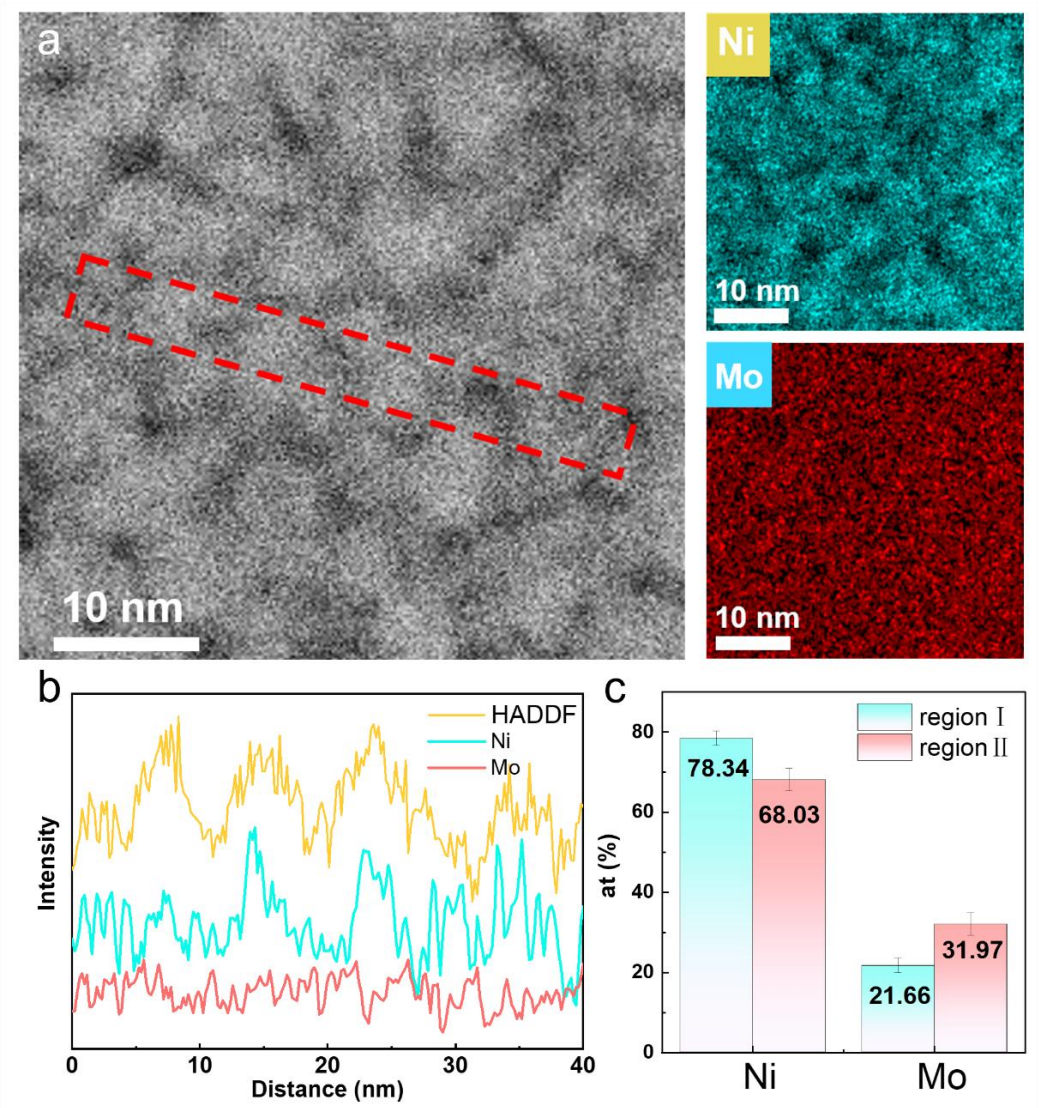

Fig 6. 9 Nanoscale compositional uniformity and elemental distribution of Ni–Mo particles(a) Corresponding EDS elemental maps for Ni and Mo and the associated HAADF-STEM image revealing nanoscale compositional uniformity. (b) Line scan of elemental distribution across a selected region from panel i confirming the spatial variation of Ni and Mo. (c) Atomic ratios of Ni and Mo from two distinct regions identified in the panel i.

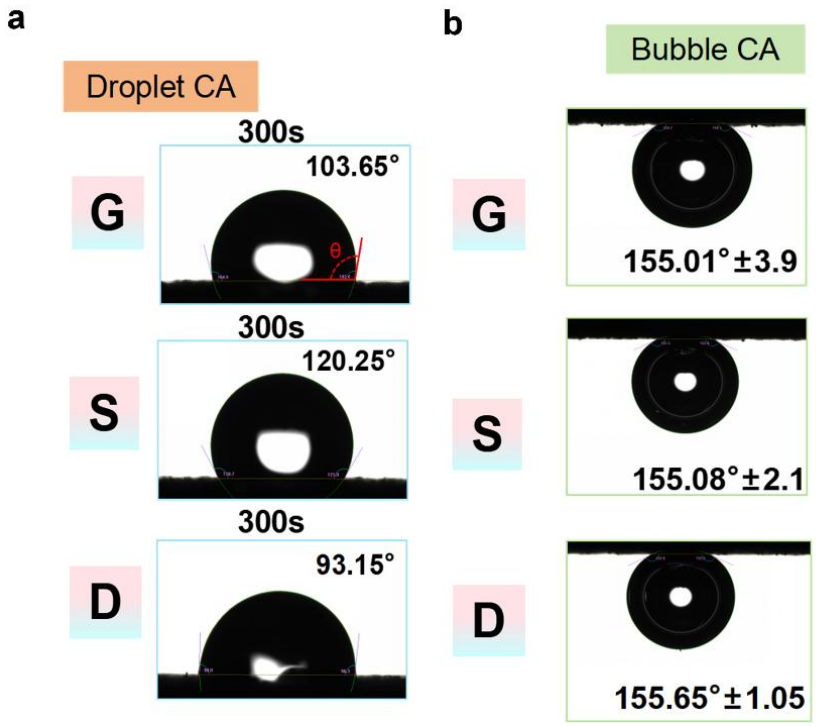

Fig 6. 10 Contact angles of Zr-MG substrates. (a) Images of water contact angles of different types of substrates. (b) The bubble contact angle tests of different types of substrates.

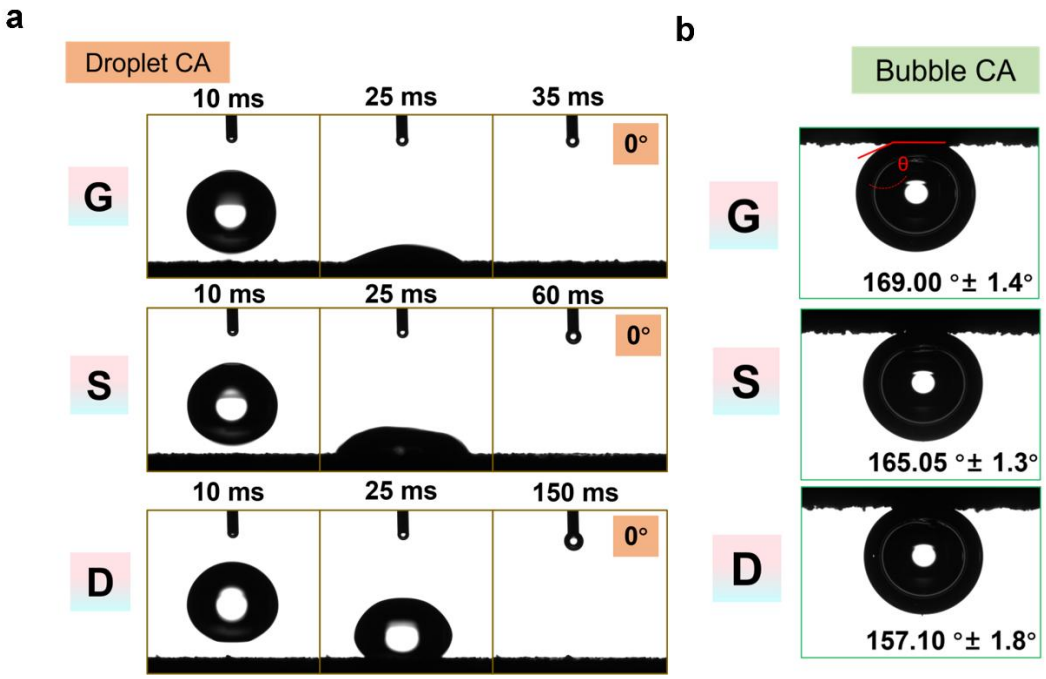

Fig 6. 11 Contact angles of NiMo@Zr MGHCs. (a) Images of water contact angles of different types of substrates. (b) The bubble contact angle tests of different types of substrates.

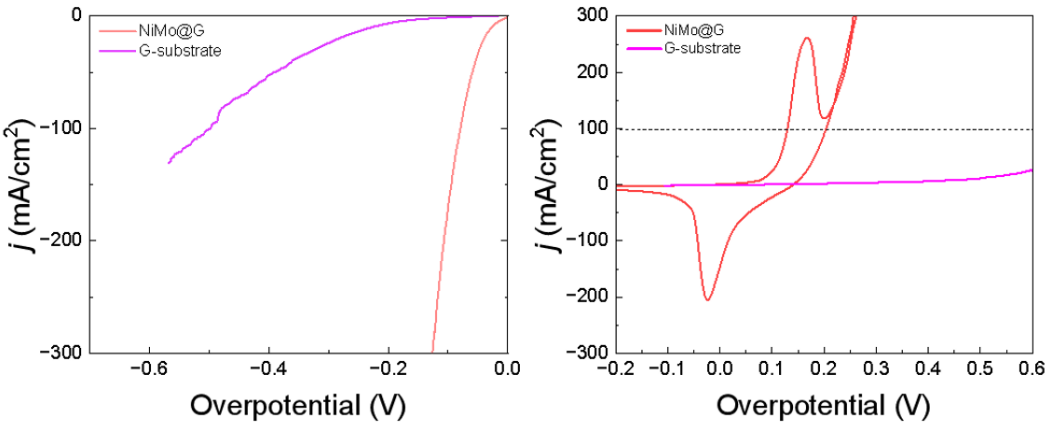

Fig 6. 12 HER and OER polarization curves of G substrate.

The contact angle of the bare substrate G is 103.65° after 300s (**Fig 6. 7c**) with all the other substates exhibiting a similar level of hydrophilicity (**Fig 6. 10a**), whereas all NiMo@Zr MGHCs exhibit superhydrophilicity (**Fig 6. 11a**), with water droplets spreading completely upon contact, particularly for NiMo@G (**Fig 6. 7d**) which achieves instantaneous wetting (0° contact angle within just 35 ms). Concurrently, these NiMo@Zr MGHCs demonstrate remarkable superaerophobic characteristics in aqueous environments. Specifically, the bubble contact angle of substrate G is 155° (**Fig 6. 7e**) whereas the NiMo@G shows the ultra-hydrophobicity (CA > 169°) (**Fig 6. 7f**). The bubble contact angles significantly improved to varying extents after surface modification of all the different substrates via PED (**Fig 6. 10b and Fig 6. 11b**).

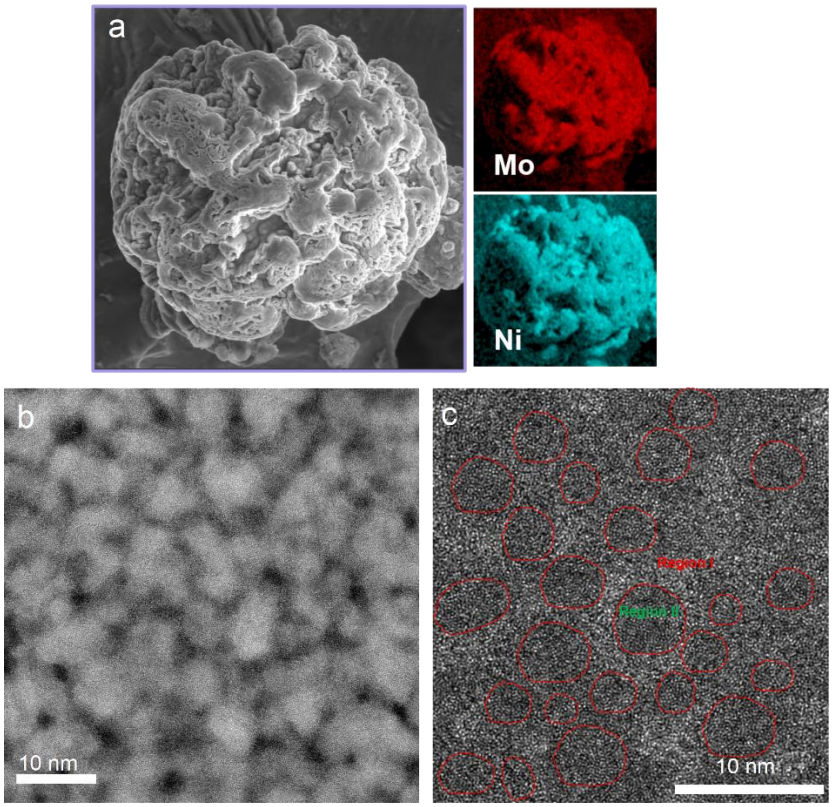

Fig 6. 13 Microstructure of NiMo particles. (a) EDX elemental mapping showing the uniform distribution of Ni (cyan) and Mo (red) elements across the deposited structures. (b) HADDF and (c) HRTEM images of NiMo flower, two distinct regions found in the image: region (I) and region (II).

A closer inspection (**Fig 6. 8a-b**) reveals the detailed morphology of the NiMo particles, characterized by a highly wrinkled and uneven surface, which increases the specific surface area and exposes more active catalytic sites. The bare substrates, without NiMo deposition, exhibited minimal catalytic activity (**Fig 6. 12**). To further boost catalytic activity, we modulate the microstructure of the NiMo particles. While elemental mapping demonstrates macroscale uniformity in Ni and Mo distribution across the entire flower-like structures (**Fig 6. 13a**), nanoscale analysis through HAADF-STEM reveals distinct contrast variations (**Fig 6. 13b**), indicating phase separation. The overall selected area electron diffraction (SAED) pattern (**Fig 6. 8c**

insert) exhibits a halo ring, indicative of an amorphous structure. HRTEM analysis reveals a disordered region (region I) and a more loosely arranged, medium-range ordered atomic cluster (region II) (**Fig 6. 8c** and **Fig 6. 13c**). The interface region (I) exhibits a highly disordered maze-like structure with inner circular fringes (**Fig 6. 8d**) and a featureless FFT pattern, whereas the cluster region (II) displays clear crystalline fringes (**Fig 6. 8e**) with distinct diffraction spots in the FFT pattern. HAADF-STEM reveals distinct contrast variations (**Fig 6. 9a**), indicating phase separation into Ni-rich (bright) and Mo-rich (dark) amorphous domains. EDS mapping confirms this structural heterogeneity, showing significant local Ni concentration variations while Mo maintains a relatively uniform distribution.

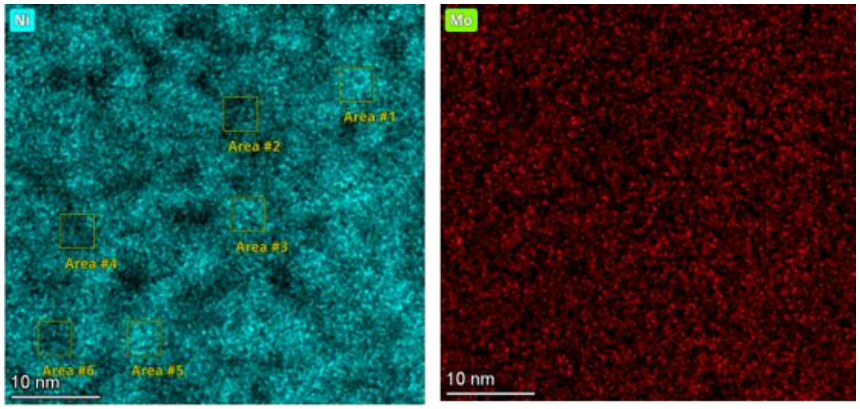

	Area#1	Area#3	Area#5	
Ni(at%)	76.27	79.16	79.6	**78.343**
Mo(at%)	23.73	20.84	20.4	**21.656**

	Area#2	Area#4	Area#6	
Ni(at%)	69.11	64.82	70.17	**68.033**
Mo(at%)	30.89	35.18	29.83	**31.966**

Fig 6. 14 EDX mapping of the Ni and Mo elements.

Integrated compositional line scans (**Fig 6. 9b**) quantitatively verify that the brighter STEM regions correspond to $Ni_{78}Mo_{22}$ domains, while darker areas exhibit $Ni_{68}Mo_{32}$ stoichiometry - a 10% compositional difference statistically confirmed by EDX mapping (**Fig 6. 9c and Fig 6. 14**). Atomic-scale characterization reveals that the PED-fabricated NiMo hydrangea structures form an amorphous chemical heterostructure, featuring numerous interfaces between compositionally distinct domains ($Ni_{78}Mo_{22}$ and $Ni_{68}Mo_{32}$). These interfaces are believed to offer abundant highly active sites for catalytic reactions.

6.3.4 Excellent bi-functional performance with HER and OER of NiMo@Zr MGHCs

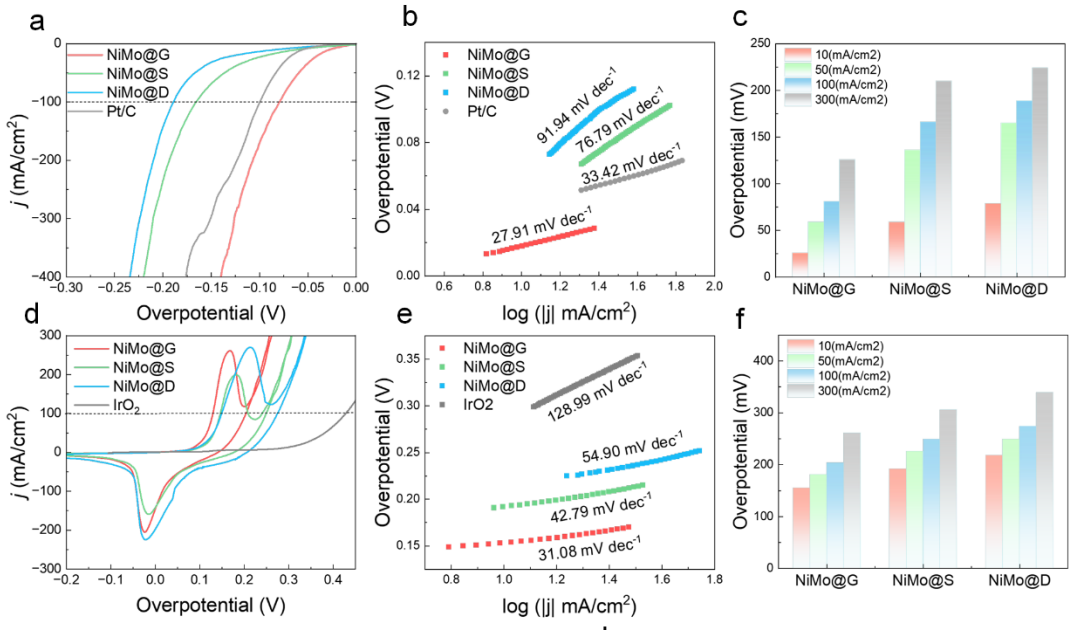

Fig 6. 15 HER and OER performance of the NiMo@Zr MGHCs. (a) HER polarization curves and (b) corresponding Tafel plots of NiMo@Zr MGHCs. (c) Overpotentials at 10, 50, 100, and 300 mA cm^{-2} for HER (d) OER polarization curves of different NiMo@Zr MGHCs. (e) Tafel plots of NiMo@Zr MGHCs for OER. (f) Overpotentials at 10, 50, 100, and 300 mA cm^{-2} for OER. (g) PDOS for the Ni and Mo active sites in different NiMo MGs ($Ni_{78}Mo_{22}$, interface, and $Ni_{68}Mo_{32}$).

We further evaluated the electrocatalytic performance of the NiMo@Zr MGHCs for water electrolysis in 1 M KOH, as shown in **Fig 6. 15**. NiMo@G (**Fig 6. 15a**) exhibits a remarkably low HER overpotential of 26 mV at 10 mA cm^{-2}, significantly outperforming NiMo@S (59 mV), NiMo@D (81 mV), and commercial Pt/C (55 mV). Tafel analysis (**Fig 6. 15b**) reveals NiMo@G's exceptional HER kinetics with a record-low 27.91 mV dec^{-1} slope, outperforming NiMo@S (76.79 mV dec^{-1}), NiMo@D (91.94 mV dec^{-1}), and commercial Pt/C (76.79 mV dec^{-1}) by 2.7-3.3 times, demonstrating its superior charge transfer efficiency. NiMo@G exhibits outstanding HER performance at industrially relevant current densities (**Fig 6. 15c**), requiring only 79 mV and 126 mV of overpotential to achieve 100 and 300 mA cm^{-2}, respectively. This performance surpasses that of NiMo@S (165/210 mV) and NiMo@D (189/224 mV) by 53–98 mV. This superior activity under high-current conditions highlights its strong potential for practical water-splitting applications. The OER remains the primary bottleneck in water splitting due to its sluggish kinetics and high overpotential, necessitating high-performance electrodes for efficient operation. Therefore, we further assessed the OER performance of the NiMo@G, as shown in **Fig 6. 15d**. All samples display a prominent oxidation peak during the OER process, attributed to the oxidation of Ni, which promotes OER activity. This indicates that the NiMo@Zr MGHCs possess excellent electrocatalytic performance. To accurately evaluate the overpotential and minimize the influence of the oxidation peak, cyclic voltammetry was employed. NiMo@G demonstrates exceptional OER performance with an ultralow overpotential of 155 mV at 10 mA cm^{-2}, significantly outperforming NiMo@S (181 mV), NiMo@D (204 mV)

and commercial IrO_2 (**Fig 6. 15d**). Tafel analysis (**Fig 6. 15e**) reveals NiMo@G's superior OER kinetics with a record-low Tafel slope of 31.08 mV dec^{-1}, outperforming NiMo@S (42.79 mV dec^{-1}), NiMo@D (54.90 mV dec^{-1}), and IrO_2 (128.99 mV dec^{-1}), demonstrating significantly faster reaction rates. **Fig 6. 15f** presents the overpotentials at various current densities (10, 50, 100, and 300 mA cm^{-2}). Notably, NiMo@G consistently delivers the lowest overpotentials across all current densities, especially in industrial-grade currents. For example, NiMo@G demonstrates superior performance with significantly lower overpotentials (204 mV @ 100 mA cm^{-2}; 261 mV @ 300 mA cm^{-2}) compared to NiMo@S (249 mV; 306 mV) and NiMo@D (274 mV; 339 mV), representing a 18-23 % reduction in overpotential across industrial-relevant current densities

6.4 Discussion

6.4.1 Evaluation of the overall water splitting performance of NiMo@Zr MGHCs

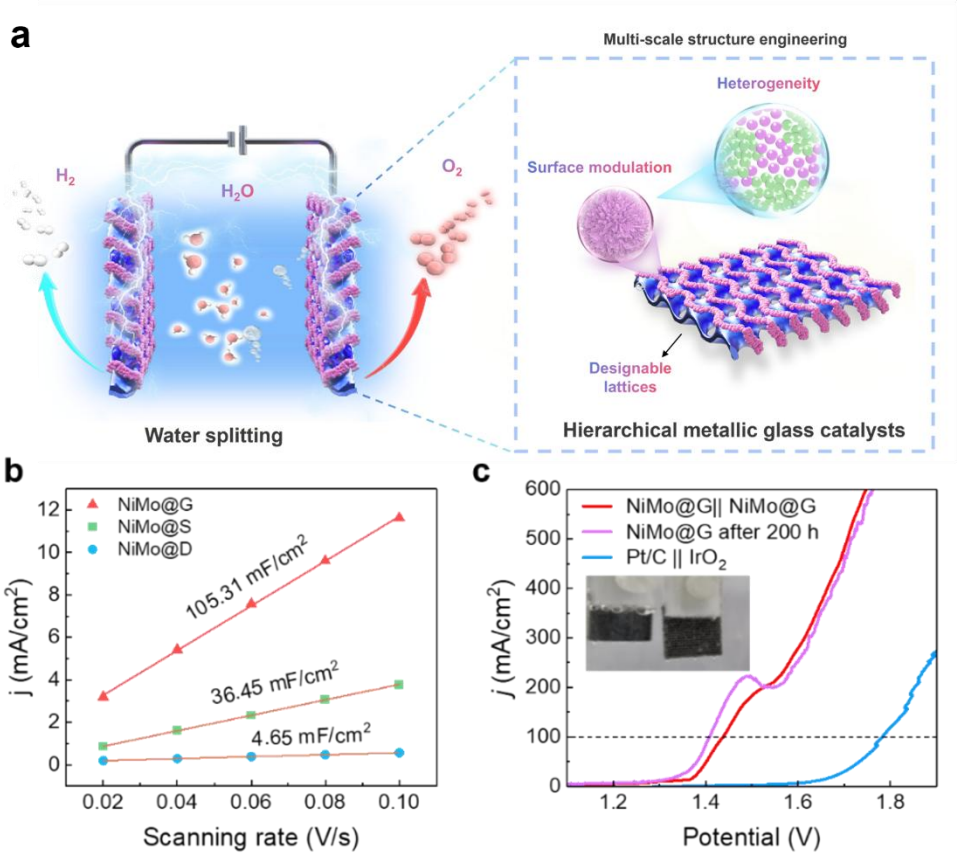

Fig 6. 16 Overall water splitting performance of NiMo@G. (a) Schematic illustration of overall water splitting using NiMo@G as the double electrode. (b) The Cdl values of NiMo@Zr MGHCs. (c) Overall water splitting polarization curves before and after a 200-h stability test, demonstrating performance retention.

The NiMo@G hierarchical catalysts demonstrate exceptional HER and OER performance, rendering them highly suitable for overall water-splitting applications. A dual-electrode electrolyzer was assembled using NiMo@G as both the anode and cathode (**Fig 6. 16a**). The electrochemically active surface area (ECSA) was evaluated by extracting the double-layer capacitance (C_{dl}) from the cyclic voltammetry (CV)

curves in the non-Faradaic region (**Fig 6. 16b**). NiMo@S, with a C_{dl} of 36.45 mF cm^{-2}, exposes more active sites than NiMo@D (C_{dl} = 4.65 mF cm^{-2}), leading to higher catalytic activity. Remarkably, NiMo@G exhibits the highest active site density, with a C_{dl} of 105.31 mF cm^{-2}, which correlates with its outstanding catalytic performance. The polarization curves (**Fig 6. 16c**) reveal that this system achieves current densities of 100 and 500 mA cm^{-2} at ultra-low cell voltages of 1.438 V and 1.707 V, respectively—significantly lower than that of the benchmark IrO_2//Pt/C system (1.783 V @ 100 mA cm^{-2}).

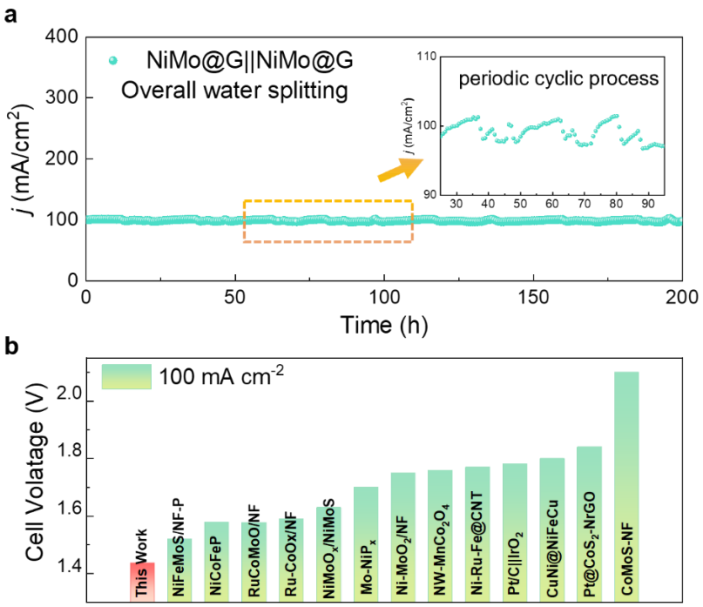

Fig 6. 17 Chronopotentiostatic stability and catalytic performance comparison.(a) Chronopotentiostatic stability test at 100 mA cm^{-2}, showing minimal voltage fluctuation over 200 hours of continuous operation. (b) Comparison of cell voltages at 100 mA cm^{-2}, benchmarking NiMo@G against state-of-the-art catalysts reported in literature (Data in Table 6.2).

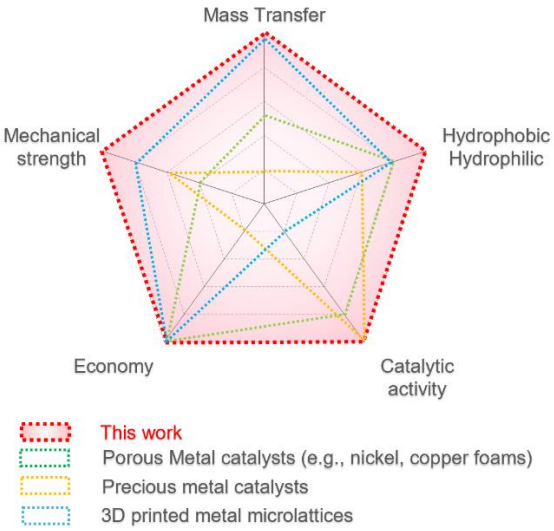

Fig 6. 18 The radar chart comparing the properties of the different types of electrolytes.(more details presented in Supplementary Table 6.3).

Table 6. 2 Comparison of the overpotentials of NiMo@G catalyst and recently reported noble metal catalyst for overall water splitting at 100 mA cm-2 in 1.0 M KOH solution.

Electrocatalysts	Current density (mA cm^{-2})	Cell Voltage (V)	References
NiMo@G	100	1.438	This work
NiFeMoS/NF-P	100	1.52	[263]
Ni-Co-Fe-P NBs	100	1.58	[264]
a/c-RuCoMoyOx/NF	100	1.578	[251]
Ru-CoOx/NF	100	1.59	[265]
$NiMoO_x$/NiMoS	100	1.63	[266]
Mo-NiPx/NiSy	100	1.7	[267]
Ni-MoO2/NF-IH	100	1.75	[268]
NW-MnCo2O4/GDY	100	1.76	[269]
Ni-Ru-Fe@CNT	100	1.77	[270]
Pt/C//IrO2	100	1.783	This work
CuNi@NiFeCu	100	1.8	[271]
Pt@CoS_2-NrGO	100	1.84	[272]
CoMoS-NF-31	100	2.1	[273]

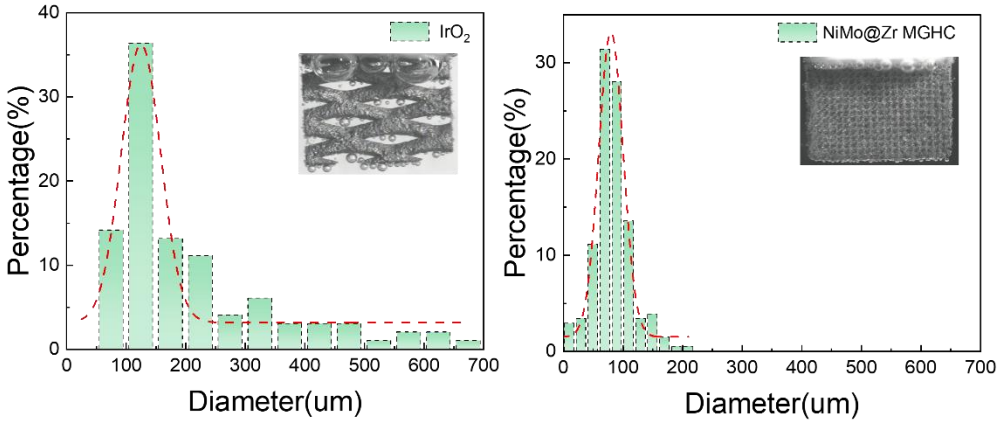

Fig 6. 19 Bubble size distribution of the IrO2 electrode and NiMo@G electrode.

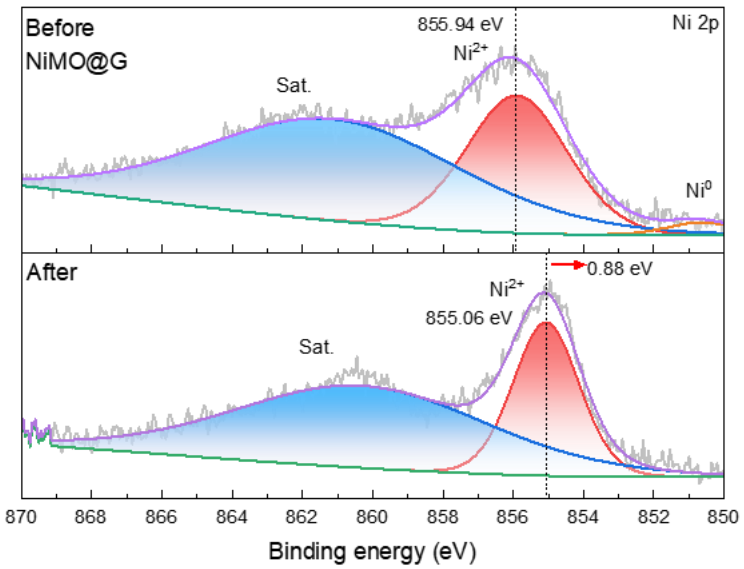

Fig 6. 20 XPS survey spectra of NiMo@G before and after the stability test.

High-speed imaging of bubble dynamics at 100 mA cm^{-2} clearly demonstrates the operational advantages of this design (**Fig 6. 19**): while the bubble-release behaviors of conventional porous IrO2 electrodes suffer from persistent bubble adhesion and coalescence into large (> 500 μm) gas pockets that block active sites, the NiMo@G catalyst enables rapid release of small (~ 70 μm) bubbles. Stability testing via

chronopotentiometry (**Fig 6. 17a**) confirms the excellent durability of NiMo@G, with negligible current density loss over 200 hours of continuous operation at 1.438 V. Interestingly, the overall water splitting performance slightly improved after the 200-hour test, as shown by the enhanced polarization curve (pink line in **Fig 6. 16c**). XPS analysis reveals that, after extended stability testing, the Ni^{2+} binding energy decreases by 0.88 eV, which may contribute to the observed enhancement in catalytic performance (**Fig 6. 20**). Furthermore, during the initial operation, the NiMo@G//NiMo@G configuration demonstrated one of the lowest cell voltages among reported catalysts at high current densities (1.438 V @ 100 mA cm^{-2}; **Fig 6. 17b**). This work highlights the synergistic combination of 3D printing technology, which enables precise geometric control, flexible design capabilities, and tunable mechanical/mass transfer properties, with PED that addresses the limitations in microstructural control. Compared to conventional porous metal catalysts, precious metal catalysts, and metal microlattices, the NiMo@G hierarchical catalysts fabricated through this integrated 3D printing-PED approach uniquely combine the multiple advantages of structural strength, super hydrophobic and superhydrophilicity, low economic costs and extraordinary catalytic activity (**Fig 6. 18**), establishing a new paradigm for designing high-performance electrocatalytic system.

Table 6. 3 Comparison of the overpotentials of NiMo@G catalyst and recently reported noble metal catalyst for overall water splitting at 100 mA cm-2 in 1.0 M KOH solution.

Types	Materials	Mass Transfer	Hydrophilic/ Hydrophobic	Mechanical strength	Economics cost	Catalytic performance	References
Non-porous precious metal catalysts	Pt-Ni_2Fe_1-T	√	√√√	√√√	√	√√√√√	[274]
Porous Metal catalysts	NiFe-MOF	√	√√√√	√	√√√√√	√√√√	[275]
	Cu2O/Cu	√	√√√√	√√√	√√√√√	√√√√	[276]
	N-(Co-Cu)Sx	√	√√√√	√√	√√√√√	√√√√	[277]
3D printed metal microlattices	316 L	√√√√√	√√√√	√√√√	√√√√√	√	[278]
This work	*NiMo@G*	√√√√√	√√√√√	√√√√√	√√√√√	√√√√√	

6.5 Conclusions

In summary, this work presents a comprehensive strategy for designing high-performance electrocatalysts through multiscale structural engineering. By integrating 3D-printed Zr-based MG substrates with precisely controlled TPMS geometries and subsequent PED of NiMo amorphous particles, we achieve simultaneous optimization of catalytic activity, mechanical robustness, and mass transport properties of NiMo@Zr MGHCs. In the macro architecture scale, the Gyroid (G-Zr MG) architecture emerges as the optimal substrate, combining efficient mass transfer with exceptional compressive strength (>300 MPa) and enhanced transverse flow characteristics. In the micro-scale, hydrangea-shaped NiMo particles (60–100 μm) were fabricated on the

substrates via a controlled PED process, exhibiting combined superhydrophilic and superaerophobic properties. This NiMo@Zr MGHCs catalyst fabricated through multiscale structure engineering demonstrates exceptional overall water-splitting performance, in which NiMo@G requires only 1.438 V to achieve 100 mA cm^{-2} in a 1.0 M KOH solution while maintaining stable operation for 200 hours. This study establishes a new paradigm in electrocatalyst design, demonstrating how multiscale architectural control from macroscale substrates to atomic-scale compositional engineering can overcome traditional performance trade-offs in electrochemical energy conversion systems.

Chapter 7 Overall conclusions

In this project, we additively manufactured a series of MG lattices through the different L-PBF approaches. Structure–mechanical property relationship has been established for MGs, a novel class of materials, which can serve as a foundation for the future design of MG lattice structures. Through the implementation of diverse lattice architectures, outstanding mechanical performance has been achieved, characterized by high strength and exceptional energy absorption capacity. Building on this, the functional properties of MG lattices were further investigated, with a particular focus on catalytic performance. A multiscale structural design strategy, integrated with AM and PED techniques, was employed to develop catalysts with outstanding bifunctional water-splitting performance. Owing to the limited prior research on MG lattices, this study systematically investigates their characteristics, encompassing parameter optimization, fabrication using different L-PBF systems, and the tailoring of mechanical and functional properties. The findings provide significant insights and strong support for their potential applications. The main conclusions are as follows:

1) BMG lattices with BCC and TPMS architectures were fabricated using the conventional L-PBF method, and three distinct deformation stages were identified: elastic deformation, abrupt collapse, and progressive localized fracture. Based on these observations, BCT lattices were subsequently designed by modifying the unit cell geometry to promote localized cracking and enhance damage tolerance. Compression tests confirmed that this strategy

markedly improved performance, with energy absorption increasing by nearly 8.5 times and compressive strength by approximately 2.5 times compared to the original BCC design. These results highlight the effectiveness of this design approach in mitigating brittle failure and advancing the application potential of BMG lattice structures for high-strength, energy-absorbing systems

2) BMG lattices with four bioinspired TPMS architectures were successfully fabricated using the μL-PBF technique, achieving high precision, excellent quality, and outstanding mechanical performance. The enhanced energy absorption was attributed to controlled fracture modes that prevented catastrophic failure and induced macroscopic plasticity. In-situ X-ray CT combined with DVC analysis revealed that the location and mode of the initial fracture play a critical role in determining damage tolerance. Among the designs, IWP-type lattices exhibited uniform stress distribution and progressive layer-by-layer collapse, while D-type structures demonstrated high energy absorption due to the formation of extensive damage bands. Fractographic analysis indicated a multiscale ductilization mechanism, in which localized fractures generated complex stress fields that promoted shear band formation at both micro- and nano-scales. This synergistic interaction enhanced toughness and plasticity in otherwise brittle MGs. Overall, these findings demonstrate a promising strategy for achieving high strength and superior energy absorption in MG lattices through bioinspired structural

design, positioning them as strong candidates for next-generation energy-absorbing materials in engineering applications.

3) A multi-scale structural engineering strategy was proposed to design high-performance hierarchical MG electrocatalysts. By combining 3D-printed Zr-based MG TPMS architectures with electrodeposited hydrangea-like NiMo amorphous particles, the resulting NiMo@Zr MGHCs catalysts exhibit optimized catalytic activity, mechanical strength, and mass transport properties. Among the macro-architectures, the Gyroid structure offers the best performance, featuring efficient mass transfer, superior compressive strength (>300 MPa), and enhanced transverse flow. At the microscale, the engineered NiMo particles (60–100 μm) provide superhydrophilic and superaerophobic properties. As a result, the NiMo@G catalyst achieves outstanding water-splitting performance, requiring only 1.438 V to reach 100 mA cm^{-2} in 1.0 M KOH and demonstrating long-term operational stability (200 hours). This work establishes a new design paradigm by leveraging hierarchical structural control to break conventional trade-offs in electrocatalyst performance.

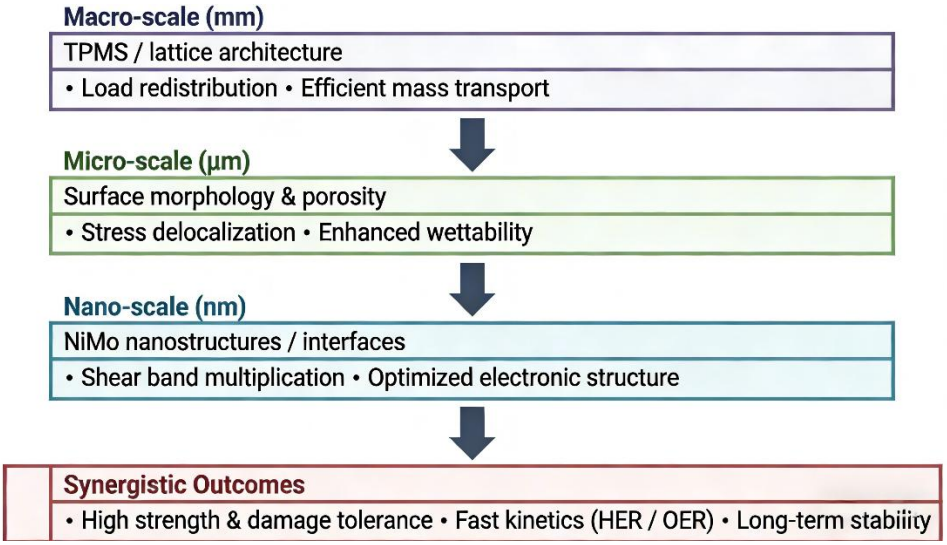

Fig 7. 1 Macro-micro-nano scale structural features and their synergistic effects on strength, kinetics and stability.

Overall, this work demonstrates that multiscale structural engineering is an effective and universal strategy for unlocking the full potential of metallic glass lattices (**Fig 7. 1**). By deliberately coupling architectural design at the macro-scale, deformation and surface engineering at the micro-scale, and interfacial and compositional control at the nano-scale, a strong structure–mechanism–function synergy is established. This synergy enables the simultaneous optimization of mechanical robustness, mass transport efficiency, and catalytic activity, which are traditionally considered competing properties. The insights gained from this study not only deepen the fundamental understanding of deformation and functional mechanisms in metallic glass lattices, but also provide a clear design framework for developing next-generation multifunctional metamaterials for structural and energy-related applications.

Chapter 8 Suggested future work

8.1 Break the strength-ductility tradeoff through metamaterial structure design.

Traditional MG materials struggle to overcome the strength–ductility trade-off. Metamaterial structural design offers a novel pathway to enhance ductility while maintaining high strength in cellular MG materials. Therefore, future work should explore metamaterial architectures tailored to the unique properties of metallic glasses, aiming to further mitigate their intrinsic brittleness through structural design. Pursuing excellent mechanical performance for potential MG applications, such as implants and impact-resistant components. Metallic implants are widely used biomaterials in orthopedics. They can be applied in both bone fixation and joint arthroplasty. Their mechanical properties, biocompatibility, and corrosion resistance make them extensively used in orthopedic applications. However, conventional medical metals such as Co-based and Ti-based alloys still exhibit certain limitations when used as implants, such as poor mechanical compatibility (i.e., high elastic modulus) and relatively low corrosion resistance. The unique properties of BMGs offer promising solutions to these challenges. Additionally, 3D-printed porous bone implants can fully reconstruct the structure of human bone and allow for customized designs tailored to specific clinical needs, thereby meeting patient-specific requirements. In this study, we conducted an investigation into the static compressive performance of MG lattice structures and obtained promising results. In the next phase of our research, we will

further explore their dynamic impact resistance to provide more comprehensive data support for practical applications.

8.2 Design, additive manufacture, and evaluation of mechanical strength, catalytic activity, and mass transport performance in MG metamaterials.

In this study, we demonstrate that mechanical properties, catalytic performance, and mass transport can be synergistically tuned through targeted metamaterial design strategies. Building on these findings, our next stage of work will focus on the precise design and fabrication of hierarchical structures across multiple length scales, achieved through structural engineering in combination with advanced fabrication techniques. This integrated design approach aims to develop MG metamaterials for multifunctional applications, enabling the simultaneous optimization of mechanical strength alongside catalytic activity, heat transfer, electrical conductivity, and mass transport performance.

References

[1] V.S. Deshpande, M. Ashby, N. Fleck, Acta Materialia. 2001, 1035-104049, 10.1016/S1359-6454(00)00379-7.

[2] Q. Ma, L. Zhang, J. Ding, S. Qu, J. Fu, M. Wang Fu, X. Song, M. Yu Wang, Mater Design. 2023, 111995230, https://doi.org/10.1016/j.matdes.2023.111995.

[3] X. Li, X. Yu, W. Zhai, Adv Mater. 2021, 210455233(44), https://doi.org/10.1002/adma.202104552.

[4] R.A. Shelby, D.R. Smith, S. Schultz, Science. 2001, 77-79292(5514), doi:10.1126/science.1058847.

[5] A. Mirabolghasemi, A.H. Akbarzadeh, D. Rodrigue, D. Therriault, Acta Materialia. 2019, 61-80174, https://doi.org/10.1016/j.actamat.2019.04.061.

[6] V. Egorov, U. Gulzar, Y. Zhang, S. Breen, C. O'Dwyer, Adv Mater. 2020, 200055632(29), https://doi.org/10.1002/adma.202000556.

[7] J.A. Jackson, M.C. Messner, N.A. Dudukovic, W.L. Smith, L. Bekker, B. Moran, A.M. Golobic, A.J. Pascall, E.B. Duoss, K.J. Loh, C.M. Spadaccini, Sci Adv. 2018, eaau64194(12), 10.1126/sciadv.aau6419.

[8] W. Klement, R.H. Willens, P.O.L. Duwez, Nature. 1960, 869-870187(4740), 10.1038/187869b0.

[9] H.S. Chen, Acta Metallurgica. 1974, 1505-151122(12), https://doi.org/10.1016/0001-6160(74)90112-6.

[10] H.W. Kui, A.L. Greer, D. Turnbull, Appl Phys Lett. 1984, 615-61645(6), 10.1063/1.95330.

[11] A. Inoue, N. Nishiyama, H. Kimura, Materials Transactions, JIM. 1997, 179-18338(2), 10.2320/matertrans1989.38.179.

[12] J. Schroers, B. Lohwongwatana, W.L. Johnson, A. Peker, Appl Phys Lett. 2005, 06191287(6), 10.1063/1.2008374.

[13] P. Jia, H. Guo, Y. Li, J. Xu, E. Ma, Scripta Materialia. 2006, 2165-216854(12), https://doi.org/10.1016/j.scriptamat.2006.02.042.

[14] A. Inoue, T. Zhang, Materials Transactions, JIM. 1996, 185-18737(2), 10.2320/matertrans1989.37.185.

[15] A. Inoue, A. Kato, T. Zhang, S.G. Kim, T. Masumoto, Materials Transactions, JIM. 1991, 609-61632(7), 10.2320/matertrans1989.32.609.

[16] B.A. Sun, M.X. Pan, D.Q. Zhao, W.H. Wang, X.K. Xi, M.T. Sandor, Y. Wu, Scripta Materialia. 2008, 1159-116259(10), https://doi.org/10.1016/j.scriptamat.2008.08.003.

[17] J. Shen, Q.J. Chen, J.F. Sun, H.B. Fan, G. Wang, Exceptionally High Glass-Forming Ability of an FeCoCrMoCBY Alloy, in: Q. Chen (Ed.), Fe-Based Amorphous Alloys with High Glass Forming Ability, Springer Nature Singapore, Singapore, 2025, pp. 43-49.

[18] T. Zhang, Q. Yang, Y. Ji, R. Li, S. Pang, J. Wang, T. Xu, Chinese Science Bulletin. 2011, 3972-397756(36), 10.1007/s11434-011-4765-8.

[19] Y.H. Liu, G. Wang, M.X. Pan, P. Yu, D.Q. Zhao, W.H. Wang, Journal of Materials Research. 2007, 869-87522(4), 10.1557/jmr.2007.0104.

[20] B. Zhang, D.Q. Zhao, M.X. Pan, R.J. Wang, W.H. Wang, Acta Materialia. 2006, 3025-303254(11), https://doi.org/10.1016/j.actamat.2006.02.044.

[21] D.V. Louzguine-Luzgin, A. Inoue, Bulk Metallic Glasses, Encyclopedia of Glass Science, Technology, History, and Culture2021, pp. 919-936.
[22] N. Nishiyama, K. Takenaka, H. Miura, N. Saidoh, Y. Zeng, A. Inoue, Intermetallics. 2012, 19-2430, https://doi.org/10.1016/j.intermet.2012.03.020.
[23] J. Schroers, JOM. 2005, 35-3957(5), 10.1007/s11837-005-0093-2.
[24] J. Schroers, Adv Mater. 2010, 1566-159722(14), https://doi.org/10.1002/adma.200902776.
[25] G. Kumar, H.X. Tang, J. Schroers, Nature. 2009, 868-72457(7231), 10.1038/nature07718.
[26] A. Inoue, B.L. Shen, H. Koshiba, H. Kato, A.R. Yavari, Acta Materialia. 2004, 1631-163752(6), https://doi.org/10.1016/j.actamat.2003.12.008.
[27] J. Wang, R. Li, N. Hua, T. Zhang, Journal of Materials Research. 2011, 2072-207926(16), 10.1557/jmr.2011.187.
[28] M.D. Demetriou, M.E. Launey, G. Garrett, J.P. Schramm, D.C. Hofmann, W.L. Johnson, R.O. Ritchie, Nat Mater. 2011, 123-12810(2), 10.1038/nmat2930.
[29] M. Telford, Mater Today. 2004, 36-437(3), https://doi.org/10.1016/S1369-7021(04)00124-5.
[30] A. Inoue, Progress in Materials Science. 1998, 365-52043(5), https://doi.org/10.1016/S0079-6425(98)00005-X.
[31] H. Ding, L. Liu, L. Shao, J. Zhou, D. Zuo, H. Ke, W. Wang, Acta Physica Sinica. 2025, 74, 10.7498/aps.74.20250585.
[32] L. Shao, R. Bai, Y. Wu, J. Zhou, X. Tong, H. Peng, T. Liang, Z. Li, Q. Zeng, B. Zhang, H. Ke, W. Wang, Materials Futures. 2024, 0253013(2), 10.1088/2752-5724/ad2ae8.
[33] W. Lu, M. He, D. Yu, X. Xie, H. Wang, S. Wang, C. Yuan, A. Chen, Mater Design. 2021, 110027210, https://doi.org/10.1016/j.matdes.2021.110027.
[34] M. Stiehler, K. Georgarakis, IEEE Transactions on Plasma Science. 2024, 1-6PP, 10.1109/TPS.2024.3459809.
[35] Y. Zhang, A. Greer, Appl Phys Lett. 2006, 07190789(7),
[36] J.J. Lewandowski, A.L. Greer, Nat Mater. 2006, 15-185(1), 10.1038/nmat1536.
[37] X. Du, J. Huang, K. Hsieh, Y. Lai, H.-M. Chen, S.C. Jang, P. Liaw, Appl Phys Lett. 2007, 131901-13190191, 10.1063/1.2790380.
[38] Y.H. Liu, G. Wang, R.J. Wang, D.Q. Zhao, M.X. Pan, W.H. Wang, Science. 2007, 1385-8315(5817), 10.1126/science.1136726.
[39] H. Choi-Yim, J. Schroers, W. Johnson, Appl Phys Lett. 2002, 80, 10.1063/1.1459766.
[40] L. Liu, K.C. Chan, M. Sun, Q. Chen, Materials Science and Engineering: A. 2007, 697-706445-446, https://doi.org/10.1016/j.msea.2006.10.004.
[41] S. Pauly, L. Löber, R. Petters, M. Stoica, S. Scudino, U. Kühn, J. Eckert, Mater Today. 2013, 37-4116(1), https://doi.org/10.1016/j.mattod.2013.01.018.
[42] B. Zheng, Y. Zhou, J.E. Smugeresky, E.J. Lavernia, Metallurgical and Materials Transactions A. 2009, 1235-124540(5), 10.1007/s11661-009-9828-y.
[43] G. Yang, X. Lin, F. Liu, Q. Hu, L. Ma, J. Li, W. Huang, Intermetallics. 2012, 110-11522, https://doi.org/10.1016/j.intermet.2011.10.008.
[44] Y. Zhang, X. Lin, L. Wang, L. Wei, F. Liu, W. Huang, Intermetallics. 2015, 22-3066, https://doi.org/10.1016/j.intermet.2015.06.007.
[45] X. Lin, Y. Zhang, G. Yang, X. Gao, Q. Hu, J. Yu, L. Wei, W. Huang, Journal of Materials

Science & Technology. 2019, 328-33535(2), https://doi.org/10.1016/j.jmst.2018.10.033.
[46] S. Katakam, J.Y. Hwang, S. Paital, R. Banerjee, H. Vora, N.B. Dahotre, Metallurgical and Materials Transactions A. 2012, 4957-496643(13), 10.1007/s11661-012-1312-4.
[47] Y. Lu, Y. Huang, J. Wu, X. Lu, Z. Qin, D. Daisenberger, Y.-L. Chiu, Intermetallics. 2018, 67-71103, https://doi.org/10.1016/j.intermet.2018.10.005.
[48] C. Zhang, W. Wang, Y.-C. Li, Y.-G. Yang, Y. Wu, L. Liu, Journal of Materials Chemistry A. 2018, 6800-68056(16), 10.1039/C8TA00405F.
[49] M.A. Gibson, N.M. Mykulowycz, J. Shim, R. Fontana, P. Schmitt, A. Roberts, J. Ketkaew, L. Shao, W. Chen, P. Bordeenithikasem, J.S. Myerberg, R. Fulop, M.D. Verminski, E.M. Sachs, Y.-M. Chiang, C.A. Schuh, A. John Hart, J. Schroers, Mater Today. 2018, 697-70221(7), https://doi.org/10.1016/j.mattod.2018.07.001.
[50] N. Gorodesky, S. Sedghani-Cohen, M. Altman, O. Fogel, G. Cohen-Taguri, Y. Fleger, Z. Kotler, Z. Zalevsky, Advanced Functional Materials. 2020, 200126030(25), https://doi.org/10.1002/adfm.202001260.
[51] Y. Shen, Y. Li, C. Chen, H.-L. Tsai, Mater Design. 2017, 213-222117, https://doi.org/10.1016/j.matdes.2016.12.087.
[52] E. Duoss, LDRD Annual Report FY2017. 2017,
[53] C. Yang, C. Zhang, Z.J. Chen, Y. Li, W.Y. Yan, H.B. Yu, L. Liu, ACS Appl Mater Interfaces. 2021, 7227-723713(6), 10.1021/acsami.0c20832.
[54] D. OUYANG, C. ZHANG, L. LIU, SCIENTIA SINICA Physica, Mechanica & Astronomica. 2025, 28611255(8), https://doi.org/10.1360/SSPMA-2024-0413.
[55] Y. Li, Y. Shen, C. Chen, M.C. Leu, H.-L. Tsai, J Mater Process Tech. 2017, 249-261248, https://doi.org/10.1016/j.jmatprotec.2017.05.032.
[56] A. Simchi, H. Pohl, Materials Science and Engineering: A. 2003, 119-128359(1), https://doi.org/10.1016/S0921-5093(03)00341-1.
[57] C. Zhang, D. Ouyang, S. Pauly, L. Liu, Mat Sci Eng R. 2021, 145, https://doi.org/10.1016/j.mser.2021.100625.
[58] D. Ouyang, N. Li, W. Xing, J. Zhang, L. Liu, Intermetallics. 2017, 128-13490, https://doi.org/10.1016/j.intermet.2017.07.010.
[59] W. Xing, D. Ouyang, Z. Chen, L. Liu, Science China Physics, Mechanics & Astronomy. 2019, 22611163(2), 10.1007/s11433-019-1485-8.
[60] X.P. Li, C.W. Kang, H. Huang, L.C. Zhang, T.B. Sercombe, Materials Science and Engineering: A. 2014, 370-379606, https://doi.org/10.1016/j.msea.2014.03.097.
[61] W. Xing, D. Ouyang, N. Li, L. Liu, Materials. 2018, 148011(8),
[62] W. Xing, D. Ouyang, N. Li, L. Liu, Intermetallics. 2018, 101-106103, https://doi.org/10.1016/j.intermet.2018.10.011.
[63] J.P. Best, H.E. Ostergaard, B. Li, M. Stolpe, F. Yang, K. Nomoto, M.T. Hasib, O. Murá nsky, R. Busch, X. Li, J.J. Kruzic, Additive Manufacturing. 2020, 10141636, https://doi.org/10.1016/j.addma.2020.101416.
[64] P. Zhang, Z. Cheng, L. and Liu, Materials Research Letters. 2022, 377-38410(6), 10.1080/21663831.2022.2054291.
[65] X.P. Li, M.P. Roberts, S. O'Keeffe, T.B. Sercombe, Mater Design. 2016, 217-226112, https://doi.org/10.1016/j.matdes.2016.09.071.

[66] S. Pauly, C. Schricker, S. Scudino, L. Deng, U. Kühn, Mater Design. 2017, 133-141135, https://doi.org/10.1016/j.matdes.2017.08.070.
[67] L. Deng, A. Gebert, L. Zhang, H.Y. Chen, D.D. Gu, U. Kühn, M. Zimmermann, K. Kosiba, S. Pauly, Mater Design. 2020, 108532189, https://doi.org/10.1016/j.matdes.2020.108532.
[68] B. Liu, P. Zhang, Z. Liu, D. Wu, Q. Jiang, T. Sun, C. Liu, H. Yan, H. Shi, S. Ma, R. Li, Journal of Manufacturing Processes. 2024, 506-516120, https://doi.org/10.1016/j.jmapro.2024.04.064.
[69] P. Zhang, D. Ouyang, L. Liu, J Alloy Compd. 2019, 476-483803, https://doi.org/10.1016/j.jallcom.2019.06.303.
[70] P. Zhang, C. Zhang, D. Ouyang, L. Liu, Scripta Materialia. 2021, 7-12192, https://doi.org/10.1016/j.scriptamat.2020.09.044.
[71] P. Zhang, C. Zhang, J. Pan, D. Ouyang, L. Liu, Journal of Materials Science & Technology. 2024, 95-102170, https://doi.org/10.1016/j.jmst.2023.06.031.
[72] C. Zhang, X.-m. Li, S.-Q. Liu, H. Liu, L.-J. Yu, L. Liu, J Alloy Compd. 2019, 963-973790, https://doi.org/10.1016/j.jallcom.2019.03.275.
[73] B. Li, V. Yakubov, K. Nomoto, S.P. Ringer, B. Gludovatz, X. Li, J.J. Kruzic, Acta Materialia. 2024, 119685266, https://doi.org/10.1016/j.actamat.2024.119685.
[74] L. Deng, S. Wang, P. Wang, U. Kühn, S. Pauly, Materials Letters. 2018, 346-349212, https://doi.org/10.1016/j.matlet.2017.10.130.
[75] X. Lu, M. Nursulton, Y. Du, W. Liao, Journal. 2019, 12(Issue), 10.3390/ma12050775.
[76] L. Deng, L. Zhang, K. Kosiba, R. Limbach, L. Wondraczek, G. Wang, D. Gu, U. Kühn, S. Pauly, Journal of Materials Science & Technology. 2021, 139-15081, https://doi.org/10.1016/j.jmst.2021.01.008.
[77] C. Chen, S. Li, C. Ling, Y. Yang, C. Gao, Y. Li, X. Xiao, W. Zhou, C. Shuai, Journal of Materials Research and Technology. 2023, 6961-697327, https://doi.org/10.1016/j.jmrt.2023.11.095.
[78] N. Sohrabi, J. Jhabvala, G. Kurtuldu, R. Frison, A. Parrilli, M. Stoica, A. Neels, J.F. Löffler, R.E. Log é , Applied Materials Today. 2021, 10108024, https://doi.org/10.1016/j.apmt.2021.101080.
[79] N. Li, J. Zhang, W. Xing, D. Ouyang, L. Liu, Mater Design. 2018, 285-296143, https://doi.org/10.1016/j.matdes.2018.01.061.
[80] S. Maietta, A. Gloria, G. Improta, M. Richetta, R. De Santis, M. Martorelli, Journal of Healthcare Engineering. 2019, 32125942019(1), https://doi.org/10.1155/2019/3212594.
[81] S.L. Sing, F.E. Wiria, W.Y. Yeong, Robotics and Computer-Integrated Manufacturing. 2018, 170-18049, https://doi.org/10.1016/j.rcim.2017.06.006.
[82] B.K. Nagesha, V. Dhinakaran, M. Varsha Shree, K.P. Manoj Kumar, D. Chalawadi, T. Sathish, Materials Today: Proceedings. 2020, 916-91921, https://doi.org/10.1016/j.matpr.2019.08.158.
[83] D. Gu, X. Shi, R. Poprawe, D.L. Bourell, R. Setchi, J. Zhu, Science. 2021, eabg1487372(6545), doi:10.1126/science.abg1487.
[84] T. Maconachie, M. Leary, B. Lozanovski, X. Zhang, M. Qian, O. Faruque, M. Brandt, Mater Design. 2019, 108137183, https://doi.org/10.1016/j.matdes.2019.108137.
[85] I. Quintana-Alonso, N.A. Fleck, Fracture of Brittle Lattice Materials: A Review, in: I.M.

Daniel, E.E. Gdoutos, Y.D.S. Rajapakse (Eds.), Major Accomplishments in Composite Materials and Sandwich Structures, Springer Netherlands, Dordrecht, 2009, pp. 799-816.
[86] S. Xu, J. Shen, S. Zhou, X. Huang, Y.M. Xie, Mater Design. 2016, 443-44793, https://doi.org/10.1016/j.matdes.2016.01.007.
[87] S.J. Park, J.H. Lee, J. Yang, W. Heogh, D. Kang, S.M. Yeon, S.H. Kim, S. Hong, Y. Son, J. Park, Journal of Manufacturing Processes. 2022, 759-76679, https://doi.org/10.1016/j.jmapro.2022.05.022.
[88] J. Bauer, A. Schroer, R. Schwaiger, O. Kraft, Advanced Engineering Materials. 2016, 1537-154318(9), https://doi.org/10.1002/adem.201600235.
[89] Z. Jia, F. Liu, X. Jiang, L. Wang, J Appl Phys. 2020, 150901127(15), 10.1063/5.0004724.
[90] B. Lozanovski, M. Leary, P. Tran, D. Shidid, M. Qian, P. Choong, M. Brandt, Mater Design. 2019, 107671171, https://doi.org/10.1016/j.matdes.2019.107671.
[91] V.S. Deshpande, N.A. Fleck, M.F. Ashby, Journal of the Mechanics and Physics of Solids. 2001, 1747-176949(8), https://doi.org/10.1016/S0022-5096(01)00010-2.
[92] V.S. Deshpande, M.F. Ashby, N.A. Fleck, Acta Materialia. 2001, 1035-104049(6), https://doi.org/10.1016/S1359-6454(00)00379-7.
[93] W.W.S. Ma, H. Yang, Y. Zhao, X. Li, J. Ding, S. Qu, Q. Liu, Z. Hu, R. Li, Q. Tao, H. Mo, W. Zhai, X. Song, Advanced Science. 2025, 240583512(8), https://doi.org/10.1002/advs.202405835.
[94] J. Feng, B. Liu, Z. Lin, J. Fu, Mater Design. 2021, 109595203, https://doi.org/10.1016/j.matdes.2021.109595.
[95] H. Yang, B. Wang, L. Ma, International Journal of Solids and Structures. 2019, 13-29180-181, https://doi.org/10.1016/j.ijsolstr.2019.07.007.
[96] W.P. Moestopo, A.J. Mateos, R.M. Fuller, J.R. Greer, C.M. Portela, Adv Sci (Weinh). 2020, 20012717(20), 10.1002/advs.202001271.
[97] T. Tancogne-Dejean, D. Mohr, Extreme Mechanics Letters. 2018, 13-1822, https://doi.org/10.1016/j.eml.2018.04.005.
[98] L. Wang, G. Ulliac, B. Wang, J.A. Iglesias Martínez, K.K. Dudek, V. Laude, M. Kadic, Advanced Science. 2022, 22047219(34), https://doi.org/10.1002/advs.202204721.
[99] T. Tancogne-Dejean, D. Mohr, International Journal of Solids and Structures. 2018, 24-39138, https://doi.org/10.1016/j.ijsolstr.2017.12.025.
[100] D. Yan, J. Chang, H. Zhang, J. Liu, H. Song, Z. Xue, F. Zhang, Y. Zhang, Nature Communications. 2020, 118011(1), 10.1038/s41467-020-14996-5.
[101] T.S. Lumpe, T. Stankovic, Proceedings of the National Academy of Sciences. 2021, e2003504118118(7), doi:10.1073/pnas.2003504118.
[102] J. Han, X. Zhai, L. Wang, D. Zhang, J. Ding, W.W.S. Ma, X. Song, W.-H. Liao, L. Liu, J. Wu, X.-M. Fu, Mater Design. 2024, 113350247, https://doi.org/10.1016/j.matdes.2024.113350.
[103] J.B. Berger, H.N. Wadley, R.M. McMeeking, Nature. 2017, 533-537543(7646), 10.1038/nature21075.
[104] T. Tancogne-Dejean, M. Diamantopoulou, M.B. Gorji, C. Bonatti, D. Mohr, Adv Mater. 2018, 180333430(45), https://doi.org/10.1002/adma.201803334.
[105] C. Crook, J. Bauer, A. Guell Izard, C. Santos de Oliveira, E.S.J. Martins de Souza, J.B. Berger, L. Valdevit, Nat Commun. 2020, 157911(1), 10.1038/s41467-020-15434-2.

[106] Z. Hashin, S. Shtrikman, Journal of the Mechanics and Physics of Solids. 1963, 127-14011(2), https://doi.org/10.1016/0022-5096(63)90060-7.
[107] P.M. Suquet, Journal of the Mechanics and Physics of Solids. 1993, 981-100241(6), https://doi.org/10.1016/0022-5096(93)90051-G.
[108] C. Gao, J. Shi, H. Tang, H. Tang, Z. Xiao, Y. Bi, Z. Liu, J.H. Rao, Journal of Materials Research and Technology. 2024, 3851-386230, https://doi.org/10.1016/j.jmrt.2024.04.114.
[109] B. Sun, X. Yan, P. Liu, Y. Xia, L. Lu, Additive Manufacturing. 2023, 10362672, https://doi.org/10.1016/j.addma.2023.103626.
[110] X. Chen, P. Yu, H. Ma, P. Zhang, C. Ding, S. Liu, X. Zhang, H. Tan, Acta Materialia. 2024, 120085276, https://doi.org/10.1016/j.actamat.2024.120085.
[111] A. Almesmari, B. Imad, R.K. and Abu Al-Rub, Virtual and Physical Prototyping. 2024, e230851419(1), 10.1080/17452759.2024.2308514.
[112] S. Duan, W. Wen, D. Fang, Acta Materialia. 2020, 397-412199, https://doi.org/10.1016/j.actamat.2020.08.063.
[113] Q. Ma, L. Zhang, J. Ding, S. Qu, J. Fu, M. Zhou, M.W. Fu, X. Song, M.Y. Wang, Additive Manufacturing. 2021, 10229347,
[114] S.C. Han, J.W. Lee, K. Kang, Advanced Materials (Deerfield Beach, Fla.). 2015, 5506-551127(37),
[115] C. Bonatti, D. Mohr, Acta Materialia. 2019, 301-321164,
[116] O. Al-Ketan, R. Rezgui, R. Rowshan, H. Du, N.X. Fang, R.K. Abu Al-Rub, Advanced Engineering Materials. 2018, 180002920(9),
[117] L. Han, S. Che, Adv Mater. 2018, 170570830(17),
[118] C. Bonatti, D. Mohr, Journal of the Mechanics and Physics of Solids. 2019, 1-26122,
[119] Q. Ma, L. Zhang, M.Y. Wang, Mater Design. 2022, 110426215,
[120] Y.C. Jeong, S.C. Han, C.H. Wu, K. Kang, Nature Communications. 2024, 35315(1),
[121] L. Zhang, Q. Ma, J. Ding, S. Qu, J. Fu, M.W. Fu, X. Song, M.Y. Wang, Additive Manufacturing. 2022, 10318559,
[122] B. Deng, G.J. Cheng, Materials Horizons. 2021, 987-9968(3),
[123] Y. Xu, H. Pan, R. Wang, Q. Du, L. Lu, Additive Manufacturing. 2023, 10377977,
[124] P. Liu, B. Sun, J. Liu, L. Lu, Additive Manufacturing. 2022, 10325860,
[125] Z. Zeng, S. Gao, D.K. Pokkalla, S. Zhang, C. Han, F. Liu, Z. Xiao, S.Y. Kandukuri, Y. Liu, K. Zhou, International Journal of Machine Tools and Manufacture. 2024, 104172199,
[126] Z. Dong, X. Zhao, Engineered Regeneration. 2021, 154-1622, https://doi.org/10.1016/j.engreg.2021.09.004.
[127] J. Kadkhodapour, H. Montazerian, S. Raeisi, Materials Science and Engineering: C. 2014, 587-59743, https://doi.org/10.1016/j.msec.2014.07.047.
[128] H.A. Almeida, P.J. Bártolo, Medical Engineering & Physics. 2014, 1033-104036(8), https://doi.org/10.1016/j.medengphy.2014.05.006.
[129] D.-J. Yoo, International Journal of Precision Engineering and Manufacturing. 2014, 1657-166615(8), 10.1007/s12541-014-0516-5.
[130] J. Feng, B. Liu, Z. Lin, J. Fu, Mater Design. 2021, 110050210,
[131] Z. Chen, Y.M. Xie, X. Wu, Z. Wang, Q. Li, S. Zhou, Mater Design. 2019, 108109183,
[132] G.H. Loh, E. Pei, D. Harrison, M.D. Monzón, Additive Manufacturing. 2018, 34-4423,

[133] A. du Plessis, F. Berto, N. Razavi, 2 - Introduction to metal additive manufacturing and unique aspects relating to fatigue, in: F. Berto, A. du Plessis (Eds.), Fatigue in Additive Manufactured Metals, Elsevier2024, pp. 5-22.
[134] Y. Miyamoto, W. Kaysser, B. Rabin, A. Kawasaki, R.G. Ford, Functionally graded materials: design, processing and applications, Springer Science & Business Media2013.
[135] S.Y. Choy, C.-N. Sun, K.F. Leong, J. Wei, Mater Design. 2017, 112-120131,
[136] F. Veloso, J. Gomes-Fonseca, P. Morais, J. Correia-Pinto, A.C. Pinho, J.L. Vilaça, Advanced Engineering Materials. 2022, 220048324(11),
[137] H. Yang, L. Ma, Thin-Walled Structures. 2021, 108373169,
[138] M.F. Ashby, Philosophical Transactions of the Royal Society A: Mathematical, Physical and Engineering Sciences. 2006, 15-30364(1838), doi:10.1098/rsta.2005.1678.
[139] C.R. Calladine, International Journal of Solids and Structures. 1978, 161-17214(2), https://doi.org/10.1016/0020-7683(78)90052-5.
[140] M. Alkhader, M. Vural, International Journal of Engineering Science. 2008, 1035-105146(10), https://doi.org/10.1016/j.ijengsci.2008.03.012.
[141] L.J. Gibson, Mrs Bulletin. 2003, 270-27428(4),
[142] F. Bobbert, K. Lietaert, A.A. Eftekhari, B. Pouran, S. Ahmadi, H. Weinans, A. Zadpoor, Acta biomaterialia. 2017, 572-58453,
[143] A. Du Plessis, I. Yadroitsava, I. Yadroitsev, S. Le Roux, D. Blaine, Virtual and Physical Prototyping. 2018, 266-28113(4),
[144] D. Zhu, S. Hu, G. Zhang, Y. Fu, D. Liu, Journal of Materials Engineering and Performance. 2025, 7149-716134(8), 10.1007/s11665-024-09656-4.
[145] L.E. Murr, Journal of the Mechanical Behavior of Biomedical Materials. 2017, 164-17776, https://doi.org/10.1016/j.jmbbm.2017.02.019.
[146] M.F. Ashby, Metal foams: a design guide, Elsevier2000.
[147] G. Lu, T. Yu, Energy absorption of structures and materials, Elsevier2003.
[148] J. Harris, R. Winter, G.J. McShane, International Journal of Impact Engineering. 2017, 177-191104,
[149] A.S. Phani, Dynamics of lattice materials. 2017, 53-92,
[150] M. Smith, W. Cantwell, Z. Guan, S. Tsopanos, M. Theobald, G. Nurick, G. Langdon, Journal of Sandwich Structures & Materials. 2011, 479-50113(4),
[151] I. Yadroitsava, A. Du Plessis, I. Yadroitsev, Titanium for Consumer Applications. 2019, 197-233,
[152] S. Zhou, I. Usman, Y. Wang, A. Pan, Energy Storage Materials. 2021, 141-15638,
[153] F. Caiazzo, V. Alfieri, B.D. Bujazha, The International Journal of Advanced Manufacturing Technology. 2021, 2909-2923113,
[154] Y. Lv, B. Wang, G. Liu, Y. Tang, E. Lu, K. Xie, C. Lan, J. Liu, Z. Qin, L. Wang, Frontiers in Bioengineering and Biotechnology. 2021, 6411309,
[155] D. Barba, E. Alabort, R. Reed, Acta biomaterialia. 2019, 637-65697,
[156] D. Ali, M. Ozalp, S.B. Blanquer, S. Onel, European Journal of Mechanics-B/Fluids. 2020, 376-38579,
[157] J.M. Kemppainen, S.J. Hollister, Biomaterials. 2010, 279-28731(2),
[158] M. Zhianmanesh, M. Varmazyar, H. Montazerian, ACS Biomaterials Science &

Engineering. 2019, 1228-12375(3),
[159] H. Montazerian, M. Mohamed, M.M. Montazeri, S. Kheiri, A. Milani, K. Kim, M. Hoorfar, Acta biomaterialia. 2019, 149-16096,
[160] S. Ma, Q. Tang, X. Han, Q. Feng, J. Song, R. Setchi, Y. Liu, Y. Liu, A. Goulas, D.S. Engstrøm, Mater Design. 2020, 109034195,
[161] R. Liontas, J.R. Greer, Acta Materialia. 2017, 393-407133, https://doi.org/10.1016/j.actamat.2017.05.019.
[162] C. Yang, C. Zhang, W. Xing, L. Liu, Intermetallics. 2018, 22-2894, https://doi.org/10.1016/j.intermet.2017.12.018.
[163] P. Verma, V. Shah, P. Baldrian, J. Gabriel, P. Stopka, T. Trnka, F. Nerud, Chemosphere. 2004, 291-554(3), 10.1016/j.chemosphere.2003.07.006.
[164] J. Deng, H. Li, S. Wang, D. Ding, M. Chen, C. Liu, Z. Tian, K.S. Novoselov, C. Ma, D. Deng, X. Bao, Nature Communications. 2017, 144308(1), 10.1038/ncomms14430.
[165] M. Chen, Annual Review of Materials Research. 2008, 445-46938(Volume 38, 2008), https://doi.org/10.1146/annurev.matsci.38.060407.130226.
[166] A.R. Yavari, J.J. Lewandowski, J. Eckert, MRS Bulletin. 2007, 635-63832(8), 10.1557/mrs2007.125.
[167] M.D. Demetriou, J.P. Schramm, C. Veazey, W.L. Johnson, J.C. Hanan, N.B. Phelps, Appl Phys Lett. 2007, 91(16), 10.1063/1.2799248.
[168] J. Schroers, C. Veazey, W.L. Johnson, Appl Phys Lett. 2003, 370-37282(3), 10.1063/1.1537514.
[169] B. Sarac, J. Ketkaew, D.O. Popnoe, J. Schroers, Advanced Functional Materials. 2012, 3161-316922(15), https://doi.org/10.1002/adfm.201200539.
[170] A.H. Brothers, D.C. Dunand, Acta Materialia. 2005, 4427-444053(16), https://doi.org/10.1016/j.actamat.2005.06.002.
[171] X. Wei, J.H. Chen, L.H. Dai, Scripta Materialia. 2012, 721-72466(10), https://doi.org/10.1016/j.scriptamat.2012.01.039.
[172] S.R. Hirshorn, Journal. 2007, (Issue),
[173] W. Wang, C. Dong, C. Shek, Materials Science and Engineering R: Reports. 2004, 45-8944(2-3), https://doi.org/10.1016/j.mser.2004.03.001.
[174] B.T. Lee, S.K. Sarkar, Scripta Materialia. 2009, 686-68961(7), https://doi.org/10.1016/j.scriptamat.2009.05.047.
[175] J. Wang, R. Li, N. Hua, T. Zhang, Journal of Materials Research. 2011, 2072-207926, https://doi.org/10.1557/jmr.2011.187.
[176] H.X. Li, Z.C. Lu, S.L. Wang, Y. Wu, Z.P. Lu, Progress in Materials Science. 2019, 235-318103, https://doi.org/10.1016/j.pmatsci.2019.01.003.
[177] J. Farmer, J.-S. Choi, C. Saw, J. Haslam, D. Day, P. Hailey, T. Lian, R. Rebak, J.H. Perepezko, J. Payer, D. Branagan, B. Beardsley, A. D'amato, L. Aprigliano, Metallurgical and Materials Transactions A. 2009, 1289-130540, https://doi.org/10.1007/s11661-008-9779-8.
[178] M. Davidson, S. Roberts, G. Castro, R.P. Dillon, A. Kunz, H. Kozachkov, M.D. Demetriou, W.L. Johnson, S. Nutt, D.C. Hofmann, Advanced Engineering Materials. 2013, 27-3315(1-2), https://doi.org/10.1002/adem.201200313.
[179] W.H. Wang, Progress in Materials Science. 2007, 540-59652(4),

https://doi.org/10.1016/j.pmatsci.2006.07.003.
[180] J. Qiao, H. Jia, P.K. Liaw, Materials Science and Engineering: R: Reports. 2016, 1-69100, https://doi.org/10.1016/j.mser.2015.12.001.
[181] M.J. Duarte, J. Klemm, S.O. Klemm, K.J.J. Mayrhofer, M. Stratmann, S. Borodin, A.H. Romero, M. Madinehei, D. Crespo, J. Serrano, S.S.A. Gerstl, P.P. Choi, D. Raabe, F.U. Renner, Science. 2013, 372-376341(6144), doi:10.1126/science.1230081.
[182] M.-X. Li, S.-F. Zhao, Z. Lu, A. Hirata, P. Wen, H.-Y. Bai, M. Chen, J. Schroers, Y. Liu, W.-H. Wang, Nature. 2019, 99-103569(7754), 10.1038/s41586-019-1145-z.
[183] P. Bordeenithikasem, Y. Shen, H.-L. Tsai, D.C. Hofmann, Additive Manufacturing. 2018, 95-10319, https://doi.org/10.1016/j.addma.2017.11.010.
[184] S. Chen, H. Cheng, K. Chan, G. Wang, Metals. 2018, 6898(9), https://doi.org/10.3390/met8090689.
[185] C. Zhang, D. Ouyang, S. Pauly, L. Liu, Materials Science and Engineering: R: Reports. 2021, 100625145, https://doi.org/10.1016/j.mser.2021.100625.
[186] D. Ouyang, P. Zhang, C. Zhang, L. Liu, Applied Materials Today. 2021, 10098823, https://doi.org/10.1016/j.apmt.2021.100988.
[187] P. Zhang, C. Zhang, L. Liu, Materials Research Letters. 2022, 377-38410(6), https://doi.org/10.1080/21663831.2022.2054291.
[188] A.G. Evans, J.W. Hutchinson, N.A. Fleck, M.F. Ashby, H.N.G. Wadley, Progress in Materials Science. 2001, 309-32746(3), https://doi.org/10.1016/S0079-6425(00)00016-5.
[189] Y. Lin, W. Shi, J. Li, Y. Liu, S. Liu, J. Li, Materials Science and Engineering: A. 2023, 144986872, https://doi.org/10.1016/j.msea.2023.144986.
[190] L. Zhang, S. Feih, S. Daynes, S. Chang, M.Y. Wang, J. Wei, W.F. Lu, Additive Manufacturing. 2018, 505-51523, https://doi.org/10.1016/j.addma.2018.08.007.
[191] S.J. Li, Q.S. Xu, Z. Wang, W.T. Hou, Y.L. Hao, R. Yang, L.E. Murr, Acta Biomater. 2014, 4537-4710(10), 10.1016/j.actbio.2014.06.010.
[192] S. Rajagopalan, R.A. Robb, Medical Image Analysis. 2006, 693-71210(5), https://doi.org/10.1016/j.media.2006.06.001.
[193] D. Ouyang, N. Li, L. Liu, J Alloy Compd. 2018, 603-609740, https://doi.org/10.1016/j.jallcom.2018.01.037.
[194] L.-Y. Chen, S.-X. Liang, Y. Liu, L.-C. Zhang, Materials Science and Engineering: R: Reports. 2021, 100648146, https://doi.org/10.1016/j.mser.2021.100648.
[195] L.J. Gibson, M.F. Ashby, Cellular solids : structure & properties, 2nd ed., Cambridge University Press, Cambridge, 1997.
[196] L.J. Gibson, M.F. Ashby, B.A. Harley, M.F. Ashby, B.A. Harley, Cellular materials in nature and medicine, Cambridge University Press, Cambridge ; New York, 2010.
[197] L. Zhang, B. Song, L. Yang, Y. Shi, Acta Biomater. 2020, 298-315112, https://doi.org/10.1016/j.actbio.2020.05.038.
[198] O. Alketan, R. Abu Al-Rub, R. Rowshan, Journal of Materials Research. 2018, 1-1733, https://doi.org/10.1557/jmr.2018.1.
[199] O. Alketan, R. Rowshan, R. Abu Al-Rub, Additive Manufacturing. 2018, 167–18319, https://doi.org/10.1016/j.addma.2017.12.006.
[200] J. Song, Y. Wang, W. Zhou, R. Fan, B. Yu, Y. Lu, L. Li, Composites Part B: Engineering.

2019, 402-411160, https://doi.org/10.1016/j.compositesb.2018.12.027.
[201] M. Mieszala, M. Hasegawa, G. Guillonneau, J. Bauer, R. Raghavan, C. Frantz, O. Kraft, S. Mischler, J. Michler, L. Philippe, Small. 2017, 160251413(8), https://doi.org/10.1002/smll.201602514.
[202] L.J. Gibson, M.F. Ashby, Proceedings of the Royal Society of London. Series A, Mathematical and Physical Sciences. 1982, 43-59382(1782), https://doi.org/10.1098/rspa.1982.0088.
[203] L.J. Gibson, M.F. Ashby, G.S. Schajer, C.I. Robertson, P Roy Soc Lond a Mat. 1982, 25-42382(1782), https://doi.org/10.1098/rspa.1982.0087.
[204] S. Wu, L. Yang, X. Yang, P. Chen, J. Su, H. Wu, Z. Liu, H. Wang, C. Wang, C. Yan, Y. Shi, Smart Manufacturing. 2022, 215000101(01), https://doi.org/10.1142/S2737549821500010.
[205] M. Mazur, M. Leary, S. Sun, M. Vcelka, D. Shidid, M. Brandt, The International Journal of Advanced Manufacturing Technology. 2016, 1391-141184(5), https://doi.org/10.1007/s00170-015-7655-4.
[206] H. Yin, Z. Liu, J. Dai, G. Wen, C. Zhang, Composites Part B: Engineering. 2020, 107565182, https://doi.org/10.1016/j.compositesb.2019.107565.
[207] L. Zhang, S. Feih, S. Daynes, S. Chang, M.Y. Wang, J. Wei, W.F. Lu, Journal of the European Ceramic Society. 2020, 408-41640(2), https://doi.org/10.1016/j.jeurceramsoc.2019.09.048.
[208] L. Zhang, H. Liu, B. Song, J. Gu, L. Li, W. Shi, G. Li, S. Zhong, H. Liu, X. Wang, J. Fan, Z. Zhang, P. Wang, Y. Yao, Y. Shi, J. Lu, Nature Communications. 2024, 204615(1), 10.1038/s41467-024-46337-1.
[209] B. Wijerathne, T. Liao, K. Ostrikov, Z. Sun, Small Structures. 2022, 21002283(9), https://doi.org/10.1002/sstr.202100228.
[210] S.D. Papka, S. Kyriakides, International Journal of Solids and Structures. 1998, 239-26735(3-4), https://doi.org/10.1016/S0020-7683(97)00062-0.
[211] Z. Huang, Z. Pan, H. Li, Q. Wei, X. Li, Journal of Materials Research. 2014, 1573-157829(14), https://doi.org/10.1557/jmr.2014.179.
[212] J. Sun, B. Bhushan, Rsc Advances. 2012, 7617-76322(20), 10.1039/C2RA20218B.
[213] Z. Xin, X. Zhang, Y. Duan, W. Xu, Composite Structures. 2018, 102-109184, https://doi.org/10.1016/j.compstruct.2017.09.075.
[214] N.S. Ha, G. Lu, Composites Part B: Engineering. 2020, 107496181, https://doi.org/10.1016/j.compositesb.2019.107496.
[215] S.H. Siddique, P.J. Hazell, H. Wang, J.P. Escobedo, A.A.H. Ameri, Additive Manufacturing. 2022, 10305158, https://doi.org/10.1016/j.addma.2022.103051.
[216] M.I. Osotsi, W. Zhang, I. Zada, J. Gu, Q. Liu, D. Zhang, Natl Sci Rev. 2021, nwaa1078(3), 10.1093/nsr/nwaa107.
[217] T. Sullivan, B. Wang, H. Espinosa, Mater Today. 2017, 20, 10.1016/j.mattod.2017.02.004.
[218] T. Yang, Z. Wu, H. Chen, Y. Zhu, L. Li, Acta Biomaterialia. 2020, 204-217107, https://doi.org/10.1016/j.actbio.2020.02.034.
[219] R.W. Corkery, E.C. Tyrode, Interface Focus. 2017, 201601547(4), doi:10.1098/rsfs.2016.0154.
[220] L. Wang, S. Qu, H. Fu, X. Zhou, J. Ding, H. Yang, Q. Zhao, X. Song, Y. Lu, Scripta

Materialia. 2024, 115801239, https://doi.org/10.1016/j.scriptamat.2023.115801.
[221] J.U. Surjadi, L. Gao, H. Du, X. Li, X. Xiong, N.X. Fang, Y. Lu, Advanced Engineering Materials. 2019, 180086421(3), https://doi.org/10.1002/adem.201800864.
[222] J. Ding, Q. Ma, X. Li, L. Zhang, H. Yang, S. Qu, M.Y. Wang, W. Zhai, H. Gao, X. Song, Advanced Science. 2024, 240272711(41), https://doi.org/10.1002/advs.202402727.
[223] Y. Amani, S. Dancette, P. Delroisse, A. Simar, E. Maire, Acta Materialia. 2018, 395-407159, https://doi.org/10.1016/j.actamat.2018.08.030.
[224] J. Cook, J.E. Gordon, C.C. Evans, D.M. Marsh, Proceedings of the Royal Society of London Series A. 1964, 508-520282, 10.1098/rspa.1964.0248.
[225] T. Yang, Z. Jia, Z. Wu, H. Chen, Z. Deng, L. Chen, Y. Zhu, L. Li, Nature Communications. 2022, 608313(1), 10.1038/s41467-022-33712-z.
[226] T. Yang, H. Chen, Z. Jia, Z. Deng, L. Chen, E.M. Peterman, J.C. Weaver, L. Li, Science. 2022, 647-652375(6581), doi:10.1126/science.abj9472.
[227] A.L. Greer, Y.Q. Cheng, E. Ma, Materials Science and Engineering: R: Reports. 2013, 71-13274(4), https://doi.org/10.1016/j.mser.2013.04.001.
[228] B. Sarac, J. Schroers, Nature Communications. 2013, 21584(1), 10.1038/ncomms3158.
[229] B. Sun, W. Wang, Progress in Materials Science. 2015, 211-30774,
[230] P. Wang, F. Yang, B. Zheng, P. Li, R. Wang, Y. Li, H. Fan, X. Li, Advanced Functional Materials. 2023, 230597833(45), https://doi.org/10.1002/adfm.202305978.
[231] G. Feng, S. Li, L. Xiao, W. Song, International Journal of Impact Engineering. 2023, 104554176, https://doi.org/10.1016/j.ijimpeng.2023.104554.
[232] P. Khanna, S. Sood, P. Mishra, V. Bharadwaj, A. Aggarwal, S. Singh, Structures. 2024, 10658064, https://doi.org/10.1016/j.istruc.2024.106580.
[233] L. Zhang, B. Song, L. Yang, Y. Shi, Acta Biomaterialia. 2020, 298-315112, https://doi.org/10.1016/j.actbio.2020.05.038.
[234] C. Yang, D. Ouyang, L. Zhang, Y. Zhang, X. Tong, H. Ke, K.C. Chan, W. Wang, Additive Manufacturing. 2024, 10412585, https://doi.org/10.1016/j.addma.2024.104125.
[235] C. Yang, J. Ding, S. Qu, D. Ouyang, L. Zhang, Y. Zhang, H.-B. Ke, X. Song, K.C. Chan, W.-H. Wang, Acta Materialia. 2025, 120688285, https://doi.org/10.1016/j.actamat.2024.120688.
[236] O. Al-Ketan, R. Rowshan, R.K. Abu Al-Rub, Additive Manufacturing. 2018, 167-18319, 10.1016/j.addma.2017.12.006.
[237] S. Chu, A. Majumdar, nature. 2012, 294-303488(7411),
[238] Y. Huang, M. Zhu, Y. Huang, Z. Pei, H. Li, Z. Wang, Q. Xue, C. Zhi, Adv Mater. 2016, 8344-836428(38), https://doi.org/10.1002/adma.201601928.
[239] J.R. McKone, S.C. Marinescu, B.S. Brunschwig, J.R. Winkler, H.B. Gray, Chemical Science. 2014, 865-8785(3),
[240] B. Tang, X. Yang, Z. Kang, L. Feng, Applied Catalysis B: Environmental. 2020, 119281278,
[241] F. Amiripour, S. Ghasemi, Fuel. 2023, 128299346,
[242] C. Wang, X. Shao, J. Pan, J. Hu, X. Xu, Applied Catalysis B: Environmental. 2020, 118435268,
[243] Y. Yao, Q. Dong, A. Brozena, J. Luo, J. Miao, M. Chi, C. Wang, I.G. Kevrekidis, Z.J. Ren,

J. Greeley, G. Wang, A. Anapolsky, L. Hu, Science. 2022, eabn3103376(6589), doi:10.1126/science.abn3103.
[244] Y. Yan, Y. Chen, M. Shao, J. Hou, X. Chen, L. Fan, F. Kong, M. Chen, Fuel. 2024, 131551367, https://doi.org/10.1016/j.fuel.2024.131551.
[245] S. Li, Z. Xin, Y. Luo, J. Pan, G. Liao, Q. Li, Y. Sun, Z. Feng, R. Tan, International Journal of Hydrogen Energy. 2024, 1081-110082, https://doi.org/10.1016/j.ijhydene.2024.08.026.
[246] A. Kazemi, F. Manteghi, Z. Tehrani, ACS Omega. 2024, 7310-73359(7), 10.1021/acsomega.3c07911.
[247] M.A. Qadeer, X. Zhang, M.A. Farid, M. Tanveer, Y. Yan, S. Du, Z.-F. Huang, M. Tahir, J.-J. Zou, Journal of Power Sources. 2024, 234856613, https://doi.org/10.1016/j.jpowsour.2024.234856.
[248] C. Han, Y. Yuan, G. Chen, Z. Ye, Z. Guo, Y. Zhao, ChemSusChem. 2024, e20240081217(22), https://doi.org/10.1002/cssc.202400812.
[249] D. Wu, J. Zhou, Y. Li, AIChE Journal. 2007, 2618-262953(10), https://doi.org/10.1002/aic.11291.
[250] M. Zakeri, S. Abdolreza, S.A. Mahdi, A. and Salehirad, Particulate Science and Technology. 2018, 96-10336(1), 10.1080/02726351.2016.1220437.
[251] J. Ren, Y. Du, Y. Wang, S. Zhao, B. Yang, B. Li, L. Wang, Chemical Engineering Journal. 2023, 143993469, https://doi.org/10.1016/j.cej.2023.143993.
[252] C. Pei, S. Chen, J. Xie, S. Feng, M. Yu, C. Zhan, Y. Qian, G. Yang, Y. Chen, S. Lan, E. Kan, D. Wang, X. Mu, H. Hahn, B. Sun, G. Wilde, T. Feng, Mater Today. 2025, https://doi.org/10.1016/j.mattod.2025.02.024.
[253] X. Jian, W. Zhang, Y. Yang, Z. Li, H. Pan, Q. Gao, H.-J. Lin, ACS Catalysis. 2024, 2816-282714(5), 10.1021/acscatal.3c05820.
[254] K. Wu, F. Chu, Y. Meng, K. Edalati, Q. Gao, W. Li, H.-J. Lin, Journal of Materials Chemistry A. 2021, 12152-121609(20), 10.1039/D1TA00769F.
[255] C. Pei, S. Chen, T. Zhao, M. Li, Z. Cui, B. Sun, S. Hu, S. Lan, H. Hahn, T. Feng, Adv Mater. 2022, 220085034(26), https://doi.org/10.1002/adma.202200850.
[256] F. Chu, X. Jian, K. Edalati, Y. Yan, H. Ke, P. Zhang, H.-J. Lin, J Alloy Compd. 2023, 170964960, https://doi.org/10.1016/j.jallcom.2023.170964.
[257] T. Li, Q. Dong, Z. Huang, L. Wu, Y. Yao, J. Gao, X. Wang, H. Zhang, D. Wang, T. Li, R. Shahbazian-Yassar, L. Hu, Adv Mater. 2022, 210643634(9), https://doi.org/10.1002/adma.202106436.
[258] S.A. Lee, J.W. Yang, S. Choi, H.W. Jang, Exploration. 2021, 202100121(3), https://doi.org/10.1002/EXP.20210012.
[259] D.K. Rajak, M. Gupta, Applications of Metallic Foams, in: D.K. Rajak, M. Gupta (Eds.), An Insight Into Metal Based Foams: Processing, Properties and Applications, Springer Singapore, Singapore, 2020, pp. 21-37.
[260] X. Shan, J. Liu, H. Mu, Y. Xiao, B. Mei, W. Liu, G. Lin, Z. Jiang, L. Wen, L. Jiang, Angewandte Chemie International Edition. 2020, 1659-166559(4), https://doi.org/10.1002/anie.201911617.
[261] Y. Liao, S. Deng, Y. Qing, H. Xu, C. Tian, Y. Wu, Journal of Energy Chemistry. 2023, 566-57576, https://doi.org/10.1016/j.jechem.2022.10.007.

[262] J. Feng, J. Fu, X. Yao, Y. He, International Journal of Extreme Manufacturing. 2022, 0220014(2), 10.1088/2631-7990/ac5be6.
[263] K.-L. Yan, J.-F. Qin, Z.-Z. Liu, B. Dong, J.-Q. Chi, W.-K. Gao, J.-H. Lin, Y.-M. Chai, C.-G. Liu, Chemical Engineering Journal. 2018, 922-931334, https://doi.org/10.1016/j.cej.2017.10.074.
[264] A. Li, L. Zhang, F. Wang, L. Zhang, L. Li, H. Chen, Z. Wei, Applied Catalysis B: Environmental. 2022, 121353310,
[265] D. Wu, D. Chen, J. Zhu, S. Mu, Small. 2021, 210277717(39),
[266] P. Zhai, Y. Zhang, Y. Wu, J. Gao, B. Zhang, S. Cao, Y. Zhang, Z. Li, L. Sun, J. Hou, Nature Communications. 2020, 546211(1), 10.1038/s41467-020-19214-w.
[267] J. Wang, M. Zhang, G. Yang, W. Song, W. Zhong, X. Wang, M. Wang, T. Sun, Y. Tang, Advanced Functional Materials. 2021, 31(33), 10.1002/adfm.202101532.
[268] G. Xiong, Y. Chen, Z. Zhou, F. Liu, X. Liu, L. Yang, Q. Liu, Y. Sang, H. Liu, X. Zhang, Advanced Functional Materials. 2021, 200958031(15),
[269] L. Qi, Z. Zheng, C. Xing, Z. Wang, X. Luan, Y. Xue, F. He, Y. Li, Advanced Functional Materials. 2022, 210717932(11),
[270] T. Gao, X. Li, X. Chen, C. Zhou, Q. Yue, H. Yuan, D. Xiao, Chemical Engineering Journal. 2021, 130416424,
[271] D. Cao, H. Xu, D. Cheng, Applied Catalysis B: Environmental. 2021, 120600298,
[272] N. Logeshwaran, S. Ramakrishnan, S.S. Chandrasekaran, M. Vinothkannan, A.R. Kim, S. Sengodan, D.B. Velusamy, P. Varadhan, J.-H. He, D.J. Yoo, Applied Catalysis B: Environmental. 2021, 120405297,
[273] Y. Yang, H. Yao, Z. Yu, S.M. Islam, H. He, M. Yuan, Y. Yue, K. Xu, W. Hao, G. Sun, H. Li, S. Ma, P. Zapol, M.G. Kanatzidis, Journal of the American Chemical Society. 2019, 10417-10430141(26), 10.1021/jacs.9b04492.
[274] L. Wang, L. Zhang, W. Ma, H. Wan, X. Zhang, X. Zhang, S. Jiang, J.Y. Zheng, Z. Zhou, Advanced Functional Materials. 2022, 220334232(31), https://doi.org/10.1002/adfm.202203342.
[275] C. Li, W. Zhang, Y. Cao, J.-Y. Ji, Z.-C. Li, X. Han, H. Gu, P. Braunstein, J.-P. Lang, Advanced Science. 2024, 240178011(28), https://doi.org/10.1002/advs.202401780.
[276] J. Zhou, F. Pan, Q. Yao, Y. Zhu, H. Ma, J. Niu, J. Xie, Applied Catalysis B: Environmental. 2022, 121811317, https://doi.org/10.1016/j.apcatb.2022.121811.
[277] J.-C. He, D.-C. Duan, Y.-C. Du, Z.-Q. Ding, S.-S. Yan, X. Chen, H. Zhang, X.-X. Bi, R.-Y. Wang, X.-B. Ge, Rare Metals. 2025, 10.1007/s12598-024-03035-7.
[278] M.S. Pham, C. Liu, I. Todd, J. Lertthanasarn, Nature. 2019, 305-311565(7739), 10.1038/s41586-018-0850-3.